University of Zagreb

FACULTY OF SCIENCE
DEPARTMENT OF PHYSICS

Lucija Sudić

STUDY OF ASSOCIATED W AND Z BOSON PRODUCTION IN PROTON PROTON COLLISIONS WITH THE CMS DETECTOR AT THE LARGE HADRON COLLIDER

DOCTORAL THESIS

Zagreb, 2017.

Sveučilište u Zagrebu

PRIRODOSLOVNO-MATEMATIČKI FAKULTET

Lucija Sudić

PROUČAVANJE ZAJEDNIČKE TVORBE BOZONA W I Z DETEKTOROM CMS U SUDARIMA PROTONA I PROTONA NA VELIKOM HADRONSKOM SUDARIVAČU

DOKTORSKI RAD

Zagreb, 2017.

University of Zagreb

FACULTY OF SCIENCE
DEPARTMENT OF PHYSICS

Lucija Sudić

STUDY OF ASSOCIATED W AND Z BOSON PRODUCTION IN PROTON PROTON COLLISIONS WITH THE CMS DETECTOR AT THE LARGE HADRON COLLIDER

DOCTORAL THESIS

Supervisor: Professor Vuko Brigljević, PhD

Zagreb, 2017.

Sveučilište u Zagrebu

PRIRODOSLOVNO-MATEMATIČKI FAKULTET

Lucija Sudić

PROUČAVANJE ZAJEDNIČKE TVORBE BOZONA W I Z DETEKTOROM CMS U SUDARIMA PROTONA I PROTONA NA VELIKOM HADRONSKOM SUDARIVAČU

DOKTORSKI RAD

Mentor: Prof. dr. sc. Vuko Brigljević

Zagreb, 2017.

Doktorski rad izrađen je na Institutu Ruđer Bošković u Zavodu za eksperimentalnu fiziku.

Mentor: prof. dr. sc. Vuko Brigljević

Acknowledgements

I would like to thank all the people who helped me during my work at CMS and with this thesis. Thanks to collegues from Instituto de Fisica de Cantabria and Universidad de Oviedo for their effort and collaboration in this measurement.
I would like specially thank to Cory Fantasia from Boston University. Although I never met him personally he spent hours with me on Skype, helping me with pat tuple production at my very beginings in the CMS, while everyone was on summer holidays.

I would like to thank all members of CMS group from Ruđer Bošković Institute. Thanks to Srećko for helping me fight with the CMS code in the beginnings and fighting my weird errors in code. Thanks to Jelena for sharing with me her little genial hacks for making everyday fight with the code easier, for discussions about physics, for understanding and for being a good friend. Thanks to Senka, Tanja, Benjamin, Darko and Saša for all the help, interesting discussions and for making our group nice working environment. Special thanks to my supervisor Vuko Brigljević for all the help during this years: for long discussions, for understanding and patience.

Posbno želim zahvaliti cijeloj svojoj obitelji na pomoći i potpori. Bez vas nikada ne bih završila. Hvala svekrvi Dubravki, svekru Draženu i šogoru Matiji na ohrabrenjima i bodrenjima, ali i na pomoću svakodnevnim dužnostima koja mi je omogućila da više vremena posvetim doktoratu. Hvala mami Jadranki, tati Đuru, sestrama Mihaeli, Ozani, Mariji Katarini i bratu Ivu. Hvala što ste imali strpljenja, što ste čuvali Tomislava, pospremali stan, kuhali ručak i hrabrili me. Hvala mužu Ivanu, na velikoj potpori svih ovih godina, na svim razgovorima, strpljenju, čuvanju Tomislava, pomoći oko borbe sa latex errorima i što si me spriječio da odustanem na samom kraju. Na kraju, hvala mom sinu Tomislavu što se pobrinuo da se svaki dan smijem i budem sretna.

Abstract

In this thesis a measurement of WZ production cross section is presented. Total and differential cross sections are measured by the CMS experiment at the CERN LHC in proton-proton collision data samples corresponding to an integrated luminosity of 19.6 fb^{-1} at $\sqrt{s} = 8$ TeV. The measurements are performed using the fully-leptonic WZ decay modes with electrons and muons in the final state. The measured total cross section for $71 < m_Z < 111$ GeV is $\sigma(\text{pp} \to \text{WZ}) = 24.09 \pm 0.87(\text{ stat.}) \pm 1.62(\text{ syst.}) \pm 0.63(\text{ lumi.})$ pb.
Differential cross sections with respect to the Z boson p_T, the leading jet p_T, and the number of jets are obtained. The results are consistent with standard model predictions.

Key words: LHC, CMS, Standard model, WZ, cross section

Contents

List of Figures

List of Tables

Chapter 1

Introduction

The Large Hadron Collider (LHC), located at the European Organization for Nuclear Research (CERN) in Switzerland, is the particle collider which operates at today's highest energies. The LHC is designed for achieving center-of-mass energies up to 14 TeV in proton-proton collisions. In 2010 and 2011, which marked the beginning of the collider operation, collision energies were limited up to 7 TeV due to technical constraints. Besides yielding the largest energy collisions ever achieved at a collider, the LHC has also achieved very high beam intensities, which enables us to have a unique insight into processes with small cross sections, previously unavailable for study. The Standard Model (SM) of elementary particles predicts a large variety of processes. Among them is the production of the Higgs boson, whose discovery was announced in July 2012. Apart from the confirmation of the validity of the SM at this new energy scale, a central objective of the LHC is the detection and discovery of new particles and interactions not described in the SM, if they are within reach of the LHC energies. Such discoveries could also lead to explanations of astrophysiscal observations, such as the presence of large amounts of dark matter in the Universe. Some theoretical models are offering answers to those questions (e.g. supersymmetric theories) and predict deviations from the SM detectable at the LHC. In addition to the proton collision program, the LHC devoted part of the year to collisions of heavy ion nuclei (e.g. Pb), to create and study quark-gluon plasma, a state of matter which is predicted to have existed in the early stages of the Universe.

The measurement of the production of electroweak heavy vector boson pairs (diboson production) in proton-proton collisions represents an important test of the SM description of electroweak and strong interactions at the TeV scale. Diboson production is sensitive to the self-interactions between electroweak gauge bosons as predicted by the $SU(2)_L \times U(1)_Y$ gauge structure of electroweak interactions. Triple and quartic gauge couplings (TGCs and QGCs) can be affected by new physics phenomena involving new particles at higher energy scales. The WZ cross section measured in this paper is sensitive to WWZ couplings, which are non-zero in the SM. The WZ production also represents an important background in several searches for

physics beyond the SM.

Chapter 2

Standard Model of particle physics

The Standard Model of particle physics combines all our current knowledge about particles and their interactions. It has been thoroughly tested in laboratories at all available energies and also with the LHC. The final formulation of the SM incorporates several theories: quantum electrodynamics, the Glashow-Weinberg-Salam theory of electroweak processes and quantum chromodynamics [4]. The first steps towards a formulation of the SM occured in 1961. when Glashow unified electromagnetic and weak interactions. The difference in strength between the weak and electromoagnetic forces was puzzling for physicists at that time, and Glashow proposed that it can be accounted for if the weak force were mediated by massive bosons. However, he was not able to explain the origin of the mass for such mediators. The explanation came in 1967 when Steven Weinberg and Abdul Salam used the Higgs mechanism in the electroweak theory, which suggested the existence of an additional particle called Higgs boson [5, 6]. After the discovery of neutral currents, which arise from the exchange of the neutral Z boson, the electroweak theory became generally accepted. The W and Z bosons were discovered in 1983 at CERN [7, 8], and their masses were in agreement with the SM prediction. The theory describing strong interactions got its final form in 1974 when it was shown that hadrons consist of quarks. The final missing part of the SM, the Higgs boson, was discovered in 2012 at CERN [9, 10]. So far SM predictions were confirmed through numerous experimental tests, however, there are several unexplained phenomena which suggest the existence of physics beyond SM. In this chapter small introduction to the SM together with mechanisms of WZ production in SM and in some models beyond SM physics will be given.

2.1 Standard Model overview

We usually imagine particles as point like objects which are subject to some forces between them. These particles are fermions, leptons and quarks of spin 1/2. There are three charged leptons: electron, muon and tau whose properties are the same except for their mass. Each of

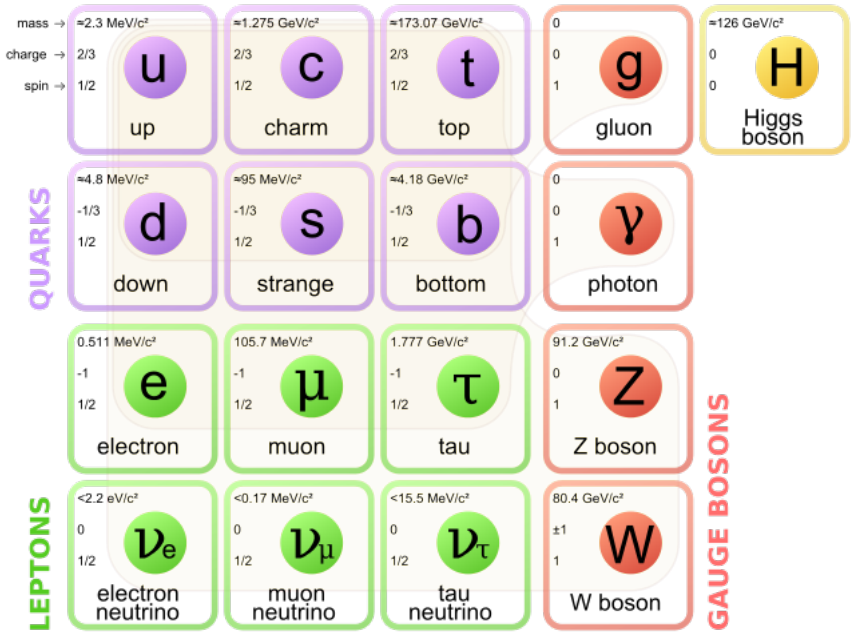

Figure 2.1: List of elementary particles in SM. Source: Wikimedia

the leptons has corresponding neutrally charged neutrino with a very small mass. There are six different types of quarks with charge either $Q = 2/3$ or $Q = -1/3$ as seen in Figure 2.1. Quarks also carry one additional quantum number: colour charge. All objects observed in nature are colorless, giving rise to the concept of quark confinement, which will be explained later. Colourless composite objects are classified into two categories: baryons and mesons. Baryons are made out of three quarks (e.q. proton, neutron). Mesons are made of a quark and an anti-quark (e.q. pions). There are three generations of quarks with identical properties except for the masses of the particles.

The SM is based on the gauge symmetry $SU(3)_C \times SU(2)_L \times U(1)_Y$. Strong interaction symmetries are described by $SU(3)_C$ group while the electroweak sector is described by the $SU(2)_L \times U(1)_Y$. All interactions within SM are mediated by elementary particles which are spin 1 bosons. In the case of electromagnetic interactions, the mediator is the massless photon, Thus the range of electromagnetic interaction is infinite. For the weak force the mediators are the three massive bosons $W^{\pm}$ and Z and its range is very small (10^{-16} m). These four bosons are the linear combinations of gauge fields of the $SU(2)_L \times U(1)_Y$ group. The interaction between electroweak bosons is allowed in the SM as long as charge conservation principle remains valid. The strong force is mediated by the exchange of 8 massless gauge bosons for $SU(3)_C$ called gluons. Although gluons are massless, the range of the strong force is approximately the size of the lightest hadrons (10^{-13}cm).

Particles are classified based on their spin: fermions, half integer spin fields, and bosons, integer-spin particles. Fermions can be further divided into quarks and leptons depending on

whether they interact in terms of strong interaction or only through the electroweak interaction. For the electroweak interaction the quantum numbers of charge are: the third projection of the weak isospin T_3 and the weak hypercharge. Electromagnetic charge Q_{EM} is derived using relation $Y_W = 2\left(\frac{Q_{EM}}{e} - T_3\right)$.

2.2 Electroweak interaction

In the langauge of Quantum field theory fermions can be described by the fermionic quantum field operator ψ of spin 1/2, or Dirac spinor. The Lagrangian of a free fermion with mass m is

$$\mathscr{L}_D = \bar{\psi}(i\gamma^\mu \partial_\mu - m)\psi \tag{2.1}$$

Dirac Lagrangian is trivially invariant under the global (constant) phase transformation $\psi \to e^{i\Phi}\psi$. The local gauge invariance requires the Dirac Lagrangian to be invariant under the field phase transformation $\psi \to e^{i\phi(x)}\psi$ where $\phi(x)$ is an arbitrary complex function of the space-time coordinates. For this, it is necessary to introduce a gauge field A^μ which interacts with the fermion field and transforms simultaneously with the Dirac field as

$$\psi \to \psi' = e^{i\phi(x)}\psi \qquad A_\mu \to A'_\mu - \frac{1}{e}\partial_\mu \phi(x) \tag{2.2}$$

The Dirac Lagrangian incorporating the interaction term $e\bar{\psi}\gamma^\mu A_\mu \psi$ becomes

$$\mathscr{L}_D = \bar{\psi}(i\gamma^\mu(\partial_\mu + ieA_\mu) - m)\psi \equiv \bar{\psi}(i\gamma^\mu D_\mu - m)\psi \tag{2.3}$$

where $D_\mu \equiv \partial_\mu + ieA_\mu$ is the covariant derivative. Under the local gauge transformation, the Lagrangian becomes

$$\mathscr{L}_D \to \bar{\psi}(i\gamma^\mu(\partial_\mu + ieA'_\mu + i\partial_\mu\phi - i\partial_\mu\phi) - m)\psi' = \bar{\psi}'(i\gamma^\mu D'_\mu - m)\psi' \tag{2.4}$$

The D_μ transforms in a same way as ψ itself, leading to the gauge invariance of the Lagrangian. The Lagrangian term for the gauge field A_μ:

$$\mathscr{L} = -\frac{1}{4}F^{\mu\nu}F_{\mu\nu} \qquad F_{\mu\nu} \equiv \partial_\mu A_\nu - \partial_\nu A_\mu = D_\mu A_\nu - D_\nu A_\mu \tag{2.5}$$

represents the electromagnetic field and is also gauge invariant.

The weak interaction is known to violate parity as it is not acting symmetrically under the interchange of positive-chirality and negative-chirality fermions. Thus the left-handed and

right-handed part of the Dirac field must be treated separately.

$$\psi = \psi_L + \psi_R \qquad \psi_L = P_L\psi \quad \psi_R = P_R\psi \tag{2.6}$$

where the left and right projection operators are:

$$P_L = \frac{1-\gamma_5}{2} \quad P_R = \frac{1+\gamma_5}{2} \tag{2.7}$$

the electron, muon and tau leptons have both L and R components, while neutrinos only have L component. Therefore the following "isospinors" can be constructed:

$$\begin{gathered} L_e = \begin{pmatrix} \nu_e \\ e_L \end{pmatrix} \quad L_\mu = \begin{pmatrix} \nu_\mu \\ \mu_L \end{pmatrix} \quad \begin{pmatrix} \nu_\tau \\ \tau_L \end{pmatrix} \\ R_e = e_R \quad R_\mu = \mu_R \quad R_\tau = \tau_R \end{gathered} \tag{2.8}$$

The left doublets are assigned a weak isospin, $T = 1/2$ with a third projection $T_3 = 1/2$ for the neutrino component and T_3=-1/2 for the charged lepton component, while right handed singlets have $T = 0$. The resulting Langragian

$$\mathscr{L} = \sum_{l=e,\mu,\tau} (i\bar{R}_l \partial\!\!\!/ R_l + i\bar{L}_l \partial\!\!\!/ L_l) \tag{2.9}$$

is invariant under rotations in the isospin (SU(2)) space. Under these rotations only left doublet transforms, while right singlets remain invariant

$$\begin{aligned} L_l &\to e^{-i\frac{\vec{\tau}}{2}\vec{\alpha}} L_l \\ R_l &\to R_l \end{aligned} \tag{2.10}$$

where $\frac{\vec{\tau}}{2}$ are the generators of the $SU(2)$ group.
R_l singlets only transform under the $U(1)_Y$ symmetry and the corresponding field B_μ. As electromagnetism is known to exist free of parity violation, this puts a requirement on doublets L_l to also transform under this symmetry. The respective charge is already mentioned weak hypercharge defined by the Gell-Mann-Nishijima relation $\frac{Q_{EM}}{e} = T_3 + \frac{Y}{2}$. From the definition of weak isospin for the left doublets and right singlets, it follows that L_l has hypercharge $Y_W = -1$ and R_l has $Y_W = -2$. Transformation under $U(1)_Y$ gauge group is therefore

$$\begin{aligned} L_l &\to e^{-i\frac{\beta}{2}} L_l \\ R_l &\to e^{-i\beta} R_l \end{aligned} \tag{2.11}$$

The gauge invariant electroweak Lagrangian is obtained by constructing a covariant derivative

through introduction of the three gauge fields $\vec{W}_\mu$ (denoted also with W^i_μ where $i = 1,2,3$) associated to the $SU(2)_L$ and the $U(1)_Y$ B_μ field,

$$D_\mu = \partial_\mu - ig\frac{\vec{\tau}}{2}\vec{W}_\mu + i\frac{g'}{2}Y_W B_\mu \quad (L) D_\mu = \partial_\mu + i\frac{g'}{2}Y_W B_\mu \quad (R) \tag{2.12}$$

The electroweak Lagrangian includes kinematic terms for the gauge fields as

$$-\frac{1}{4}\vec{W_{\mu\nu}}\vec{W^{\mu\nu}} - \frac{1}{4}B_{\mu\nu}B^{\mu\nu} \tag{2.13}$$

where the field strength tensors are

$$\begin{aligned} \vec{W_{\mu\nu}} &= \partial_\mu \vec{W}_\nu - \partial_\nu \vec{W}_\mu + g\vec{W}_\mu \times \vec{W}_\nu \\ B_{\mu\nu} &= \partial_\mu B_\nu - \partial_\nu B_\mu \end{aligned} \tag{2.14}$$

The full electroweak Lagrangian can be written as:

$$\begin{aligned} \mathscr{L} = &-\frac{1}{4}\vec{W_{\mu\nu}}\vec{W^{\mu\nu}} - \frac{1}{4}B_{\mu\nu}B^{\mu\nu} \\ &+\bar{\psi_L}\gamma^\mu(i\partial_\mu - g\frac{\vec{\tau}}{2})\vec{W_m}u - \frac{g'}{2}Y_W B_\mu)\psi_L \\ &+\bar{\psi_R}\gamma^\mu(i\partial_\mu - \frac{g'}{2}Y_W B_\mu))\psi_R \end{aligned} \tag{2.15}$$

The electromagnetic interaction acts identically on left handed and right handed fermions. Therefore the B field alone cannot be responsible for it due to differing coupling strengths to left and right handed fields (due to different weak hypercharge). However it is possible to define physical fields A_μ and Z_μ (as well ass $W^\pm_\mu$) as linear combinations of the gauge fields:

$$\begin{aligned} Z_\mu &= \cos\theta_W W^3_\mu - \sin\theta_W B_\mu \\ A_\mu &= \cos\theta_W B_\mu - \sin\theta_W W^3_\mu \\ W^\pm_\mu &= \frac{1}{\sqrt{2}}(W^1_\mu \mp W^2_\mu) \end{aligned} \tag{2.16}$$

where θ_W is the electroweak mixing angle, linking the electromagnetic charge e to the weak coupling constants

$$e = g\sin\theta_W = g'\cos\theta_W \tag{2.17}$$

The field A_μ represents the electromagnetic interaction and generates the photon, while Z_μ, W^+_μ and W^-_μ generate the weak mediators, the Z and $W^\pm$ bosons.
Equivalent formalism of left and right field component under $SU(2)$ can be applied also to

quarks:

$$L_1 = \begin{pmatrix} u_L \\ d'_L \end{pmatrix} \quad L_2 = \begin{pmatrix} c_L \\ s'_L \end{pmatrix} \quad L_3 = \begin{pmatrix} t_L \\ b'_L \end{pmatrix}$$
$$R_1 = d'_R \quad R_2 = s'_R \quad R_3 = b'_R \tag{2.18}$$

The d', s' and b' are linear combination of quark mass eigenstates with the mixing parametrized by the Cabibbo-Kobayashi-Maskawa (CKM) matrix

$$\begin{pmatrix} d' \\ s' \\ b' \end{pmatrix} = \begin{pmatrix} V_{ud} & V_{us} & V_{ub} \\ V_{cd} & V_{cs} & V_{cb} \\ V_{td} & V_{ts} & V_{tb} \end{pmatrix} \begin{pmatrix} d \\ s \\ b \end{pmatrix} \tag{2.19}$$

While the Standard Model in general respects the combination of the two symmetries, charge-conjugation and parity symmetry (CP), leading to identical treatment of particles and antiparticles with inverted charges and parity and exactly the same mass, a possibility of violation arises as a consequence of a complex phase in the CKM matrix. CP violation has been detected experimentally first in K^0 meson decays [11] and later in other measurements [12–16]. QCD also allows CP violation. However this has not been observed experimentally, thus resulting in the strong CP problem, where the CP violating QCD parameter $\bar{\theta}$ appears to be unnaturally small.

2.3 Quantum chromodynamics

Quantum chromodynamics (QCD) is a theory of strong interactions. The interaction arises from the introduction of the $SU(3)$ gauge invariance. Boson fields which are introduced to preserve the local gauge invariance are called gluons. The QCD Lagrangian is:

$$\mathscr{L}_{QCD} = \bar{\psi}_i (i(\gamma^\mu D_\mu)_{ij} - m\delta_{ij})\psi_j - \frac{1}{4} G^a_{\mu\nu} G^{\mu\nu}_a \tag{2.20}$$

where quarks are described by a field ψ_i with $i \in 1..3$ and the QCD covariant derivative is:

$$D_\mu = \partial_\mu + i g_s A^a_\mu \lambda_a \tag{2.21}$$

where g_s is a strong coupling constant, A^a_μ is a gluon gauge field and λ_a is one of the Gell-Mann matrices with $a \in [1..8]$. As in QED, the fields term in 2.21 has to be introduced by the gauge invariance, with the field tensor $G^a_{\mu\nu}$ defined as

$$G^a_{\mu\nu} = \partial_\mu A^a_\nu - \partial_\nu A^a_\mu + g f^{abc} A^b_\mu A^b_\nu \tag{2.22}$$

where the third term containing the f^{abc} structure constant and the gauge coupling parameter g reflects the non-abelian nature of QCD. In the Lagrangian, this term allows non-vanishing terms with three or four field tensors and therefore couplings between gluon.
A distinct property of the strong interaction is asymptotic freedom: the strong interaction is weaker at short distances between quarks, and becomes stronger as they are pulled apart. The effective coupling in renormalizable theories is described by the beta function [17, 18] which describes the variation of the theory's coupling constant depending on the scale of the momentum transfer (which increases at shorter distances). For $SU(N)$ groups with n_f quark flavors the beta function is:

$$\beta_1(\alpha) = \frac{\alpha^2}{\pi}\left(\frac{-11N}{6} + \frac{n_f}{3}\right) \tag{2.23}$$

For QCD parameters N=3 and $n_f = 6$, the resulting beta function is negative, leading to the the asymptotic freedom. As a consequence , coloured particles are *confined*, i.e the interaction strength with other coloured particles (e.q. proton constituents) increases with distance and prevent their separation. Only neutrally coloured particle compositions can escape the confinement and be observed as free states.

2.4 The Higgs mechanism

In the described formulation, all fermionic fields and gauge bosons are massless which is of course not consistent with observations. It is not possible to simply include mass terms and preserve the gauge invariance. A solution to this problem lies in the introduction of the spontaneous symmetry breaking mechanism [19].
To achieve breaking of the global $SU(2) \times U(1)$ symmetry, a $SU(2)$ doublet with the weak hypercharge $Y_W = 1$ is constructed:

$$\Phi = \begin{pmatrix} \phi^+ \\ \phi^0 \end{pmatrix} = \frac{1}{\sqrt{2}}\begin{pmatrix} \phi_1 + i\phi_2 \\ \phi_3 + i\phi_4 \end{pmatrix} \tag{2.24}$$

where $\phi_1, ..\phi_4$ are components of the complex field Φ, called the Higgs field. The doublet is invariant under $U(1)_Y$ transformations. A Lagrangian term for the field is introduced as

$$\mathscr{L}_\Phi = (D_\mu \Phi)^\dagger (D^\mu \Phi) - V(\Phi) \tag{2.25}$$

where $V(\Phi)$ is potential defined as:

$$V(\Phi) = \mu \Phi^\dagger \Phi + \frac{\lambda}{4}(\Phi^\dagger \Phi)^2 \tag{2.26}$$

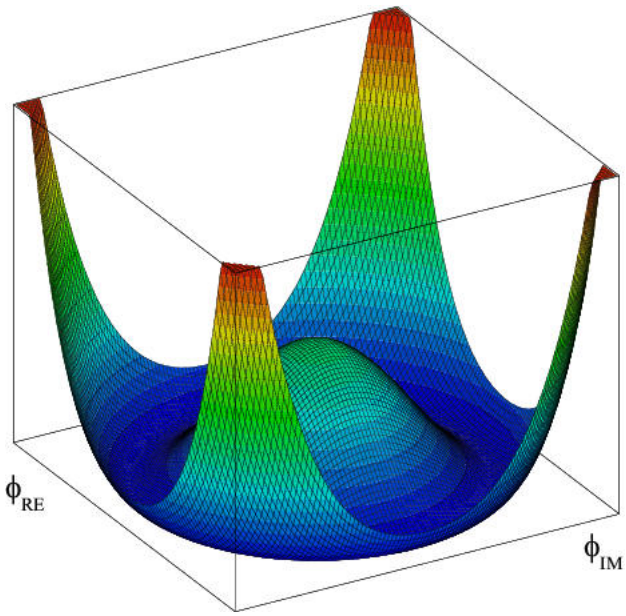

Figure 2.2: Higgs potential. Source Wikimedia

For a regime where $\lambda > 0$ and $\mu^2 < 0$, the potential forms a "Mexican hat" shape as a function of the field Φ, as illustrated in Figure 2.2. The minimum of the potential is not at the value of the field $\Phi = 0$ and is instead located at a continuous circle in the complex plane satisfying the condition:

$$min(\Phi\Phi^\dagger) = -\frac{\mu^2}{2\lambda} \tag{2.27}$$

This can be interpreted as the condition of the vacuum expectation value (*vev*)

$$\langle 0|\Phi^\dagger\Phi|0\rangle = \frac{v^2}{2} \tag{2.28}$$

where $|0\rangle$, the initial (lowest potential) vacuum state, does not share the initial symmetry of the potential. The *vev* can be obtained through the measurement of the Fermi constant in muon decays:

$$\frac{G_F}{\sqrt{2}} = \frac{g^2}{8M_W} = \frac{1}{2v^2} \tag{2.29}$$

The Fermi constant is $G_F = 1.6637 \cdot 10^{-15}\text{GeV}^{-2}$, resulting in $v \approx 245$ GeV.
The appropriate choice of potential at the minimum is

$$\langle 0|\Phi_0|0\rangle = \frac{1}{\sqrt{2}}\begin{pmatrix}0\\v\end{pmatrix} \tag{2.30}$$

A consequence of such a choice of Φ_0 is the breaking of the three degrees of freedom associated with the flat plane of the potential, resulting with the appearance of three Goldstone bosons. These massless bosons are integrated as longitudinal spin components into the W and Z boson fields which thus acquire mass. The photon remains massles, as the Φ_0 has neutral charge and

$U(1)_{EM}$ remains unbroken.
In the first order expansion around the minimum, the field expressed in terms of the real fields $\theta(i)_i (i = 1,2,3)$ and $H(x)$ is

$$\Phi(x) = \frac{-exp(\vec{\theta}(x) \cdot \vec{\tau}/2)}{\sqrt{2}} \begin{pmatrix} 0 \\ v + H(x) \end{pmatrix} \tag{2.31}$$

It can be shown that the $\vec{\theta}(x)$ fields can be gauged away by choosing an appropriate $SU(2)$ gauge, the so called *unitarity gauge*, and the expanded field becomes:

$$\Phi(x) = \frac{1}{\sqrt{2}} \begin{pmatrix} 0 \\ v + H(x) \end{pmatrix} \tag{2.32}$$

The expanded scalar potential is thus

$$V = \frac{\mu^2}{2}(v+H)^2 + \frac{\lambda}{4}(v+H)^4 \tag{2.33}$$

The combined Lagrangian is:

$$\begin{aligned} \mathscr{L}_{G\phi} = & \frac{1}{2}\partial_\mu \partial^\mu H \\ & + \frac{1}{8} g^2 (v+H)^2 (W_\mu^1 - iW_\mu^2)(W^{1\mu} + iW^{2\mu}) \\ & + \frac{1}{8}(v+H)^2 (g' B_\mu - g W_\mu^3)(g' B^\mu - g W^{3\mu}) \\ & - \frac{\mu^2}{2}(v+H)^2 - \frac{\lambda}{16}(v+H)^4 \\ & - \frac{1}{4}\vec{W}_{\mu\nu}\vec{W}^{\mu\nu} - \frac{1}{4} B_{\mu\nu} B^{\mu\nu} \end{aligned} \tag{2.34}$$

In the fourth row there is a term proportional to H^2 which describes a scalar field with the mass $m_H = \sqrt{2}\mu = \sqrt{\lambda v/2}$. λ remains a free parameter and the Higgs mass is therefore not fixed in the model. In the same row there are also terms proportional to H^3 and H^4 which describe the Higgs self-coupling. After retaining only mass terms related to vector boson fields and using identities 2.16, the Lagrangian becomes:

$$\mathscr{L}_{\text{vector boson mass terms}} = \frac{v g^2}{4} W_\mu^+ + W^{\mu -} + \frac{v^2}{8}(g^2 + g'^2)(Z_\mu)^2 + o(A_\mu)^2 \tag{2.35}$$

It follows that the masses acquired by the W and Z bosons are

$$m_W = \frac{1}{2}\sqrt{v^2 g^2} \qquad m_Z = \frac{1}{2}\sqrt{(g^2 + g'^2)v^2} \tag{2.36}$$

while the photon does not acquire mass.

Mass terms for fermions can be introduced in a gauge invariant way through Yukawa couplings, where the scalar field couples left and right projection of fermionic fields (2.8 and 2.10):

$$\mathscr{L}_{Yukawa} = -g_f(\bar{L}_f)\Phi R_f + \bar{R}_f\Phi^{\dagger}L_f \tag{2.37}$$

Substitution of the expanded Higgs field 2.32 results in

$$\mathscr{L}_{Yukawa} = g_f\frac{v+H(x)}{\sqrt{2}}(\bar{\psi}_L\psi_R + \bar{\psi}_R\psi_L) = -\frac{v}{\sqrt{2}}\bar{\psi}\psi - \frac{H(x)}{\sqrt{2}}\bar{\psi}\psi \tag{2.38}$$

with the first terms equivalent to the Dirac mass term, while the second term allow fermionic coupling to the Higgs field. Coupling strength is proportional to the fermion mass as

$$m_f = g_f\frac{v}{\sqrt{2}} \tag{2.39}$$

2.5 Physics at hadron colliders

Hadrons are described as bound states of quarks and gluons (partons) that interact via strong interaction. Therefore, QCD plays a fundamental role in the description the physics produced by proton-proton collisions. The theoretical calculations of the low-energy regime of the interacting partons inside the proton are subject to non-perturbative (soft) QCD. However, when considering a high energy collision, the interactions take places at small distances between the partons of the two incoming protons giving rise to a collision with high-momentum transfer, called the hard scattering. The partons involved in the hard scattering can be considered as free partons because of asymptotic freedom. The strong force coupling constant α_S depends on the scale of the process. For high momentum transfers ($Q >> \Lambda_{QCD} \approx 200$ MeV) it becomes sufficiently small to make perturbative expansion in α_S possible. This feature is called *asymptotic freedom* and allows us to determine the hard process cross section. Using perturbative expansions in α_S in order to calculate the observables of the hard scattering. The soft and hard aspects of hadron colliders collisions can be split because of the *factorization theorem*, which states that hard scattering between partons is independent from the proton internal structure. The perturbative and process-dependent scattering can be separated from the non-preturbative but universal (process-independent) structure inside the proton. Qualitatively, the hard scattering taking place with a momentum transfer Q^2 has a typical timescale of $1/Q$. The soft interactions inside the proton have an energy typically close to the QCD scale, i.e. Λ_{QCD}, therefore with a typical interaction timescale of $1/\Lambda_{QCD}$. Hard scattering processes, as vector boson production, usually have $Q >> \Lambda_{QCD}$, the time scale of the hard scattering is much shorter than the soft physics in inside the proton. Therefore, during the hard scattering interaction, the internal structure of the proton in not going to change significantly and thus can be determined before the interaction

took place. The internal structure of a hadron is summarized by a set of probability distributions of quarks and gluons, called Parton Distribution Functions (PDF). These PDFs encapsulate all the non-perturbative QCD that determines the probability of finding a parton of a given flavour and momentum inside a hadron. The calculation of cross section of a hard scattering involves the amplitudes for hard scattering between partons which must be convoluted with the PDF in order to incorporate the probability of finding the necessary partons and its energy for the hard scattering.

The valence quarks in the case of the proton are two u and one d quark. The total sum of valence quarks charges yields the overall charge of the hadron. Those valence quarks are continuously interacting by exchange of gluons and those gluons can also self-interact to produce more gluons or produce additional quark-antiquark pairs, called *sea quarks*. The momentum of the hadron is distributed amongst valence quarks, sea quarks and gluons. The PDFs describe the probability to find a parton with a given fraction of the hadron momentum , i.e. $p_i = xP_i$, where p_i is the momentum of the parton i carrying a fraction x of the hadron momentum P. At low energies, the three valence quarks essentially carry all of the hadron's momentum. But when the energy transfer is large, $Q^2 \gtrsim 1$ GeV, the other substructure components of the hadron, sea quarks and gluons can be resolved. The hadron substructure depends on Q^2 because partons at high x tend to radiate and drop down to lower values of x, while at the same time additional new partons at low x arise from radiation. Therefore, with increasing energy of the hadron, the hadron momentum is shared amongst a larger number of constituents, although the valence quarks tend to carry a significant fraction of the hadron momentum. The PDFs take the form $f_i(x, Q^2)$ where i is the parton type, x is the momentum fraction, and Q^2 is the scale. The PDF cannot be calculated from first principles due to the presence of non-perturbative effects, but the evolution of the PDFs with Q^2 can be calculated [20]. The PDFs are obtained by a fit to experimental data at one scale and then evolved to different scales.

2.6 WZ production

2.6.1 WZ production in the Standard Model

The associated production of a W and a Z boson is possible in the SM through several modes, one of which involves the direct coupling between heavy gauge bosons. This self-coupling is a consequence of the non-abelian nature of the $SU(2) \times U(1)$ gauge symmetry, whose generators don't commute (as in the third $\vec{W}_{\mu\nu}$ term in 2.14). The $-\frac{1}{4}\vec{W}_{\mu\nu}\vec{W}^{\mu\nu}$ term of the electroweak

Lagrangian can be expanded as

$$\begin{aligned}\frac{1}{4}\vec{W}_{\mu\nu}\vec{W}^{\mu\nu} &= 2[\partial_\mu W_\nu^- - \partial_\nu W_\mu^- - ig\cos\theta_W(W_\mu^- Z_\nu - W_\nu^- Z_\mu) - ie(W_\mu^- A_\nu - W_\nu^- A_\mu)] \\ &\times[\partial_\mu W^{+\nu} - \partial^\nu W^{+\mu} + ig\cos\theta_W(W^{+\mu}Z^\nu - W^{+\nu}Z_\mu) + ie(W^{+\mu}A_\nu - W^{+\nu}A_\mu)] \\ &+[\cos\theta(\partial_\mu Z_\nu - \partial_\nu Z_\mu) + \sin\theta(\partial_\mu A_\nu - \partial_\nu A_\mu) + ig(W_\mu^- W_\nu^+ - W_\nu^- W_\mu^+)] \\ &\times[\cos\theta(\partial^\mu Z^\nu - \partial^\nu Z^\mu + \sin\theta(\partial^\mu A^\nu - \partial^\nu A^\mu) + ig(W^{-\mu}W^{+\nu} - W^{+\nu}W^{+\mu}))\end{aligned} \tag{2.40}$$

The expansion contains terms allowing triple and quartic couplings of vector bosons. In the case of the *triple gauge couplings* (TGC), the Lagrangian term, using identities in 2.16, becomes

$$\mathscr{L}_{WWV}^{TGC} = ig_{WWV}[(W_{\mu\nu}^- W^{+\mu} - W_{\mu\nu}^+ W^-\nu)V^\nu + V_{\mu\nu}W^{+\mu}W^{-\nu}] \tag{2.41}$$

where the operator V^μ is A^μ or Z^μ, the field strength tensors are defined as $W_{\mu\nu}^\pm = \partial_\mu W_\nu^\pm - \partial_\nu W^\pm$ and $V_{\mu\nu} = \partial_\mu V_\nu - \partial_\nu V_\mu$, and the coupling constants are $g_{WWZ} = g\cos\theta_W$ and $g_{WW\gamma} = e$. It can be shown that only TGC couplings involving $W^\pm$ boson fields are allowed in the Standard Model.

At the LHC, the WZ production mainly unfolds through quark-antiquark interaction in proton-collisions. There is an excess of valence u over d quarks in protons leading to an asymmetry between the cross section of W^+Z and W^-Z production [21]. Precisely, the probability for a charged current interaction of a u quark with an antiquark (where W^+ is produced) is higher than the probability for a d quark interaction with an antiquark (where a W^- is produced).

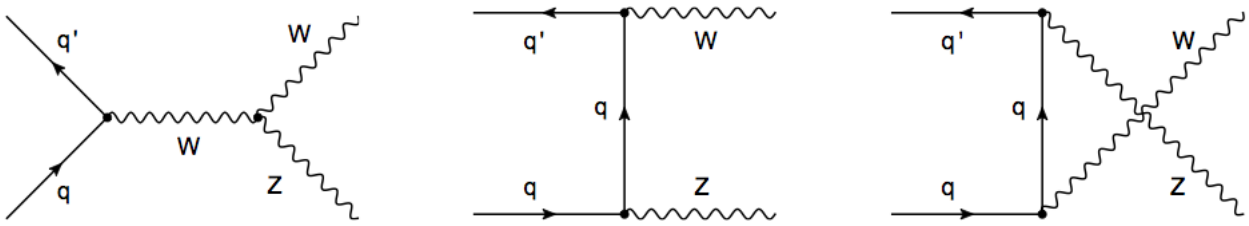

Figure 2.3: Leading-order Feynman diagrams for WZ production in proton-proton collisions. The three diagrams represent contributions from (left) *s*-channel through TGC, (middle) *t*-channel, and (right) *u*-channel

WZ is produced through several contributions, for which leading order Feynman diagrams are shown in Figure 2.3. The TGC or s-channel contribution is described by first diagram. It represents production of a virtual W boson (if Z is on shell) with sufficiently high invariant mass to allow decay into the W and Z pair. In the t-channel mode (second diagram), W and Z are emitted by quark and antiquark exchange through a mediator quark.

WZ production has been measured on Tevatorn [22, 23] and LHC [22, 23] so far. The W and Z decay can result in fully leptonic ($W \to l\nu$, $Z \to l^+l^-$), semi leptonic ($W \to l\nu$, $Z \to qq$ or

Table 2.1: W and Z boson branching ratio [1] and branching ratios of WZ final states

W decay	W Br(%)	Z decay	Z Br(%)
$e^{\pm}\nu$	10.75	$e^{+}e^{-}$	3.363
$\mu^{\pm}\nu$	10.57	$\mu^{+}\mu^{-}$	3.366
$\tau^{\pm}\nu$	11.25	$\tau^{+}\tau^{-}$	3.370
hadronic	67.60	hadronic	69.91
		$\bar{\nu}\nu$	20.0
WZ final states			
	Br(%)		Br(%)
$eee\nu$	0.3615	$\mu\mu e\nu$	0.3555
$ee\mu\nu$	0.3618	$\mu\mu\mu\nu$	0.3558
$lll\nu$	3.329	$4j$	47.26
$lljj$	6.827	$\nu\mu l\nu$	6.51
$jjl\nu$	22.77	$\nu\nu jj$	13.52

$W \to qq, Z \to l^{+}l^{-}$) or purely hadronic ($W \to qq, Z \to qq$) final states where l, ν and q represent charged leptons (later referred just as leptons), neutrinos and quarks respectively. Branching ratios of W and Z bosons are reported in Table 2.1. Their low branching ratio for leptonic decays results in only approx. 0.35% WZ branching ratio for each combination of leptonic W and Z decay mode (s channel). However, the leptonic final states have a very clean signatures compared to decay modes with jets (hadronic modes), allowing a better discrimination from hadronic backgrounds which have a high presence at hadron colliders such as the LHC.

2.6.2 WZ production through non Standard Model processes

Various extensions of the Standard Model predict the existance of a new heavy charged gauge boson, generically known as W', that decays into a pair of W and Z bosons. A new gauge boson could arise if there are additional gauge symmetry present, often found in Grand Unifyng Theories (GUTs) which try to encompass QCD and the electroweak sector under a unified gauge symmetry (e.g. $SU(5)$)

Chapter 3

Experimental setup: The CMS Detector at the Large Hadron Collider

3.1 The Large Hadron Collider

CERN is the largest particle physics laboratory in the world, located near the city of Geneva, on the French-Swiss border. It was founded in 1954 by 12 countries. Today it consists of 22 member states. Its main function is to provide particle accelerators and infrastructure for high energy experiments. Major physics results at CERN include the discovery of neutral currents, the discovery of W and Z bosons, creation of antihydrogen atoms and direct observation of CP violation among others.

The Large Hadron Collider [2] located at CERN is currently the most powerful collider in the world.The LHC was installed in the existing LEP tunnel, a 26.7 km ring consisting of eight straight sections connected by eight arcs, housed at a depth of 45 m to 170 m near the France-Switzerland border. Beams circulating inside the LHC, collide at four interaction points. At each of these points, a detector has been built to record the products of particle collisions. This thesis was done using data collected with the CMS [24](Compact Muon Solenoid) detector. Another detector with the same purpose but different design is the ATLAS [25] (A Toroidal LHC Apparatus) detector located at the opposite side of the LHC ring. These two are so called multiple purpose particle detectors as they cover a wide range of physics topics, from searches for the Higgs boson, supersymmetry and many other beyond Standard Model manifestations, to SM precision measurements. ALICE (A Large Ion Collider Experiment)[26] is designed to study quark-gluon plasma by measuring mainly lead-lead collisions and in addition lead-proton and proton-proton collisions. LHCb (LHC Beauty) [27] is optimized for the detection of B-hadrons and hence the study of B decay. Two other experiments TOTEM and LHCf are placed away from the interaction point to measure the collision products along the beam direction.

The use of the existing LEP tunnel for the LHC accelerator created the design challenges for the

LHC, specifically in terms of the size and power of magnets needed to direct the LHC proton beams. The CERN accelerator complex includes a series of components which progressively accelerate the proton beams to higher energies (Figure 3.2). The LEP injection chain is used to accelerate the protons to an energy of 450 GeV before entering the main ring. The first stage uses the Linac2 to boost the protons to 50 MeV in a series of radio frequency (RF) cavities. Next the Proton Synchrotron Booster(PSB) accelerates to 1.4 GeV and then the Proton Synchrotron (PS) to 24 GeV. The Super Proton Synchrotron (SPS) accelerates protons up to the full injection energy of 450 GeV. Once they reach the LHC, the bunched charged particles are accelerated by 400 MHz RF cavities resulting in high energy bunches of protons with 25 ns gaps or multiples of it.
Since the start of the LHC in 2009, there were three years of machine operation, which yielded many physics results among which the discovery of a Higgs boson should be highlighted. The first year of operation, when LHC center of mass energy was 900 GeV, was devoted to commissioning and understanding the machine characteristics with the emphasis on safety and test of the machine protection systems. In 2010 new energy of 7 TeV broke the record of 1.96 TeV previously set by the Tevatron. This record was superseded once again in 2012 with center of mass energy going to 8 TeV.

The achieved high bunch intensity with 50 ns bunch spacing resulted in a good instantaneous luminosity performance. This came at cost of high number of collisions in one bunch crossing (pile-up) which was around 12 collisions during 2011, and in some cases this number went as high as 20 interactions. With increase of instantaneous luminosity in 2012, number of pile-up interactions was even higher. Besides proton-proton collisions, LHC successfully delivered lead-lead ion runs, primarily for the ALICE experiment, but also for CMS and ATLAS. On top of that, in the beginning of 2013 there was a successful proton-lead run performed for the first time. Some LHC design parameters together with the achieved values during 2012 shown in Table 3.1.

Table 3.1: LHC performance in 2012 together with design performance [2]

Parameter	Design value	Value in 2012
Beam energy [TeV]	7	4
Bunch spacing [ns]	25	50
Number of bunches	2808	1374
Protons per bunch	1.15×10^{11}	$1.6 - 1.7 \times 10^{11}$
Peak luminosity [cm^{-}2s^{-}1]	1×10^{34}	7.7×10^{33}
Max. number of events per bunch crossing	19	≈ 40
Stored beam energy [MJ]	362	$\approx$140

Due to their higher mass protons loose less energy than electrons via synchrotron radiation

which allows to reach higher energies. The main production process for the Higgs boson, and many other massive particles in high energy proton-(anti)proton is gluon fusion. Since gluon density functions are identical in proton and antiproton and production of high intensity antiproton beams is much more challenging and expensive, proton-proton collisions were the better choice. The pp design of the LHC allows it to achieve instantaneous luminosities beyond those seen in the Tevatron $p\bar{p}$ collisions.

The luminosity (L) indicates the number of collisions per unit of time over interaction cross section σ:

$$L = \frac{1}{\sigma}\frac{dN}{dt} \tag{3.1}$$

The instantaneous luminosity for a symmetric colliding beam experiment such as the LHC is given as:

$$L = \frac{nN^2 f}{A_{eff}} \tag{3.2}$$

where n is the number of bunches per beam, N the number of particles per bunch, f the revolution frequency, and A_{eff} the effective cross-sectional area of the beams. The beams are focused in each of the transverse directions (σ_x and σ_y) which can be used to calculate the value of $A_{eff} = 4\pi\sigma_x\sigma_y$. The amount of data collected in a certain period of time is expressed by the total integrated luminosity, defined as:

$$\mathscr{L} = \int L dt \tag{3.3}$$

During the Run 1 data taking period the LHC delivered around 24 fb^{-1} of data (Figure 3.1) at the energy of 8 TeV with highest instantaneous luminosity of $8 \cdot 10^{33}\text{cm}^{-2}\text{s}^{-1}$.

During *Long shutdown* (LS) consolidation work on the LHC was carried out, that allowed to accelerate protons to the record energy of 6.5 TeV per beam, which is close to the design. In 2015 LHC run (*Run2*) has begun with a peak luminosity of $5 \times 10^{33}\text{cm}^{-2}\text{s}^{-1}$ at a bunch spacing of 25 ns, which allowed to keep the number of simultaneous pp-interactions per crossing (pileup) low. The total integrated luminosity delivered before LS is shown on the Figure 3.1.

3.2 The CMS detector

The Compact Muons Solenoid (CMS) is designed as a multi-purpose detector for studying a wide variety of processes from proton as well as heavy ion collisions. It consists of a large number of detector systems placed concentrically around the beam collision point. It contains

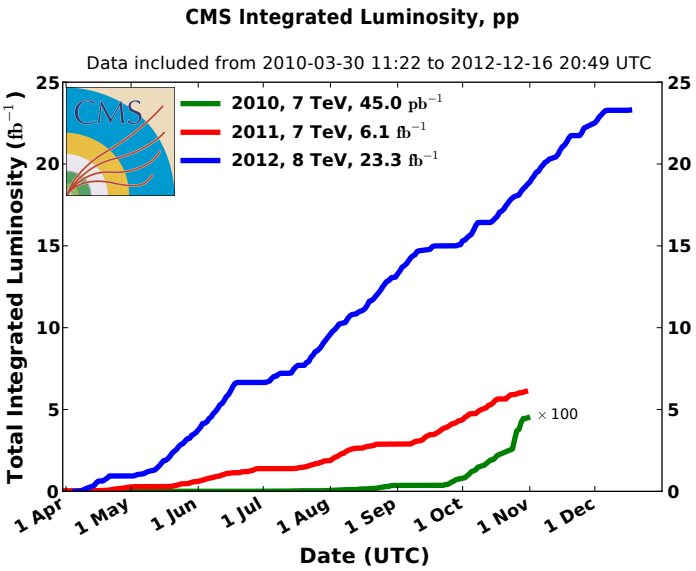

Figure 3.1: Luminosity delivered to the CMS experiment

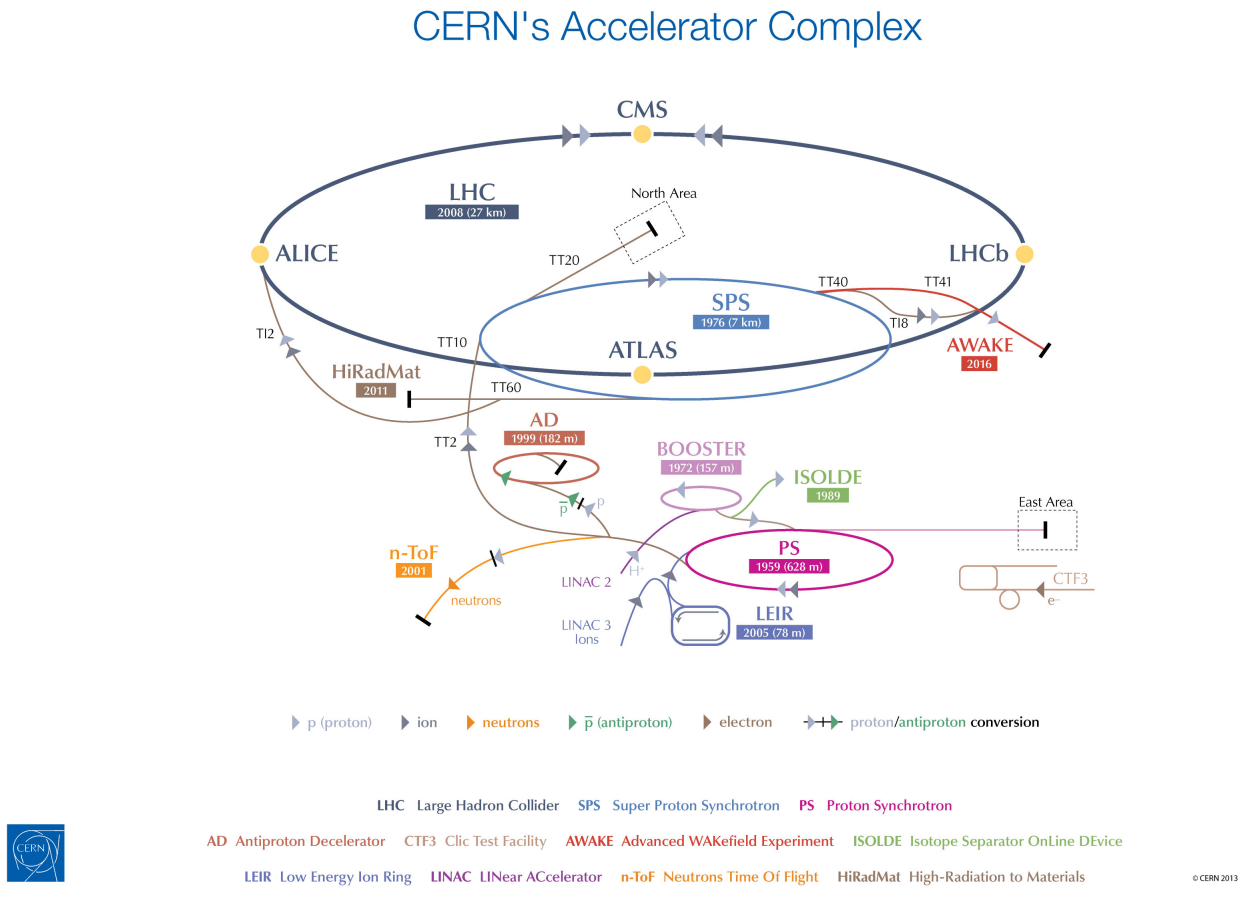

Figure 3.2: CERN accelerator complex

tracking detectors for the measurement of charged particle trajectories, calorimeters, which measure the energy of single particles or hadronic jets, and muon detectors located in the outer layers because muons are particles which reach the outer parts of the detector with a small loss of energy. Considering that it is almost hermetically sealed, it is able to detect with high efficiency particles arising from collisions. This is especially true for interactions with particles having high transverse momentum, of order of magnitude several GeV or higher with respect to the beam axis, characteristic for interactions with high exchange of energy and momentum.

The CMS detector is installed about 100 meters underground close to the French village of Cessy, between Lake Geneva and the Jura mountains. A prime motivation of the LHC was to elucidate the nature of electroweak symmetry breaking for which the Higgs mechanism is presumed to be responsible.

The detector requirements for CMS to meet the goals of the LHC physics programme can be summarised as follows:

- Good muon identification and momentum resolution over a wide range of momenta and angles, good dimuon mass resolution (approx. 1% at 100 GeV), and the ability to determine unambiguously the charge of muons with $p \leq 1$ TeV;
- Good charged-particle momentum resolution and reconstruction efficiency in the inner tracker. Efficient triggering and offline tagging of τ's and b-jets, requiring pixel detectors close to the interaction region.
- Good electromagnetic energy resolution, good diphoton and dielectron mass resolution (approx 1% at 100 GeV), wide geometric coverage, π^0 rejection, and efficient photon and lepton isolation at high luminosities;
- Good missing-transverse-energy and dijet-mass resolution, requiring hadron calorimeters with large hermetic geometric coverage and with fine lateral segmentation.

The main distinguishing features of CMS are a high field solenoid, a full-silicon-based inner tracking system, and a homogeneus scintillating-crystals-based electromagnetic calorimeter.

3.2.1 Coordinate system

The coordinate system has its origin centered at the nominal collision point inside the experiment, the $y-$axis pointing vertically upward, and $x-$axis pointing radially inward toward the center of the LHC. Thus, the $z-$axis points along the beam direction toward the Jura mountains from LHC Point 5. The azimutal angle ϕ is measured from the $x-$axis in the $x-y$ plane. The polar angle θ is measured from the $z-$axis. Pseudorapidity is defined as $\eta = -\ln\tan(\theta/2)$. Thus, the momentum and energy measured transverse to the beam direction, denoted by p_T and E_T, respectively, are computed from the x and y components. The imbalance of energy in the transverse plane is denoted by E_T^{miss}.

CMS consists of subdetector modules grouped in the so called central *barrel* region, and detach-

able *endcaps* which are fitted on both sides of the central region. The pseudorapidity boundary at which the barrel region end is roughly at $\eta \approx \pm 1.5$. The exact bounday, however, depends more precisely on the subdetector considered. Often, angular distances or cones are expressed by ΔR, defined as

$$\Delta R = \sqrt{\Delta\eta^2 + \Delta\phi^2} \tag{3.4}$$

3.2.2 Magnet

The CMS magnet provides a nearly homogeneous $B = 3.8$ T field in the whole inner volume of around 300m^3. By the stored energy, it is the most powerful magnet ever built. The strong magnetic field results in higher particle trajectory curvature, which gives high sensitivity for estimating momentum of particles at the TeV scale. Muon detectors in the outside range operate under a 2 T field enhanced by the massive iron yoke.

3.2.3 Tracker

The closest subdetector to the interaction point is the tracker, which is based on silicon semiconductor technology. Fine granularity in the innermost part is essential to identify the different vertices in a bunch crossing. Vertices correspond to the interaction points of the proton collisions (primary vertices) or the displaced decays of short-lived particles (secondary vertices).
The sensors are constructed as reversed-biased p-n diodes, which yield a detectable current when the bias voltage across the diode is lowered by the ionization depositions caused by passing charged particle. Charged particle excites electrons which jump over the band gap, resulting with charged vacancies and free electrons. The high voltage imposed on the detector separated charges and they are collected as an electric pulse, indicating a particle "hit" or passage through the sensor.
The tracks can be divided into three regions containing detectors with different characteristics for regions with different particle fluxes.
The particle flux is highest closest to the interaction point, and pixel detectors are placed there. Dimensions of pixel are 100×150 μm^2 along the $(r-\phi)$ and the z coordinates. The position resolution for reconstructed particle is $\approx 10\mu$m in the r-ϕ plane and 20μm along z. There are 3 layers of hybrid pixel detectors at radii 4, 7, and 11 cm.
In the intermediate region (20$\leq$r$\leq$55 cm), the particle flux is low enough to enable the use of silicon microstrip detectors with a minimum cell size of 10cm$\times$80 μm.
In the outermost region (55 cm $\leq$r$\leq$120 cm) of the inner tracker, the particle flux has dropped sufficiently to allow use of larger-pitch silicon microstrips with a maximum cell size of 25 cm x 180 μm.

3.2.4 Electromagnetic calorimeter

The Electromagnetic Calorimeter (ECAL) is designed to detect and precisely measure the energy of electrons and photons. Placing the ECAL inside the magnet, one avoids the significant degradation seen in previous hadron collider experiment due to interactions with magnet material. This requires the ECAL to be compact, and therefore made with highly transparent and dense interacting material. Lead tungstate ($PbWO_4$) fulfils this condition. It has high density (8.28 g/cm^{-3}), short radiation length (0.89 cm) and small Moliere radius* (2.2 cm). This enables absorption of electron and photon showers with reasonably short crystals. The ECAL is a hermetic, homogeneous calorimeter comprising 61200 lead tungstate crystals in the central barrel part in the range $|\eta| \leq 1.4442$, closed by 7324 crystals in each endcap in the range $1.566 \leq |\eta| \leq 3.0$.
Radiation damage is manifested as a change in crystal transparency, resulting in non-uniform scintillation light transmittance as a function of time. This is monitored and corrected by using a laser calibration system that records the change in transparency.

3.2.5 Hadronic calorimeter

The hadronic calorimeter (HCAL) is surrounding the ECAL. The HCAL is designed to detect particles which primarily interact with atomic nuclei via the strong force. Strongly interacting particles typically start showering in the ECAL. A measurement of a particle energies should therefore combine information from both calorimeters. The HCAL consists of three sub-systems: the HCAL barrel (HB), which covers $|\eta| \leq 1.305$, the HCAL endcap (HE) in the range $1.305 \leq |\eta| \leq 3.0$ and the HCAL forward (HF) in the range $3.0 \leq |\eta| \leq 5.0$. In the barrel region it consists of layers of brass, which acts as a non-ferromagnetic absorber, and plastic scintillator layers. Showers occur mostly in the brass layers, and are detected in the scintillator layers, where they are absorbed by fibres and remitted in the narrow wavelength range that photo detectors collect. The encap regions use steel as absorber and quartz as scintillator for higher radiation resistance, The hadronic jet shower usually starts in the ECAL and propagates into HCAL layers so the measurements from both subdetectors contribute to the energy measurement. The particles produced in nuclear interactions of hadronic particles with the brass travel through the scintillating material and produce light. The collected light is used as an estimate of the energy of the shower. In the case of HF, the Cherenkov radiation from the particles in the evolving shower traversing quartz fibres is used as energy estimate.

*The Moliere radius is a characteristic constant of a material giving the scale of the transverse dimension of the fully contained electromagnetic showers initiated by an incident high energy electron or proton [28].

3.2.6 Muon system

Muons produced in proton collisions in the center of CMS are measured in the inner tracker and in the muon chambers placed outside of the magnet.
The muon system consists of three types of gaseous particle detectors optimized for different environments and goals - drift tubes (DT) in the barrel($|\eta| \leq 1.2$), cathode strip chambers (CSC) in the endcaps ($|\eta| \leq 2.4$), and resistive plate chambers (RPC) covering nearly the entire barrel and endcap regions. Drift tubes are filled with gas. Each tube contains an anode wire held at high voltage and two cathode strips on either side. gas is ionized by passing particles and the charges are collected by wires held at high voltage.The position determination is based on the measured drift time of the collected charge. In the endcaps, where DTs would be challenged by increased rate, CSCs are used. These are multi-wire proportional chambers composed of multiple anodes which collect the charge from the gas ionization and serve as proportional counters. RPCs are found in both, barrel and endcaps. They consist of parallel plates imposing uniform electric field on the gas in the gap. Electrodes found on the plates are highly resistive. When a muon causes ionization, the resulting electron avalanche passes through the plates and is collected by external metallic strips. While inferior in spatial resolution compared to DT and CSCs, RPCs provide superior time resolution and are able to identify muons coming from a specific bunch crossing. Therefore they are used for triggering.

3.2.7 Reconstruction of objects

Reconstruction is the operation of extracting physics quantities from the raw detector signals collected in the experiment. Detector signals are hits in the tracker and muon chambers which can be reconstructed in tracks and clusters in the calorimeter and in reconstruction process we get physics objects such as muons, electrons, jets... The reconstruction process can be divided into 3 steps, corresponding to: local reconstruction within an individual detector module, global reconstruction within a whole detector, and combination of these reconstructed objects to produce higher-level objects.

3.2.8 Trigger

The LHC provides proton-proton and heavy-ion collisions at high interaction rates. In the 2010-2012, the physics program has been executed at a rate of up to 20 MHz, corresponding to bunch crossing intervals of 50 ns. Detector records of interactions at each bunch crossing are called events. Depending on luminosity, several collisions occur at each crossing of the proton bunches (approximately 20 simultaneous pp collisions at the nominal design luminosity of $10^{34}\text{cm}^{-2}\text{s}^{-1}$). Since it is impossible to store and process the large amount of data associated with the resulting high number of events, a drastic rate reduction has to be achieved. This task

is performed by the trigger system, which is the start of the physics event selection process. The rate is reduced in two steps, called Level-1 (L1) Trigger and High-Level Trigger (HLT), respectively. The Level-1 Trigger consists of custom-designed, largely programmable electronics, whereas the HLT is a software system implemented in a filter farm of about one thousand commercial processors, The rate reduction capability is designed to be at least a factor of 10^6 for the combined L1 Trigger and HLT. The first level trigger selects events in less than 1μs, while the HLT further decreases the event rate from around 100 kHz to about 300 Hz before data storage. At the HLT events are accepted if they match at least one of hundreds of different "interesting" signatures in the detector.

3.2.9 Data processing and simulation

To predict the results of colliding protons involves modelling of the makeup of a proton, the calculation of scattering amplitudes, the hadronization of quarks and gluons into hadrons and the decay of unstable particles. Next the response of the detector to these final state particles must be modelled. The knowledge of detector materials and positions of these materials is necessary for accurate modelling of the detector response. "Monte Carlo" techniques are generally used, in which a random number generator is interfaced with the equation governing a certain process in order to produce large number of simulated collision events. The simulation of proton-proton collisions happens in several steps, each being specialized to emulate a particular aspect of particle collisions. The first stage is a matrix element calculation which describes the differential cross section for a given hard scattering process. The next stage takes the coloured partons (quarks) and gluons produced in the hard scattering interaction along with any radiated gluons and describes how they hadronize into colorless composite particles in a parton showering process. The following stage describes the underlying event consisting of soft interactions of the spectator partons which did not directly participate in the hard scattering. These programs rely on parametrizations tuned first by input from previous colliders extrapolated to LHC energies and later retuned based on data from initial LHC runs. A detailed description of the CMS detector and magnetic field is used as input to the GEANT4 package [29], a software toolkit for simulating the passage of particles through the CMS detector.

3.2.10 Luminosity measurement

The luminosity is measured by CMS either based on the activity in the forward hadronic calorimeter (HF) or the pixel tracker. The HF measurement, performed in the pseudorapidity range $3<|\eta|<5$, relies on the fraction of non-empty calorimetric towers to estimate the number of interactions. The overall accuracy of the HF-based luminosity measurement in 2012 is 2.6% [30]. The dominant uncertainty comes from the nonlinear response of the HF to luminosity and

the afterglow, wherein energy originating from a given bunch crossing creates a small response in subsequent bunch crossings. Accounting for this effects requires complex corrections with consequential increase in the systematic uncertainty. The more precise luminosity measurement method was devised using the pixel tracker [31]. The advantage of this method is that pixel clusters are, due to their small cross section, rarely exposed to simultaneous hits of multiple tracks, resulting in low saturation, and thus a highly linear response to luminosity in the operating range of the LHC. The average number of cluster hits is proportional to the per-bunch instantaneous luminosity L_B as

$$< N_{cluster} >= \frac{\sigma_{cluster}}{f} L_B \tag{3.5}$$

where the orbital frequency f =11.246 kHz and the pixel cluster cross section $\sigma_{cluster}$ can be precisely estimated from the Van der Meer scan [32], a procedure involving dynamically modified transverse beam separation.

Chapter 4

Physics objects definition

In this chapter the physics objects used in this analysis are presented. Since the WZ signature in the detector is 3 leptons and missing energy, the main objects of interest are electrons, muons and missing transverse energy. In the second part of this analysis the differential cross section as a function of transverse momentum of Z, number of jets and leading jet transverse momentum is computed. Therefore jets are also relevant object of interest in this analysis.
First the process of reconstruction of candidates in the CMS detector is described. Aftewards the selection to ensure the quality of candidates and to reject background is described.

4.1 Muons

4.1.1 Reconstruction of muons

Detailed description of muon reconstruction in CMS detector can be found in [33, 34]. Muon is detected as charged track in the tracker which can be connected to a track in the muon chambers. Due to the 3.8 T longitudinal magnetic field in the tracker and $\approx$ 2T field in the muon chambers in the opposite direction, the muon trajectory is curved in opposite orientations in the tracker and in the muon chambers. Reconstruction of muon starts from a seed in the innermost muon chambers, used as a starting point by a *standalone* algorithm which uses a Kalman-filter [35] * technique to fit individual track segments from chambers into a standalone muon track. This is followed by a *global muon* algorithm which matches the standalone track to a track found in the inner tracker, respecting their geometrical and kinematic compatibility. A global muon momentum is calculated using hits from all available systems. Because of better measurement of the track curvature this approach results in improved momentum precision compared to the standalone algorithm or a tracker-only measurement especially for muons with p_T >100 GeV. Alternatively, if the reconstruction is performed by matching the inner track with track segments

*Track fitting that uses an iterative algorithm to correctly account for the effects of multiple scattering and energy loss along the track tajectory

in the muon system, a *tracker muon* is produced.
The degree of curvature gives the muon transverse momentum, while the orientation of the curvature determines its charge. For a global muon, these parameters are mainly based on the tracker information, because of the very precise inner tracking system. However the combination of these two systems becomes important for muons with high momentum where the reduced bending of the muon tracks limits the p_T resolution of the inner tracking measurement. Muons are detected in the range $|\eta|\leq$2.4 by spatially matching the tracks from the inner tracker and the outer muon system, resulting in a transverse momentum (p_T) resolution of 1-5% for muons with p_T up to 1 TeV.

4.1.2 Muon selection

For any muon object considered in this analysis, a transverse momentum requirement of $p_T >$ 10 GeV is imposed. Global and tracker muons are used in the analysis. Global muons are required to have a good fit quality, χ^2/ndof<10. Tracker muons with the requirement that it has to be matched to track segments in two different muon stations at 3σ in local X and Y coordinates with one being in the outermost muon station which suppress accidental track-to-segments matches and punch through hadrons. This is useful to reject muons from hadrons decaying in flight and kaons punching through the calorimeter.
The track has to be built with more than 5 hits in inner tracker layers and with at least one hit in the pixel detector. To reject cosmic muons the impact parameter in the transverse plane $|d_0|$ is required to be smaller than 0.2 cm and the longitudinal impact parameter $|d_z|$ has to be smaller than 0.1 cm. Both impact parameters are calculated with respect to the primary vertex.Also the p_T resolution is required to better than 10% to reject poorly measured muons.
The muon is required to be reconstructed using a particle-flow algorithm [36]. This is an algorithm which aims at identifying and reconstructing individually each particle arising from the LHC proton-proton collision by combining the information from all the subdetectors.
Leptons from W and Z decays are in general expected to be well spatially isolated from other particles in the final state. Considering this, to reject muons from heavy flavour quark decays, the muon is required to be isolated. For the purpose of rejecting non-isolated muon, a particle flow based isolation variable is implemented using a Multivariate Analysis (MVA) [37]. The energy deposits of PF candidates are used in three different categories, charged hadrons, photons, and neutral hadrons in concentric isolation cones. Neutral components are corrected by subtracting the pileup contribution, which is calculated by $\rho \times A_{eff}$ where ρ (`kt6PFJets`) is the event-by-event energy density and A_{eff} is the effective area. Effective area values are shown in Table 4.1. Isolations are used as an input for the MVA.

$\text{Iso}_{\text{charged}}$, Iso_{γ} and $\text{Iso}_{\text{neutral}}$ are the scalar sum of the p_T of charged hadron, photon and neutral hadron PF candidates, respectively, subscripts 01, 12, 23, 34 and 45 is the annulus of

Table 4.1: Effective areas used for muon isolation.

PF gamma						
$\lvert\eta\rvert$	$0.0-1.0$	$1.0-1.479$	$1.479-2.0$	$2.0-2.2$	$2.2-2.3$	$2.3-$
$0.0<\Delta R<0.1$	0.004	0.002	0.003	0.009	0.003	0.011
$0.1<\Delta R<0.2$	0.012	0.008	0.006	0.012	0.019	0.024
$0.2<\Delta R<0.3$	0.026	0.020	0.012	0.022	0.027	0.034
$0.3<\Delta R<0.4$	0.042	0.033	0.022	0.036	0.059	0.068
$0.4<\Delta R<0.5$	0.060	0.043	0.036	0.055	0.092	0.115
PF neutral hadron						
$\lvert\eta\rvert$	$0.0-1.0$	$1.0-1.479$	$1.479-2.0$	$2.0-2.2$	$2.2-2.3$	$2.3-$
$0.0<\Delta R<0.1$	0.002	0.004	0.004	0.004	0.010	0.014
$0.1<\Delta R<0.2$	0.005	0.007	0.009	0.009	0.015	0.017
$0.2<\Delta R<0.3$	0.009	0.015	0.016	0.018	0.022	0.026
$0.3<\Delta R<0.4$	0.013	0.021	0.026	0.032	0.037	0.042
$0.4<\Delta R<0.5$	0.017	0.026	0.035	0.046	0.063	0.135

Table 4.2: Selection requirements imposed on muons. The isolation requirements are also included. The *MB* and *ME* labels are referring to barrel and endcap muons

Variable		cut value
Loose		
Max. relative p_T resolution $\Delta p_T/p_T$		0.1
Max nomrmalized χ^2 fro global fit		10
Min. number of pixel hits		1
Min. number of layers in the inner tracker with hits		6
Min. number of matched muon segments		2
Tight		
Max. transverse impact parameter, $\lvert d_0\rvert$[cm]		0.01
Max. longitudinal impact parameter, $\lvert d_z\rvert$[cm]		0.1
Min. MVA isolation output	($p_T \leq 20$ GeV, MB)	0.86
	($p_T \leq 20$ GeV, ME)	0.82
	($p_T > 20$ GeV, MB)	0.82
	($p_T > 20$ GeV, ME)	0.86

ΔR where isolation is computed.

Multivariate Analysis uses the discrimination power of the ΔR between the muon and other particles to discriminate between isolated and non-isolated muons. Once the Boosted Decision Tree (BDT) is trained in a enriched sample of isolated muons (sample defined with a Z resonance similar to the tag and probe method) in order to discriminate between prompt and non-isolated muons, it can be used to classify the muons as prompt or non-isolated. The BDT output is dependent of the kinematics of the muon.

Two levels of selection are used in analyisis: *loose* and *tight* (which is subset of loose) selection. A summary of all selection cuts applied on muons is in the table 4.2.

4.2 Electrons

4.2.1 Reconstruction of electrons

Detailed description of electron reconstruction can be found in [38].The basic signature of electrons in the CMS detector is an energy deposit in the ECAL (produced by the electromagnetic shower created on impact) matched to a charged track built from hits in the pixel and strip tracker. In the ECAL, several neighbouring cells containing energy deposits from the electromagnetic shower are joined to form a *cluster*. As the electron bends in the magnetic field and interacts with the detector material, it is likely to emit bremsstrahlung photons. These photons produce clusters spread in a Φ band, perpendicular to the magnetic field axis. These clusters are combined with the cluster formed by the electron impact to form a *supercluster*(SC).
A reconstructed electron contains inner tracker and ECAL information. Algorithms have to match these individual detector signatures into a unified object. The tracker-driven class of algorithms attempt this starting from a track object and try to match it to the ECAL signature. Such an approach is robust for electrons surrounded by high activity, and is mainly used for electrons with low transverse momenta, below 5 GeV.
As electrons originating from W and Z bosons have spectra predominantly over 20 GeV, the preferred method is the *Gaussian Sum Filter* algorithm [39]. This algorithm starts by attempting to match a supercluster with a hit multiplet in the innermost (pixel) tracker to form a seed. It then uses a tracking algorithm that builds a track propagations to the SC. In the process, the algorithm takes into account energy loss due to potential bremsstrahlung photon emissions. Electron reconstructed by this algorithm are called GSF-electrons.
Usually collision data undergo the reconstruction stage shortly after being recorded,lacking a precise knowledge of ECAL transparency conditions, which is an important calibration parameter. Due to this, a recalibration in form of energy corrections to the GSF electron energy and momentum is often used. Proper integration of calibration updates into datasets requires repeating the whole reconstruction procedure.

4.2.2 Electron selection

Electrons used in this analysis are reconstructed using the GSF electron algorithm. Kinematic requirements on electrons in this analysis are p_T >10 GeV and $|\eta|<$ 2.5.
A multivatiate method (MVA), boosted decision tree (BDT
A preselection step is applied so that objects on which the MVA is applied are guaranteed to have satisfied also the *triggering* criteria. In this way, the quality of electrons on which the MVA is applied is guaranteed to be the same as on the sample on which MVA was trained on.

The elctromagnetic cluster shower shape variable $\sigma_{i\eta i\eta}$ is particularly powerful in discriminating against showers produced by photons and fakes. It is defined as

$$\sigma_{i\eta i\eta} = \sqrt{\frac{\sum_i^{5\times5} w_i(\eta_i - \eta_{seed})^2 \Delta\eta_{xtal}^2}{\sum_i^{5\times5} w_i}} \tag{4.1}$$

with i running over all the crystals in a 5×5 block centered on the supercluster seed, $\eta_i - \eta_{seed}$ being the distance in number of crystals of the i^{th} crystal to the seed crystal in η direction, and $\Delta\eta_{xtal}^2$ being the average width of a single crystal. w_i is the weight of the i^{th} crystal defined as $w_i = max(0, 4.7 + \ln\frac{E_i}{E_{5\times5}})$, where a single crystal energy is E_i and $E_{5\times5}$ is the total energy deposited in the 5×5 block.
The geometrical compatibility of the track and the ECAL supercluster is controlled using the $\Delta\phi_{in}$ and $\Delta\eta_{in}$ variables, calculated as the absolute η and ϕ distance of the supercluster and the electron track extrapolated to the ECAL surface. The electron compatibility with the primary vertex is evaluated using the electron track distance from the primary vertex in both transverse and longitudinal planes, the d_0 and d_z. Finally the probablity of a photon conversion is calculated by attempting to fit the electron track with another track under the hypothesis that they descend from a converted photon originating from the primary vertex. A large value of this probability can be a signature of the conversion. Conversions are also suppressed by requiring that the candidate track is built without missing hits in any of the pixel layers.

Preselection requirements are the following:

- $p_T > 10$ GeV;
- $|\eta| < 2.5$;
- when $|\eta| < 1.479$
  - $\sigma_{i\eta i\eta} < 0.01$;
  - $|\Delta\phi_{in}| < 0.15$;
  - $|\Delta\eta_{in}| < 0.007$;
  - $H/E < 0.12$;
  - $\max\left(\sum_{\text{ECAL}} E_T - 1, 0\right) pt < 0.2$;
- when $|\eta| \geq 1.479$
  - $\sigma_{i\eta i\eta} < 0.03$;
  - $|\Delta\phi_{in}| < 0.1$;
  - $|\Delta\eta_{in}| < 0.009$;
  - $H/E < 0.1$;
  - $\sum_{\text{ECAL}} E_T/p_T < 0.2$;
- $\sum_{\text{tracker}} E_T/p_T < 0.2$;
- $\sum_{\text{HCAL}} T_T/p_T < 0.2$.

As for a muons there are two stages of selection *loose* and *tight*. To reject photons converted to electrons additional requirements are that electron track has no expected missing hits and the vertex fit probability has to be smaller than 10^{-6}. Loose electrons need furthermore to pass the following requirements to veto electrons from photon conversion:

- a reconstructed conversion vertex is looked for where one of the two tracks is compatible with the electron. The vertex fit probability is required to be $> 10^{-6}$;
- the electron track has no expected missing hits

Tight electrons have some additional requirements: MVA quality requirement, and cut on longitudinal and transverse impact parameter.

List of tight requirements:

- impact parameter in the transverse plane $|d_0| < 0.02$ cm, calculated with respect to the primary vertex;
- longitudinal impact parameter $|d_z| < 0.1$ cm, calculated with respect to the primary vertex;
- MVA ID > 0.00 when $p_T < 20$ GeV and $|\eta| \leq 0.8$;
- MVA ID > 0.10 when $p_T < 20$ GeV and $0.8 < |\eta| \leq 1.479$;
- MVA ID > 0.62 when $p_T < 20$ GeV and $|\eta| > 1.479$;
- MVA ID > 0.94 when $p_T \geq 20$ GeV and $|\eta| \leq 0.8$;
- MVA ID > 0.85 when $p_T \geq 20$ GeV and $0.8 < |\eta| \leq 1.479$;
- MVA ID > 0.92 when $p_T \geq 20$ GeV and $|\eta| > 1.479$.

Isolation requirements are then imposed by computing the particle flow isolation, defined as the scalar sum of the p_T of the particle flow candidates satisfying the following requirements:

- $\Delta R < 0.4$ to the electron in the $\eta \times \phi$ plane;
- PF electrons and muons are vetoed;
- for gamma PF candidates, require that they are outside the footprint veto region of $\Delta R < 0.08$;
- for charged hadron PF candidates, require that they are outside the footprint veto region of $\Delta R < 0.015$;
- for charged hadron PF candiates, require that they are associated with the primary vertex;
- neutral components are corrected by subtracting pileup contribution which is calculated by $\rho \times A_{\text{eff}}$,

where ρ (`kt6PFJets`) is the event-by-event energy density and A_{eff} is the effective area. The used isolation variable is thus:

$$\frac{\text{Iso}_{\text{PF}}}{p_T} = \frac{1}{p_T} \cdot \left(\text{Iso}_{\text{charged}} + \text{Iso}_{\gamma} + \text{Iso}_{\text{neutral}} - \rho \times A_{eff}\right),$$

Isolation cone around electron is 0.4. Then the last requirement is:

- $\frac{\text{Iso}_{\text{PF}}}{p_T} < 0.15$ is required for electrons in barrel and endcap.

4.3 Jets

A jet is collimated group of hadrons which emerges as a result of a quark or gluon fragmentation and hadronization process. Hadrons reconstructed in a particle detector need to be combined in order to form a jet and give information about the initial parton. A set of rules has to be created which define how to group particles and how to assign momentum to the jet. Usually this is done by summing the four-momentum of each particle in a jet.
The jets used in this analysis are built from Particle Flow objects using the anti-k_T algorithm [40]. In this algorithm called *sequential recombination algorithm* , two distances are introduced: d_{ij} which is the distance between each pair of particles, and d_{iB}, which is the particle-beam distance, These distances are defined as:

$$d_{ij} = min(k_{T,i}^{2p}, k_{T,j}^{2p}) \frac{\Delta R_{ij}^2}{R^2} \tag{4.2}$$

$$d_{i,B} = k_{T,i}^{2p} \tag{4.3}$$

where ΔR_{ij}^2 denotes the distance in the $\eta - \phi$ plane and is computed as

$$\Delta R_{ij}^2 = (\eta_i - \eta_j)^2 + (\phi_i - \phi_j)^2$$

k_T is the transverse momentum of the particle, R is an angular cut-off, and p defines which particles are clustered first as described below. Both R and p are free parameters of the algorithm. The algorithm is applied using the following approach: distances d_{ij} between each pair of particles and $d_{i,B}$ for each particle are computed and the minimal value is found. If d_{ij} is the smallest value, particles i and j are combined and treated as a new particle in the next iteration of the algorithm. In case of d_{iB} being the smallest, i is declared to be the final jet and is removed from the list of particles. The procedure continues until there are no more particles in the list.
The parameter p defines which particles are clustered first thus defining the type of algorithm. The k_T algorithm uses $p = 1$, clustering soft particles first. This results in irregularly shaped jets which are sensitive to radiation in the event and difficult to calibrate. The algorithm used in this analysis is the anti-k_T algorithm, where $p = -1$, clustering hardest particles first. Jets reconstructed in this way have circular shape because they are not affected by the softer components of the jet.
Various neasurements during the comissioning phase of the CMS detector showed that the measured jet energy at detector level in general doesn't correspond to the energy of the originating particle. A jet calibration procedure is introduced to compensate for the nonlinear response of the calorimeters. This is done using a a factorized approach where corrections on each level are determined separately.

Measurements show that the jet energy resolution (JER) in data is worse than in the simulation and the jets in MC need to be smeared to describe the data. Reconstruced jets in simulated events have to be over-smeared so that their p_T resolution would be the same as we measure in data. Reconstructed jet p_T is scaled based on the p_T difference between matched reconstructed and generated jets. Corrected reconstructed p_T is computed using $p_T \rightarrow \max[0., p_{T,\text{generated}} + c * (p_T - p_{T,\text{generated}})]$, where c is the core resolution scaling factor. , i.e. the measured data/Monte Carlo resolution ratio.
Reconstructed (corrected) jet p_T is randomly smeared using a Gaussian of the width $\sqrt{c^2-1} * \sigma_{MC}$. σ_{MC} is the jet resolution in simulation. It is retrieved using the Monte Carlo truth jet energy scale tool in the CMS software.

4.3.1 Jet selection

The jets used in this analysis are built from Particle Flow objects using the anti-k_t algorithm with parameter R =0.5 Kinematical requirements applied on reconstructed jets are: $p_T > 30$ GeV, $|\eta| < 2.5$.

4.4 Missing transverse energy

The missing transverse momentum is the imbalance in the vectorial sum of transverse momenta of all measured particles. Missing transverse energy is the magnitude of the missing transverse momentum and is calculated as:

$$E_T^{miss} = |-\sum_i \vec{p}_i| \tag{4.4}$$

where i goes over all visible particles. Momentum conservation suggests that the imbalance could arise from weakly interacting neutral particles such as neutrinos or any other particle that doesn't interact with the detector. Measurement of the missing transverse energy relies on the good measurement of all other particles in the event and as such is very sensitive to detector resolution, particle missmeasurements, limited acceptance of the detector, cosmic-ray particles, all of which can cause artificial missing energy. The E_T^{miss} used in this analysis is reconstructed using Particle Flow algorithm. It tries to identify each particle in the event by combining the information from all subdetectors and gives the best missing energy resolution.

Additional corrections (Type-I) are applied on E_T^{miss} to correct the jet energy scale. Type-I correction propagates jet energy corrections to missing energy. This correction replaces the uncorrected transverse momenta of particles in a jet by the transverse momentum of a jet to which jet energy corrections (JEC) were applied in the missing energy calculation.

Chapter 5

Event selection and background estimation

Process studied in this analysis is WZ decaying leptonicaly. Signature in the detector is: 3 leptons, 2 of which are of the same flavour and missing transverse energy. Some selection has to be applied on candidate events to reject fake and misidentified leptons, and distinguish WZ process from other processes that leave similar trace in the detector and which are called backgrounds. In this chapter the WZ selection will be described in detail: list of used data and Monte Carlo samples will be given, selection steps for selecting a WZ event will be described. Background and methods for estimating background events will be discussed.

5.1 Data and Monte Carlo samples

The data samples used in this analysis were recorded by the CMS detector in proton proton collisions during the 2012 run at a center of mass energy of 8 TeV. The total integrated luminosity of analyzed sample is 19.8 fb^{-1}. The analysis uses Primary Datasets (PD) based on double lepton triggers: double electron, double muon and electron-muon. The full list of used datasets is given in Table 5.1.

The simulated samples for signal and background processes were obtained using Monte Carlo(MC) methods, as a part of the official 2012 CMS MC production campaign. They include WZ (signal) and the following backgrounds (which will be described in detail later): $t\bar{t}$, $Z+jets$, $Z\gamma$, ZZ, WV, VVV (listed in Table 5.2.). The event generators used to produce the samples needed in the analysis are:

- **Pythia** [41, 42] is a multi-purpose generator which can also simulate parton shower. Pythia is able to calculate only tree-level $1 \to 2$ and $2 \to 2$ processes while higher orders are approximated with parton shower algorithm. Parton showering in all samples uses the so called Z2 tune for modelling the underlying event [43, 44]. *

*aspect of hadronic interaction attributed not to the hard scattering process, but rather to the accompanying interactions of the rest of the proton.

Table 5.1: List of datasets used in analysis.

/DoubleElectron/Run2012A-13Jul2012-v1
/DoubleElectron/Run2012A-recover-06Aug2012-v1
/DoubleElectron/Run2012B-13Jul2012-v1
/DoubleElectron/Run2012C-24Aug2012-v1
/DoubleElectron/Run2012C-PromptReco-v2
/DoubleElectron/Run2012D-PromptReco-v1
/DoubleMu/Run2012A-13Jul2012-v1
/DoubleMu/Run2012A-recover-06Aug2012-v1
/DoubleMu/Run2012B-13Jul2012-v4
/DoubleMu/Run2012C-24Aug2012-v1
/DoubleMu/Run2012C-PromptReco-v2
/DoubleMu/Run2012D-PromptReco-v1
/MuEG/Run2012A-13Jul2012-v1
/MuEG/Run2012A-recover-06Aug2012-v1
/MuEG/Run2012B-13Jul2012-v1
/MuEG/Run2012C-24Aug2012-v1
/MuEG/Run2012C-PromptReco-v2
/MuEG/Run2012D-PromptReco-v1

- **Madgraph**[45] calculates matrix elements at tree level for decays and $2 \to n$ scatterings (with n going up to 10). Radiation of hard gluons in the initial and final state is taken into account at the matrix element calculation level. The cross section is normalized to predictions next to leading order from other programs, such as MCFM [46] for standard model processes.
- **Powheg** [47] calculates hard process at the NLO order. For fragmentation and hadronization other programs are used (e.g. Pythia). Single top and ZZ events were produced using this generator and showered with Pythia.
- **Tauola** [48] is a package for simulation of τ decays.

The detector response is simulated using the GEANT4 [49] simulation package.

5.1.1 Monte Carlo corrections

To account for the imprecision inherent to simulation software or differences caused by detector conditions unknown at the time of MC sample production, various correction factors are applied on Monte Carlo samples to account for this differences.

Table 5.2: MC samples at 8 TeV.

process	dataset
top	/TTJets_MassiveBinDECAY_TuneZ2star_8TeV-madgraph-tauola/[1]
	/TTTo2L2Nu2B_8TeV-powheg-pythia6/[3]
	/T_tW-channel-DR_TuneZ2star_8TeV-powheg-tauola/[1]
	/Tbar_tW-channel-DR_TuneZ2star_8TeV-powheg-tauola/[1]
VVV	/WZZNoGstarJets_8TeV-madgraph/[1]
	/ZZZNoGstarJets_8TeV-madgraph/[1]
	/WWZNoGstarJets_8TeV-madgraph/[1]
	/WWWJets_8TeV-madgraph/[1]
	/TTWJets_8TeV-madgraph/[1]
	/TTZJets_8TeV-madgraph_v2/[1]
	/TTWWJets_8TeV-madgraph/[1]
	/TTGJets_8TeV-madgraph/[1]
	/WWGJets_8TeV-madgraph/[1]
WV	/WJetsToLNu_TuneZ2Star_8TeV-madgraph-tarball/[1]
	/WbbJetsToLNu_Massive_TuneZ2star_8TeV-madgraph-pythia6_tauola/[1]
	/WGstarToLNu2E_TuneZ2star_8TeV-madgraph-tauola/[1]
	/WGstarToLNu2Mu_TuneZ2star_7TeV-madgraph-tauola/[1]
	/WGstarToLNu2Tau_TuneZ2star_7TeV-madgraph-tauola/[1]
	/WGToLNuG_TuneZ2star_8TeV-madgraph-tauola/[1]
	/WW_TuneZ2star_8TeV_pythia6_tauola/[1]
	/WZJetsTo2L2Q_TuneZ2star_8TeV-madgraph-tauola/[1]
	/WZJetsTo2QLNu_8TeV-madgraph/[2]
WZ	/WZJetsTo3LNu_TuneZ2_8TeV-madgraph-tauola/[1]
$Z\gamma$	/ZGToLLG_8TeV-madgraph/[1]
Z+jets	/DYJetsToLL_M-10To50filter_8TeV-madgraph/[1]
	/DYJetsToLL_M-50_TuneZ2Star_8TeV-madgraph-tarball/[1]
	$Z/\gamma \to \ell\ell + b\bar{b}$
ZZ	/ZZTo2mu2tau_8TeV-powheg-pythia6/[1]
	/ZZTo4e_8TeV-powheg-pythia6/[1]
	/ZZTo2e2tau_8TeV-powheg-pythia6/[1]
	/ZZTo4mu_8TeV-powheg-pythia6/[1]
	/ZZTo2e2mu_8TeV-powheg-pythia6/[1]
	/ZZTo4tau_8TeV-powheg-pythia6/[1]
	/ZZJetsTo2L2Q_TuneZ2star_8TeV-madgraph-tauola/[1]
	/ZZJetsTo2L2Nu_TuneZ2star_8TeV-madgraph-tauola/[3]
	/GluGluToZZTo2L2L_TuneZ2star_8TeV-gg2zz-pythia6/[1]
	/GluGluToZZTo4L_8TeV-gg2zz-pythia6/[1]
	/GluGluToHToZZTo4L_M-125_8TeV-powheg-pythia6/[1]

Lepton scale factors

Due to different selection efficiencies ε in data and MC simulations, scale factors are introduced. They are defined as:

$$w_l^{SF} = \frac{\varepsilon_{data}}{\varepsilon_{MC}} \tag{5.1}$$

Scale factors are measured, based on the flavour and kinematic properties of each lepton found in event. They are estimated using Tag and probe method (described in 5.4.3) and they depend on the lepton p_T and η.

Pileup

In proton-proton collisions at high beam intensities, there is a high probability that multiple interactions will happen in a single bunch crossing. These additional interactions are usually referred to as pileup interactions and contain low-p_T QCD processes. Pileup is significant at the luminosities achieved by the LHC in 2012. For the hard-scattering processes of interest, this results in additional activity in the detector, mainly in form of low p_T particles that can impact the reconstruction and identification algorithms and in many cases deteriorate the ability to efficiently identify particles, or discriminate them against backgrounds. The total inelastic cross section at $\sqrt{s} = 8$ TeV is 69 mb. The luminosity per bunch crossing of 69 mb^{-1} results in one interaction per bunch crossing. Instantaneous luminosity per bunch crossing resulted in 21 primary interactions on average during 2012, with some bunch crossings going up to 70.
The Monte Carlo samples used in this analysis include a simulation of pileup. They were however generated prior to the data taking and it was thus not possible to accurately predict the conditions influencing the amount of pileup that would be present in the collected data. This disagreement is shown in Figure 5.1. To obtain a better modelling of the data, it is therefore

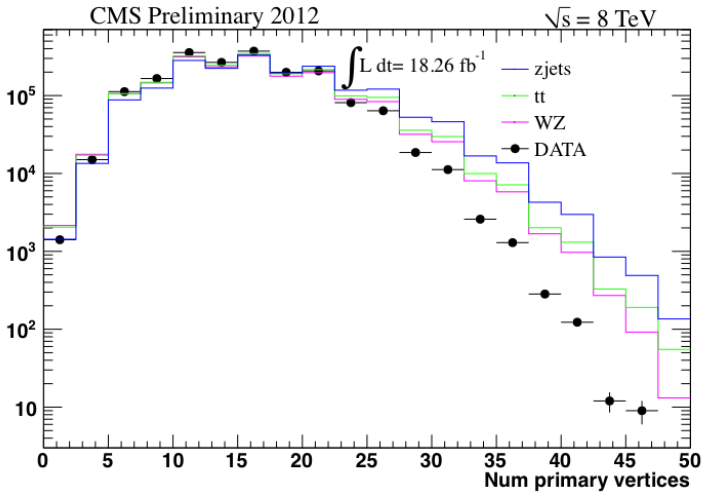

Figure 5.1: Number of primary vertices for data and Monte Carlo samples (Z+jets, $t\bar{t}$ and WZ) before pileup reweighting

necessary to apply additional correction on MC samples to obtain a pileup distribution that reflects the one in data. This is achieved by the *pileup reweighting* procedure. The current pileup distribution in data is calculated for the analysed collision period. Then a set of factors is calculated that reweight the Monte Carlo sample distribution. Based on the "true" input number of vertices in each Monte Carlo event which is provided by the generator, each event is assigned an individual weight w^{PU} which is propagated through the whole selection chain.

5.1.2 Trigger requirements

The WZ signature consists of three leptons of which at least two are of the same flavour. Therefore HLT paths requiring two electrons, two muons or one electron one muon are used for this analysis.
Double electron trigger require at least two electrons and are used for the eee and eeμ channels:

- HLT_Ele17_CaloIdT_CaloIsoVL_TrkIdVL_TrkIsoVL_Ele8_ CaloIdT_CaloIsoVL_TrkIdVL_TrkIsoVL: tresholds on trigger electrons are $p_T > 17$ and $p_T > 8$ GeV

Double muon trigger require at least two muons and are used for $\mu\mu$e and $\mu\mu\mu$ channels and tresholds on muons are p_T>17 and $p_T > 8$ GeV:

- HLT_Mu17_Mu8
- HLT_Mu17_TkMu8

Muon electron triggers are used for the mixed channels $\mu\mu$e and eeμ and treshold for muon(electron) is $p_T > 17$ GeV, and for electron (muon) is $p_T > 8$ GeV:

- HLT_Mu17_Ele8_CaloIdT_CaloIsoVL_TrkIdVL_TrkIsoVL
- HLT_Mu8_Ele17_CaloIdT_CaloIsoVL_TrkIdVL_TrkIsoVL

In Monte Carlo simulation, there is no HLT requirement. Instead, the efficiency of trigger requirements is simulated, utilizing independent measurement of the trigger efficiencies for the same data collection period. These measurements are provided as efficiencies for individual leptons passing HLT selection imposed on the first or the second lepton (*leg*) in the trigger, called *leading* and *trailing* requirements and they depend on lepton flavor and kinematic in each particular event. The total trigger efficiency is constructed from efficiencies of leading and trailing lepton legs in used HLT paths. After including cross triggers, in all cases (eee, eeμ, $\mu\mu$e and $\mu\mu\mu$) there is a trigger that will accept the event if we have one lepton passing the leading lepton criteria corresponding to that lepton *i.e.* Mu(17) for muons and Ele(17) for electrons with all corresponding cuts for the respective flavor) and one lepton passing the trailing lepton trigger. So the only (mutually exclusive) cases in which the event will not be accepted by a trigger are: all three leptons fail the leading leg trigger; one lepton passes the leading leg trigger

but the other two fail the trailing leg trigger (three cases with the combinatorics).

$$\varepsilon_{\text{trigger}}(3\ell,\ \ell=\text{e},\mu) = 1 - \left(\begin{array}{c} (1-\varepsilon_{leading}(\eta_1, p_{\text{T}1})) \times (1-\varepsilon_{leading}(\eta_2, p_{\text{T}2})) \times (1-\varepsilon_{leading}(\eta_3, p_{\text{T}3})) \\ +\varepsilon_{leading}(\eta_1, p_{\text{T}1}) \times (1-\varepsilon_{trailing}(\eta_2, p_{\text{T}2})) \times (1-\varepsilon_{trailing}(\eta_3, p_{\text{T}3})) \\ +\varepsilon_{leading}(\eta_2, p_{\text{T}2}) \times (1-\varepsilon_{trailing}(\eta_1, p_{\text{T}1})) \times (1-\varepsilon_{trailing}(\eta_3, p_{\text{T}3})) \\ +\varepsilon_{leading}(\eta_3, p_{\text{T}3}) \times (1-\varepsilon_{trailing}(\eta_1, p_{\text{T}1})) \times (1-\varepsilon_{trailing}(\eta_2, p_{\text{T}2})) \end{array} \right)$$

5.2 Event selection

The WZ $\to 3\ell$ decay signature is characterized by a couple of same-flavor, opposite-charge, high p_T isolated leptons with an invariant mass corresponding to a Z boson, together with a third high p_T isolated lepton and a significant amount of missing transverse energy (E_T^{miss}) associated to the escaping neutrino. Four different final states are considered, depending on the flavour of the W and Z leptons:

- eee: $\text{Z} \to \text{ee}, \text{W} \to \text{e}\nu$;
- eeμ: $\text{Z} \to \text{ee}, \text{W} \to \mu\nu$;
- $\mu\mu$e: $\text{Z} \to \mu\mu, \text{W} \to \text{e}\nu$;
- $\mu\mu\mu$: $\text{Z} \to \mu\mu, \text{W} \to \mu\nu$.

The four channels are treated independently through the analysis, leading to four independent cross section measurements. They are combined only at the level of the final result.
Event selection process consists of the following steps:

1. Events are required to have exactly three leptons, electrons or muons, passing the identification and isolation requirements described in the previous section and with $p_T > 10$ GeV.
2. The invariant mass of the 3 leptons has to be above 100 GeV (to reject $Z \to ll$ background).
3. **Z selection**: Z candidates are built out of two same flavor opposite sign leptons satisfying all identification and isolation criteria, as defined in chapter 4. The leading (trailing) lepton has to have a transverse momentum above 20(10) GeV. The candidate invariant mass has to be within 20 GeV of the nominal PDG Z mass. In case several Z combinations fulfilling these requirements are found, the candidate with the invariant mass closer to the nominal PDG value is retained.
4. **W selection**: After Z is selected remaining lepton is candidate for lepton from W boson leptonic decay. Requirement for this lepton p_T is: $p_T > 20$ GeV.
5. E_T^{miss} **requirement**: The final event selection consists in requiring a high amount of transverse missing energy, $E_T^{miss} > 30$ GeV, to select W boson decays and discriminate against high p_T jets faking leptons from Z+jets events.

The numbers of selected events passing the full selection in data for the four considered final states are given in Table 5.3, together with the expected yields from Monte Carlo. Kinematic distributions of selected events after the W selection step, and after the full selection, can be seen in Figures 5.2-5.10.

Table 5.3: Monte Carlo and data yields after the full WZ selection. N_{fake} is the number of events with fake leptons, dominated by the Z+jets and ttbar contributions, derived with the data driven method described in Subsection 5.4.2. The expected yields from Z+jets and ttbar simulated samples are given for comparison, but they are not used in the cross section determination. Errors are statistic and systematic, except for Z+jets, ttbar and WZ where only statistical errors are given.

sample	**eee**	**eeμ**	**$\mu\mu$e**	**$\mu\mu\mu$**	total
Non-prompt leptons	18.4 ± 12.7	32.0 ± 21.0	54.4 ± 33.0	62.4 ± 37.7	167.1 ± 55.8
ZZ	2.1 ± 0.3	2.4 ± 0.4	3.2 ± 0.5	4.7 ± 0.7	12.3 ± 1.0
Zγ	3.4 ± 1.3	0.4 ± 0.4	5.2 ± 1.8	0	9.1 ± 2.2
Wγ^*	0	0	0	2.8 ± 1.0	2.8 ± 1.0
VVV	6.7 ± 2.2	8.7 ± 2.8	11.6 ± 3.8	14.8 ± 5.1	41.9 ± 7.3
Total background (N_{bkg})	30.6 ± 13.0	43.5 ± 21.2	74.4 ± 33.3	84.7 ± 38.1	233.2 ± 56.3
WZ	211.1 ± 1.6	262.1 ± 1.8	346.7 ± 2.1	447.8 ± 2.4	1267.7 ± 4.0
Total expected	241.6 ± 13.1	305.7 ± 21.3	421.0 ± 33.3	532.4 ± 38.2	1500.8 ± 56.5
Data (N_{obs})	258	298	435	568	1559

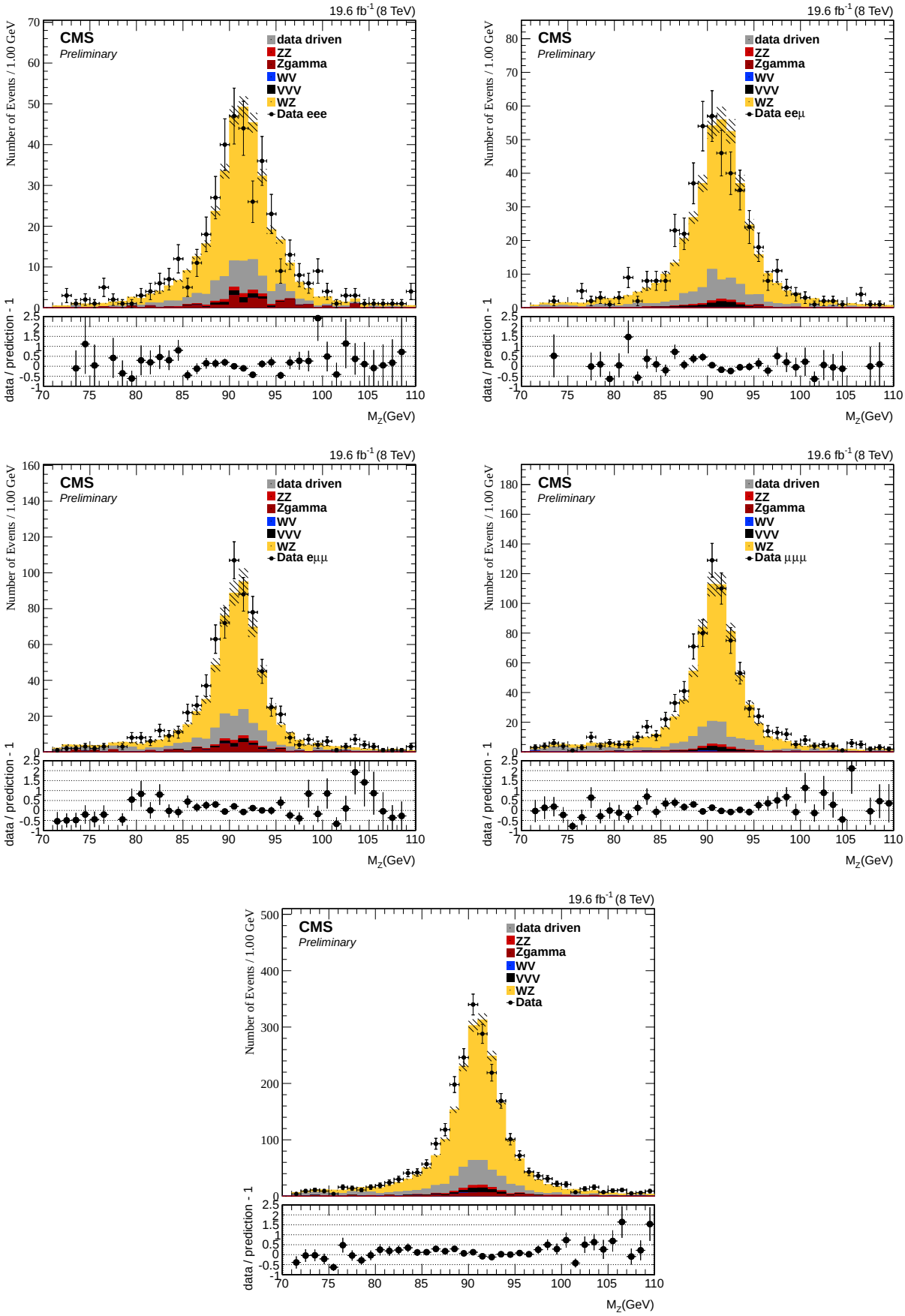

Figure 5.2: Invariant mass of two leptons after W candidate is selected for 3e (first row left), 2e1μ (first row right), 1e2μ (second row left) and 3μ (second row right) channels, and combination of all channels (third row).

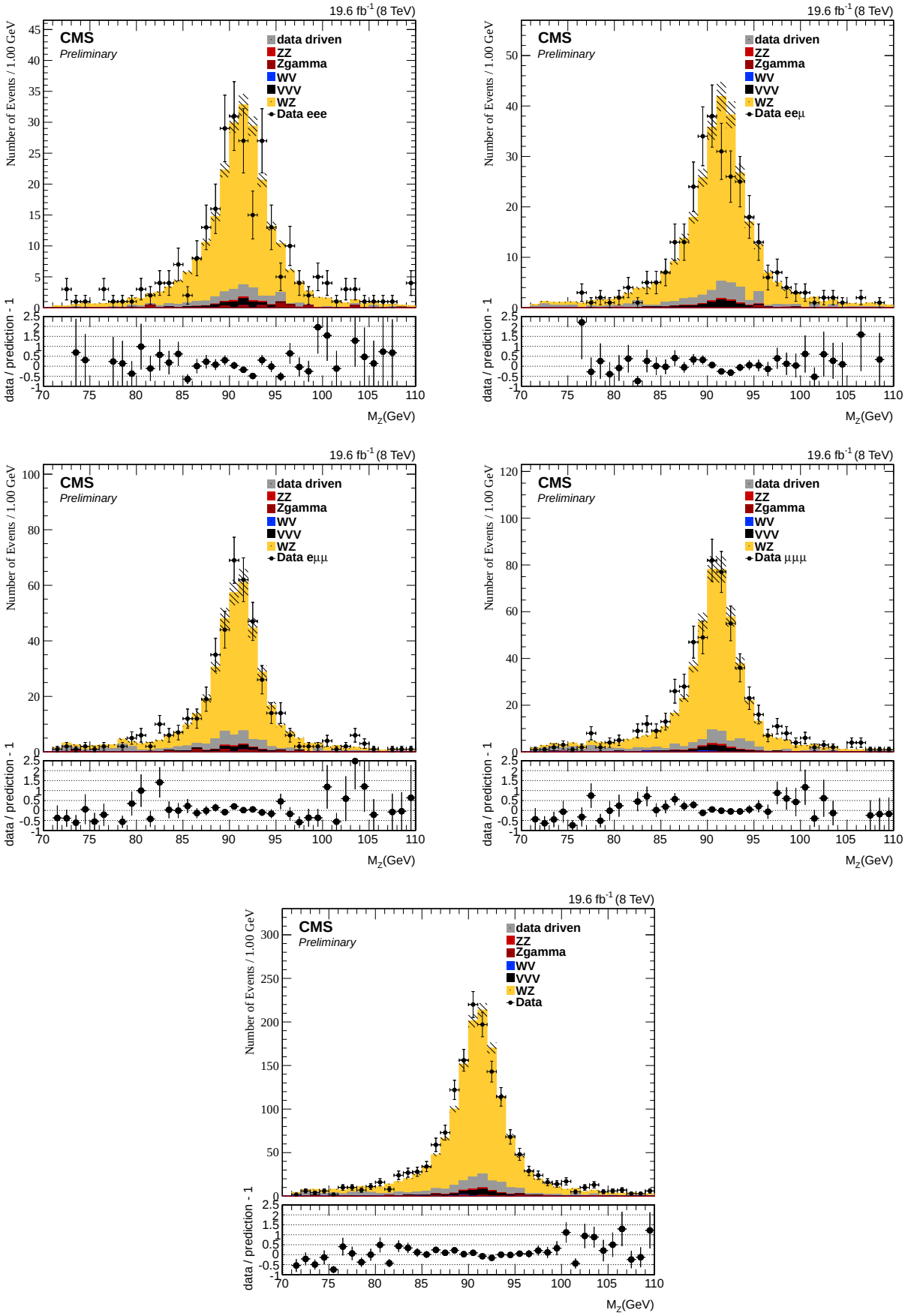

Figure 5.3: Invariant mass of two leptons after final selection for 3e (first row left), 2e1μ (first row right), 1e2μ (second row left) and 3μ (second row right) channels, and combination of all channels (third row).

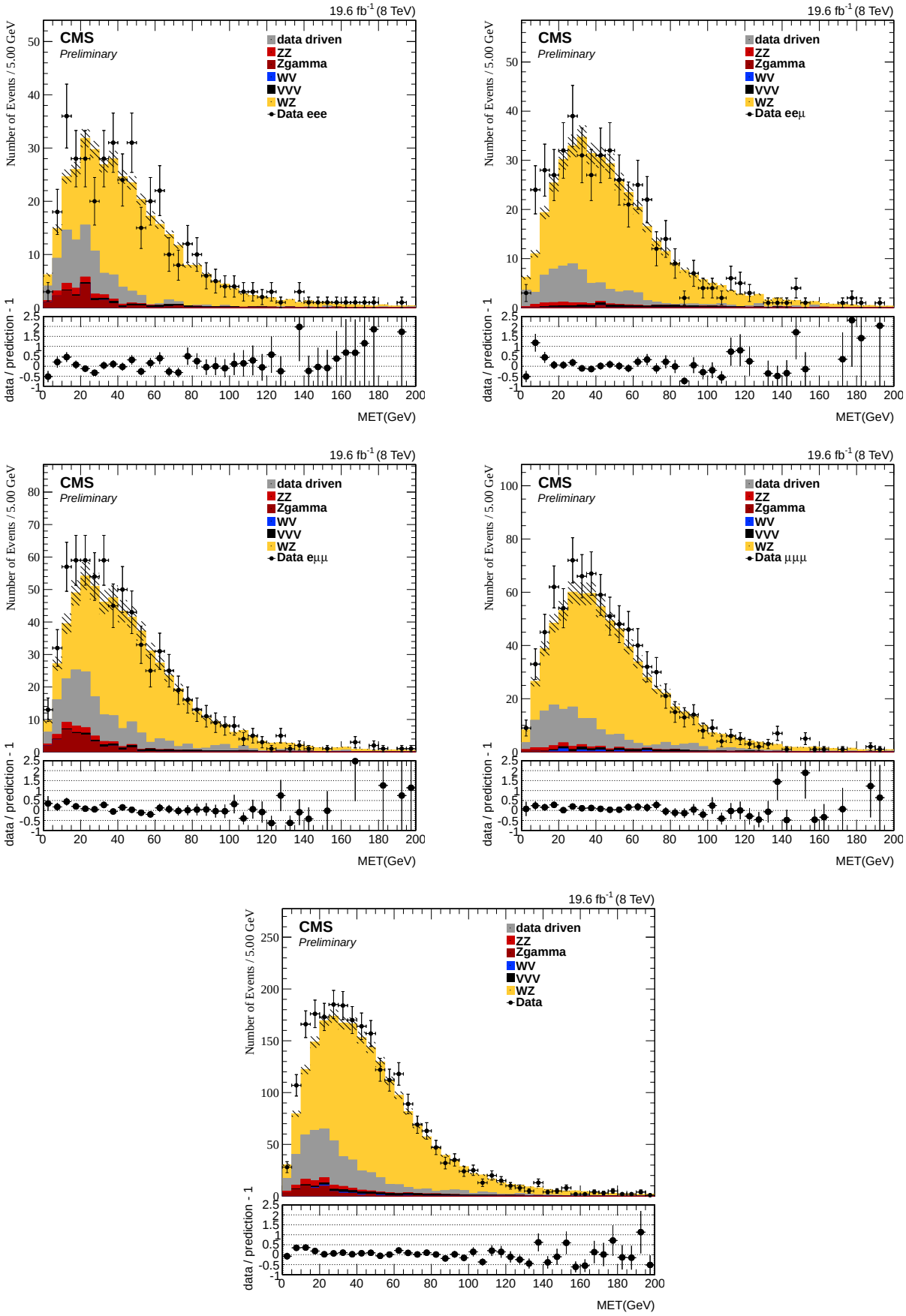

Figure 5.4: Missing transverse energy after W candidate is selected for 3e (first row left), 2e1μ (first row right), 1e2μ (second row left) and 3μ (second row right) channels, and combination of all channels (third row).

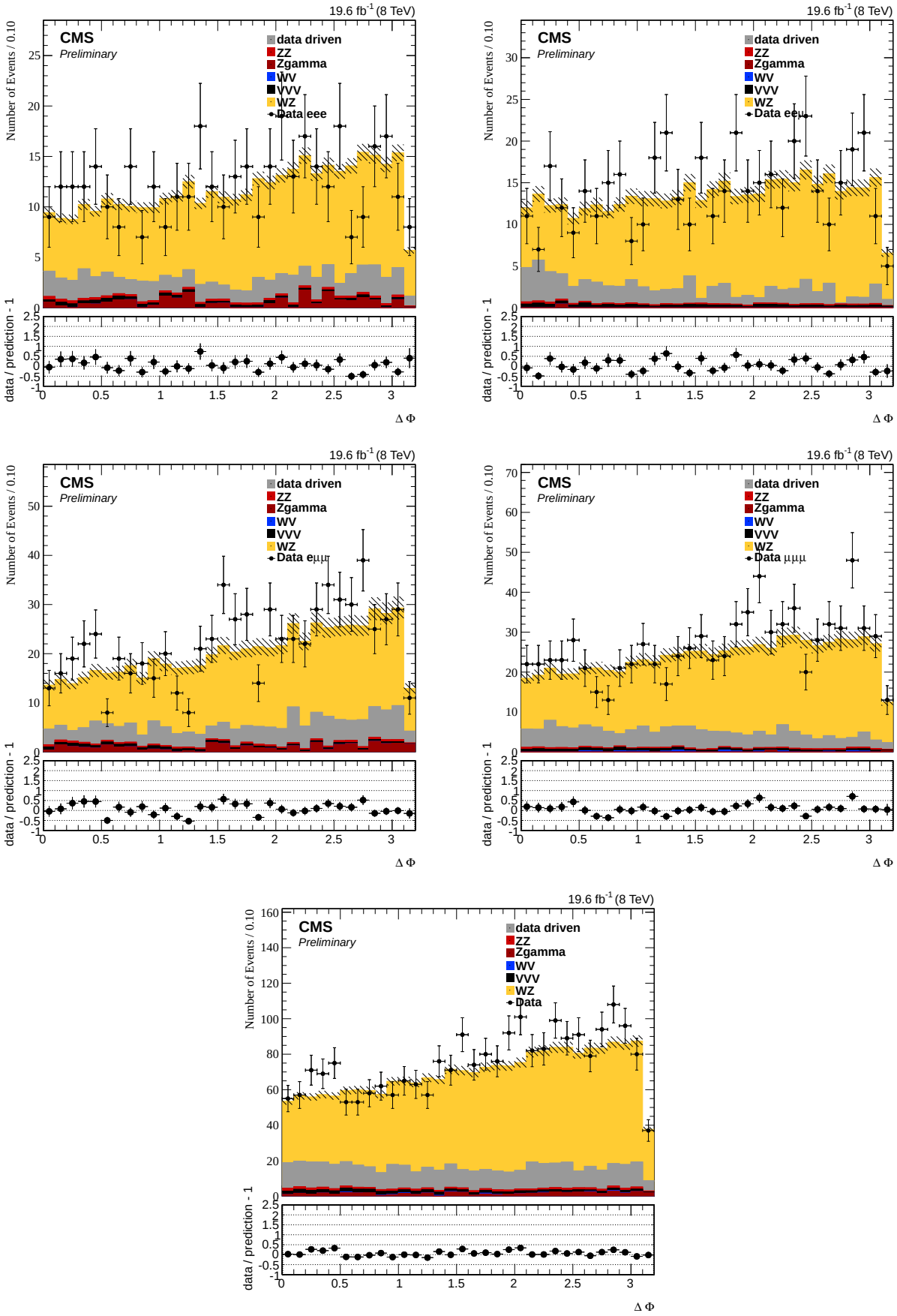

Figure 5.5: $\Delta\phi(\text{W lepton}, MET)$ after W candidate is selected for 3e (first row left), 2e1μ (first row right), 1e2μ (second row left) and 3μ (second row right) channels, and combination of all channels (third row).

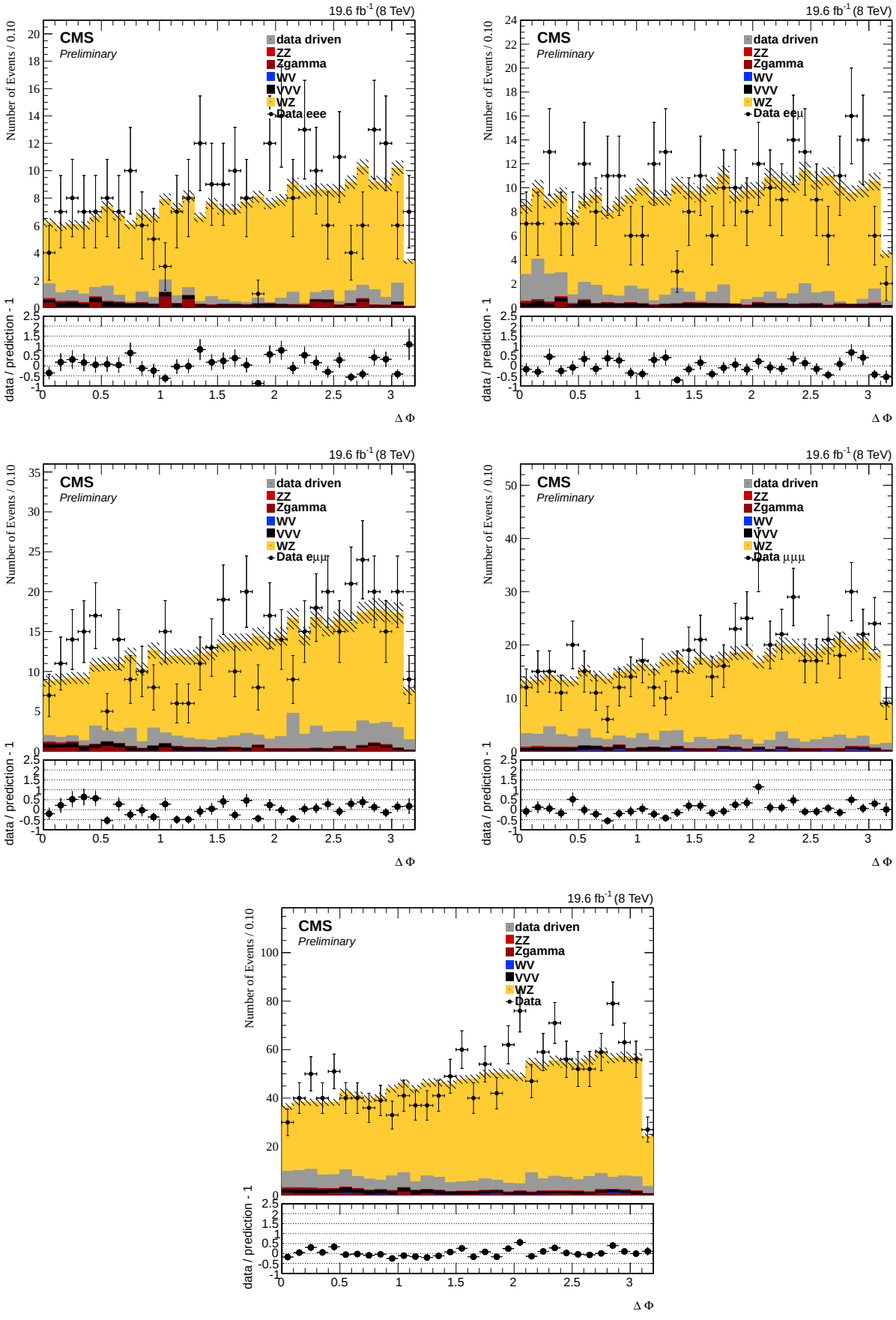

Figure 5.6: $\Delta\phi$(W lepton, MET) after final selection for 3e (first row left), 2e1μ (first row right), 1e2μ (second row left) and 3μ (second row right) channels, and combination of all channels (third row).

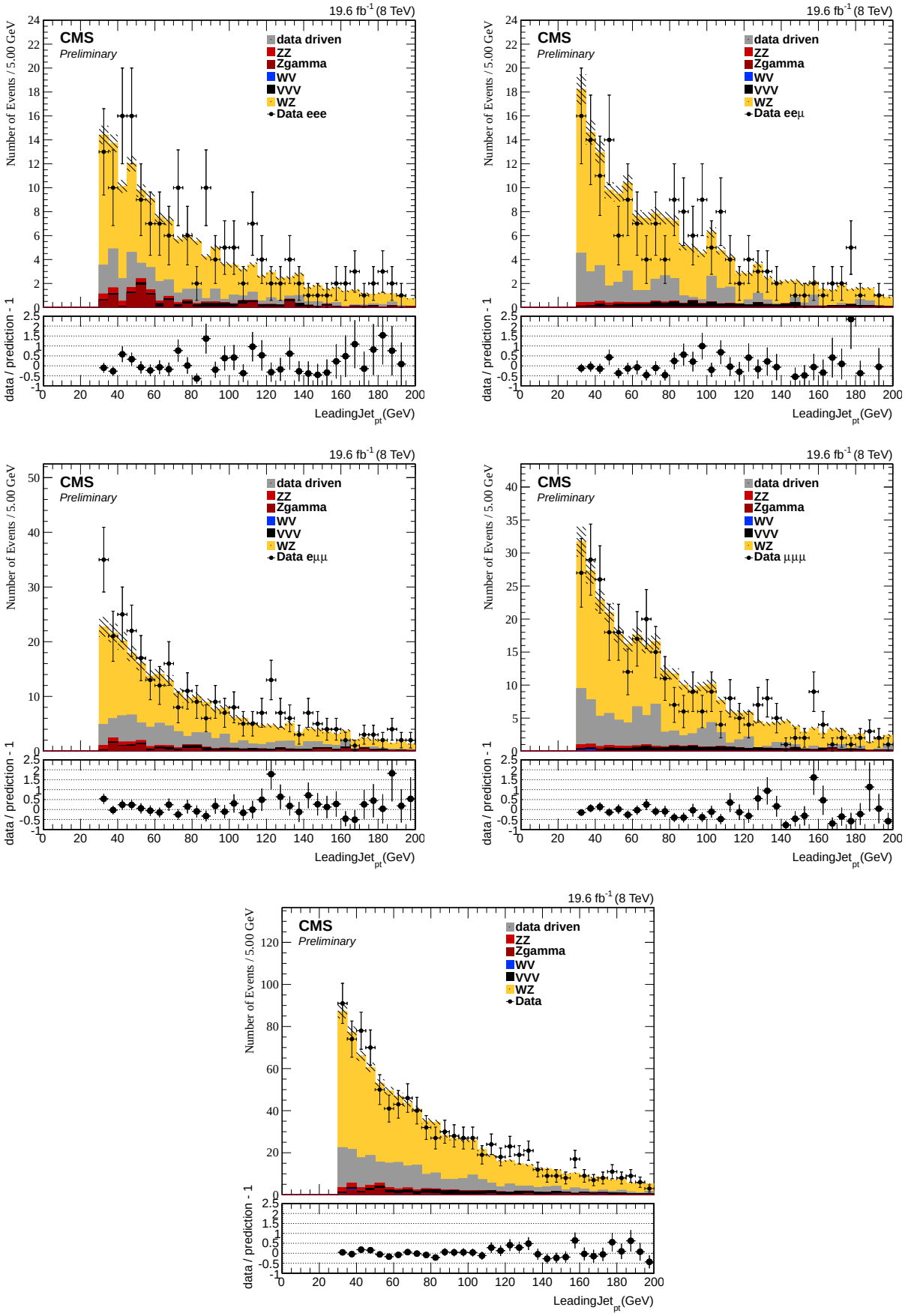

Figure 5.7: Leading jet pt after W candidate is selected for 3e (first row left), 2e1μ (first row right), 1e2μ (second row left) and 3μ (second row right) channels, and combination of all channels (third row).

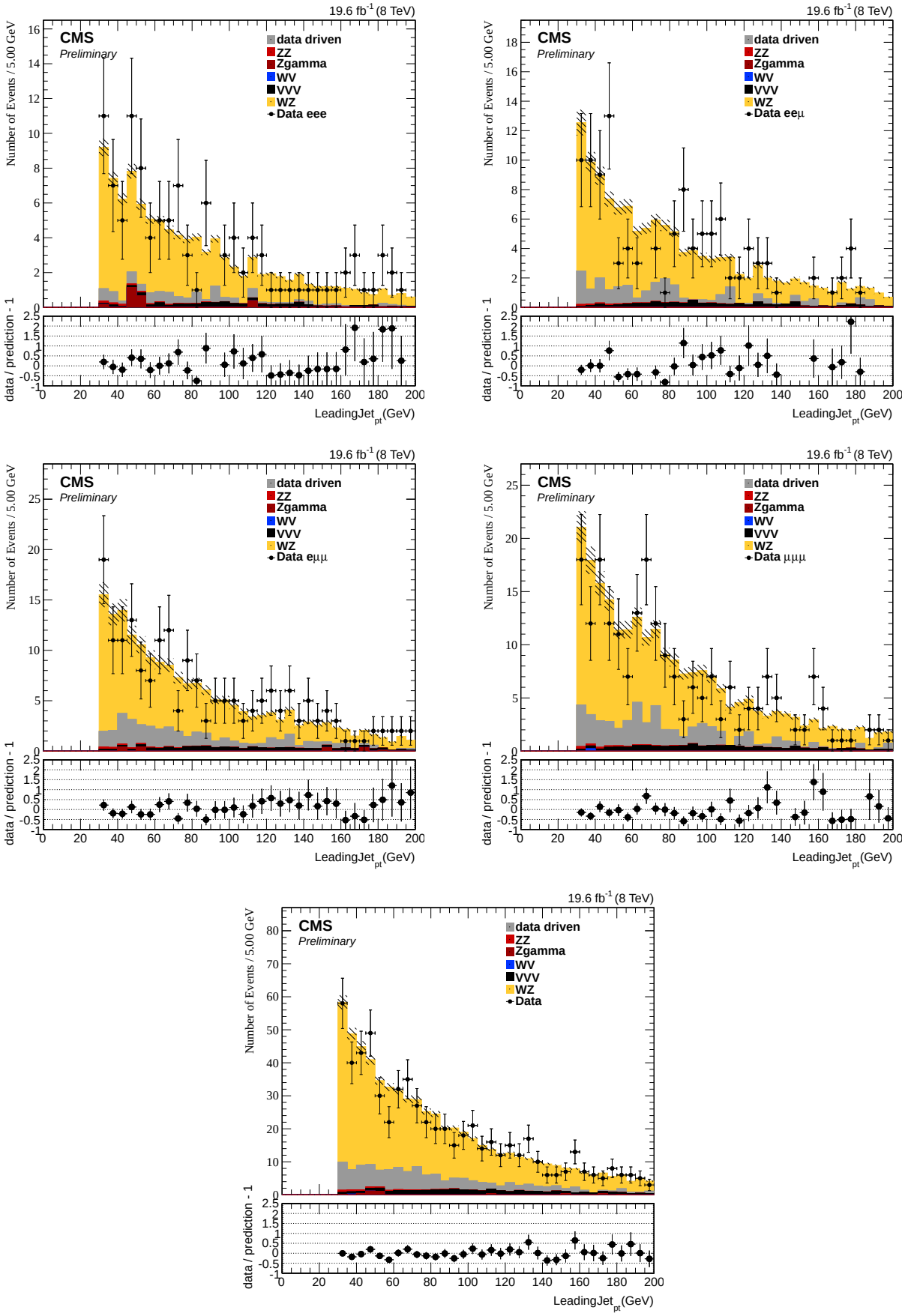

Figure 5.8: Leading jet pt after final selection for 3e (first row left), 2e1μ (first row right), 1e2μ (second row left) and 3μ (second row right) channels, and combination of all channels (third row).

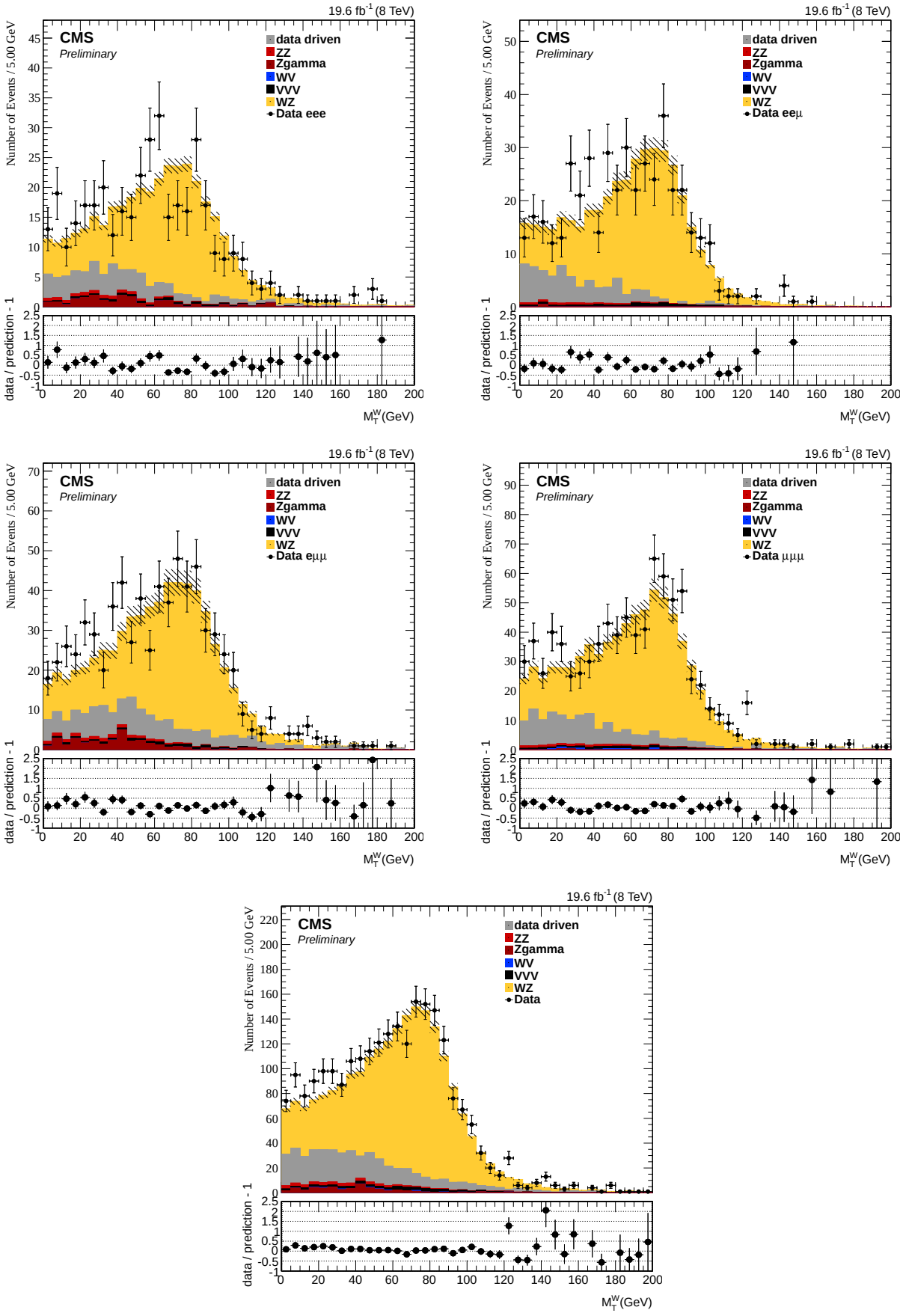

Figure 5.9: W transverse mass after W candidate is selected for 3e (first row left), 2e1μ (first row right), 1e2μ (second row left) and 3μ (second row right) channels, and combination of all channels (third row).

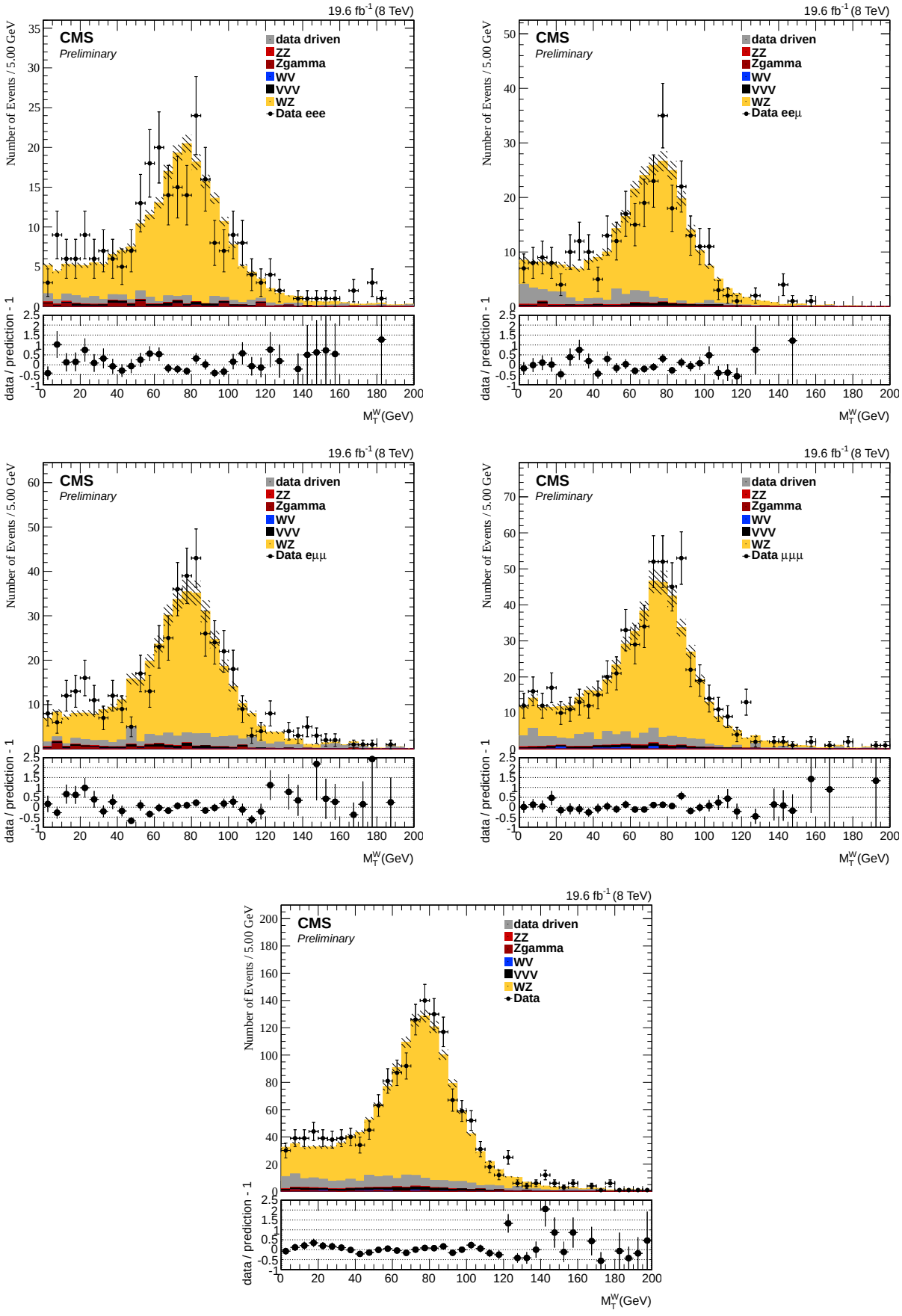

Figure 5.10: W transverse mass after final selection for 3e (first row left), 2e1μ (first row right), 1e2μ (second row left) and 3μ (second row right) channels, and combination of all channels (third row).

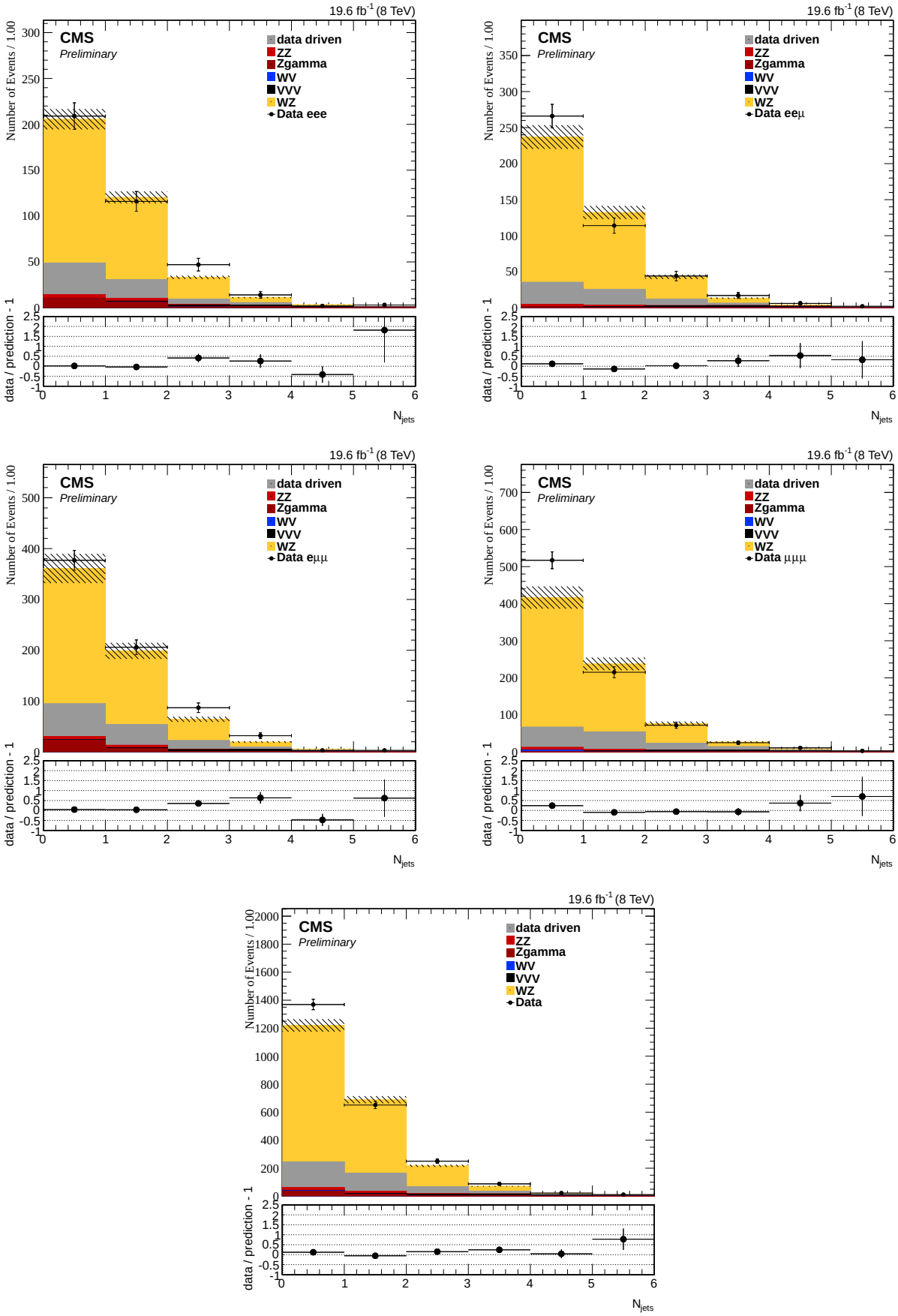

Figure 5.11: Number of jets after W candidate is selected for 3e (first row left), 2e1μ (first row right), 1e2μ (second row left) and 3μ (second row right) channels, and combination of all channels (third row).

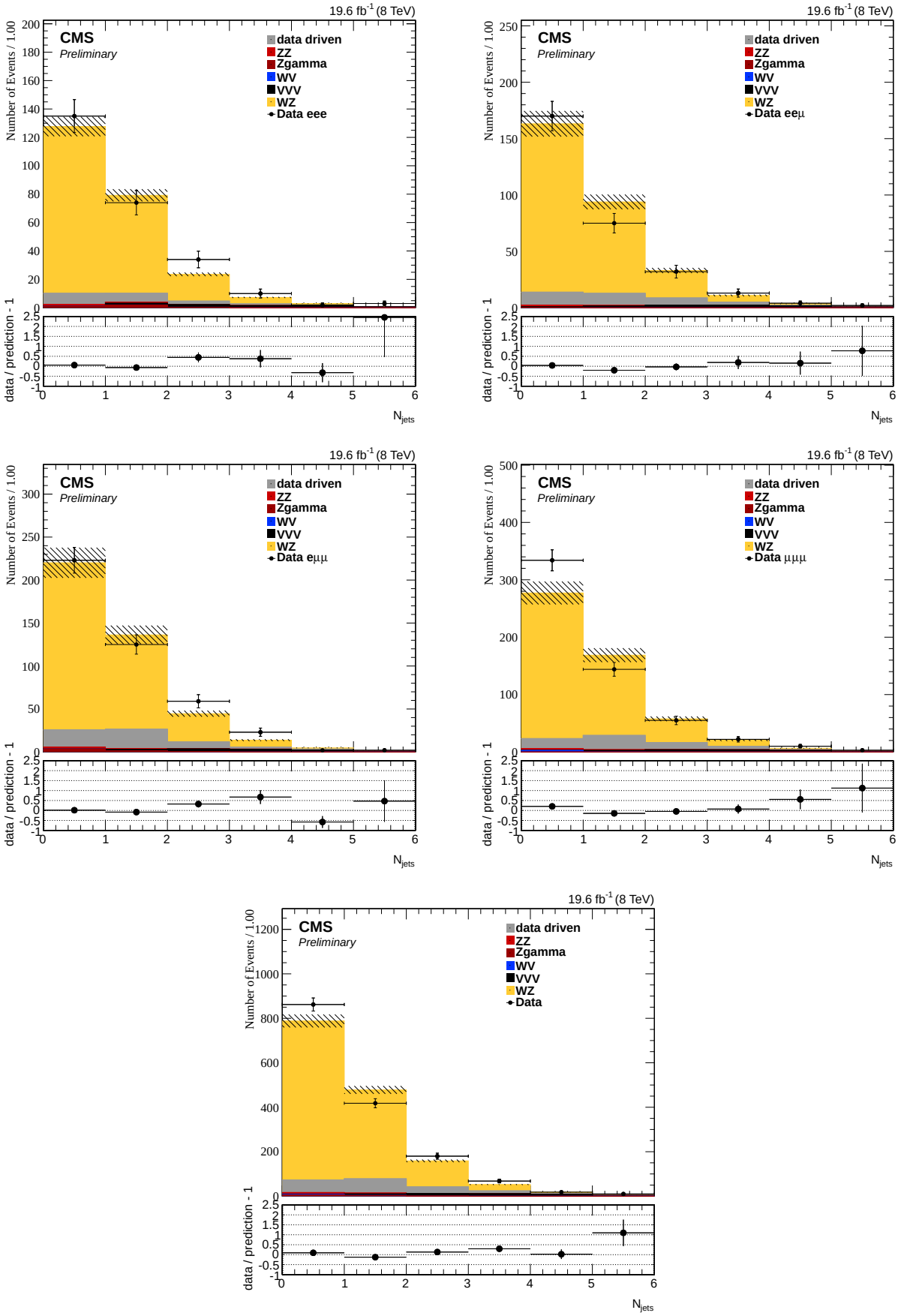

Figure 5.12: Number of jets after final selection for 3e (first row left), 2e1μ (first row right), 1e2μ (second row left) and 3μ (second row right) channels, and combination of all channels (third row).

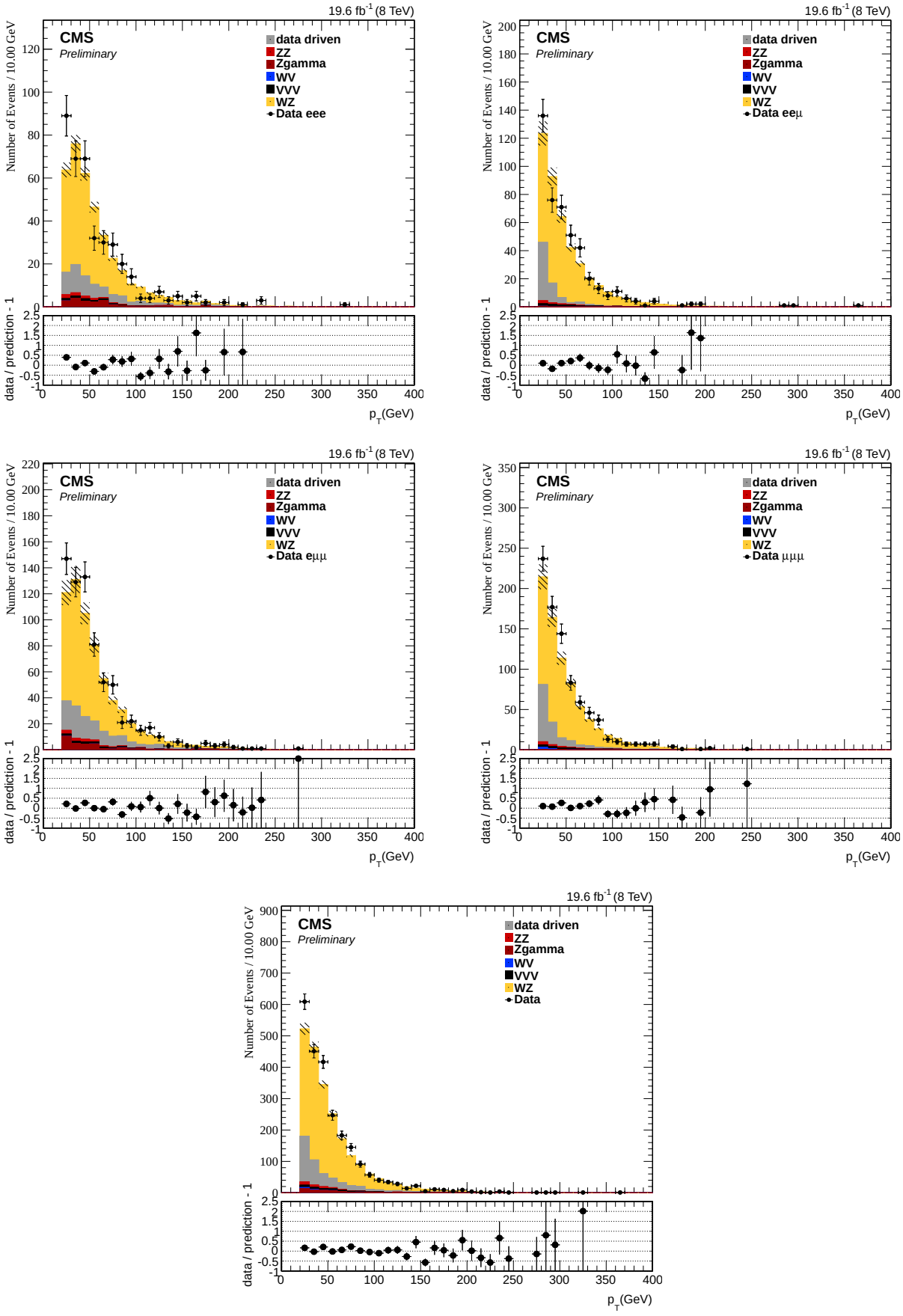

Figure 5.13: of W lepton after W candidate is selected for 3e (first row left), 2e1μ (first row right), 1e2μ (second row left) and 3μ (second row right) channels, and combination of all channels (third row).

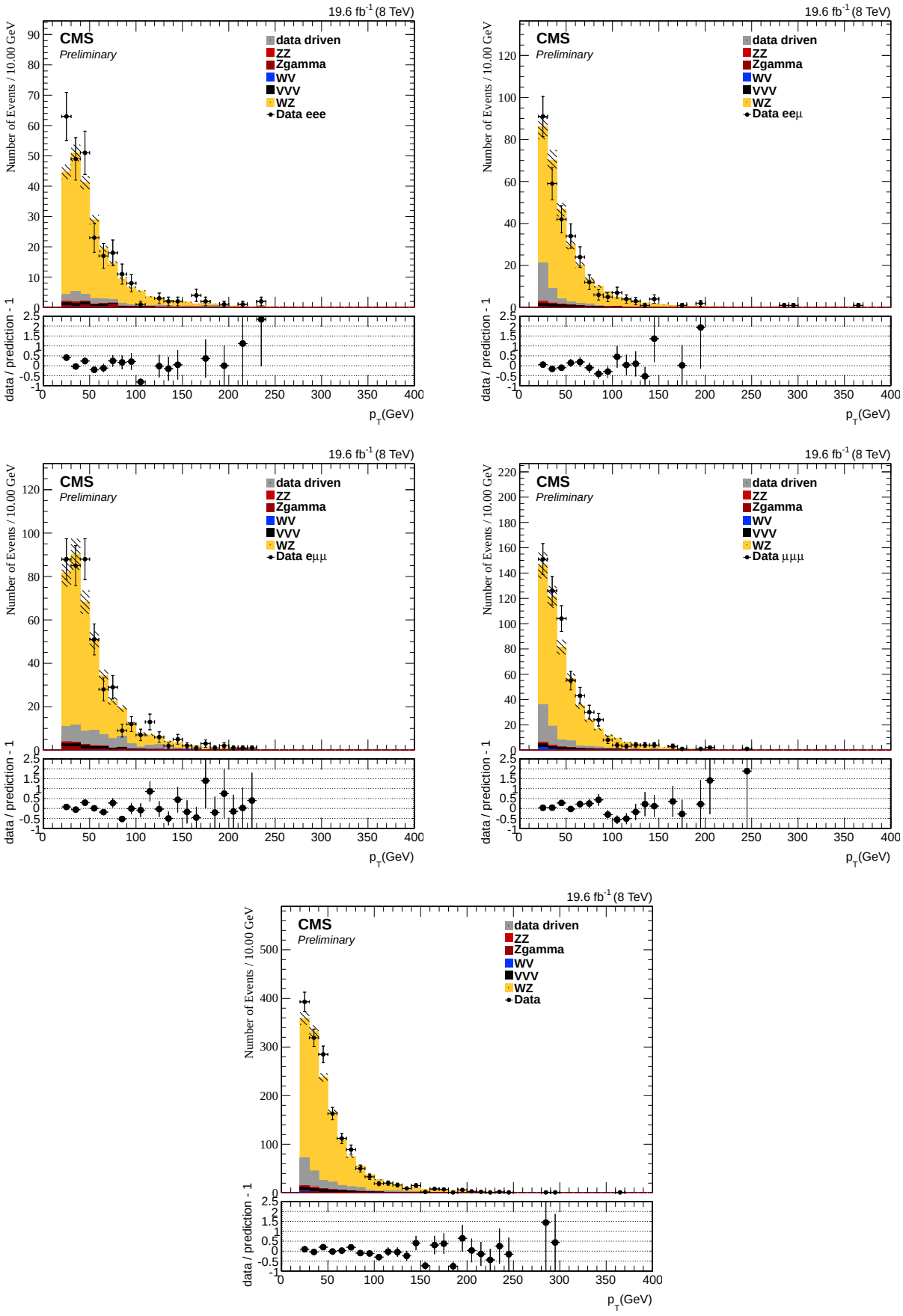

Figure 5.14: of W lepton after final selection for 3e (first row left), 2e1μ (first row right), 1e2μ (second row left) and 3μ (second row right) channels, and combination of all channels (third row).

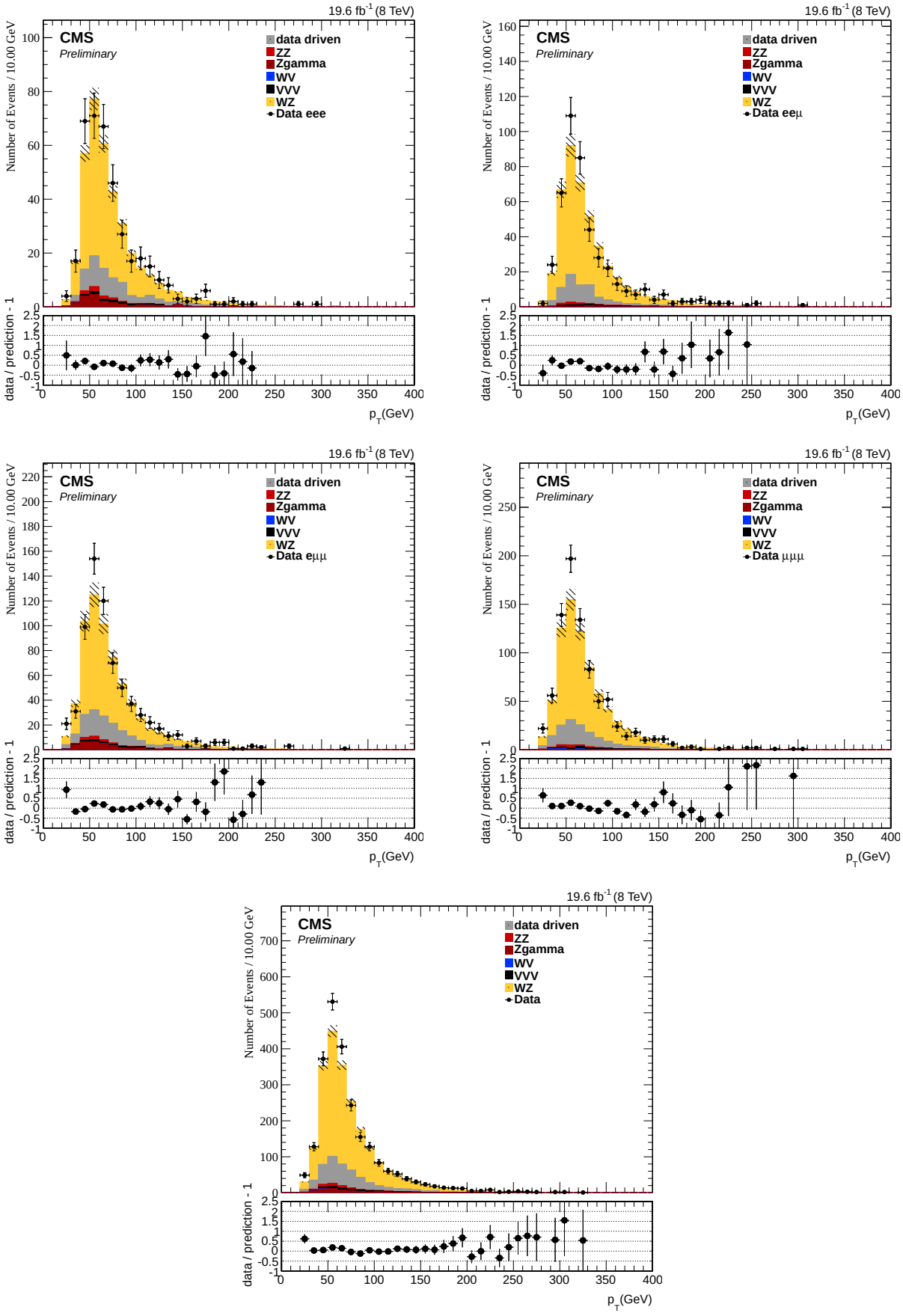

Figure 5.15: p_T of first Z lepton after W candidate is selected for 3e (first row left), 2e1μ (first row right), 1e2μ (second row left) and 3μ (second row right) channels, and combination of all channels (third row).

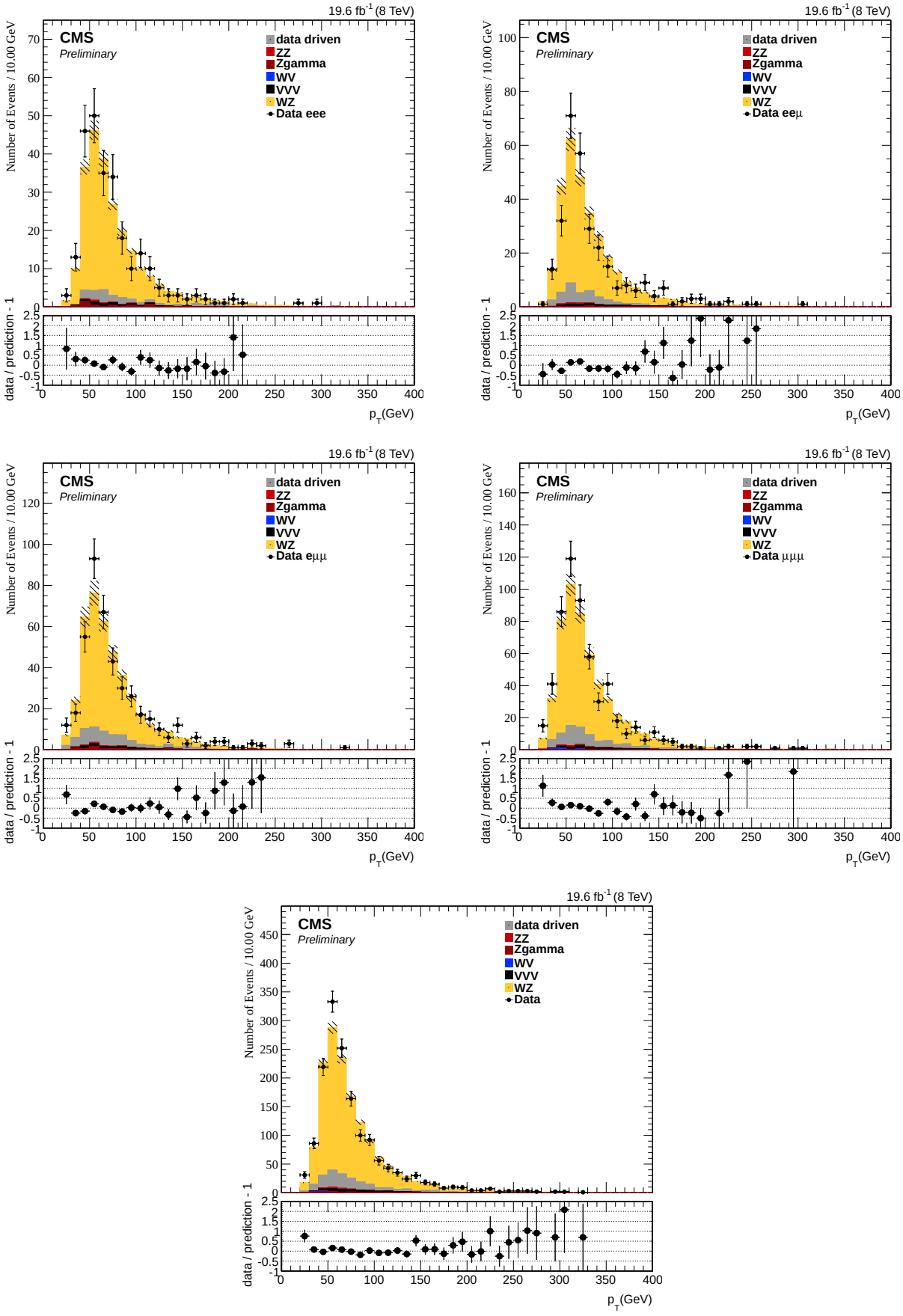

Figure 5.16: of first Z lepton after final selection for 3e (first row left), 2e1μ (first row right), 1e2μ (second row left) and 3μ (second row right) channels, and combination of all channels (third row).

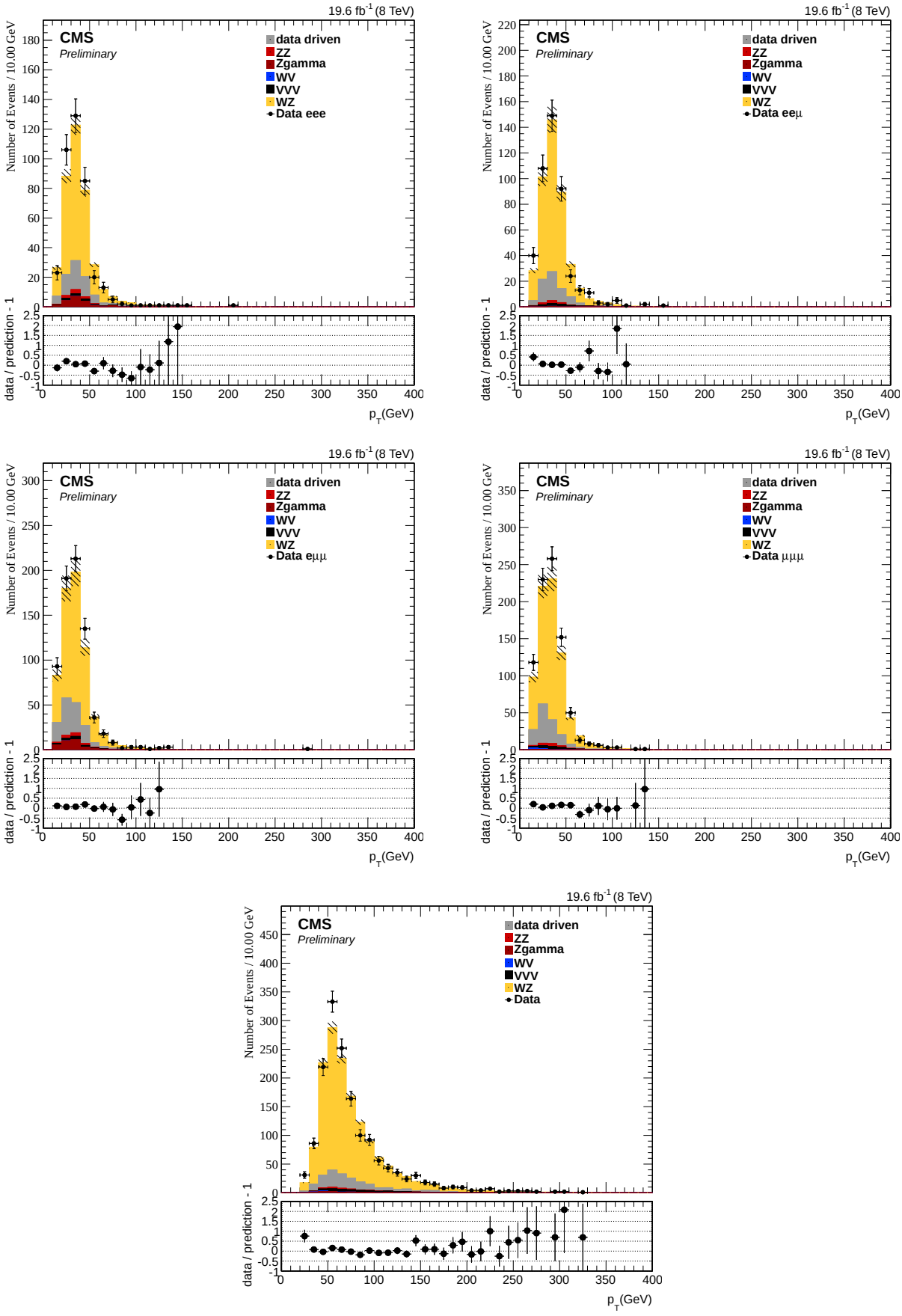

Figure 5.17: of second Z lepton after W candidate is selected for 3e (first row left), 2e1μ (first row right), 1e2μ (second row left) and 3μ (second row right) channels, and combination of all channels (third row).

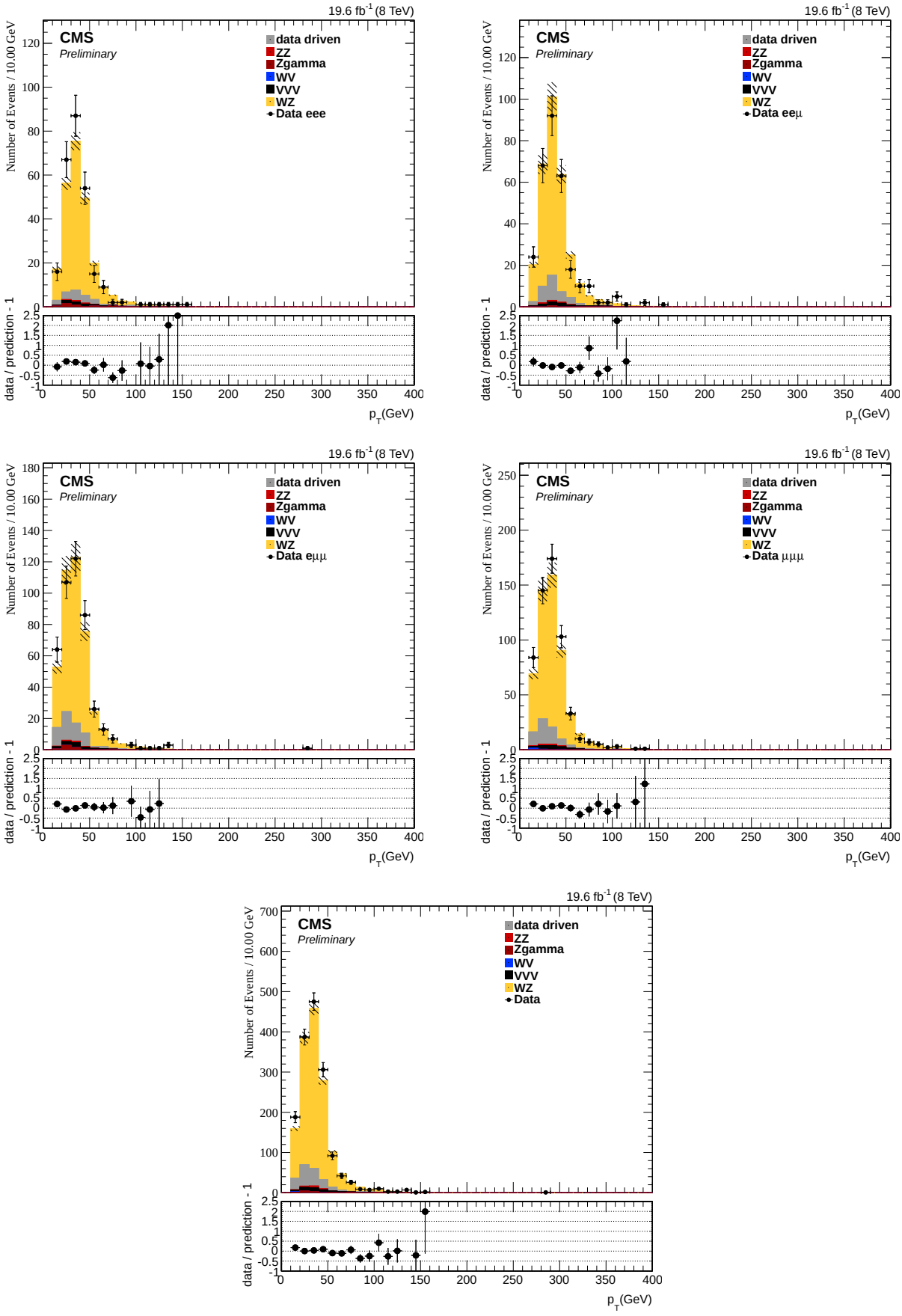

Figure 5.18: of second Z lepton after final selection for 3e (first row left), 2e1μ (first row right), 1e2μ (second row left) and 3μ (second row right) channels, and combination of all channels (third row).

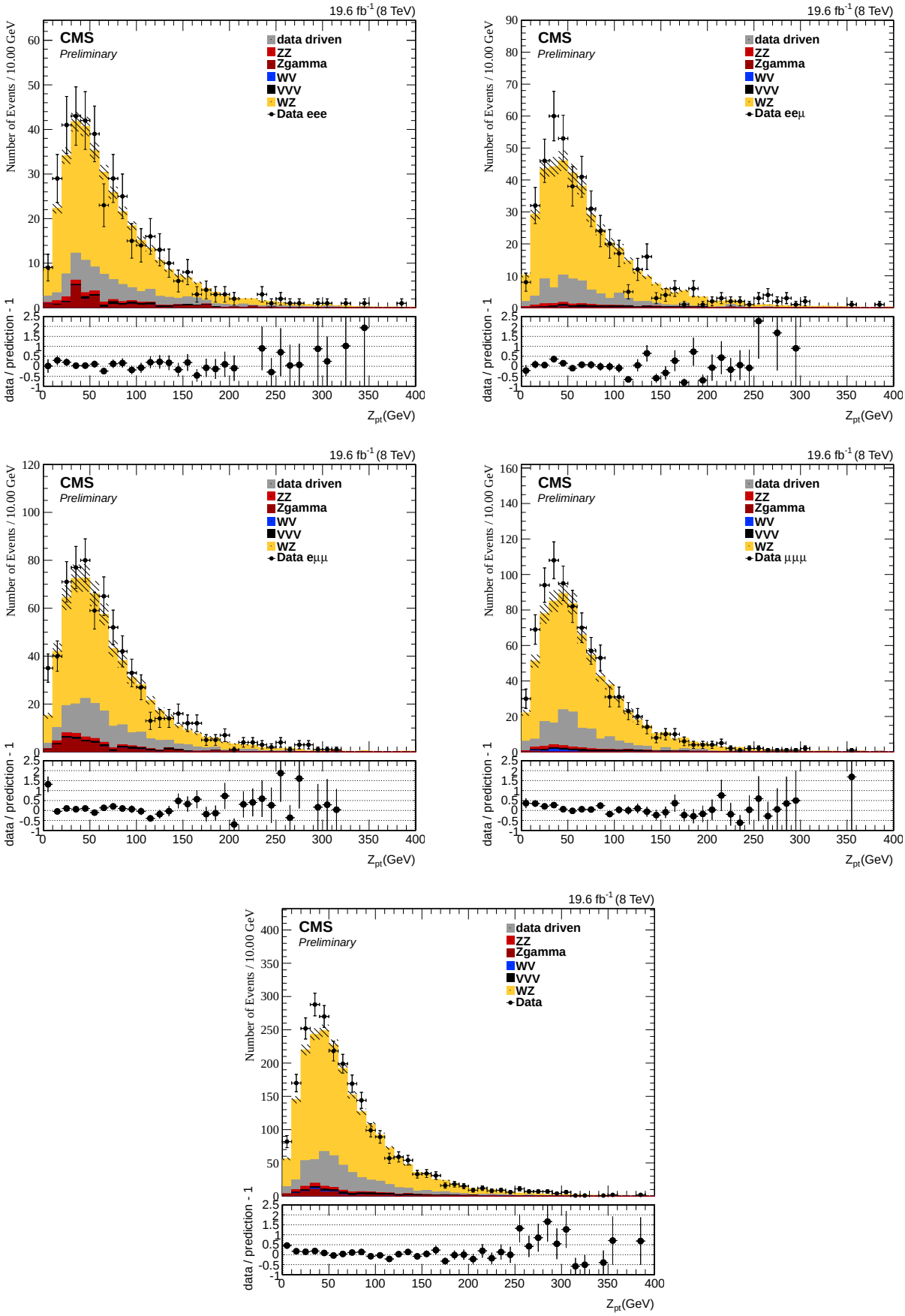

Figure 5.19: Z after W candidate is selected for 3e (first row left), 2e1μ (first row right), 1e2μ (second row left) and 3μ (second row right) channels, and combination of all channels (third row).

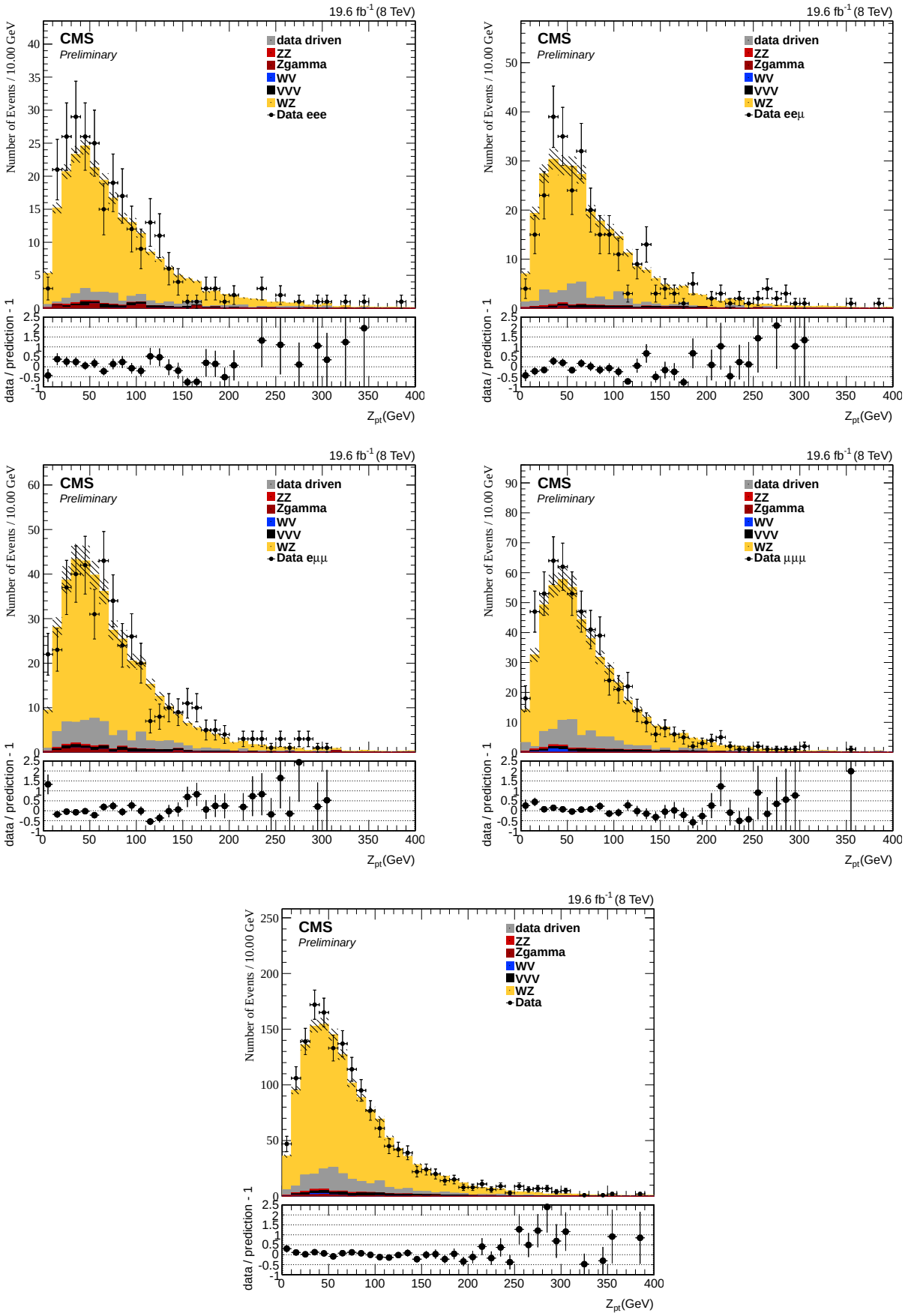

Figure 5.20: Z after final selection for 3e (first row left), 2e1μ (first row right), 1e2μ (second row left) and 3μ (second row right) channels, and combination of all channels (third row).

5.3 Backgrounds

We consider as backgrounds all processes leaving in the detector same signature as the signal process. Leptons coming from W and Z decays usually are isolated from the final state particles in the event. Such leptons are called *promt leptons*. Jets misidentified as leptons, and leptons coming from jets are called *fake leptons*. The main source of backgrounds are processes where fake leptons are identified in the final state. Here is list of background sources:

Backgrounds:

- **QCD** production processes, where final state particles are hadrons, therefore jets. This background is generically called QCD background. The requirement for three high-p_T isolated leptons strongly suppresses all QCD background. Despite the huge production rate of QCD processes, their contribution in this analysis is negligible
- **Z+jets:** The production of Z/γ^* in association with jets, where Z decays leptonicaly. Moreover, unlike the background described above, this process contains a genuine Z in the final state making more difficult to reject it through an invariant mass requirement. Thus, the process only need one fake lepton and some E_T^{miss} to present the same signature as WZ. This is one of the dominant backgrounds in this analysis, and its contribution is estimated using a data driven method.
- $t\bar{t}$: The top (antitop) quark produces $W^-(W^+)$ boson and anti-bottom (bottom) quark. Therefore, two high-p_T, opposite-charged, isolated leptons and E_T^{miss} from the Ws are going to be present in the final state signature, together with the non-isolated lepton from the quarks or any misidentified hadron. This background source together with a $Z + jets$ is dominant backgrounds. Both are estimated using data driven method explained later.
- $Z\gamma$ The Z production can be accompanied by initial state radiation, where the photon is emitted by the incoming partons, or a final state radiation where the photon is radiated by one of the charged leptons from the Z decay. A photon conversion into leptons (mostly electrons) can be produced when the photon interacts with the detector, giving the third missing lepton to complete the signal signature.
- ZZ The fully leptonic ZZ decay results in four final state leptons. When all of these leptons are detected, it is possible to distinguish a background event from the signal. Sometimes, however, one lepton can escape detection. Such events are observed as having missing transverse energy and are not separable from the WZ signal. ZZ is therefore an irreducible background.
- **WV** this background is containing W and vector boson (W, Z or γ). Processes which are part of this background are following: $WW + jets \to 2l$, $WZ \to 2q2\nu$, $WZ \to 2l2q$, $W + jets \to l\nu$, $Wbb \to l\nu$, $W\gamma^* \to e\nu$, $W\gamma^* \to \nu\mu$, $W\gamma^* \to \tau\nu$ and $W\gamma \to l\nu\gamma$. Individual contributions of each WV subsample can be seen in table 5.10. $W\gamma^*$ background is

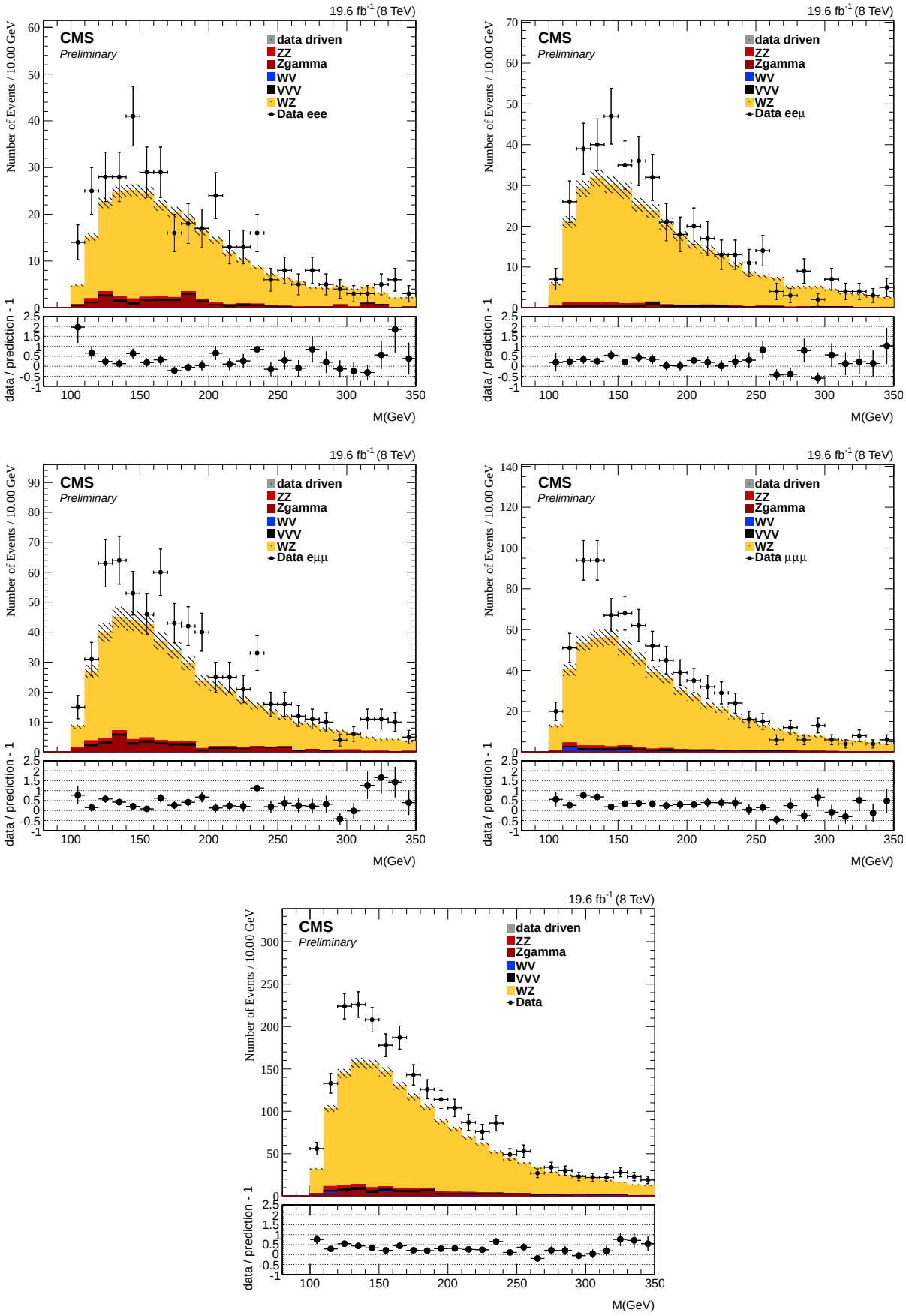

Figure 5.21: Invariant mass of three leptons after W candidate is selected for 3e (first row left), 2e1μ (first row right), 1e2μ (second row left) and 3μ (second row right) channels, and combination of all channels (third row).

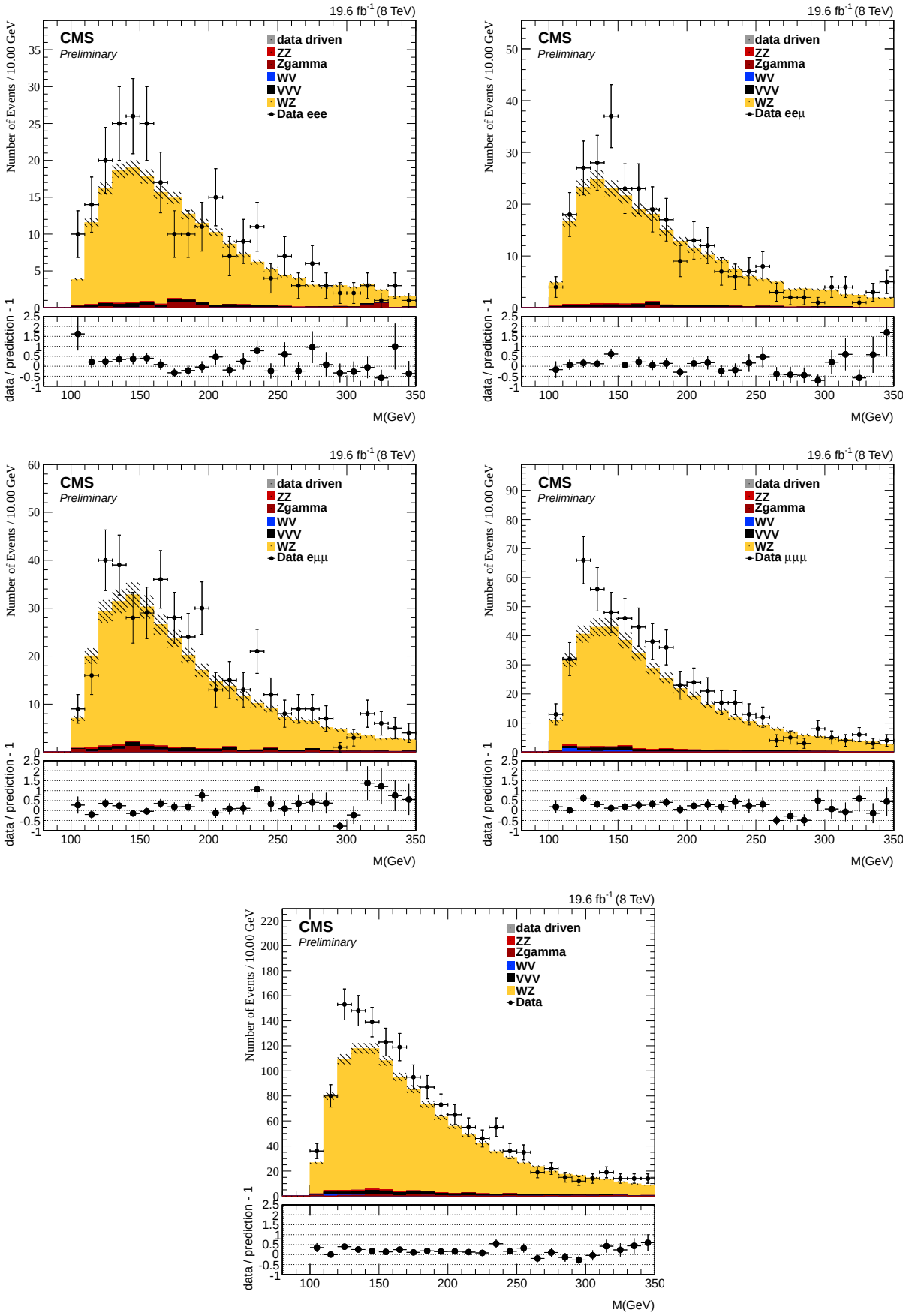

Figure 5.22: Invariant mass of three leptons after final selection for 3e (first row left), 2e1μ (first row right), 1e2μ (second row left) and 3μ (second row right) channels, and combination of all channels (third row).

estimated using MC, while other processes contain fake leptons, and are estimated using data driven method.

- **VVV** this background is containing three bosons. The following processes which are part of this background are following: WWγ+jets, WZZ+jets, ZZZ+jets, WWZ+jets, WWW+jets, $t\bar{t}$W+jets, $t\bar{t}$Z+jets, $t\bar{t}$WW+jets and $t\bar{t}\gamma$+jets. Individual contributions of each VVV subsample can be seen in table 5.9. This background is estimated using MC
- **WZ** process, where Z or W do not decay directly to muons or electrons is considered as background. While hadronic WZ decays are easily rejected and their contribution to the selected sample remains negligible, the contribution of another WZ final state is significant, where W or Z decay leptonically to one or more τ leptons.As, τ decays result with an electron in 17.82% of all cases, and with a muon in 18.39% of all cases. A fraction of momentum is however taken by the resulting neutrinos. The Feynman diagram of a leptonic τ decay is shown in Figure 5.23. This background can also be classified as irreducible when the final state satisfies imposed kinematic criteria. It has to be noted that the cross section is proportional to the one measured in analysis

5.4 Background estimation

The contribution of backgrounds with fake leptons dominated by $t\bar{t}$ and $Z + jets$ is estimated using data driven method [50]. The contribution of other backgrounds are estimated using Monte Carlo. The expected yields for all backgrounds are summarized in table 5.3.

5.4.1 WZ decays with $Z \to \tau\tau$ or $W \to \tau\nu$

All four final states receive a contribution from WZ decays

WZ$\to 3\ell\nu(\ell = \tau)$ represents a background for all final states for the cases when W or Z bosons in WZ$\to 3\ell\nu$ decay to τ leptons. Their cross section is directly proportional to the signal cross section. Their contribution is therefore not taken as absolute yield and is instead taken as a fraction (f_τ) of all WZ decays passing the full selection in each channel. For each of the four final states, we determine the ratio f_τ between the number of such selected events and the total number of events selected from the WZ signal sample. The values are given in Table 6.1. This fraction is then subtracted from the signal yield obtained after subtracting all other background contributions.

5.4.2 Backgrounds with fake leptons

Data-driven methods are used to estimate number of background events in our sample. Monte Carlo simulations depend on theoretical predictions and numerous approximations, from mod-

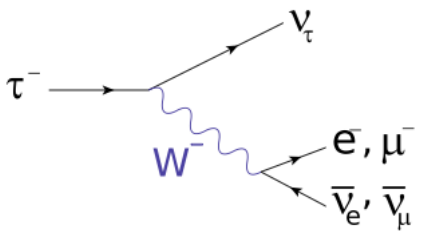

Figure 5.23: Feynman diagram of a leptonic τ decay

elling PDFs, finite order calculations, hadronization modelling, to imperfections in the detector simulation. To reduce uncertainties on these sources, various techniques are used to perform estimations and cross-checks of signal or backgrounds based on information extracted from collision data. Those methods are called *data driven* methods.

For this analysis a method is used to estimate the number of reducible background events remaining in the sample after all WZ selection criteria have been applied. The method only allows to estimate backgrounds containing jets misidentified as leptons, or produced from a heavy quark decay, resulting in leptons produced as a part of a hadronic jet. In this sense, two categories of observable leptons are distinguished according to their real origin:

- *Prompt lepton:* a true lepton originating from heavy boson decays. They will usually be isolated from other particles in the final state
- *Non-prompt lepton:* any lepton not originating from heavy boson decays, or a particle misidentified as a lepton.

In the following, the index j is used to denominate misidentified leptons, while index l is used to denominate prompt leptons. The order of indices is the following: leading Z lepton (the one with higher p_T), trailing Z lepton (lower p_T) and W lepton.
The sample of selected collision events has contributions from the following event categories:

- *lll*: all three leptons originate from prompt leptons. WZ signal events contribute to this category, as well as sources of irreducible background.
- *llj*: this category is mostly composed of Z+jets and $t\bar{t}$ events, in which the two Z leptons are prompt, while the lepton associated to the W decay is a misidentified lepton.
- *jll* and *ljl*: this category is again composed of $t\bar{t}$ and Z+jets events, largely dominated by $t\bar{t}$
- *ljj, jlj, ljj, jjj*: this categories contain two or three misidentified leptons. Several processes may contribute to this categories: W+jets, Z+jets (in which one or both leptons escape undetected), $t\bar{t}$ (whith fully hadronic top decays), or QCD multijet processes.

The method uses the distinction between a loose and a tight lepton selection. The tight selection is identical to the one used in the final selection, while some of the lepton identification requirements used in the final selection are relaxed in the loose selection. Tight and loose selection

are described in Chapter 4. Leptons in loose sample can be distinguished as *passing* or *failing* the tight selection. The following probabilities that are generally dependent on η and p_T of the reconstructed lepton, are identified:

- ε is the probability of a prompt lepton that passes the loose selection for the i-th lepton to also pass the tight selection.
- p is the probability that a misidentified lepton which passes the loose selection as the i-th lepton, also passes the tight selection.

The same sample can be split in subsamples depending on whether each of the three leptons passes or fails the tight requirement. The number of events in each subsample is labeled N_{ijk} with $i, j, k = T, F$ where T indicates leptons passing the tight selection and F stands for leptons failing the tight selection. The number of events in each category can be expressed using the efficiencies p_i and ε_i. For example the number of events with all three leptons passing the tight selection N_{TTT} can be written as:

$$\begin{aligned} N_{TTT} &= n_{j\ell\ell} p_1 \varepsilon_2 \varepsilon_3 + n_{j\ell j} p_1 \varepsilon_2 p_3 + n_{jj\ell} p_1 p_2 \varepsilon_3 + n_{jjj} p_1 p_2 p_3 \\ &\quad + n_{\ell\ell\ell} \varepsilon_1 \varepsilon_2 \varepsilon_3 + n_{\ell\ell j} \varepsilon_1 \varepsilon_2 p_3 + n_{\ell j\ell} \varepsilon_1 p_2 \varepsilon_3 + n_{\ell jj} \varepsilon_1 p_2 p_3 \end{aligned} \tag{5.2}$$

Solving the system of equation number of signal events, *i.e.* events with three prompt leptons can be obtained (details in Appendix A):

$$\begin{aligned} n_{\ell\ell\ell} = \frac{1}{(\varepsilon_1 - p_1)(\varepsilon_2 - p_2)(\varepsilon_3 - p_3)} & \\ [\ N_{TTT}(1-p_1)(1-p_2)(1-p_3) & \\ -N_{TTF}(1-p_1)(1-p_2)(\ p_3) & \\ -N_{TFT}(1-p_1)(\ p_2)(1-p_3) & \\ +N_{TFF}(1-p_1)(\ p_2)(\ p_3) & \\ -N_{FTT}(\ p_1)(1-p_2)(1-p_3) & \\ +N_{FTF}(\ p_1)(1-p_2)(\ p_3) & \\ +N_{FFT}(\ p_1)(\ p_2)(1-p_3) & \\ -N_{FFF}(\ p_1)(\ p_2)(\ p_3)] & \end{aligned} \tag{5.3}$$

The coefficients for the number of events in each category N_{ijk} in equation B.2 define weights which are applied to each event depending on category in which it belongs. These weights are then summed over all events in the loose sample. The reason of using weights instead of simply summing each N_{ijk} contribution is that ε_i and p_i values depend on the kinematic (p_t, η) properties of lepton objects in each event. To obtain the number of events remaining after requiring all leptons to pass the the tight selection, an additional weight is applied in form

of efficiencies for loose prompt leptons to pass tight selection, i.e. $n^T_{lll} = \varepsilon_1\varepsilon_2\varepsilon_3 n_{lll}$.
Statistical uncertainties are computed using error propagation and are described in Appendix B. Efficiencies ε_i and p_i are determined using separate sample selected to obtain a sample of prompt or misidentified objects resembling, as closely as possible, those found in the selected sample [50].

5.4.3 Determination of prompt lepton efficiencies

For prompt leptons, efficiencies are determined from $Z \to ll$ decays using the *Tag and Probe* (T&P) method. This method enables us to measure efficiencies of various selection cuts on prompt leptons, relying on the fact that pairs of prompt leptons from Z decays will have invariant mass consistent with the Z mass. First a *tag* lepton is required to pass all selection and isolation cuts to ensure that this is promt lepton. The other lepton called *probe* is required to have the same flavour, opposite charge and satisfy some selection requirements, but not the one whose efficiency we want to measure. the invariant mass of tag and probe leptons is required be in a defined window around the nominal PDG value for the Z mass. The number of Z candidates is determine from a fit. The efficiency is then obtained via the following equation.

$$\varepsilon = \frac{2(N_{TT} - B_{TT})}{N_{TF} - B_{TF} + 2(N_{TT} - B_{TT})} \tag{5.4}$$

N_{ij} is the total number of events in the Z-candidate mass window, while B is the combinatorial background from W events, as estimated from a fit on events outside Z window (sideband region). The index TT means that both leptons pass the isolation cuts and TF means that exactly one of the leptons fails the cut.
Prompt lepton efficiencies for electrons and muons are listed in tables 5.4 and 5.6.

5.4.4 Determination of fake rate efficiencies

Fake rate is efficiency of tight selection on QCD sample whose selection will be described in this section. A special set of requirements, optimized for isolating processes containing jets is used to select the control sample. Single electron or single muon HLT tiggers are used. Single lepton triggers with the lowest available thresholds are used in order to select samples mainly composed of QCD events. The imposed loose criteria are tighter than the lepton requirements in these triggers to avoid a bias coming from the trigger. The selection is optimized to suppress prompt leptons from W and Z boson decays. In order to suppress prompt leptons from W missing transverse energy is required to be less than 20 GeV and the W transverse mass less than 20 GeV. The muons from Drell-Yan and Z decays are removed with $m_{\mu\mu} > 20$ GeV and the $m_{\mu\mu} \notin [76, 106]$ GeV constraints (Z-peak veto). For electrons the W transverse mass cut is

not applied and the Z-peak veto is $m_{ee} \notin [60, 120]$ GeV. ΔR between jet and lepton is required to be bigger than 1. For each event, the leading jet transverse momentum is required to be above a certain threshold, affecting the p_T spectrum of the jet misidentified as lepton. This requirement ensures that there is no bias from the leading jet and that the misidentified object is recoiling against it. Nominal values of the leading jet are taken to be 35 GeV for electrons 20 GeV for muons.

Fake rate efficiencies for electrons and muons are listed in the tables 5.5 and 5.7.

Table 5.4: Electron efficiency rate binned in p_T and η.

	$0 < \|\eta\| \leq 1.479$	$1.479 < \|\eta\| \leq 2.5$
10 <p_T≤ 15GeV	0.8145 ± 0.0033	0.6048 ± 0.0053
15 <p_T≤ 20GeV	0.8145 ± 0.0033	0.6048 ± 0.0053
20 <p_T≤ 25GeV	0.9031 ± 0.0014	0.8058 ± 0.0026
25 <p_T≤ 30GeV	0.9244 ± 0.0009	0.8406 ± 0.0020
30 <p_T≤ 9999GeV	0.9572 ± 0.0002	0.8980 ± 0.0005

Table 5.5: Electron fake rate binned in p_T and η.

	$0 < \|\eta\| \leq 1$	$1 < \|\eta\| \leq 1.479$	$1.479 < \|\eta\| \leq 2$	$2 < \|\eta\| \leq 2.5$
10 <p_T≤ 15GeV	0.045 ± 0.005	0.033 ± 0.004	0.008 ± 0.002	0.021 ± 0.005
15 <p_T≤ 20GeV	0.044 ± 0.003	0.049 ± 0.003	0.017 ± 0.001	0.017 ± 0.002
20 <p_T≤ 25GeV	0.041 ± 0.002	0.064 ± 0.003	0.025 ± 0.002	0.025 ± 0.002
25 <p_T≤ 30GeV	0.059 ± 0.003	0.101 ± 0.005	0.041 ± 0.003	0.043 ± 0.003
30 <p_T≤ 9999GeV	0.084 ± 0.006	0.111 ± 0.009	0.058 ± 0.006	0.066 ± 0.005

Table 5.6: Muon efficiency rate binned in p_T and η.

	$0 < \|\eta\| \leq 1.479$	$1.479 < \|\eta\| \leq 2.5$
10 <p_T≤ 15GeV	0.7119 ± 0.0003	0.7582 ± 0.0006
15 <p_T≤ 20GeV	0.8059 ± 0.0018	0.8495 ± 0.0001
20 <p_T≤ 30GeV	0.9027 ± 0.0008	0.8948 ± 0.0012
30 <p_T≤ 50GeV	0.9741 ± 0.0001	0.9627 ± 0.0002
50 <p_T≤ 9999GeV	0.9900 ± 0.0001	0.9875 ± 0.0003

Results

The method outlined in the previous subsections was used to determine the number of events with three prompt leptons in the sample passing the full WZ selection. This corresponds to determining $\varepsilon_1\varepsilon_2\varepsilon_3 n_{\ell\ell\ell}$, using Equation 5.3. The results are given in Table 5.8 for the four studied final states. For additional information we also give the event yields N_{ijk}. Note however

Table 5.7: Muon fake rate binned in p_T and η.

	$0 < \|\eta\| \leq 1$	$1 < \|\eta\| \leq 1.479$	$1.479 < \|\eta\| \leq 2$	$2 < \|\eta\| \leq 2.5$
10 <p_T≤ 15GeV	0.084 ± 0.005	0.100 ± 0.008	0.128 ± 0.012	0.20 ± 0.02
15 <p_T≤ 20GeV	0.073 ± 0.009	0.080 ± 0.014	0.10 ± 0.02	0.21 ± 0.04
20 <p_T≤ 25GeV	0.098 ± 0.005	0.134 ± 0.009	0.11 ± 0.01	0.12 ± 0.02
25 <p_T≤ 30GeV	0.136 ± 0.009	0.191 ± 0.016	0.16 ± 0.02	0.23 ± 0.04
30 <p_T≤ 9999GeV	0.19 ± 0.02	0.25 ± 0.03	0.23 ± 0.04	0.31 ± 0.10

that these numbers are not directly used to extract $n_{\ell\ell\ell}$, as the rates p_i and ε_i are not constant as a function of transverse momentum, and $n_l ll$ is computed as a sum of event weights.

Table 5.8: Matrix method yields requiring three loose leptons. The quoted uncertainties are purely statistical and do not contain systematic uncertainties on the fake rate method.

	eee	eeμ	$\mu\mu$e	$\mu\mu\mu$
$\varepsilon_1\varepsilon_2\varepsilon_3 n_{\ell\ell\ell}$	239.64 ± 17.54	266.00 ± 18.30	380.65 ± 22.81	505.64 ± 24.97
$N_{TTT} - \varepsilon_1\varepsilon_2\varepsilon_3 n_{\ell\ell\ell}$	18.36 ± 6.13	32.00 ± 4.71	54.35 ± 7.82	62.36 ± 4.84
N_{TTT}	258	298	435	568
N_{TTF}	236	123	441	166
N_{TFT}	69	94	121	149
N_{TFF}	57	27	57	40
N_{FTT}	18	18	25	23
N_{FTF}	12	7	16	6
N_{FFT}	15	5	5	10
N_{FFF}	6	2	4	7

5.4.5 Other backgrounds

The other backgrounds are estimated from Monte Carlo simulations. The expected event yields for all background sources, scaled to the luminosity, are given in Table 5.3, and for WV and VVV backgrounds, each background separately are given in Tables 5.9 and 5.10.

In WV sample contributions from samples $WW + jets$, $WZ \to 2qlv$ and $WZ \to 2l2q$ are not substracted from the data yield, since these processes give us fake lepton from jets whose contribution is determined using the data driven method explained in the previous section. Therefore the only contribution left is $W\gamma^*$ with W decaying to a muon and a neutrino. As can be seen in Table 5.10, the only $W\gamma^*$ channel that contributes is $W\gamma^* \to 3\mu\nu$. The reason for this is following:

Characteristics of γ^* lepton pair is that two leptons are spatially close together. Their invariant mass is dominantly low. Both of this can be seen on Figures 5.24 and 5.25. This means that Z candidate for WZ can be built only from one γ^* and W lepton. Therefore Z candidates will be found only in $W\gamma^*$ channels decaying to channels with three muons and three electrons. One

of γ^* leptons will be used to reconstruct the Z and the other one will be associated to the W. The lepton associated to the W will be close to one of the Z leptons, and it should be a lepton of the opposite charge. Muon momentum doesn't contribute to the isolation variable, and electron does. This results in fact that isolation cut on electrons doesn't allow two electrons too close, while muons don't have this restriction. Therefore only $W\gamma^*$ contribution is in three muon channel.

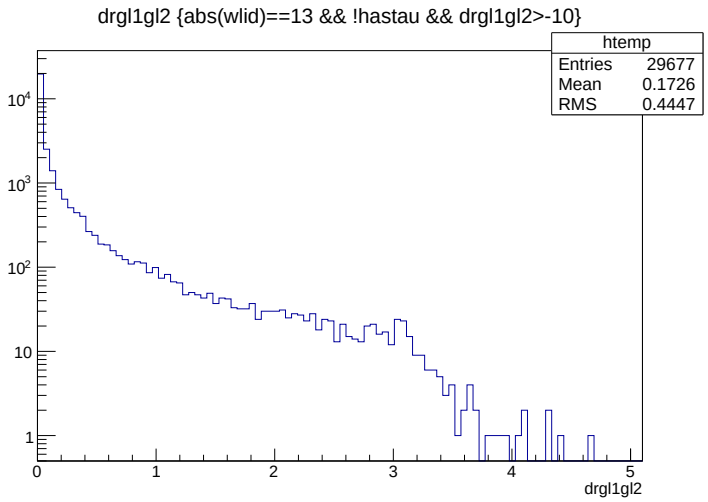

Figure 5.24: ΔR between γ^* lepton pair.

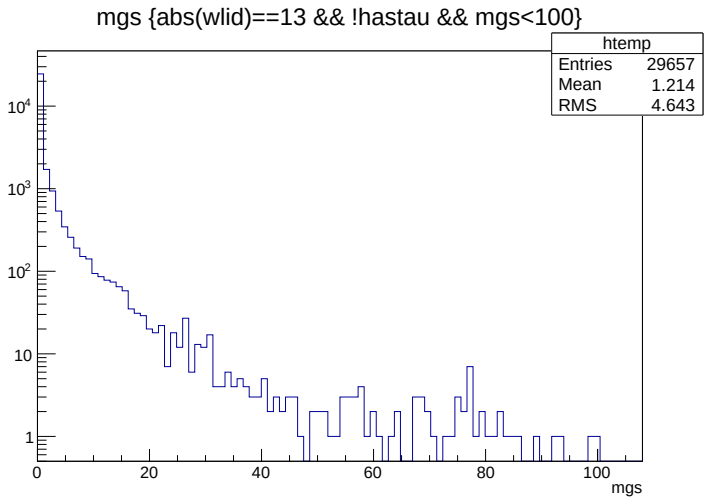

Figure 5.25: Invariant mass of γ^* lepton pair in GeV.

Table 5.9: Monte Carlo yields for VVV sample.

sample	eee	eeμ	$\mu\mu$e	$\mu\mu\mu$	total
WWG+jets	0.052 $\pm$ 0.052	0	0	0	0.052 $\pm$0.052
WZZ+jets	0.46 $\pm$ 0.03	0.58 $\pm$ 0.03	0.70 $\pm$ 0.04	0.97 $\pm$ 0.04	2.71 $\pm$ 0.07
ZZZ+jets	0.043 $\pm$ 0.005	0.040$\pm$ 0.004	0.082 $\pm$ 0.007	0.069 $\pm$ 0.006	0.23 $\pm$ 0.01
WWZ+jets	1.28 $\pm$ 0.08	1.70$\pm$0.10	2.18$\pm$ 0.11	2.70 $\pm$0.12	7.86 $\pm$ 0.21
WWW+jets	0.19 $\pm$ 0.04	0.32$\pm$0.05	0.33$\pm$ 0.05	0.38 $\pm$ 0.06	1.22 $\pm$ 0.10
TTW+jets	0.44 $\pm$ 0.10	0.84$\pm$0.15	1.09$\pm$ 0.17	1.22 $\pm$ 0.18	3.59 $\pm$ 0.31
TTZ+jets	4.21 $\pm$ 0.28	5.24$\pm$0.33	7.07$\pm$ 0.39	9.45 $\pm$ 0.45	25.97 $\pm$ 0.73
TTWW+jets	0.014$\pm$0.002	0.025$\pm$0.002	0.032$\pm$0.003	0.039 $\pm$ 0.003	0.110 $\pm$0.005
TTG+jets	0	0	0.14$\pm$0.14	0	0.14$\pm$ 0.14

Table 5.10: Monte Carlo yields for WV sample.

sample	eee	eeμ	$\mu\mu$e	$\mu\mu\mu$	total
$WW + jets \to 2l$	0.07 $\pm$ 0.06	0	0	0	0.0.07 $\pm$0.06
$WZ \to 2qlv$	0	0	0	0	0
$WZ \to 2l2q$	0.04 $\pm$ 0.04	0.05$\pm$ 0.04	0.21 $\pm$ 0.11	0.04 $\pm$ 0.04	0.34 $\pm$ 0.13
$W + jets \to lv$	0	0	0	0	0
$Wbb \to lv$	0	0	0	0	0
$W\gamma^* \to ev$	0	0	0	0	0
$W\gamma^* \to \mu v$	0	0	0	2.78 $\pm$ 0.83	2.78 $\pm$ 0.83
$W\gamma^* \to T\tau v$	0	0	0	0	0
$W\gamma \to lvg$	0	0	0	0	0

Chapter 6

WZ cross section measurement

This chapter describes the measurement of the WZ cross section at center of mass energy $\sqrt{s} = 8$ TeV. Analysis is performed on the full 2012 dataset collected by CMS.
The signal is restricted to the phase space where the invariant mass of two leptons lies within 20 GeV of the nominal Z boson mass. This restriction largely removes interfering contribution from the $WW\gamma$ vertex as the virtual photon contribution is significant in the lower mass range. The cross section is measured in four channels corresponding to the four possible combinations of WZ leptonic decay into electrons and muons.

6.1 Cross section measurement

The cross section is computed using the relation:

$$\sigma = \frac{N_{sig}}{A \times \varepsilon \cdot L} \tag{6.1}$$

where N_{sig} is the estimated number of signal events. $A \times \varepsilon$ is the detector acceptance and efficiency for signal, and L is the integrated luminosity. The integrated luminosity of the analysed dataset is 19.8 fb^{-1}.The number of signal events is defined as:

$$N_{sig} = (1 - f_\tau)(N_{signal}^{data_driven} - N_{ZZ} - N_{Z\gamma} - N_{WV} - N_{VVV}) \tag{6.2}$$

where f_τ is the fraction of WZ decays to τ reported in Table 6.1. N_{ZZ}, $N_{Z\gamma}$, N_{WV} and N_{VVV} are combinations of ZZ, $Z\gamma$, WV, VVV estimated from Monte Carlo. $N_{signal}^{data_driven}$ is the number of events with three prompt leptons estimated using the data driven method described in detail in Section 5.4.2.

Table 6.1: Fraction of selected WZ decays coming from W or Z decays to τ leptons for the four studied final states.

channel	f_τ
eee	0.074 ± 0.002
$ee\mu$	0.075 ± 0.002
$\mu\mu$e	0.071 ± 0.002
$\mu\mu\mu$	0.076 ± 0.001

6.2 Acceptance and efficiency

In the measurement of the production cross section, a very important quantity is the overall fraction of produced signal events that is detected and selected. Only a fraction of produced events will decay in such a way that the phase space of all detectable final state particles is covered by functional (*fiducial*) parts of detector. This fraction of phase space, covered with the detector is called acceptance (A). Some events within the acceptance of the detector are not detected due to detector inefficienceis or because an event doesn't satisfy the trigger and analysis selection. Acceptance and efficiency are estimated together as a single fraction. It is estimated using the WZ signal simulation, and is defined as:

$$A \times \varepsilon = \frac{\text{number of selected signal events}}{\text{number of generated signal events}} \tag{6.3}$$

Acceptance times efficiency is computed separately for each channel. In both, numerator and denominator, only signal events generated in particular channel are selected. In denominator events with additional requirement that generated Z mass (before final state radiation) lies window $[71.18, 111.18]$ GeV are selected. Such computed acceptance times efficiency has to be additionally corrected to account for differences between data and Monte Carlo. Using the corrections described in Section 5.1.1 the acceptance times efficiency is computed using the following expression:

$$(A \times \varepsilon)^{ch} = \frac{\sum_{i=1..N}^{selected(ch)} \prod_{l=1..3} w_{il}^{SF} w_i^{PU} \varepsilon_{TRG(ch)}^i}{N_{gen}^{ch}} \tag{6.4}$$

where w^{SF}, w^{PU} and ε_{TRG} are the lepton scale factors, the pileup weights and trigger efficiency.

6.3 Systematic uncertainties

Systematic uncertainties can affect any of the parameters used to calculate the cross section. They can be grouped in the following categories:

- **Uncertainties that affect acceptance and efficiency**: this product is determined from

Monte Carlo and is affected by several sources of uncertainty. For each source, it is reevaluated by varying some of the parameters described in the following subsections within uncertainties. The effect on the total cross section is taken as systematic uncertainty. The following sources of this uncertainties are considered: pileup, lepton and trigger efficiencies, lepton momentum and energy scales and uncertainty on missing transverse energy.

- **Uncertainties that affect the background estimation**: uncertainty on the non-promt lepton background as well as uncertainties on the other backgrounds (ZZ, $Z\gamma$, VVV, and $W\gamma^*$) are considered
- **Uncertainties that affect the luminosity**: an additional uncertainty of 2.6 % due to the measurement of the integrated luminosity is considered.

Each systematic contribution is evaluated as the effect on the overall cross section following the prescription

$$\Delta^i_{rel}(\sigma_{WZ}) = max\left(\frac{|\sigma(WZ)^i_{up} - \sigma(WZ)^i|}{\sigma(WZ)^i}, \frac{\sigma(WZ)^i_{down} - \sigma(WZ)^i}{\sigma(WZ)^i}\right) \tag{6.5}$$

where σ_{up} and σ_{down} denote the cross section for the upward and downward effect of variation by the respective uncertainty. This estimate is calculated for each particular channel and contribution i. Finally all contributions are added in quadrature to obtain the overall systematic uncertainty $\Delta_{syst} = \sqrt{\sum_i (\Delta^i_{rel}(\sigma_{WZ}))^2}$. The methods used to determine the systematic uncertainty for each individual contribution are discussed in the following, with the results of each method summarized in Table 6.5.

6.3.1 PDF

The uncertinties on PDF have an effect both on the predicted cross section of the process and on the fraction of selected events affected due to modified kinematic properties, These uncertainties are estimated by applying PDF variations on the $A \times \varepsilon$, affecting simultaneously its nominator and denominator. PDF uncertainty is estimated using CTEQ6L PDF set [51] and the perscription in [52].

6.3.2 QCD and factorization scale

The effect of uncertainties of the used factorization and renormalization scales on the geometric acceptance of the described selection is studied with the MCFM program by varying each scale by a factor two up and down with respect to its nominal value which is set to the average mass of the final state bosons. The largest variation is 3%, which is taken as systematic uncertainty.

6.3.3 Pileup

The efficiency and acceptance used in the cross section determination are obtained using Monte Carlo samples that were reweighted to reproduce the expected distribution of the number of pileup interaction in data. The target distribution for data is generated using the central minimum bias cross section ($\sigma_{pp} = 69.4$ mb). The same procedure is repeated for a minimum bias cross section scaled up and down by 5% [53]. The relative difference of acceptance and efficiency from the central one is taken as systematic uncertainty from pileup.

6.3.4 Lepton and trigger efficiencies

Uncertainties on lepton and trigger efficiencies will affect acceptance and efficiency (as can be seen in equation 6.4). They also affect the background yields estimated from MC which are substracted from the prompt lepton yield in the Equation 6.1. To account for these uncertainties, the trigger, reconstruction and identification, lepton scale factors are varied by 0.01 up and down. This was done separately for electrons and for muons. To obtain the uncertainty on the cross section this variation was applied in the $A \times \varepsilon$ determination as well as on the MC backgrounds.

6.3.5 Missing transverse energy

The missing transverse energy is a composite object, and it is highly dependent on the resolution and scale of its components. Missing transverse energy is factorized into components and they are separately varied by their respective uncertainties determined from dedicated studies. Those components are:

- electron energy
- jet energy
- jet resolution
- muon energy
- tau energy
- unclustered energy

The effect of the variation of each component on differential cross section cis given in Table 6.2 . The total effect is computed by adding all components quadraticaly.

6.3.6 Uncertainty on lepton momentum and energy scales

Electron energy scale and muon momentum scale uncertainties are determined by scaling the corresponding lepton type four-momentum, and performing the full selection procedure with lepton objects modified in such way and obtaining relative difference on cross sections. To

Table 6.2: Relative effect (in percent) of the variation of each E_T^{miss} component on the cross section.

Source	$3e$	$2e1\mu$	$1e2\mu$	3μ
Electron energy	0.53	0.13	0.48	0.01
Jet energy	0.57	0.50	0.48	0.55
Jet resolution	0.82	0.49	0.83	0.50
Muon energy	0.01	0.18	0.01	0.09
Tau energy	0.15	0.06	0.03	0.003
Unclustered energy	0.91	1.31	1.18	0.89
All	1.46	1.50	1.59	1.17

account for uncertainties in the muon momentum scale measurement, the momentum of muons in the simulated signal and background samples was varied by 0.2%. The same was done for the electron energies, which were varied within the uncertainty of the energy scale measurement, which is p_T and η dependent, the bulk being below 1% (figure 6.1).

6.3.7 Data driven systematics

Leading jet p_T threshold determines composition of QCD sample: whether it contains more fake leptons from Z+jets or $t\bar{t}$. To account for this, we studied the behaviour of the data-driven background estimation in two enriched regions. A region enriched in Z+jets is defined by tightening the Z mass window ($|m_{ll} - m_Z| < 15$ GeV) and removing events with real missing transverse energy ($E_T^{miss} < 20$ GeV). For the top enriched region we look for events away of the Z peak ($|m_{ll} - m_Z| > 10$ GeV) and we require at least on b-jet with $p_T > 30$ GeV in the event. In these two regions we compare the yields from data with the yields estimated using the matrix method, for jet p_T variations from 15 to 50 GeV. These results can be seen in figure 6.2.
This uncertainty is taken into account taking computing numbers of fake rates using different values of leading jet p_T cut. Results of data driven method using this fake rates are shown in Table 6.3. For muons (electrons) as a systematic uncertainty we take the largest difference with respect to the background estimations with the leading jet p_T from 10 (15) to 50 GeV.

6.3.8 Uncertainties on other backgrounds

Other backgrounds are estimated from Monte Carlo. The systematics from these contributions is estimated by varying the cross sections assumed in the simulation:

- A 15% uncertainty is assumed on the ZZ cross section, based on the uncertainty of the measurement performed by CMS [54, 55].
- For Zγ, an uncertainty of 15% is taken. The uncertainty on the CMS measurement [56, 57] amounts to 5.5%. We set a higher uncertainty to account for a possible disagreement in the fake E_T^{miss} description between data and MC.

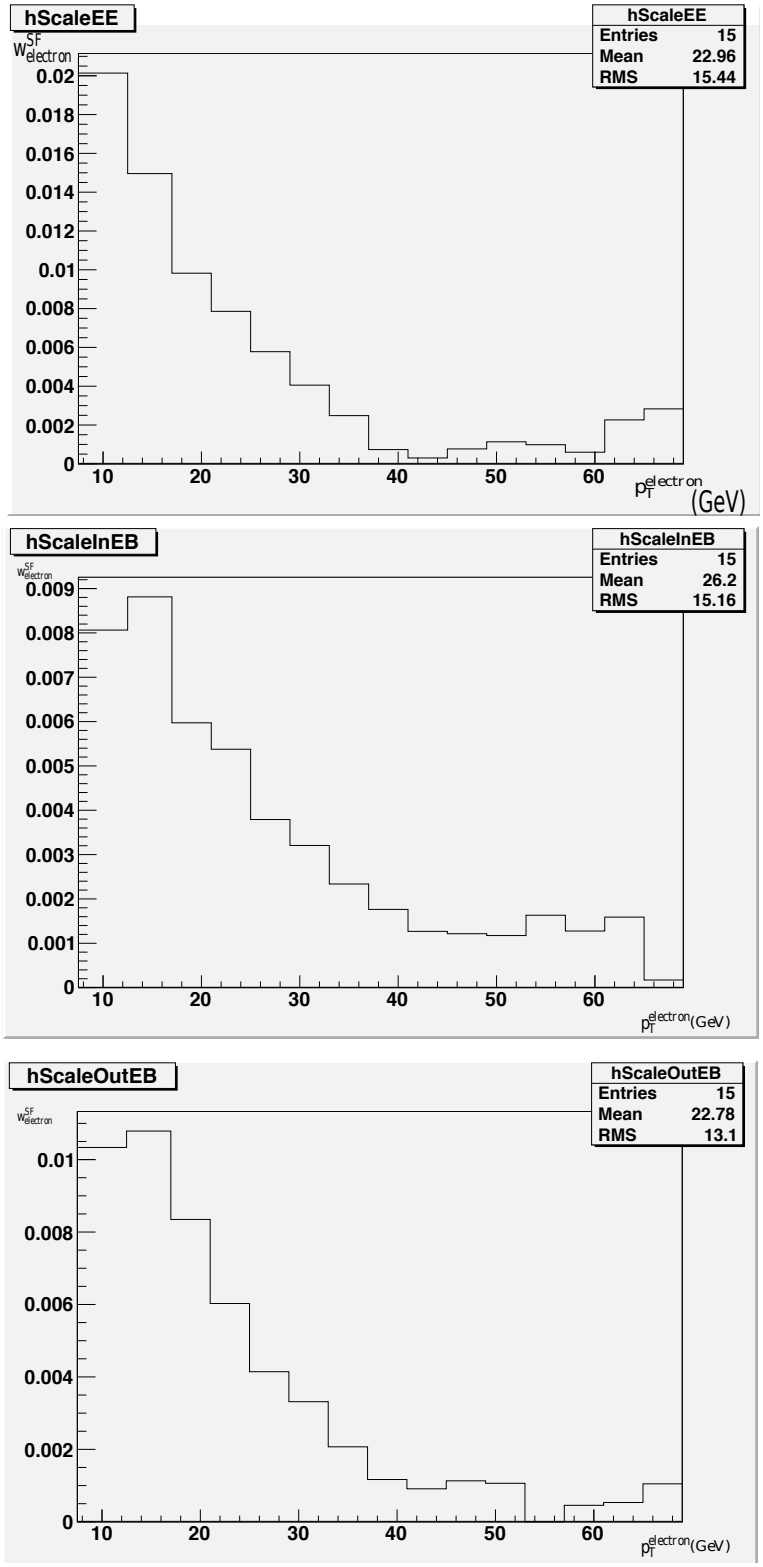

Figure 6.1: Electron scales dependent on p_T of electron for η <0.8 (upper plot), η between 0.8 and 1.479 and $\eta > 1.479$ (down).

Table 6.3: Matrix method results for different combinations of the leading jet p_T.

leading jet p_T	channel	N_{good}	N_{fake}
nominal p_T^{μ} and $p_T^{\text{e}} > 15$ GeV	eee	237.9 ± 17.9	20.1 ± 6.8
	eeμ	265.2 ± 18.5	32.8 ± 5.2
	$\mu\mu$e	377.6 ± 23.1	57.4 ± 8.4
	$\mu\mu\mu$	505.6 ± 25.0	62.4 ± 4.8
$p_T^{\mu} > 15$ GeV and $p_T^{\text{e}} > 15$ GeV	eee	237.9 ± 17.9	20.1 ± 6.8
	eeμ	264.6 ± 18.5	33.4 ± 5.2
	$\mu\mu$e	375.1 ± 23.2	59.9 ± 8.5
	$\mu\mu\mu$	501.8 ± 25.1	66.2 ± 5.2
p_T$^{\mu} > 35GeV$ and p_T$^{\text{e}} > 35GeV$	eee	239.6 ± 17.5	18.4 ± 6.1
	eeμ	277.1 ± 18.1	20.9 ± 4.1
	$\mu\mu$e	388.5 ± 22.6	46.5 ± 7.5
	$\mu\mu\mu$	529.7 ± 24.5	38.3 ± 3.3
nominal p_T$^{\mu}$ and p_T$^{\text{e}} > 50GeV$	eee	250.1 ± 16.7	7.9 ± 3.9
	eeμ	267.7 ± 18.0	30.3 ± 3.9
	$\mu\mu$e	398.2 ± 22.0	36.8 ± 5.3
	$\mu\mu\mu$	505.6 ± 25.0	62.4 ± 4.8
p_T$^{\mu} > 10GeV$ and nominal p_T$^{\text{e}}$	eee	239.6 ± 17.5	18.4 ± 6.1
	eeμ	264.9 ± 18.3	33.1 ± 4.8
	$\mu\mu$e	375.7 ± 23.0	59.3 ± 8.1
	$\mu\mu\mu$	498.3 ± 25.2	69.7 ± 5.5
p_T$^{\mu} > 30GeV$ and nominal p_T$^{\text{e}}$	eee	239.6 ± 17.5	18.4 ± 6.1
	eeμ	271.9 ± 18.2	26.1 ± 4.4
	$\mu\mu$e	384.4 ± 22.7	50.6 ± 7.7
	$\mu\mu\mu$	519.6 ± 24.7	48.4 ± 4.0
p_T$^{\mu} > 10GeV$ and p_T$^{\text{e}} > 15$	eee	237.9 ± 17.9	20.1 ± 6.8
	eeμ	264.0 ± 18.5	34.0 ± 5.2
	$\mu\mu$e	372.6 ± 23.3	62.4 ± 8.7
	$\mu\mu\mu$	498.3 ± 25.2	69.7 ± 5.5
p_T$^{\mu} > 30GeV$ and p_T$^{\text{e}} > 50$	eee	250.1 ± 16.7	7.9 ± 3.9
	eeμ	273.6 ± 17.9	24.4 ± 3.5
	$\mu\mu$e	402.0 ± 21.9	33.0 ± 5.1
	$\mu\mu\mu$	519.6 ± 24.7	48.4 ± 4.0
p_T$^{\mu} > 50GeV$ and nominal p_T$^{\text{e}}$	eee	239.6 ± 17.5	18.4 ± 6.1
	eeμ	284.4 ± 18.0	13.6 ± 3.8
	$\mu\mu$e	393.7 ± 22.5	41.3 ± 7.4
	$\mu\mu\mu$	543.0 ± 24.3	25.1 ± 2.4
p_T$^{\mu} > 50GeV$ and p_T$^{\text{e}} > 50$	eee	250.1 ± 16.7	7.9 ± 3.9
	eeμ	286.2 ± 17.7	11.8 ± 2.7
	$\mu\mu$e	411.5 ± 21.7	23.5 ± 4.7
	$\mu\mu\mu$	543.0 ± 24.3	25.1 ± 2.4

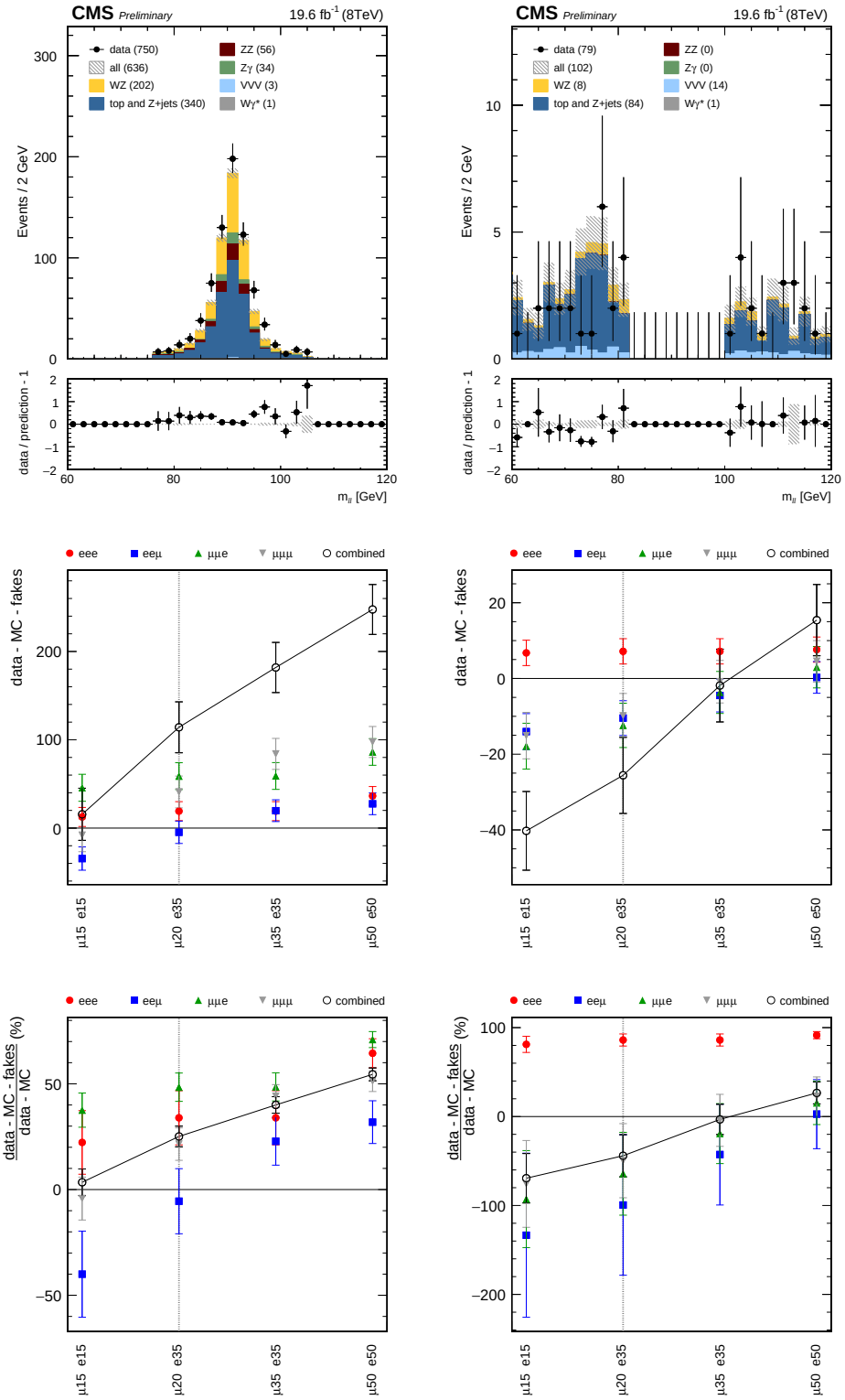

Figure 6.2: The left column corresponds to a Z+jets enriched region ($|m_{\ell\ell} - m_Z| < 15$ GeV and $E_T^{miss} < 20$ GeV. The right column corresponds to a top enriched region ($|m_{\ell\ell} - m_Z| > 10$ GeV and at least one b-jet with $p_T > 30$ GeV). The upper distributions are $m_{\ell\ell}$ with the nominal leading jet p_T thresholds. The middle figures show the difference between data minus MC (MC includes WZ, ZZ, Zγ and Wγ^*) and the data-driven prediction. The lower figures show the relative difference (in %) between data minus MC and the data-driven prediction.

Table 6.4: Systematic uncertainties on the cross sections for background processes extracted from MC, and impact on the WZ cross section using 8TeV data.

	Cross section	Impact on WZ cross section (in %)			
sample	Variation	3e	2e1mu	1e2mu	3mu
ZZ	15%	0.2	0.2	0.2	0.2
Zγ	15%	0.2	0	0.2	0
Wγ^*	20%	< 0.01	< 0.01	< 0.01	0.1
Triboson processes					
WWγ	50%	0.011	0	0	0
WZZ	50%	0.1	0.11	0.098	0.10
ZZZ	50%	0.009	0.008	0.012	0.007
WWZ	50%	0.28	0.34	0.30	0.28
WWW	50%	0.042	0.063	0.046	0.039
$t\bar{t}$+W	50%	0.098	0.166	0.15	0.13
$t\bar{t}$+Z	50%	0.93	1.04	0.99	0.98
$t\bar{t}$+ WW	50%	0.0032	0.0049	0.0046	0.0040
$t\bar{t}$+γ	50%	0	0	0.019	0
all VVV		0.98	1.11	1.05	1.03

- For VVV processes, an uncertainty of 50% is taken on each of these processes. The dominant processes are $t\bar{t}$+Z, WWZ and $t\bar{t}$+W, as can be seen in Table 5.9. This corresponds to the uncertainty on the CMS measurements [58] for the $t\bar{t}$+W/Z processes.
- For Wγ^*, we have assumed an uncertainty of 20%.

All these uncertainties and their impact on the WZ cross section are summarized in Table 6.4.

Luminosity uncertainnty is 2.6 % [59]. A summary of all systematic uncertainties is given in Table 6.5.

6.4 Cross section measurement in individual channels

Monte Carlo estimated yields of backgrounds, data driven results and data yields are given in Table 5.3. The Monte Carlo yields for $t\bar{t}$ and Z+jets are also given, although they are not used in the cross section computation. The value of the $A \times \varepsilon$ and cross section for each of the four channels is given in Table 6.6.

The inclusive WZ cross section $\sigma(\mathrm{pp} \to \mathrm{WZ} + \mathrm{X})$ in the $3l\nu$ final state is related to the number of observed signal events N_{sig}, through the following expression:

$$\sigma(\mathrm{pp} \to \mathrm{WZ} + \mathrm{X})\mathscr{B}(W \to l\nu)\mathscr{B}(Z \to ll) = (1 - f_\tau)\frac{N_{sig}}{A \times \varepsilon \mathscr{L}} \tag{6.6}$$

Table 6.5: Summary of systematic uncertainties, in units of percent, in the WZ cross section measurements.

source	eee	eeμ	$\mu\mu$e	$\mu\mu\mu$
QCD scale	3.0	3.0	3.0	3.0
PDFs	1.4	1.4	1.4	1.4
lepton and trigger efficiency electrons	3.4	2.2	1.1	0.0
lepton and trigger efficiency muons	0.0	1.1	2.2	3.2
E_T^{miss}	1.5	1.5	1.6	1.2
muon momentum scale	0.0	0.5	0.8	1.3
electron energy scale	1.4	0.8	0.8	0.0
pileup	0.2	0.4	0.3	0.2
ZZ cross section	0.1	0.1	0.1	0.1
Zγ cross section	0.2	0.0	0.2	0.0
data-driven electrons	4.6	0.7	4.9	0.0
data-driven muons	0.0	7.2	3.6	7.7
other MC backgrounds	1.0	1.1	1.1	1.0
statistical	7.7	7.2	6.4	5.2
systematic	7.0	8.6	7.7	9.2
luminosity	2.6	2.6	2.6	2.6

where $\mathscr{B}(W \to l\nu)$ and $\mathscr{B}(Z \to ll)$ are the W and Z boson leptonic branching fractions per lepton species.

Table 6.6: Measured WZ cross section in the four final states.

channel	acceptance [%]	σ(pp $\to$ WZ) [pb]
eee	11.99 ± 0.09	$24.80 \pm 1.92(\text{stat.}) \pm 1.74(\text{syst.}) \pm 0.64(\text{lumi.})$
eeμ	15.1 ± 0.1	$22.38 \pm 1.62(\text{stat.}) \pm 1.92(\text{syst.}) \pm 0.58(\text{lumi.})$
$\mu\mu$e	19.7 ± 0.1	$23.94 \pm 1.52(\text{stat.}) \pm 1.85(\text{syst.}) \pm 0.62(\text{lumi.})$
$\mu\mu\mu$	25.7 ± 0.1	$24.93 \pm 1.29(\text{stat.}) \pm 2.29(\text{syst.}) \pm 0.65(\text{lumi.})$

6.5 Combination of channels

The four measurements of the cross section are combined, taking into account the correlation in systematic uncertainties, using the Best Linear Unbiased Estimator (BLUE) [60].

6.5.1 Best Linear Unbiased Estimator (BLUE) method

The technique explained below can be applied to obtain combined estimates of N distinct physical quantities each of which has been measured by one or more experiments, under the hypothesis that all sources of errors are multivariate Gaussian distributed. It is also assumed that the total covariance matrix for the input data is positive definite, is known a priori and does not depend on the results of the measurements [60, 61]. The method is used in this analysis twice:

for combining the total cross section for the four channels, and for combining differential cross section measured in the next chapter.

True values of the N observables are denoted with $X_\alpha = X_1, ..X_N$ and n experimental results with $y_i = y_1, ..y_n$. Each observable is measured at least once: $n \geq N$. The link between measurement y_i and the observable X_α is expressed using $(n \times N)$ matrix $\mathscr{U}$. $\mathscr{U}_{i\alpha}$ is 1 if y_i is measurement of X_α and 0 if not.

Covariance matrix of measurement $(n \times n)$ is symmetric and positive definite:

$$\mathscr{M}_{ij} = \text{cov}(y_i, y_j) = \text{cov}(y_j, y_i) = \mathscr{M}_{ji} \tag{6.7}$$

The problem consists of finding the "Best Linear Unbiased Estimates" of the true values X_α of the N observables, i.e. their estimates $\hat{x_\alpha}$ such that:

- the $\hat{x_\alpha}$ are *linear* combinations of the input measurements y_i

$$\hat{x}_\alpha = \sum_{i=1}^{n} \lambda_{\alpha i} y_i \tag{6.8}$$

- the $\hat{x_\alpha}$ are *unbiased* estimates of the true values X_α of the observables
  This means that the expectation value for each estimate have to be equal ti the true value. Consequence of this is that n_α measurements of observable X_α contribute to $\hat{x}_\alpha$ with a total weight 1.
- the $\hat{x_\alpha}$ are the *best* amongst all estimates of the observables compatible with previous statements, i.e. those of minimum variance

Covariance matrix for linear estimates $\hat{x_\alpha}$ is given by:

$$\text{cov}(\hat{x_\alpha}, \hat{x_\beta}) = \sum_{i=1}^{n} \sum_{j=1}^{n} \lambda_{\alpha i} \mathscr{M}_{ij} \lambda_{\beta j} \tag{6.9}$$

where $\lambda_{\alpha j}$ are linear weights. The diagonal elements of this matrix represent the variances of the $\hat{x_\alpha}$:

$$\text{var}(\hat{x_\alpha}) = \text{cov}(\hat{x_\alpha}, \hat{x_\alpha}) = \sum_{i=1}^{n} \sum_{j=1}^{n} \lambda_{\alpha i} \mathscr{M}_{ij} \lambda_{\alpha j} \tag{6.10}$$

Linear weights have to be determined as those that minimize all variances. Solving this condition using Lagrange multipliers * we get the solution for $\lambda_{\alpha i}$:

$$\lambda_{\alpha i} = \sum_{\beta=1}^{N} (\mathscr{U} \mathscr{M}^{-1} \mathscr{U})^{-1}_{\alpha\beta} (\tilde{\mathscr{U}} \mathscr{M}^{-1})_{\beta i} \tag{6.11}$$

*Lagrange multipliers is method for finding the local maxima and minima of a function subject to equality constraints.

The covariance between the best linear unbiased estimates $\hat{x}_\alpha$ is:

$$\mathrm{cov}(\hat{x}_\alpha, \hat{x}_\beta) = (\tilde{\mathscr{U}} \mathscr{M}^{-1} \mathscr{U})^{-1}_{\beta\alpha} \tag{6.12}$$

It is assumed that the covariance matrix $\mathscr{M}$ can be inverted, i.e. that none of the n input measurements can be written as a linear combination of others. It two of the input measurements were 100% correlated, for instance, $\mathscr{M}$ could not be inverted as the two measurements would be redundant: one of them would bring no additional information and should then be removed form combination.
A good feature of the BLUE method is that it makes very easy to break down the error matrix for the combined estimates into its individual components, such as those of statistical and systematic origin. Let there be U independent sources of uncertainty. Total covariance matrix can be written as the sum:

$$\mathscr{M}_{ij} = \mathrm{cov}(y_i, y_j) = \sum_{u=1}^{U} \mathrm{cov}^{[u]}(y_i, y_j) = \mathscr{M}_{ij}^{[u]} \tag{6.13}$$

The individual contributions to $\mathscr{M}$ can be separately propagated to the covariance matrix for the combined estimates yielding

$$\mathrm{cov}(\hat{x}_\alpha, \hat{x}_\beta) = \sum_{u=1}^{U} cov^{[u]}(\hat{x}_\alpha, \hat{x}_\beta) \tag{6.14}$$

The contribution from the uth error source is given by:

$$\mathrm{cov}^{[u]}(\hat{x}_\alpha, \hat{x}_\beta) = \sum_{i=1}^{n} \sum_{j=1}^{n} \lambda\, \alpha i \mathscr{M}_{ij}^{[u]} \lambda_{\beta j} \tag{6.15}$$

where the weights are already available as they are needed to compute the central values.

6.5.2 Combination of channels using BLUE

Using the method described above the four measured values of total cross section are combined. The combined cross section, $\sigma_{\mathrm{WZ}}^{\mathrm{incl.}}$, is taken to be a linear combination of the measured inclusive cross sections in the four channels.

$$\sigma_{\mathrm{WZ}}^{\mathrm{incl.}} = \alpha_1 \sigma_{\mathrm{WZ}\to \mathrm{eee}\nu}^{\mathrm{incl.}} + \alpha_2 \sigma_{\mathrm{WZ}\to \mathrm{ee}\mu\nu}^{\mathrm{incl.}} + \alpha_3 \sigma_{\mathrm{WZ}\to \mu\mu\mathrm{e}\nu}^{\mathrm{incl.}} + \alpha_4 \sigma_{\mathrm{WZ}\to \mu\mu\mu\nu}^{\mathrm{incl.}}, \tag{6.16}$$

where α_1, α_2, α_3 and α_4 are weights determined by minimizing the variance of σ and subject to the constraint $\sum_{i=1..4} \alpha_i = 1$. The error matrix is defined as follows:

$$E = \begin{pmatrix} \sigma_1^2 & \sigma_{12}^{\text{corr}}\sigma_{21}^{\text{corr}} & \sigma_{13}^{\text{corr}}\sigma_{31}^{\text{corr}} & \sigma_{14}^{\text{corr}}\sigma_{41}^{\text{corr}} \\ \sigma_{21}^{\text{corr}}\sigma_{12}^{\text{corr}} & \sigma_2^2 & \sigma_{23}^{\text{corr}}\sigma_{32}^{\text{corr}} & \sigma_{24}^{\text{corr}}\sigma_{42}^{\text{corr}} \\ \sigma_{31}^{\text{corr}}\sigma_{13}^{\text{corr}} & \sigma_{32}^{\text{corr}}\sigma_{23}^{\text{corr}} & \sigma_3^2 & \sigma_{34}^{\text{corr}}\sigma_{43}^{\text{corr}} \\ \sigma_{41}^{\text{corr}}\sigma_1^{\text{corr}} & \sigma_{42}^{\text{corr}}\sigma_{24}^{\text{corr}} & \sigma_{43}^{\text{corr}}\sigma_{34}^{\text{corr}} & \sigma_4^2 \end{pmatrix}, \tag{6.17}$$

where the σ_i^2 are variances of the individual WZ cross section measurements and $\sigma_{ij}^{\text{corr}}$ are the correlated components of the uncertainties in those measurements for a combination of channels. Non diagonal elements are compu

$$\sigma_{ij} = \sum \text{cross\_section}[i] * \text{cross\_section}[j] * \sigma_{syst}[i] * \sigma_{syst}[j] \tag{6.18}$$

where i and j are channels, and σ_{syst} is particular systematic uncertainty, and sum goes over all correlated systematic uncertainties . For the cross section we take the following systematic uncertainties to be fully correlated between channels:

- The PDF uncertainties on the WZ signal acceptance and efficiency;
- The uncertainty on cross section of subtracted backgrounds which are estimated from Monte Carlo (ZZ, Zγ, Wγ^*, VVV);
- The uncertainty on QCD scale
- The uncertainty on E_T^{miss} resolution and energy scale;
- The uncertainty on the minimum bias cross-section used for the pileup reweighting
- The uncertainty on electron energy scale (channels with electrons);
- The uncertainty on muon momentum scale (channels with muons);
- The uncertainty on lepton and trigger efficiencies for muons (channels with muons)
- The uncertainty on lepton and trigger efficiencies for electrons (channels with electrons)
- The uncertainty on data-driven background estimation: $ee\mu$ and $\mu\mu\mu$ ($\mu\mu e$ and eee) channels correlated

These errors are calculated as the effect on the cross section in each signal channel.

The error matrix constructed out of statistical and systematic errors, with non-diagonal elements being populated only with correlated systematics. After including all systematic errors (for the inclusive cross-section), we obtain the error matrix:

$$E = \begin{pmatrix} 7.12 & 1.65 & 3.88 & 1.27 \\ 1.65 & 7.28 & 1.46 & 4.82 \\ 3.88 & 1.46 & 8.43 & 1.72 \\ 1.27 & 4.82 & 1.72 & 7.58 \end{pmatrix} \text{pb}^2. \tag{6.19}$$

We obtain the $\alpha_1 = 0.31$, $\alpha_2 = 0.24$, $\alpha_3 = 0.21$ and $\alpha_4 = 0.24$. The resulting combined cross section is:

$$\sigma(\mathrm{pp} \to \mathrm{WZ}) = 24.09 \pm 0.87(\mathrm{stat.}) \pm 1.62(\mathrm{syst.}) \pm 0.63(\mathrm{lumi.})\ \mathrm{pb} \tag{6.20}$$

The results can be compared with recent calculations at NLO and NNLO (via MATRIX [62]). The NLO (NNLO) predictions are $21.80^{+5.1\%}_{-3.9\%}$ ($23.68 \pm 1.8\%$) pb, where uncertainties include only scale variations. Tehse predictions are in agreement with the measured values within uncertainties. NLO predictions are slightly lower than the measured values, and a better agreement is observed fot the NNLO observations at both centre-of-mass energies. The ratios of the inclusive cross sections for the individual and combined results to the NLO and NNLO predictions are shown on Figure 6.3.

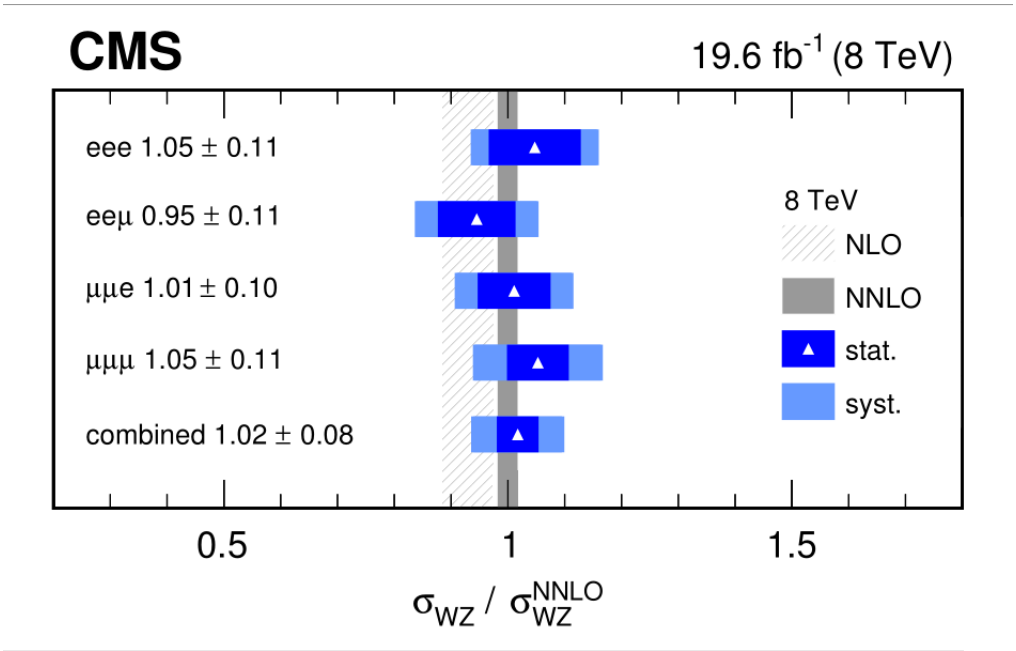

Figure 6.3: Ratio between measurement and prediction for the inclusive WZ cross section ratio at $\sqrt{s} = 8$ TeV.

6.6 Cross sections ratio measurements

The same procedure applied to measure the inclusive cross sections is exploited to measure the ratio of the W^-Z over W^+Z cross section. Dominant production mechanism of W^+Z involves an up quark and down antiquark while a down quark and up antiquark is required to produce W^-Z. The predominance of the valence u quark in the protons enhances the W^+Z production in front of the W^-Z; therefore an overall excess of W^+Zevents over W^-Z is expected.

The cross section was measured following the same procedure described before, separately

for W^+Z and W^-Z. The ratio is computed for each channel. The following systematic uncertainties are taken to be correlated between W^+Z and W^-Z: QCD uncertainty, PDF uncertainty, electron energy scale, muon momentum scale, and uncertainties on Monte Carlo backgrounds. Other systematics uncertainties from 6.5 are taken as uncorrelated. The cross sections for W^+Z and W^-Z are given in Table 6.7. The cross section ratios are given in Table 6.8. The ratios are combined using BLUE method:

$$\sigma(W-Z)/\sigma(W+Z) = 0.532 \pm 0.036(\text{stat.}) \pm 0.044(\text{syst.}) \tag{6.21}$$

$$\sigma(W+Z)/\sigma(W-Z) = 1.833 \pm 0.129(\text{stat.}) \pm 0.201(\text{syst.}) \tag{6.22}$$

The measured values are in agreement with the SM predictions 6.9. NLO predictions are obtained with MCFM using CT-10 and MSTW08 PDF sets [3].

Table 6.7: W-Z and W+Z cross sections.

channel	σ_{W^-Z}[pb]	σ_{W^+Z}[pb]
3e	$9.54 \pm 1.18 \pm 0.67$	$15.24 \pm 1.51 \pm 1.07$
2e1μ	$7.22 \pm 0.93 \pm 0.66$	$15.25 \pm 1.33 \pm 1.40$
1e2μ	$8.23 \pm 0.89 \pm 0.80$	$15.78 \pm 1.23 \pm 1.53$
3μ	$8.64 \pm 0.76 \pm 0.80$	$16.33 \pm 1.05 \pm 1.50$

Table 6.8: Cross section ratios

channel	$\sigma_{W^-Z}/\sigma_{W^+Z}$	$\sigma_{W^+Z}/\sigma_{W^-Z}$
3e	$0.63 \pm 0.05 \pm 0.10$	$1.60 \pm 0.13 \pm 0.25$
2e1μ	$0.47 \pm 0.06 \pm 0.07$	$2.11 \pm 0.25 \pm 0.33$
1e2μ	$0.52 \pm 0.07 \pm 0.07$	$1.92 \pm 0.24 \pm 0.26$
3μ	$0.53 \pm 0.06 \pm 0.06$	$1.89 \pm 0.23 \pm 0.21$

Table 6.9: NLO prediction for the $\sigma_{W^-Z}/\sigma_{W^+Z}$ and the inverse $\sigma_{W^+Z}/\sigma_{W^-Z}$ ratios obtained with MCFM using different pdf sets reported in the first column [3].

PDF set	$\sigma_{W^-Z}/\sigma_{W^+Z}$	$\sigma_{W^+Z}/\sigma_{W^-Z}$
MSTW08	0.580 ± 0.001	1.724 ± 0.003
CT-10	0.563 ± 0.001	1.777 ± 0.003
measured	$0.532 \pm 0.036 \pm 0.044$	$1.833 \pm 0.129 \pm 0.201$

Chapter 7

Differential cross section measurement

Differential cross section can give a more detailed insight and help to understand eventual differences in predictions of the inclusive cross section and measured results. It is better tool to compare the effect of higher order (in α_S or α_{ewk}) as differences may show up in a more evident way in distributions that in the total cross section. Also, signs of new physics may also be easier to spot in the differential cross section, usually as deviations at high p_T e.g. aTGC. The WZ differential cross section is measured as a function of three observables:

- the transverse momentum of the Z boson, defined as the sum of the momenta of the two leptons from the Z decay before FSR (final state) radiation
- the number of accomopanying hadronic jets
- the transverse momentum of the leading jet, i.e. the jet of the largest p_T

The measured signal spectra are corrected for the detector effects. These include efficiencies as well as bin-to-bin migrations due to finite resolution. Both effects are treated using unfolding technique. After unfolding is applied at the measured distribution , differential cross section is computed for each target distribution and compared with theory predictions.

7.1 Unfolding procedure

7.1.1 Bin migration

The differential distributions are subject to bin migrations, i.e. events that are actually produced in bin $X_{gen,j}$ might be measured in another bin $X_{rec,i}$. This is on the one hand due to the limited instrumental resolution of the variable X. But it can also result from kinematic changes induced by radiation and hadronisation effects if corrections from particle level back to parton level are applied. Thus in the latter case, dependencies on the hadronisation model are introduced. As migrations can alter the distributions, especially in the case of large slopes, they need to be corrected for. The stability s_i and the purity p_i are measures of migration out and into a bin

i, respectively. The stability describes the fraction of all events generated in one bin that are also reconstructed in the same bin out of these that are indeed reconstructed, i.e. not taking efficiency into account. On the contrary, purity gives the fraction of all events reconstructed in one bin that have been also generated in the same bin. Without migration effects, purity and stability would equal 1. The response matrix includes all detector effects , i.e. acceptance, efficiency and migration. Migrations are dealt in the following way: at first they are studied in terms of the response matrix and the quantities purity and stability which are determined from simulation. The binning of the differential variables is chosen such that migration is limited to the reasonable amount as defined below. Subsequently, a regularised unfolding approach is used to correct for the remaining migration effects.

7.1.2 Unfolding

Unfolding is a technique to decouple physical distribution from detector effects to obtain the best estimation of the true distribution starting form measured distributions. In general the detector response can be represented by a two-dimensional matrix (response matrix)

$$(C_{i,j})_{i=1,..,n,j=1,..m}$$

In the following the original values of the physics quantities are referred to as "true". The expected number of true events x^{true} in bin j can be connected to expected measured number of events y^{det} in bin i by

$$y_i^{det} = \sum_{j=1}^{m} C_{ij} x_j^{true}, i = 1, ..., n \tag{7.1}$$

The aim of unfolding is to obtain the true distribution from the measured one, i.e. solve equation 7.1 for $\vec{x}$ given the response matrix from the simulation. There are several techiniques available to obtain this goal: singular value decomposition (SVD method), iterative method (known as Bayes method), bin by bin method, simple inversion of the response matrix without regularization... More detailed explanation of Bayes method, which is used in this analysis is given in next section.

7.1.3 Bayes unfolding

In general, to solve equation 7.1 the response matrix has to be inverted, which is mathematically possible if $n = m$ and $\det C \neq 0$. The problem is that we do not have expectation values but only data, which are random variables subject to statistical fluctuations.
In this analysis an iterative approach proposed by D'Agostini in [63], based on the Bayes theorem, is used. The Bayes theorem is defined in terms of causes C_i and effects E_j. The effect

E_j can be caused by several causes C_i, but without the knowledge of the exact cause. In our measurement the cause corresponds to the true value T_i in bin i and the effect refers to the reconstructed value R_j in the detector level bin j. The aim of the unfolding is to estimate the number of expected data events in the true bin $n(T_i^{data})$, which is given by:

$$n(T_i^{data}) = \frac{1}{\varepsilon_i} \sum_{j=1}^{n_R} n(R_j^{data}) \cdot P(T_i^{MC}|R_j^{MC}) \tag{7.2}$$

with $n(R_j^{data})$ being the number of events in the detector level bin j, and $P(T_i^{MC}|R_j^{MC})$ being the conditional probability for an event to belong to the true bin T_i if it has been measured in the reconstructed bin j. It can be expressed using Bayes theorem:

$$P(T_i^{MC}|R_j^{MC}) = \frac{P(R_j^{MC}|T_i^{MC}) \cdot P_0(T_i^{MC})}{\sum_{l=1}^{n_T} P(R_j^{MC}|T_l^{MC}) \cdot P_0(T_l^{MC})} \tag{7.3}$$

and it is estimated from MC simulation. The sum in 6.2 runs over the number of detector level bins, n_R, while the sum in equation 6.3 runs over the number of true bins, n_T. $P(R_j^{MC}|T_i^{MC})$ is the conditional probability to measure an event in the detector level bin j if it belongs to the true bin i, and $P_0(T_i^{MC})$ is the prior probability for an event to be in the true bin i. The efficiency ε_i is defined as

$$\varepsilon_i = \sum_{j=1}^{n_R} P(R_j^{MC}|T_i^{MC}), 0 \leq \varepsilon_i \leq 1 \tag{7.4}$$

and corresponds to the probability that the true value T_i will be measured in any detector level bin Equation 7.2 can be written in terms of the response matrix, using Equations 7.3 and 7.4 as

$$n(T_i^{data}) = \sum_{j=1}^{n_R} M_{ij}^{MC} \cdot n(R_j^{data}) \tag{7.5}$$

with

$$M_{ij}^{MC} = \frac{P(R_j^{MC})|T_i^{MC} \cdot P_0(T_i^{MC})}{\sum_{l=1}^{n_R} P(R_l^{MC}|T_i^{MC}) \sum_{l=1}^{n_R} P(R_l^{MC}|T_i^{MC}) \cdot P_0(T_l^{MC})} \tag{7.6}$$

The number of data events in the true bin $n(T_i^{data})$ can be calculated by multiplying the response matrix M_{ij}^{MC} with the number of events in the detector level bin $n(R_j^{data})$. To relate Equation 7.1 with Equation 7.5 the matrix corresponds to the inverse of the matrix C.
The probabilities $P(R_j^{MC}|T_i^{MC})$ can be estimated from migration, efficiency and resolution using the response matrix estimated from MC generator predictions. Thus, the iterative method only requires the unfolding matrix 7.6 estimated from MC simulation. The result of the method is independent of the initial probability $P_0(T_i^{MC})$, which is used as a starting point of the iteration to calculate matrix 7.6. The distribution of $P_0(T_i^{MC})$ is arbitraty (e.g. flat or estimated from MC simulation) and is replaced in each iteration with the updated distrubution. The iterative

procedure follows the steps:

1. Starting point is the initial probability $P_0(T^{MC})$ estimated e.g. from MC predictions, and calculate the initial number of expected events from the total number of observed events N_{obs} by $n_0(T^{data}) = P_0(T^{MC}) \cdot N_{obs}$.
2. Calculate $n_1(T^{data})$ with Equations 7.5 and 7.6 using the information from the response matrix. The probabilities $P(R^{MC}|T^{MC})$ are obtained from the MC generator and $P_0(T^{MC})$ is taken as prior.
3. Calculate the updated prior distribution $P_1(T)$ with $P_1 = \frac{n_1(T^{data})}{N_{true}}$, where N_{true} is the total number of events in the true bins. Calculate $n_2(T^{data})$ using Equation 7.5, but replace $P_0(T^{MC})$ with $P_1(T)$ in Equation 7.6.
4. Compare $n_2(T^{data})$ with $n_1(T^{data})$ by performing a χ^2 fit. If the value of χ^2 is small enough the algorithm can be stopped. Otherwise continue with the program from point 3.

Employing the iterative method the output converges to the true data distribution.
The implementation of the Bayes unfolding is performed within the RooUnfold package. A regularization parameter, to control the iterative unfolding, is defined as the number of iterations. In and in this analysis is set to 5.

7.2 Unfolding Z p_T, leading jet p_T and N_{jets}

All events used for these distributions have passed the same selection as for the inclusive cross section (chapter 4). Jets are required to have $p_T > 30$ GeV and $|\eta| < 2.5$. They also must be separated from the charged leptons from W and Z boson decays by $\Delta R(\text{jet}, l)$. The jets reconstructed from PF candidates, clustered by the same algorithm, have to fulfil the same requirements. The binning is chosen such that the bin efficiencies and purities are above 70% in all bins. In addition each bin is required to contain no less than about 10 selected events in data, as unfolding uncertainties get very large with smaller statistics.
The response matrices are produced using the signal Monte Carlo sample and are shown in Figures 7.24, 7.25 and 7.26. Unfolded spectra are produced using D'Agostini unfolding with the regularization parameter set to 5, which corresponds to the range where the algorithm reaches convergence as can be seen in Figures 7.21, 7.22 and 7.23. The measured unfolded spectra are shown in Figures 7.29, 7.27 and 7.28 for the three considered observables. In these plots, the unfolded spectra using the D'Agostini unfolding are compared to unfolded spectra using a simple matrix inversion. While agreeing in most bins, a clear difference is nevertheless observed in the lower part of the jet transverse momentum distribution.

7.3 Closure tests

In order to check if the unfolding procedure provides a reasonable result, several closure test are performed.

Firstly few simple closure tests are done:

1. Monte Carlo sample is used to build the response matrix. The reconstructed spectra obtained from that sample are then unfolded and the result is compared to the true distribution. Results for all three distributions can be seen on Figures 7.1, 7.8 and 7.6. As expected, they are in perfect agreement with the true distribution.
2. One half of the Monte Carlo sample is used to create response matrix, and unfolding is done on the other half. Results can be seen on Figures 7.2, 7.9 and 7.7. and it can be seen that they are in good agreement with true distribution.
3. Expected Monte Carlo distribution is used to generate toy sample of the size corresponding to the the expected data size. The unfolded spectra (Figures 7.3, 7.4 and 7.5) again agree very well with the true generated spectra.

The dependence of the unfolding result on the spectrum of the sample used to build the response matrix has also been tested. A different spectrum has been produced for each of the three studied observables by reweighting events to produce a harder spectrum in all three cases. The modified generated spectra are shown compared to the original spectra on Figures 7.11, 7.12 and 7.10. The following cross checks have been performed to study a possible bias of the spectrum used to generate the response matrix:

1. The nominal spectrum has been unfolded using the response matrix built with the modified spectrum. Results are shown in Figures 7.13, 7.14 and 7.15.
2. The modified spectrum has been unfolded using the response matrix built with the nominal spectrum. Results are shown in Figures 7.16, 7.17 and 7.18.

For both cross-checks, the unfolded spectrum has been compared to the true spectrum obtained from the same sample used to build response matrix or on statistically independent sample (by using half of the sample to build response matrix and unfolding the other half of the sample). In all cases, it is observed that modified spectrum does not induce any bias on the unfolded result.

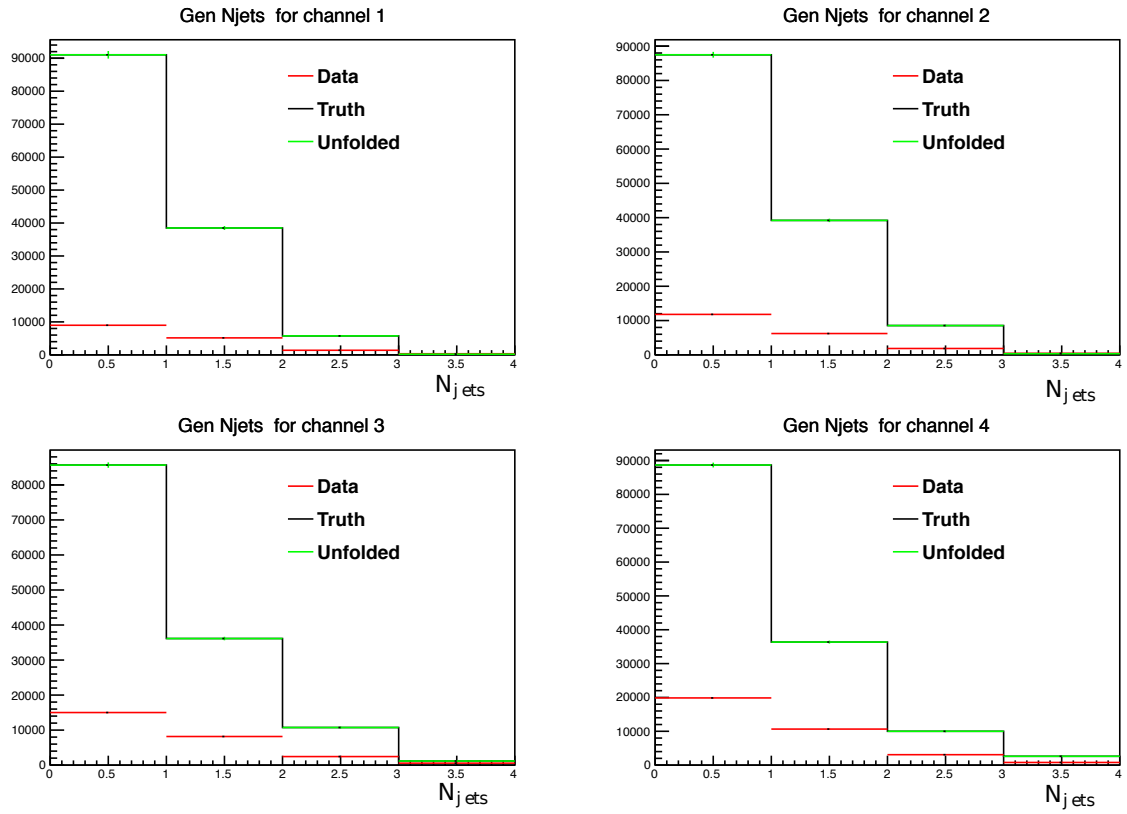

Figure 7.1: Results of closure tests for number of jets. Unfolding is done with same monte carlo sample which was used for creating response matrix.

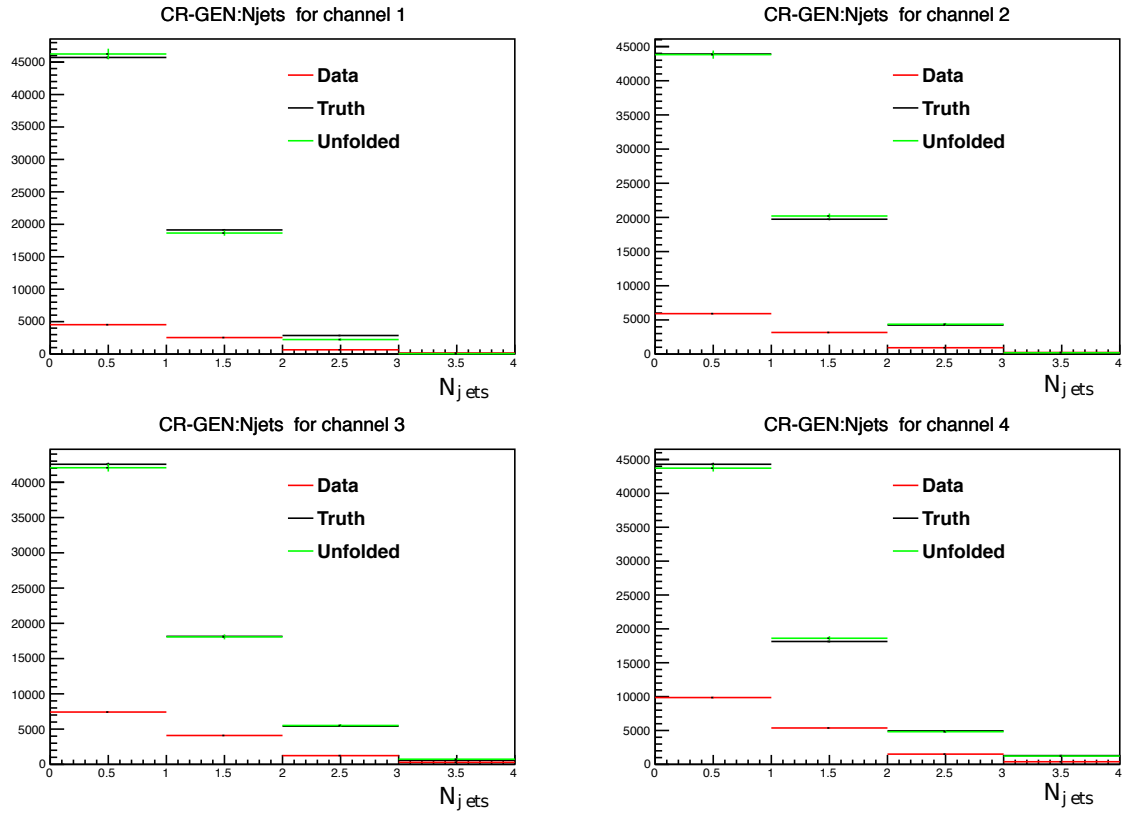

Figure 7.2: Results of closure tests for number of jets. Response matrix is created with half monte carlo sample and unfolding is done on other half.

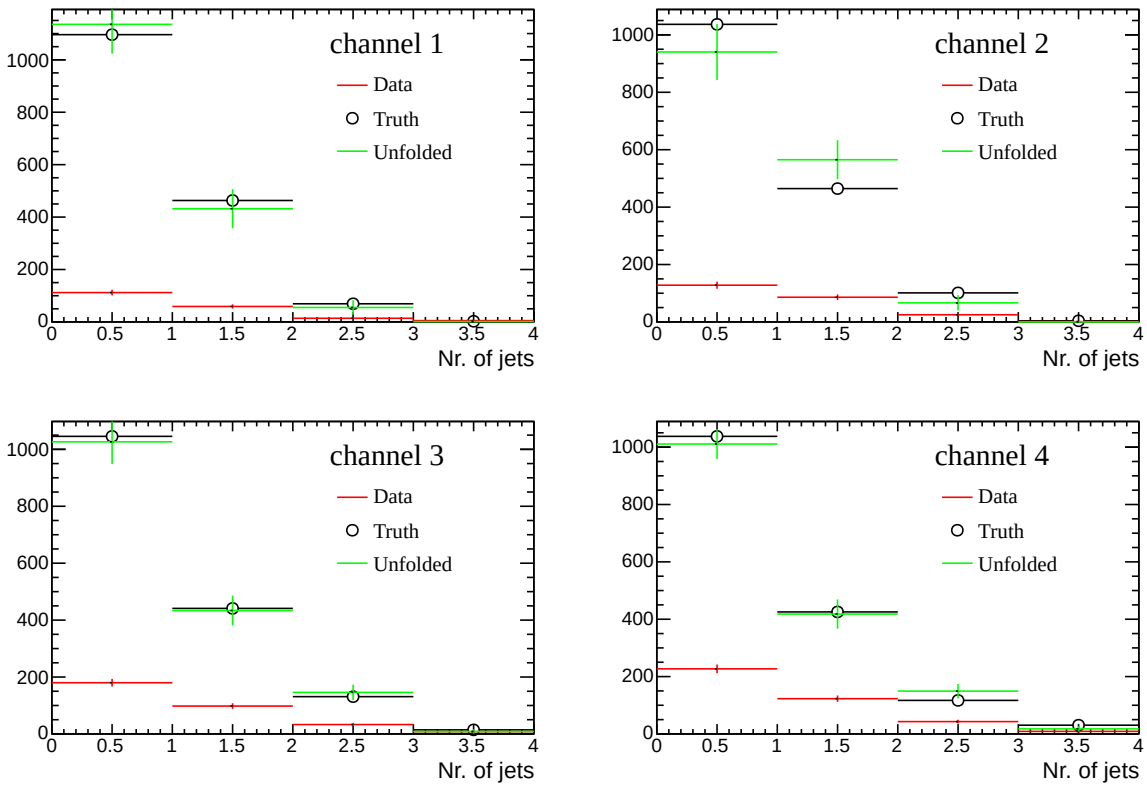

Figure 7.3: Results of closure tests for number of jets. Expected monte carlo distribution is used to generate toy sample of expected data size.

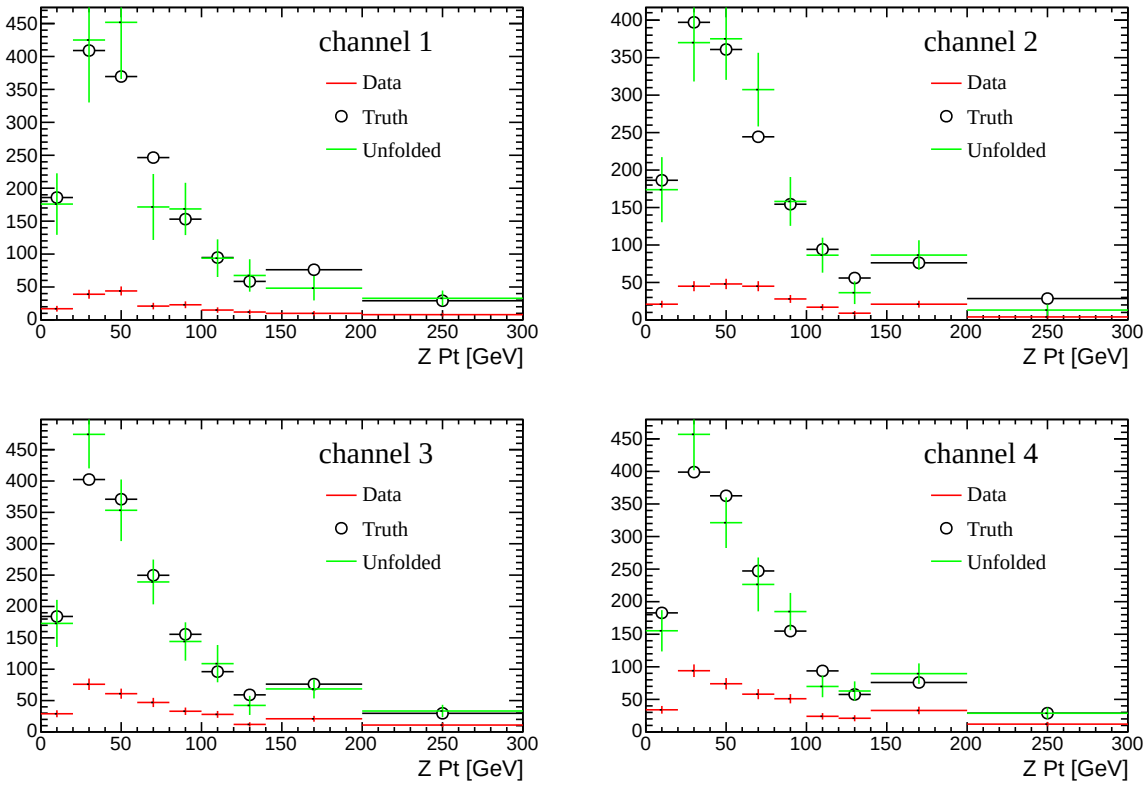

Figure 7.4: Results of closure tests for Z p_T. Expected monte carlo distribution is used to generate toy sample of expected data size.

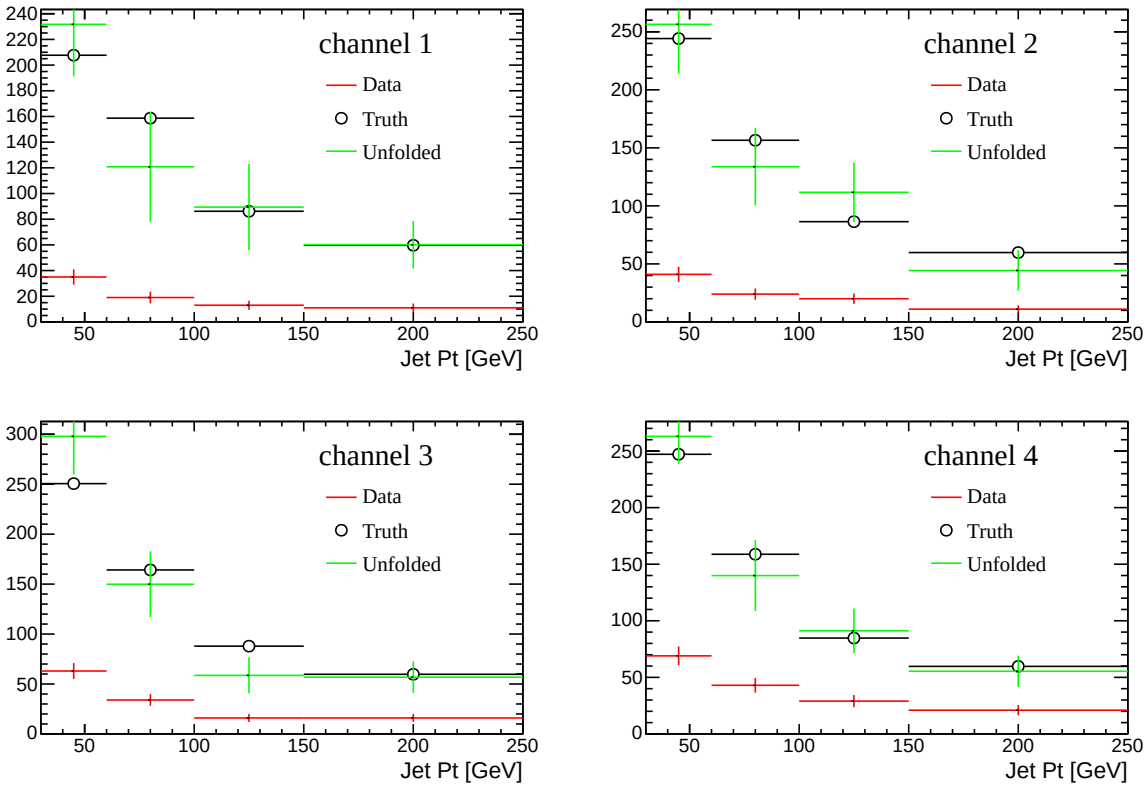

Figure 7.5: Results of closure tests for jet p_T. Expected monte carlo distribution is used to generate toy sample of expected data size.

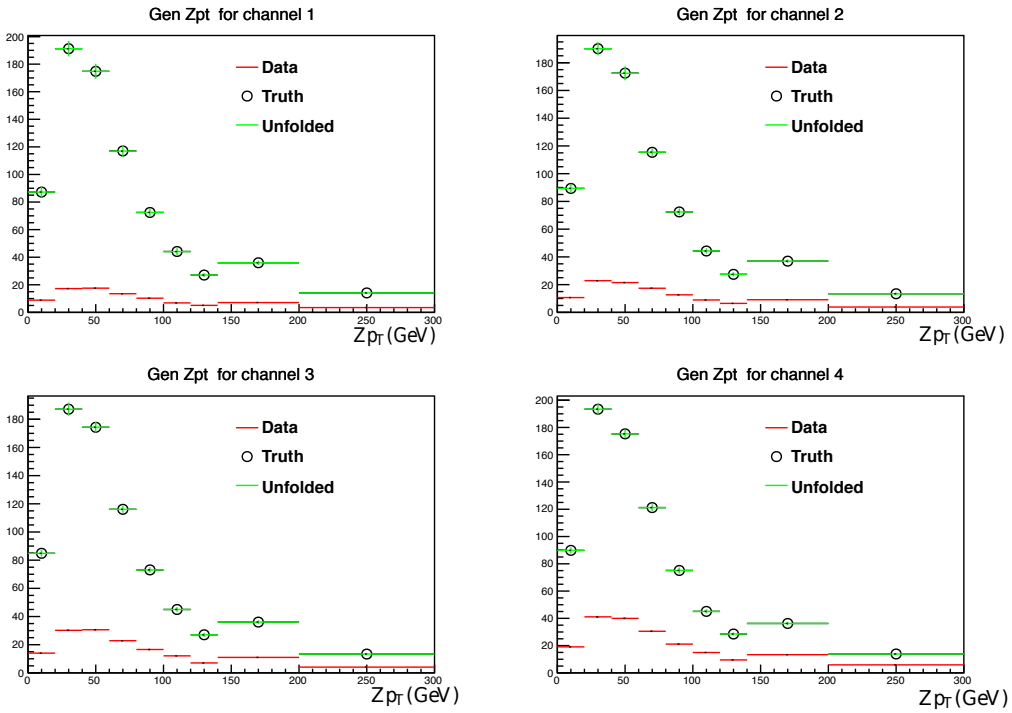

Figure 7.6: Results of unfolding closure tests for the Z transverse momentum. Unfolding is done with same monte carlo sample which was used for creating response matrix..

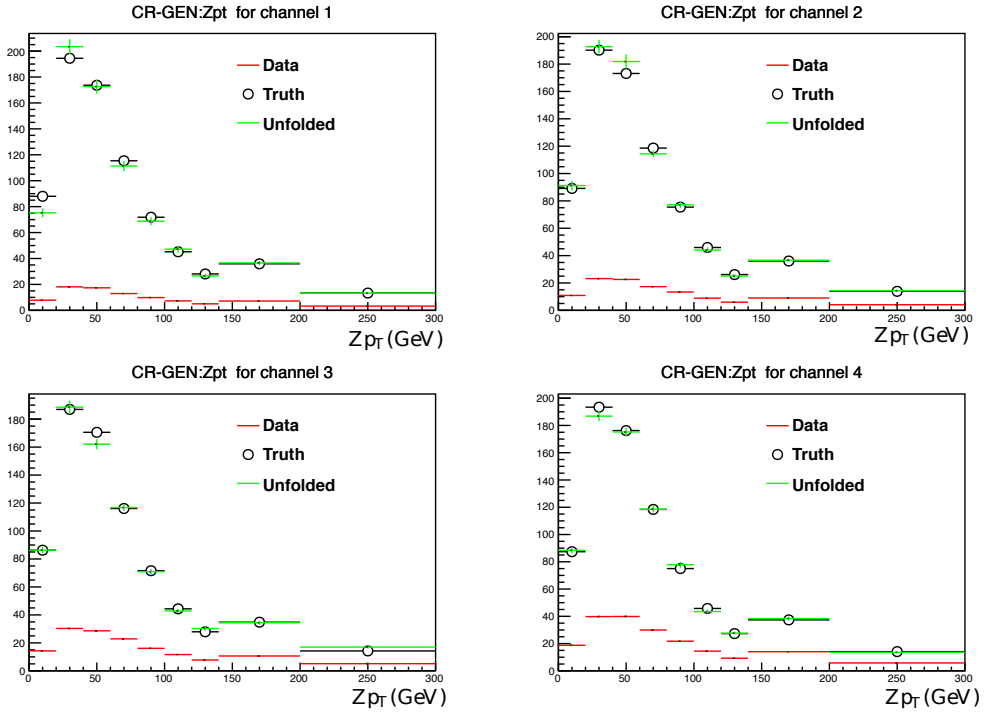

Figure 7.7: Results of unfolding closure tests for the Z transverse momentum. Response matrix is created with half monte carlo sample and unfolding is done on other half.

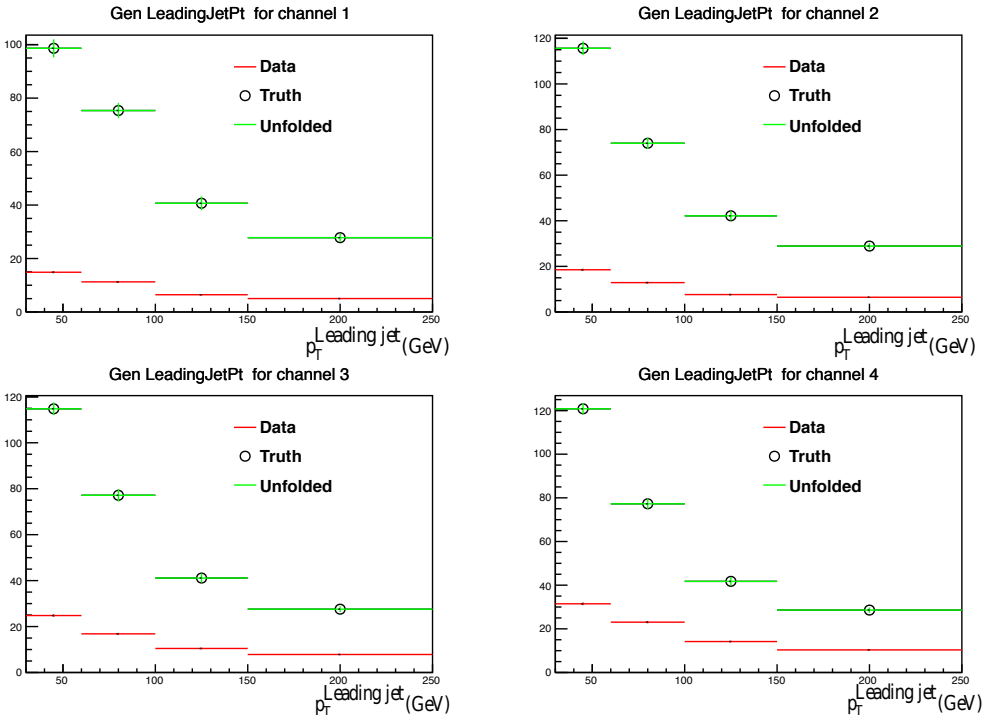

Figure 7.8: Results of unfolding closure tests for the leading jet transverse momentum. Unfolding is done with same monte carlo sample which was used for creating response matrix.

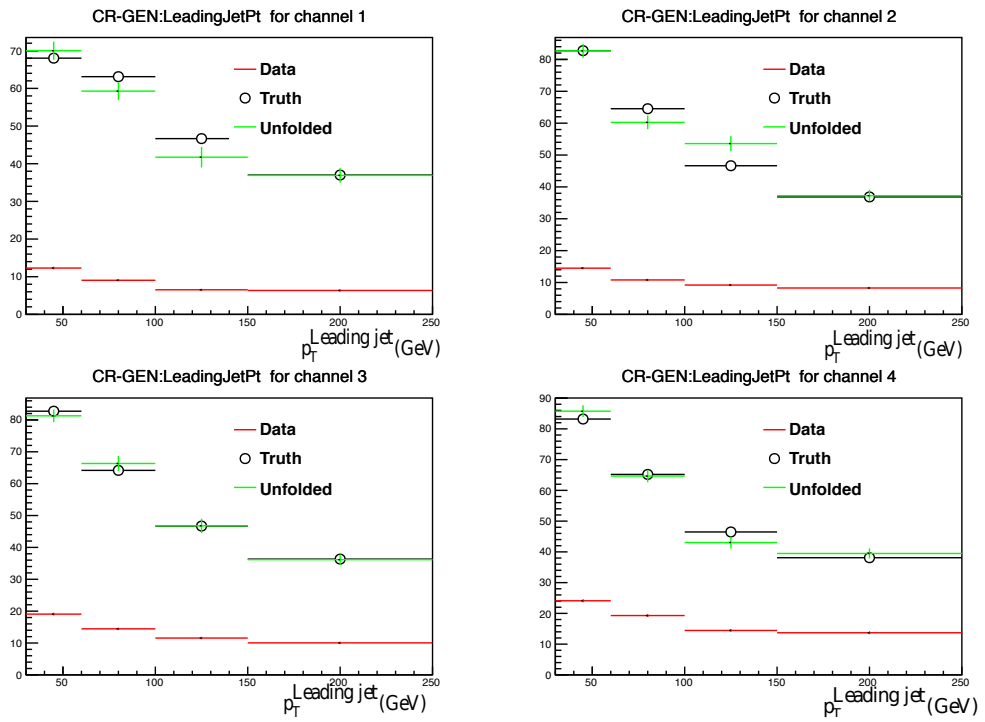

Figure 7.9: Results of unfolding closure tests for the leading jet transverse momentum. Response matrix is created with half monte carlo sample and unfolding is done on other half.

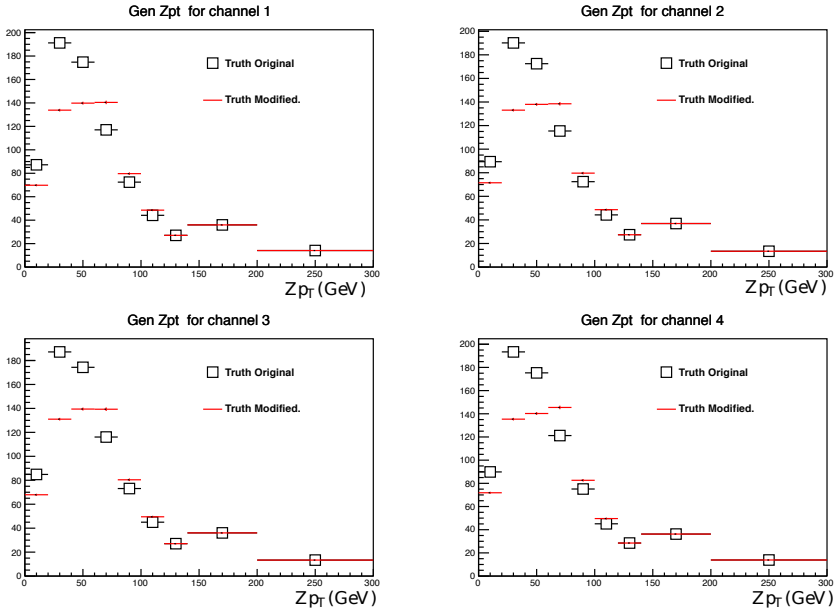

Figure 7.10: Generated Z transverse momentum spectrum: comparison of original spectrum with modifed reweighted spectrum for unfolding systematic check.

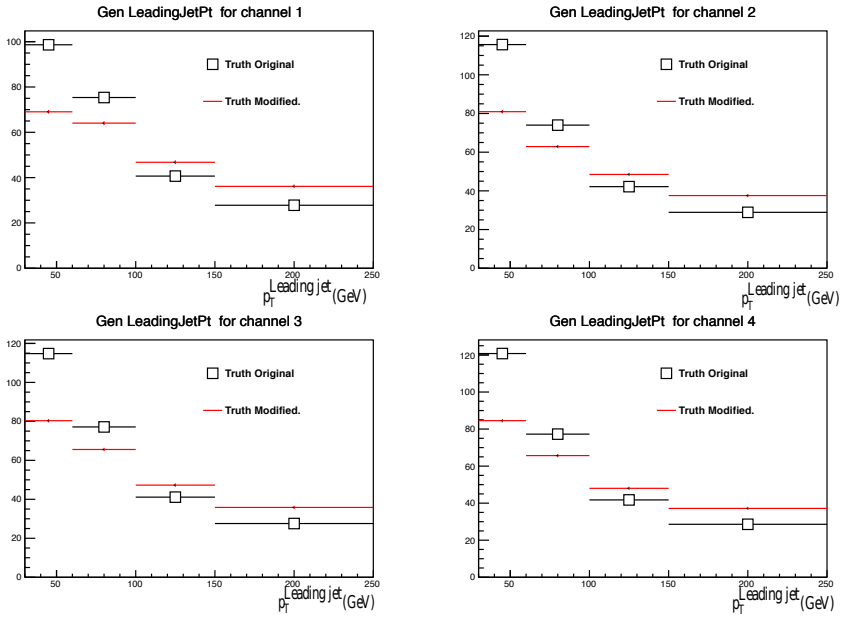

Figure 7.11: Generated leading jet transverse momentum spectrum: comparison of original spectrum with modifed reweighted spectrum for unfolding systematic check.

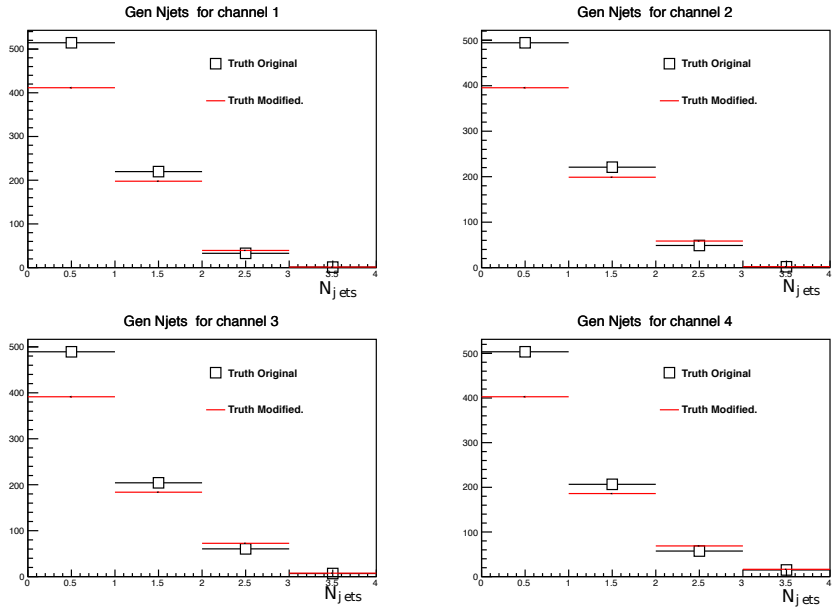

Figure 7.12: Generated jet multiplicity spectrum: comparison of original spectrum with modifed reweighted spectrum for unfolding systematic check.

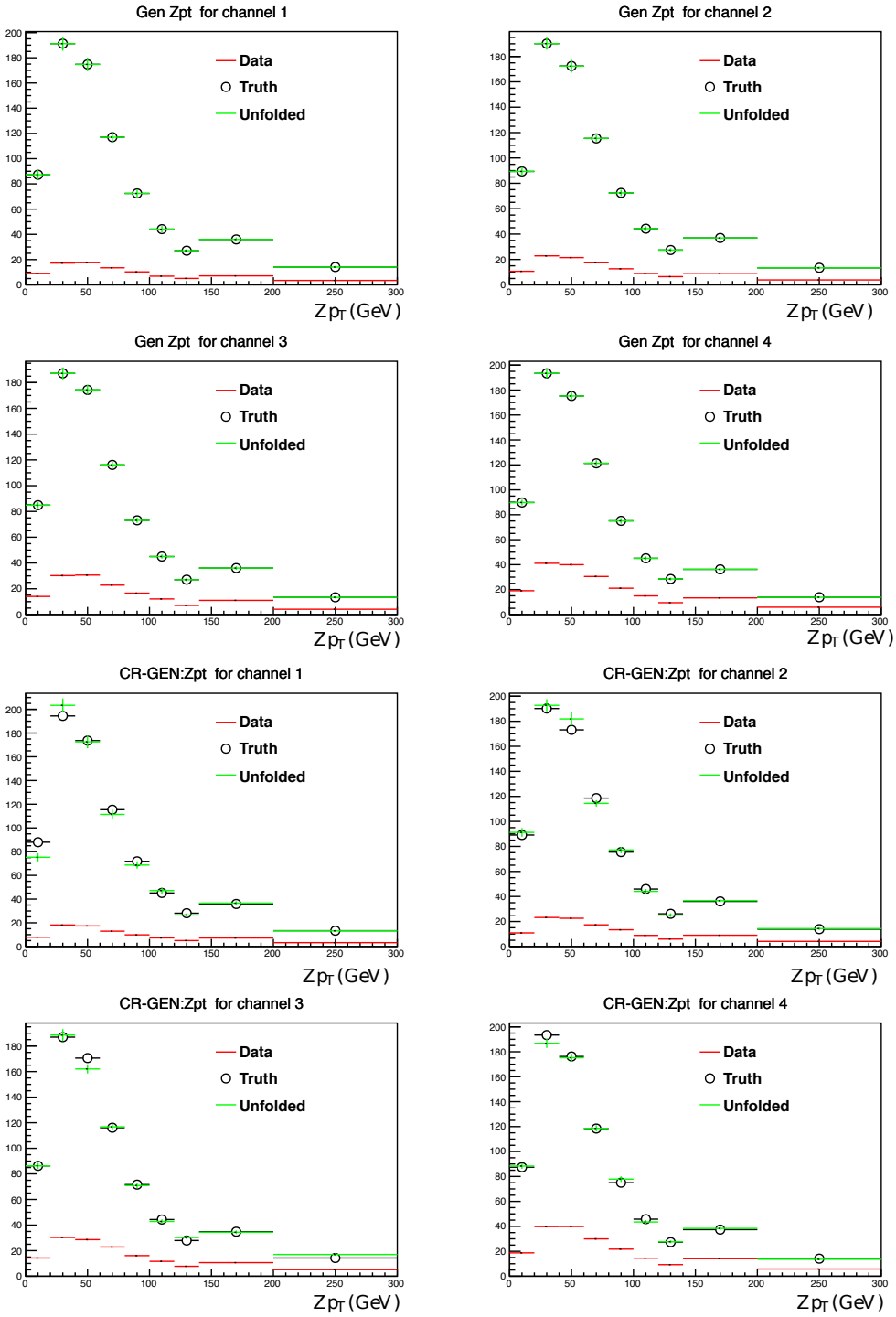

Figure 7.13: Study of unfolding dependence on the MC shape used for producing the response matrix for the Z transverse momentum: comparison of unfolded and generated spectra when using a response matrix built from a modifed spectra and applying it to the nominal spectrum. In the four upper plots, unfolded was performed on the same (reweighted) sample used to build the response matrix, while it was applied to an independent sample in the four lower plots.

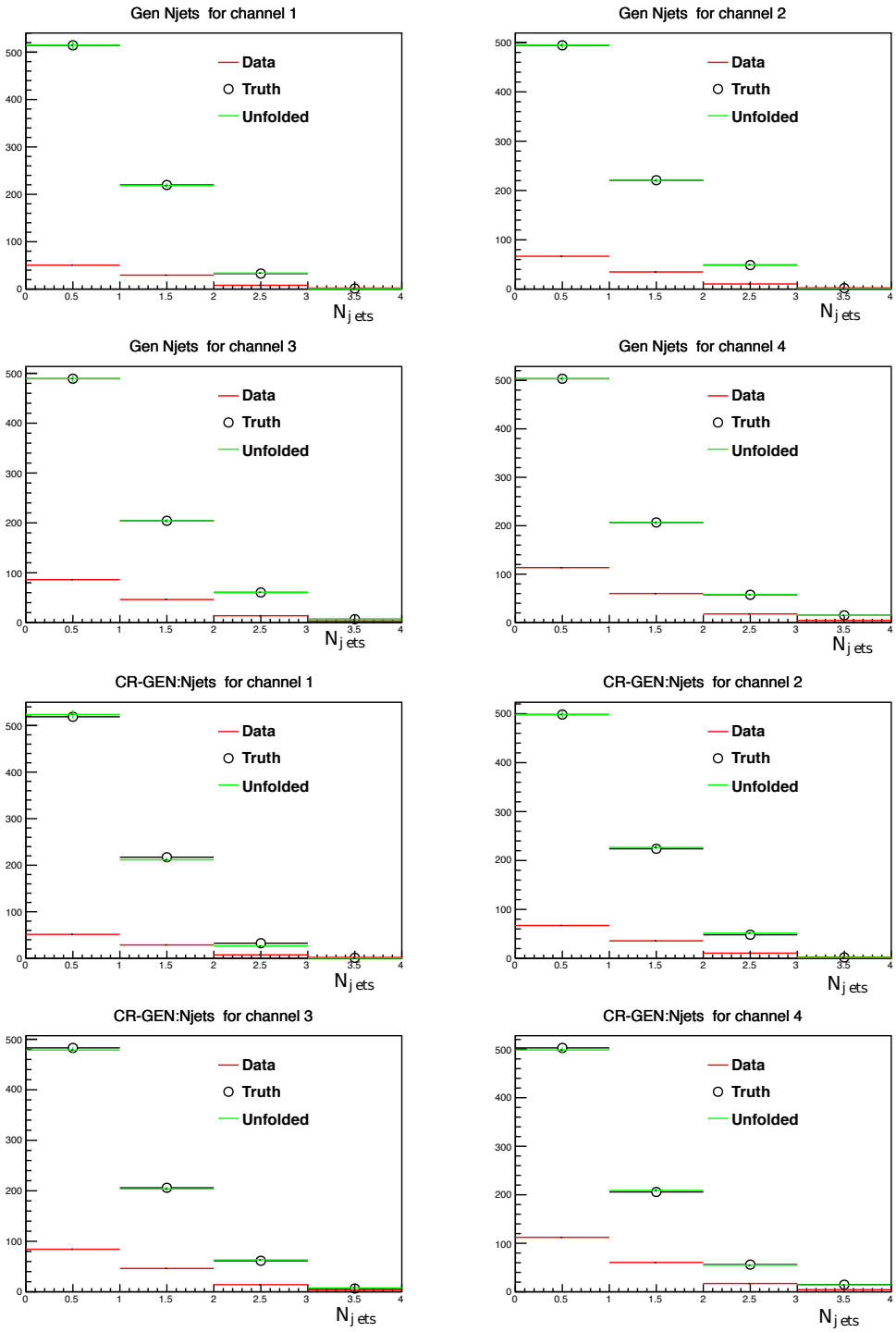

Figure 7.14: Study of unfolding dependence on the MC shape used for producing the response matrix for the number of jets: comparison of unfolded and generated spectra when using a response matrix built from a modifed spectra and applying it to the nominal spectrum. In the four upper plots, unfolded was performed on the same (reweighted) sample used to build the response matrix, while it was applied to an independent sample in the four lower plots.

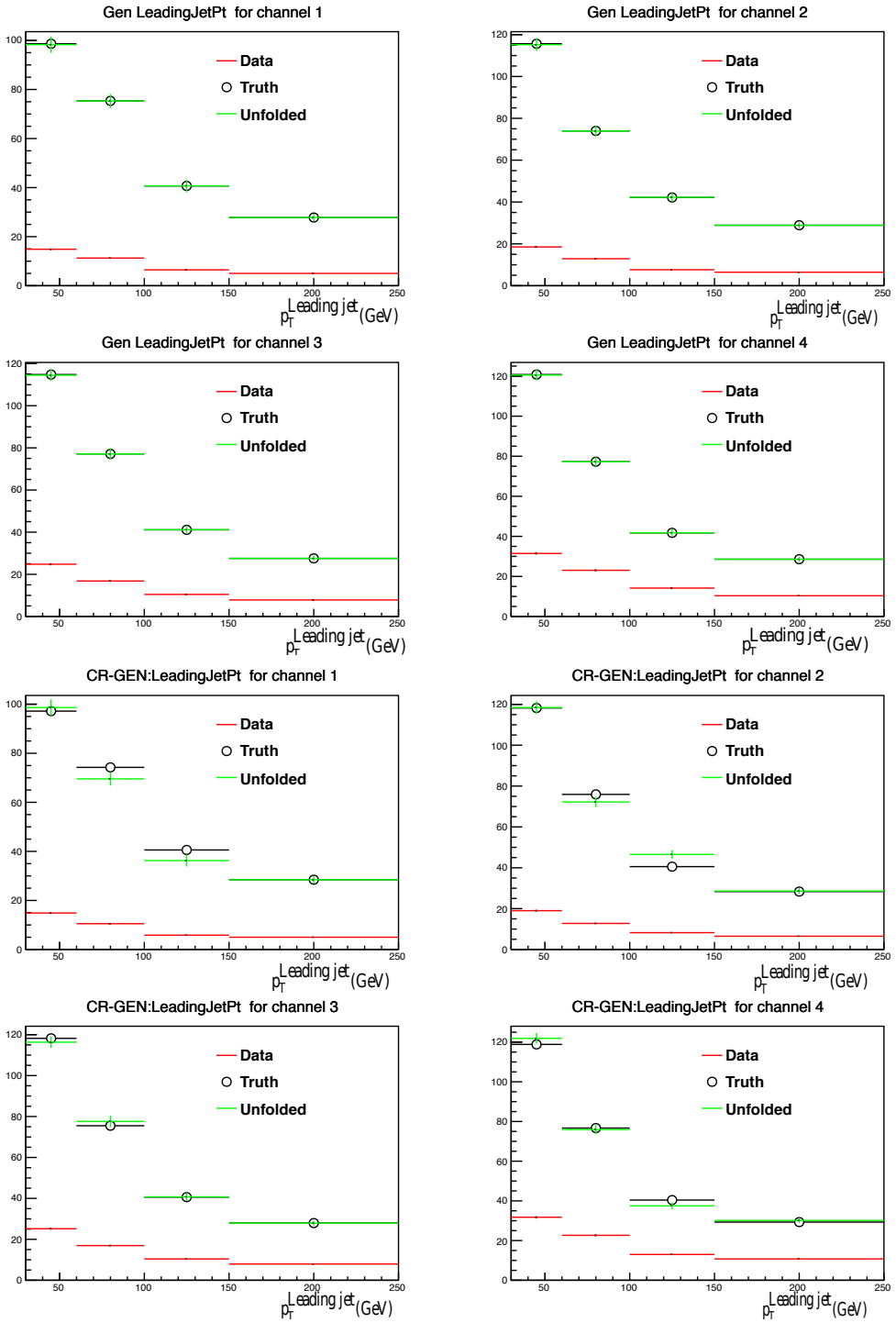

Figure 7.15: Study of unfolding dependence on the MC shape used for producing the response matrix for the leading jet transverse momentum: comparison of unfolded and generated spectra when using a response matrix built from the nominal spectrum and applying it to a modified (reweighted) spectrum. In the four upper plots, unfolded was performed on the same (reweighted) sample used to build the response matrix, while it was applied to an independent sample in the four lower plots.

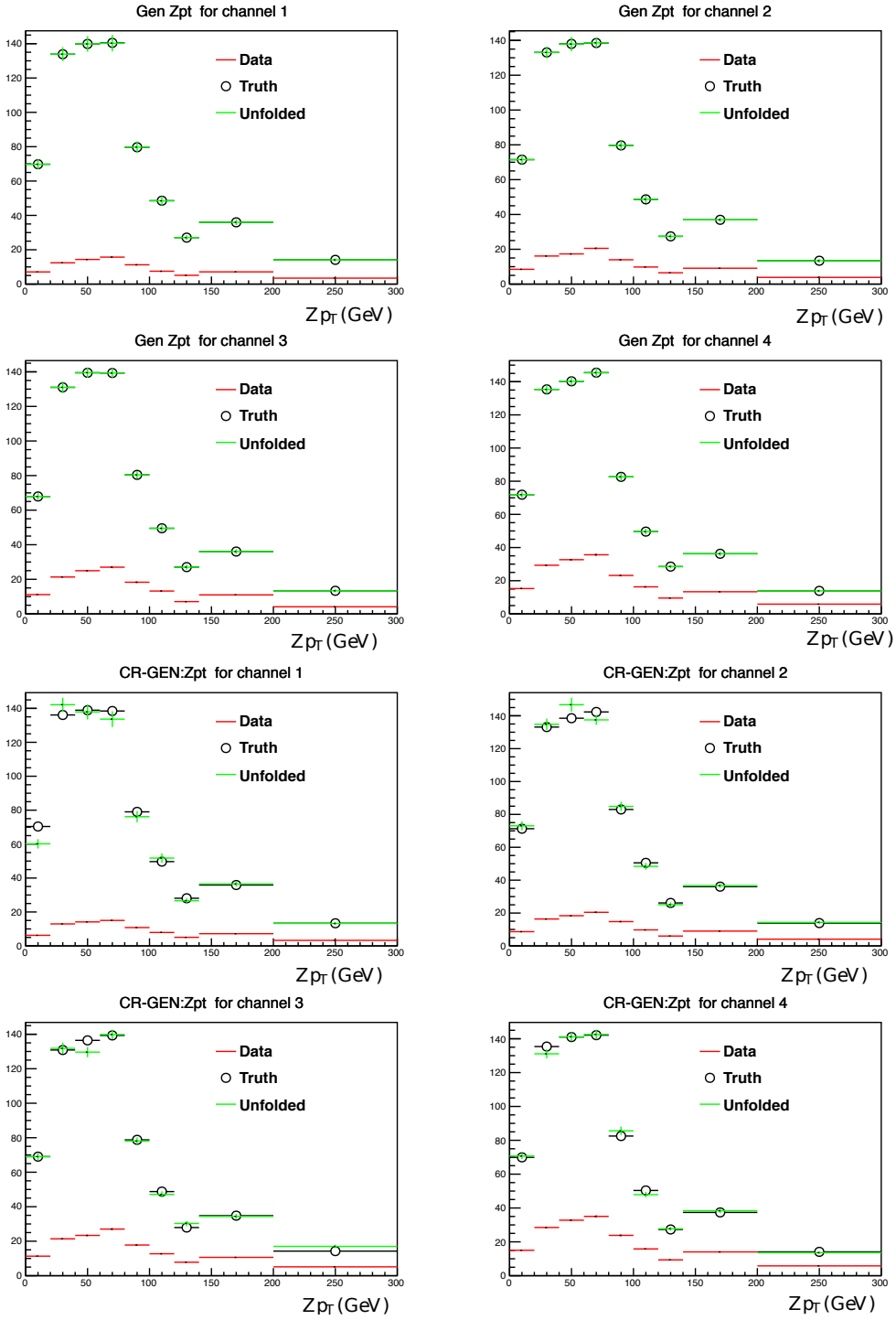

Figure 7.16: Study of unfolding dependence on the MC shape used for producing the response matrix for the Z transverse momentum: comparison of unfolded and generated spectra when using a response matrix built from the nominal spectrum and applying it to a modified spectrum. In the four upper plots, unfolded was performed on the same (reweighted) sample used to build the response matrix, while it was applied to an independent sample in the four lower plots.

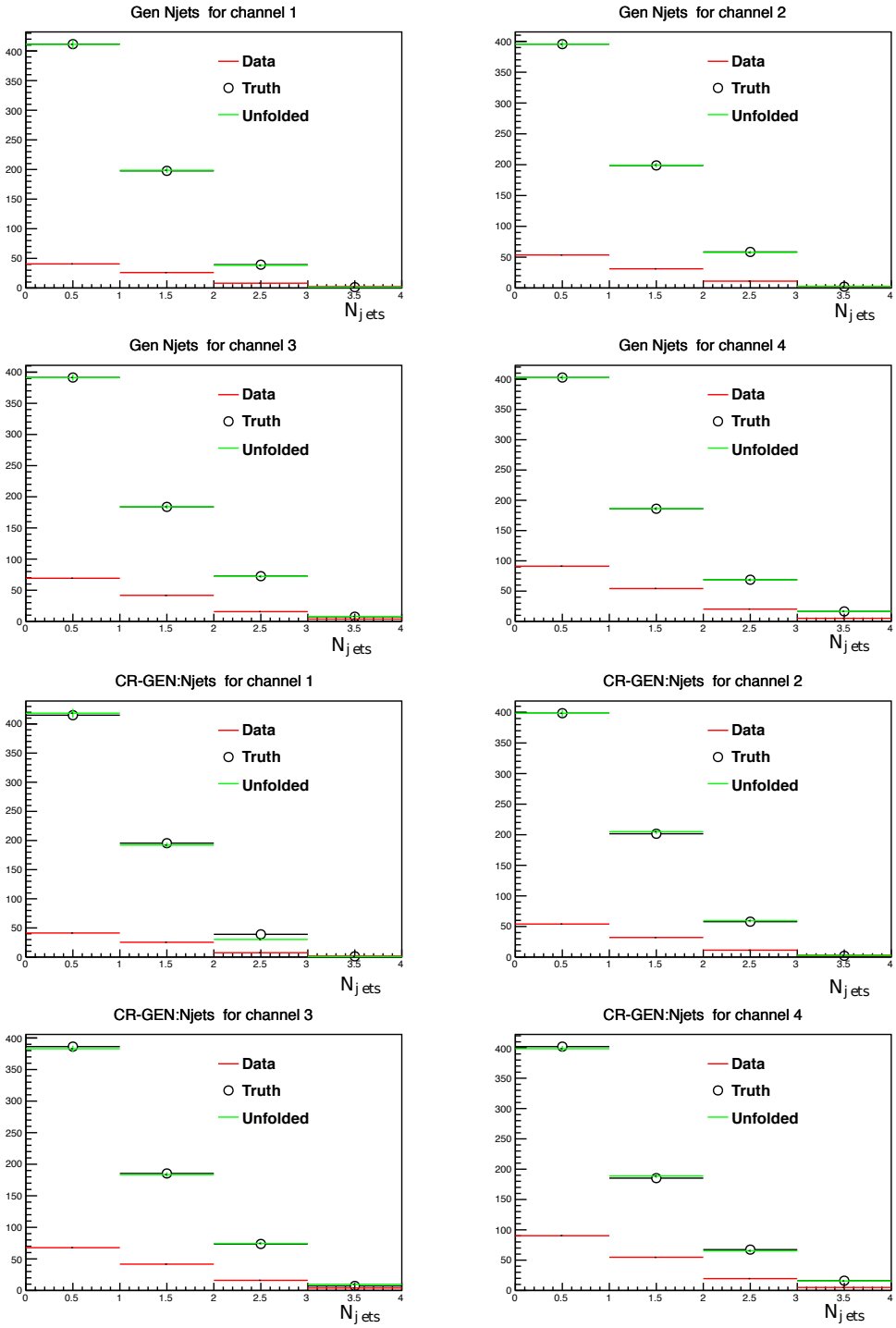

Figure 7.17: Study of unfolding dependence on the MC shape used for producing the response matrix for the number of jets: comparison of unfolded and generated spectra when using a response matrix built from the nominal spectrum and applying it to a modified spectrum. In the four upper plots, unfolded was performed on the same (reweighted) sample used to build the response matrix, while it was applied to an independent sample in the four lower plots.

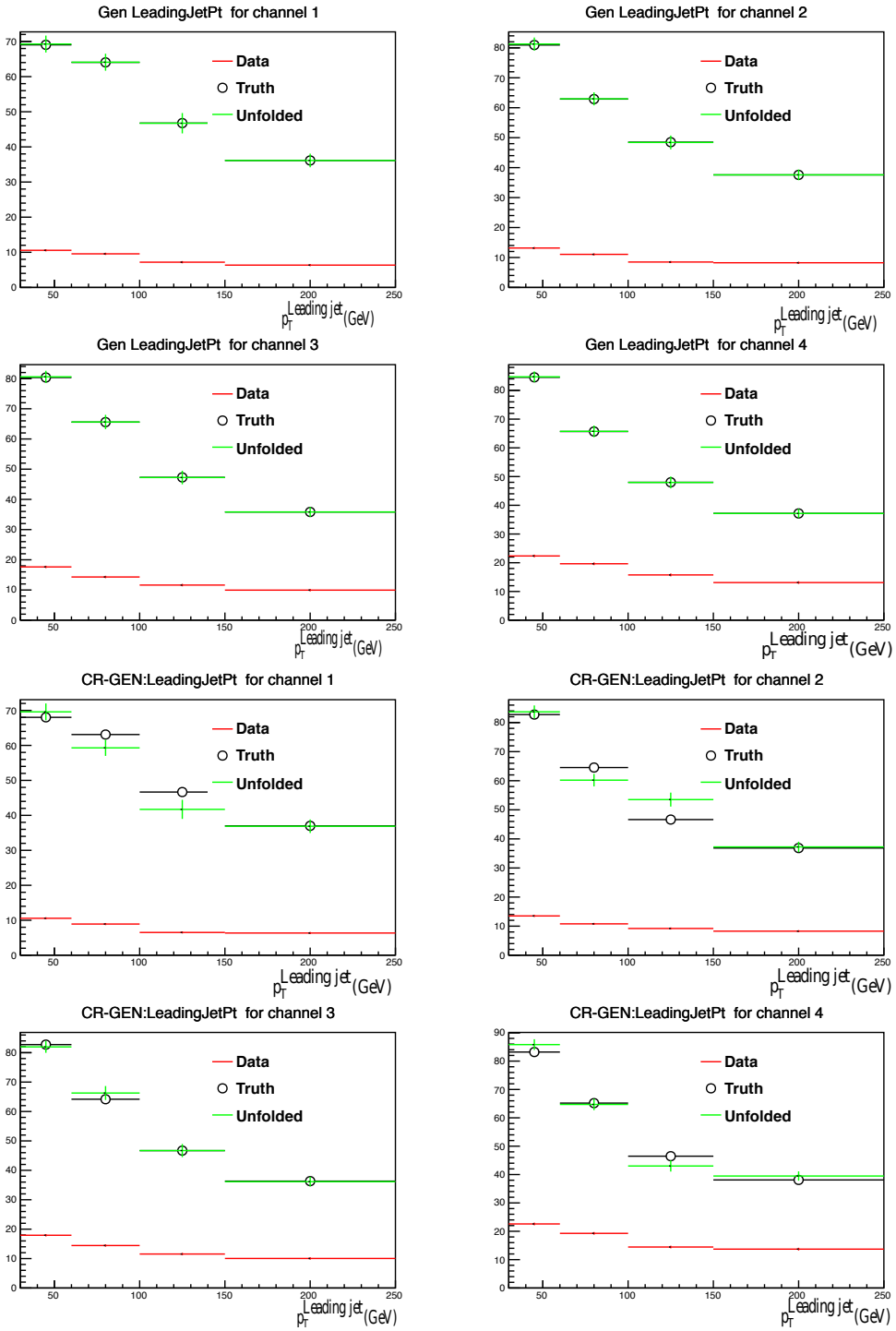

Figure 7.18: Study of unfolding dependence on the MC shape used for producing the response matrix for the leading jet transverse momentum: comparison of unfolded and generated spectra when using a response matrix built from a modifed spectra and applying it to the nominal spectrum. In the four upper plots, unfolded was performed on the same (reweighted) sample used to build the response matrix, while it was applied to an independent sample in the four lower plots.

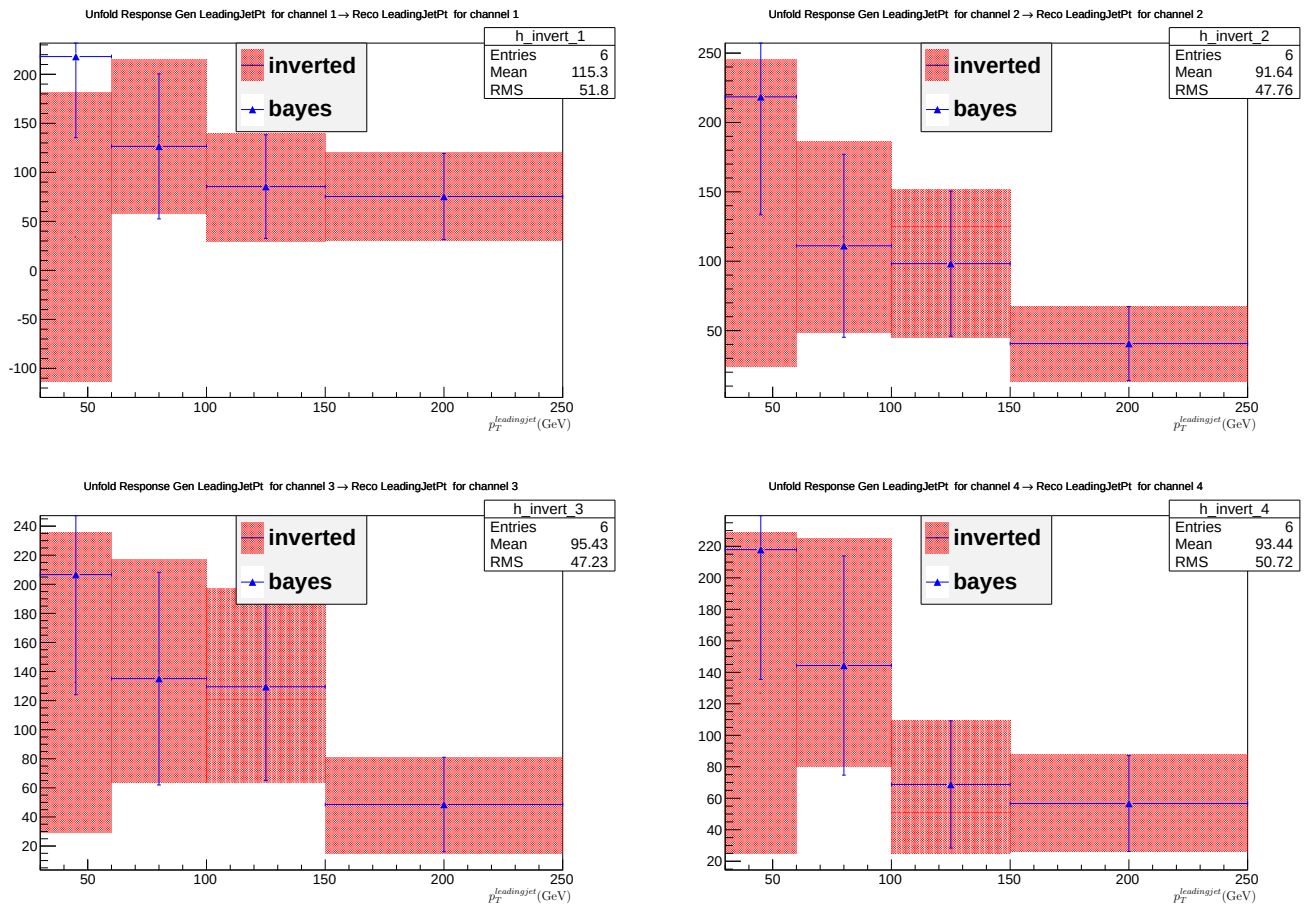

Figure 7.19: Comparison between Bayes unfolding algorithm and inversion for leading jet pt variable. Upper left plot corresponds to 3 electron channel, than 2 electrons and 1 muon (upper right), 1 electron and 2 muons (down left) and 3 muons (down right)

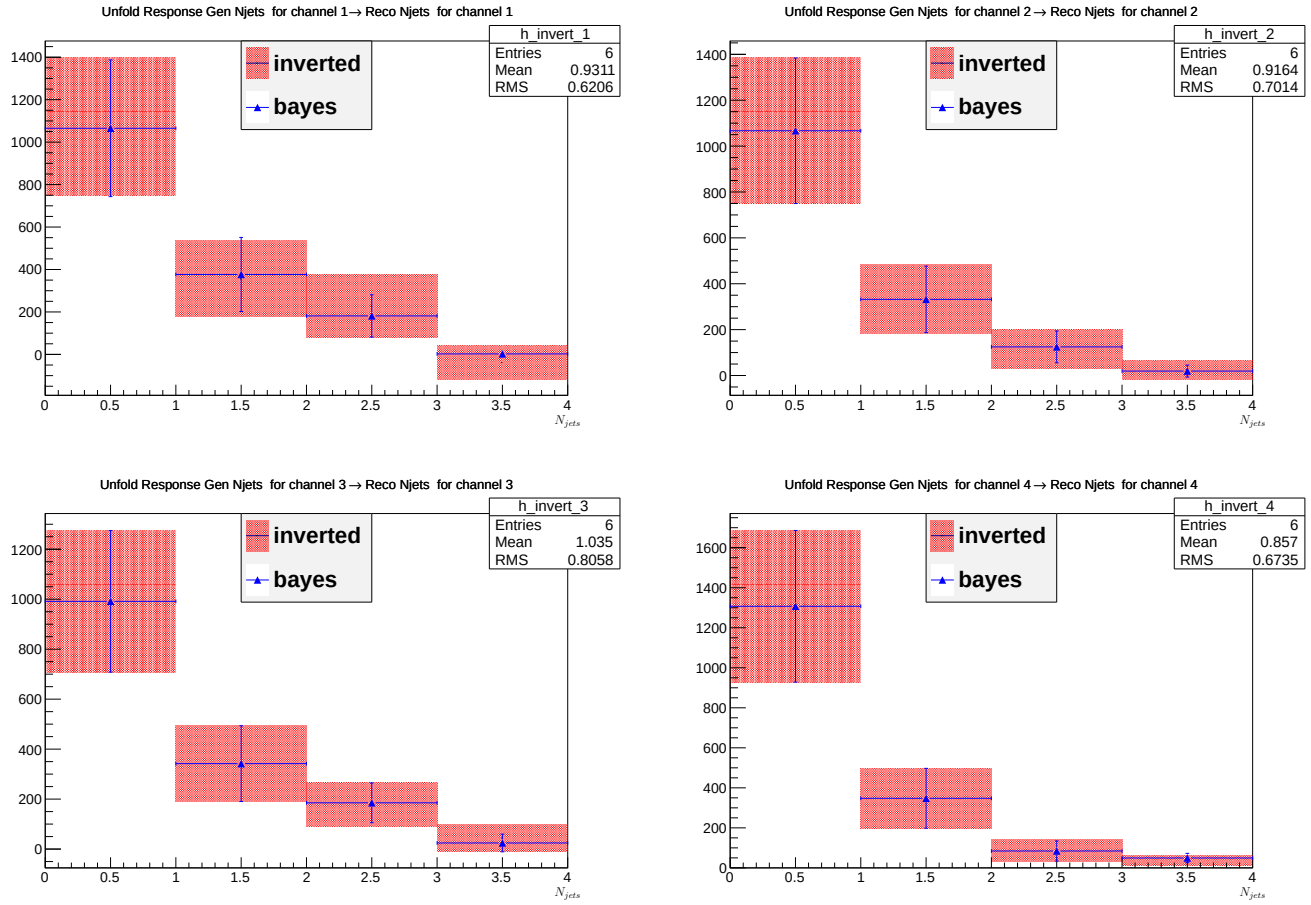

Figure 7.20: Comparison between Bayes unfolding algorithm and inversion for number of jets variable. Upper left plot corresponds to 3 electron channel, than 2 electrons and 1 muon (upper right), 1 electron and 2 muons (down left) and 3 muons (down right)

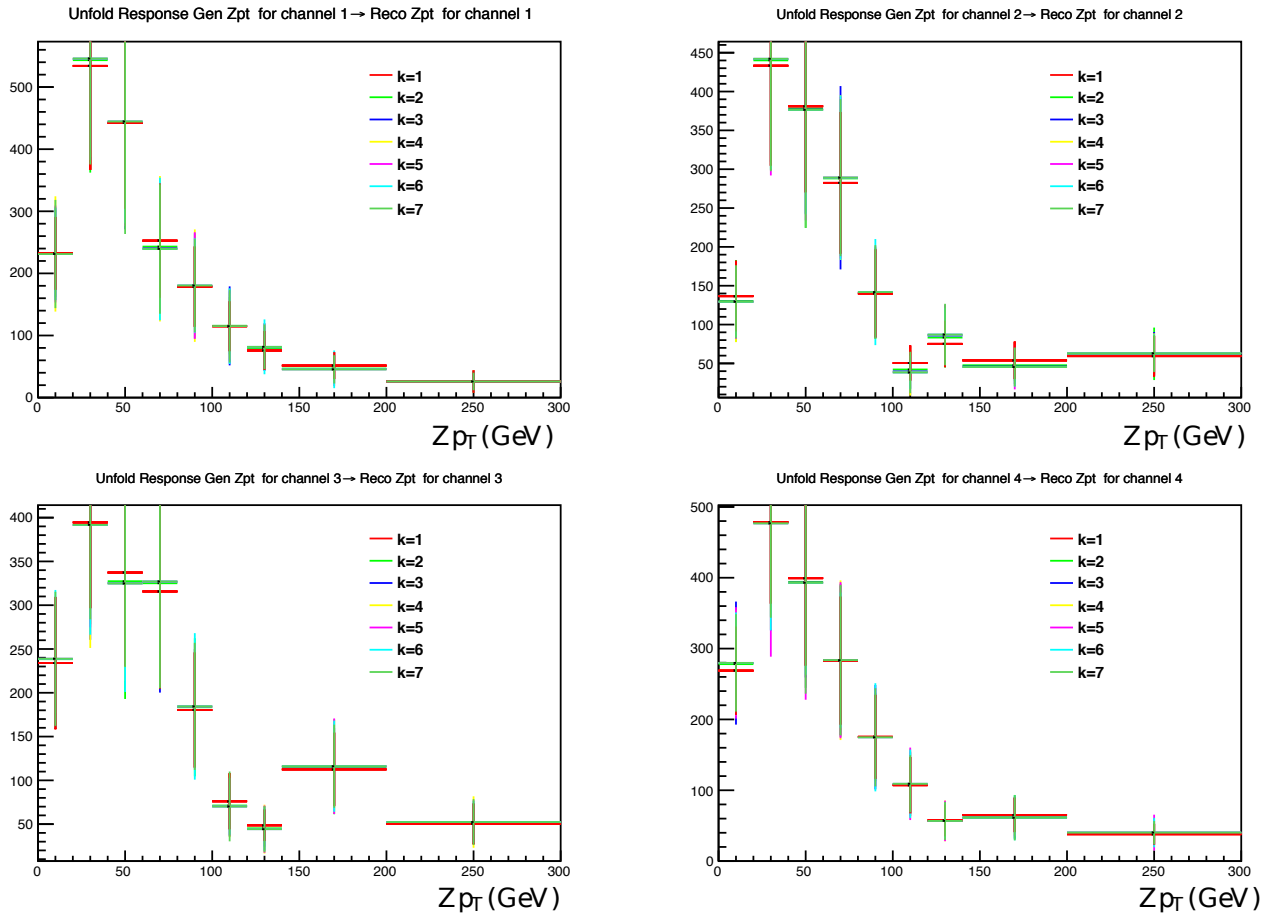

Figure 7.21: Unfolded data spectra for different values of the regularization parameter for the Z transverse momentum. The upper left plot corresponds to 3 electron channel, then 2 electrons and 1 muon (upper right), 1 electron and 2 muons (bottom left) and 3 muons (bottom right)

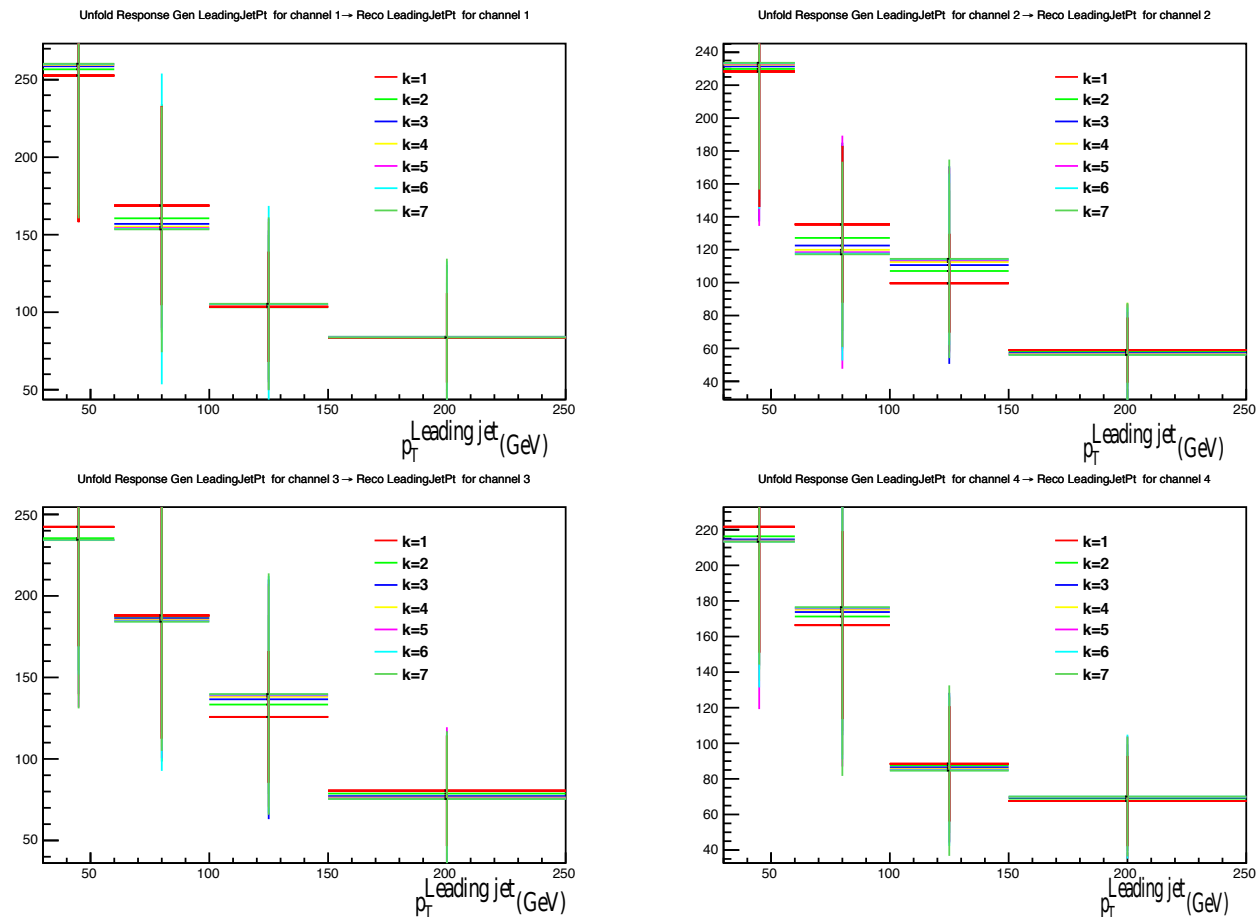

Figure 7.22: Unfolded data spectra for different values of the regularization parameter for the leading jet transverse momentum. The upper left plot corresponds to 3 electron channel, then 2 electrons and 1 muon (upper right), 1 electron and 2 muons (bottom left) and 3 muons (bottom right)

7.4 Systematic uncertainties

Sources of systematic uncertainties are the same as in the inclusive cross section measurement, computed same way just bin by bin. Few additional systematic uncertainties are introduced. The measurements involving jets are affected by the experimental uncertainties in the jet energy scale and resolution (Section 4.3). The effects on the response matrices are studied by smearing and scaling the jet energies within their uncertainties. Furthermore, an uncertainty due to the limited size of simulated sample used to build the response matrices is also included. systematics uncertainty from regularization parameter in unfolding, regularization parameter is varied by 1 up and down (nominal is 5), ans biggest difference to nominal cross section in each bin is taken as uncertainty. Jet energy scale (JES) and jet energy resolution (JER) are taken to be fully correlated between channels. For BLUE combinations, correlations are same as for inclusive cross section measurement.

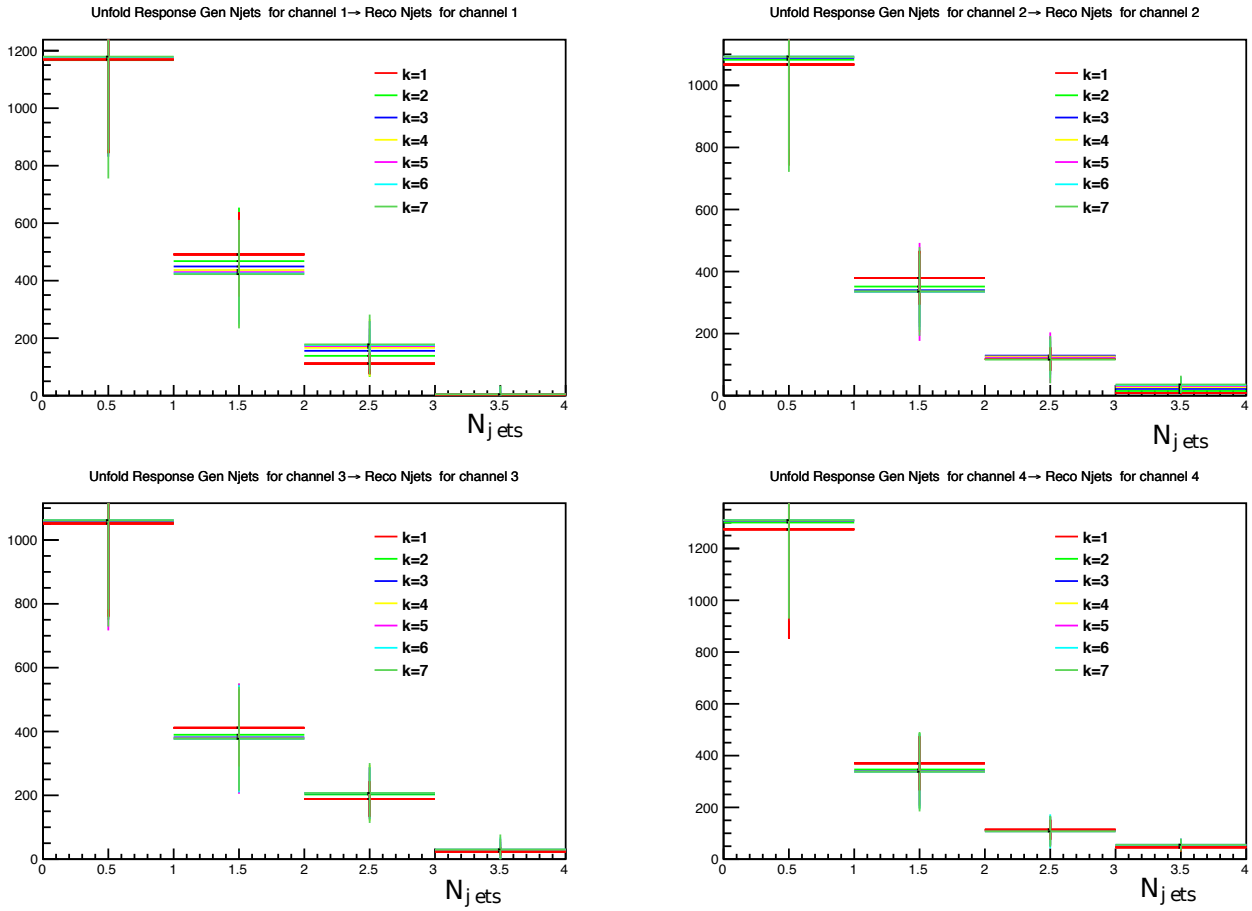

Figure 7.23: Unfolded data spectra for different values of the regularization parameter for the number of jets. The upper left plot corresponds to the 3 electron channel, then 2 electrons and 1 muon (upper right), 1 electron and 2 muons (bottom left) and 3 muons (bottom right)

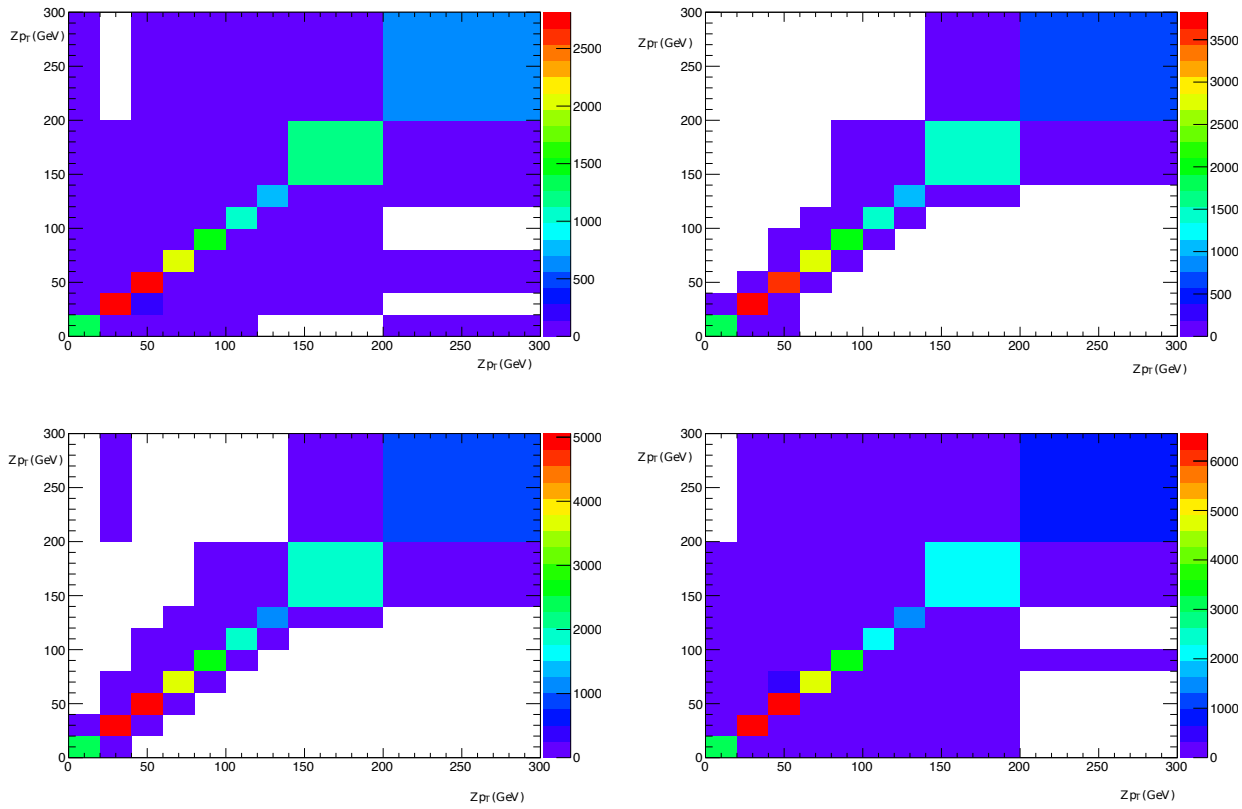

Figure 7.24: Response matrices for variable Zpt: 3e(upper left), 2e1mu (upper right), 1e2mu(down left), 2e1mu(down right))

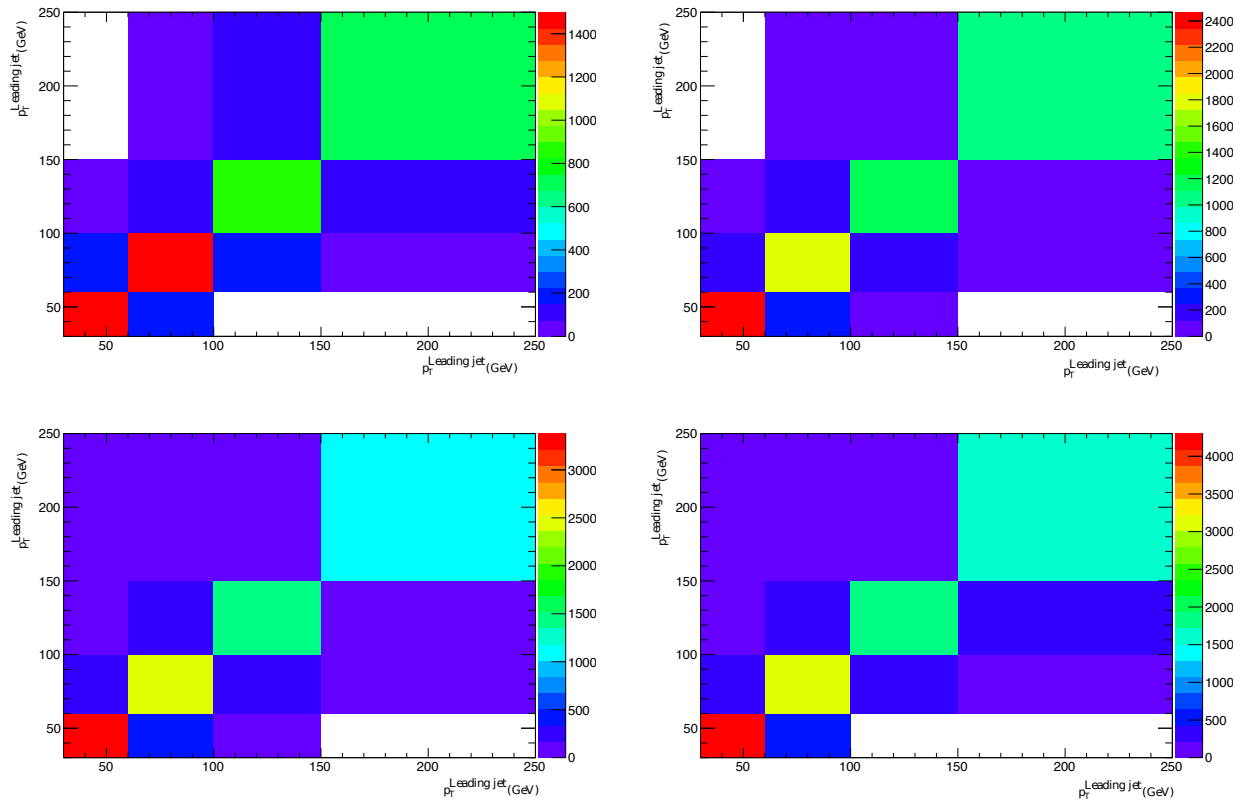

Figure 7.25: Response matrices for variable Leading jet pt: 3e(upper left), 2e1mu (upper right), 1e2mu(down left), 2e1mu(down right))

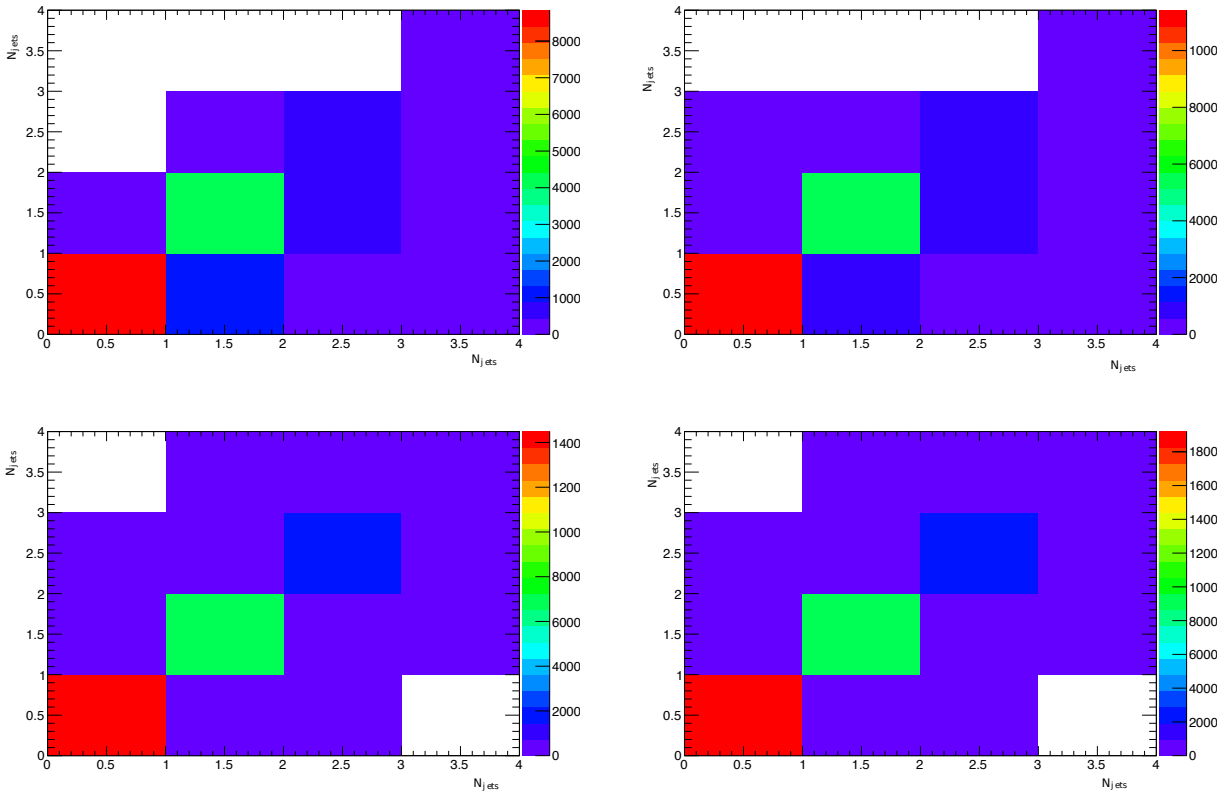

Figure 7.26: Response matrices for variable Njets: 3e(upper left), 2e1mu (upper right), 1e2mu(down left), 2e1mu(down right))

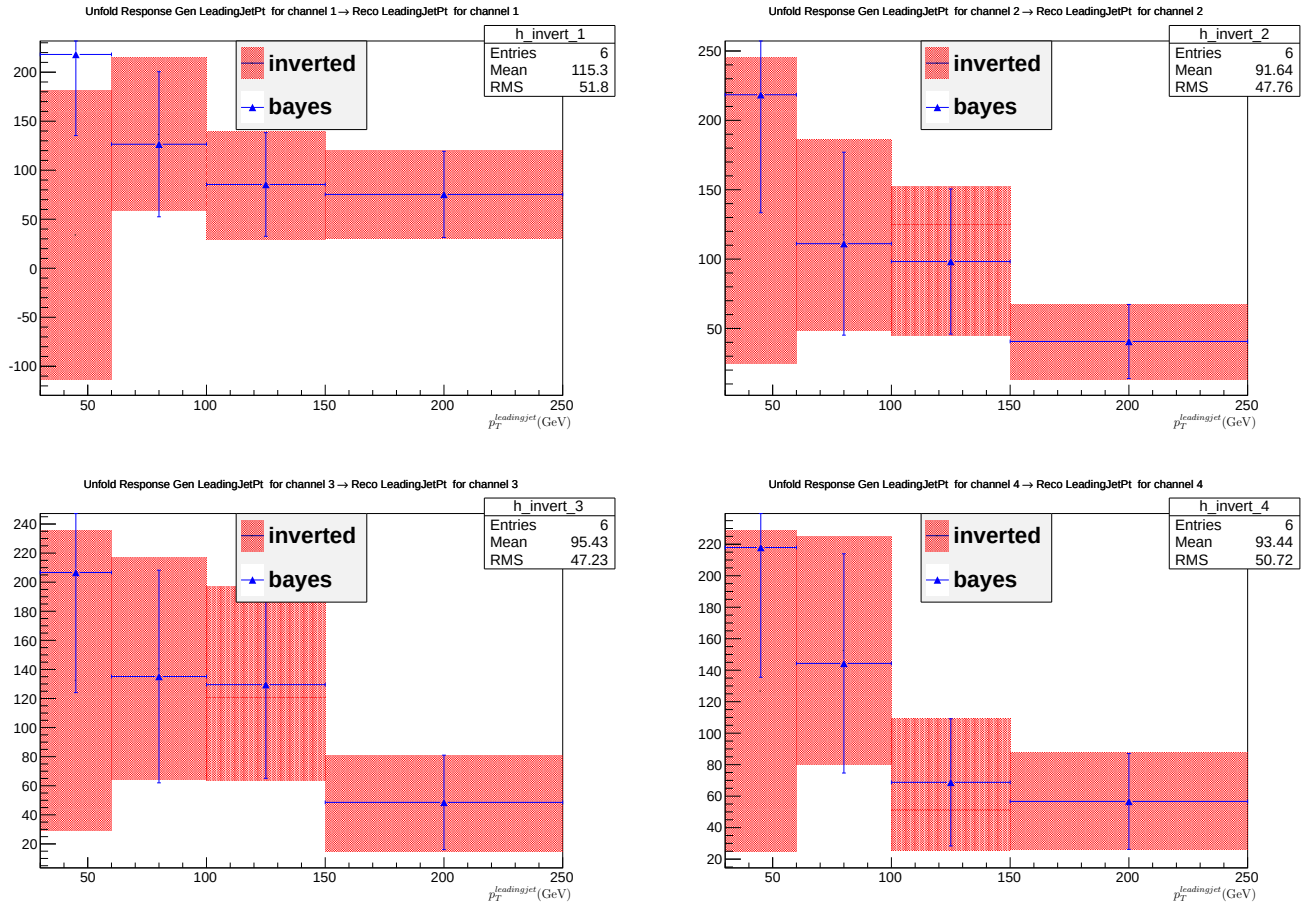

Figure 7.27: Comparison between Bayes unfolding algorithm and inversion for leading jet pt variable. Upper left plot corresponds to 3 electron channel, than 2 electrons and 1 muon (upper right), 1 electron and 2 muons (down left) and 3 muons (down right)

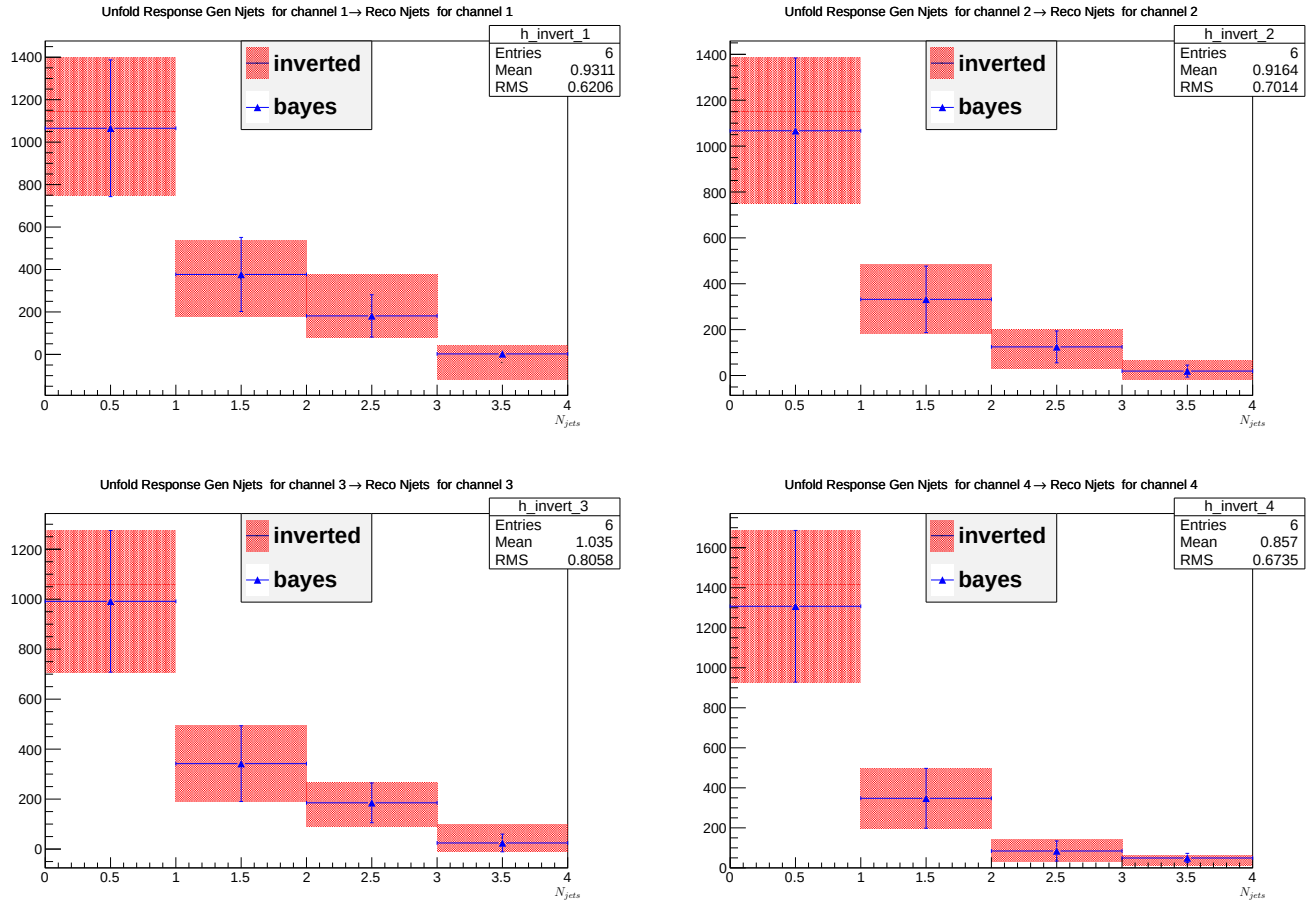

Figure 7.28: Comparison between Bayes unfolding algoritham and inversion for number of jets variable. Upper left plot corresponds to 3 electron channel, than 2 electrons and 1 muon (upper right), 1 electron and 2 muons (down left) and 3 muons (down right)

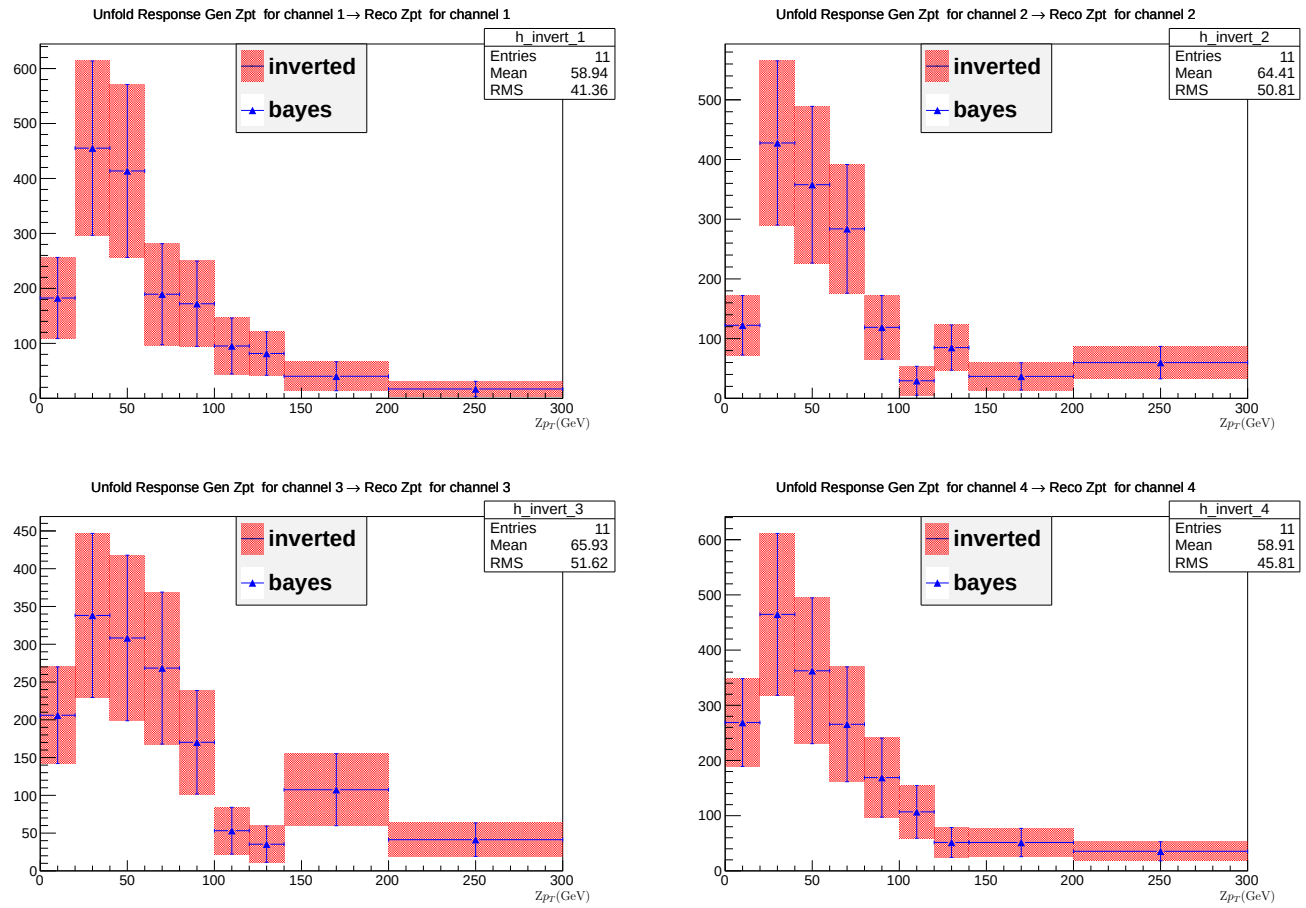

Figure 7.29: Comparison between Bayes unfolding algoritham and inversion for Z pt variable. Upper left plot corresponds to 3 electron channel, than 2 electrons and 1 muon (upper right), 1 electron and 2 muons (down left) and 3 muons (down right)

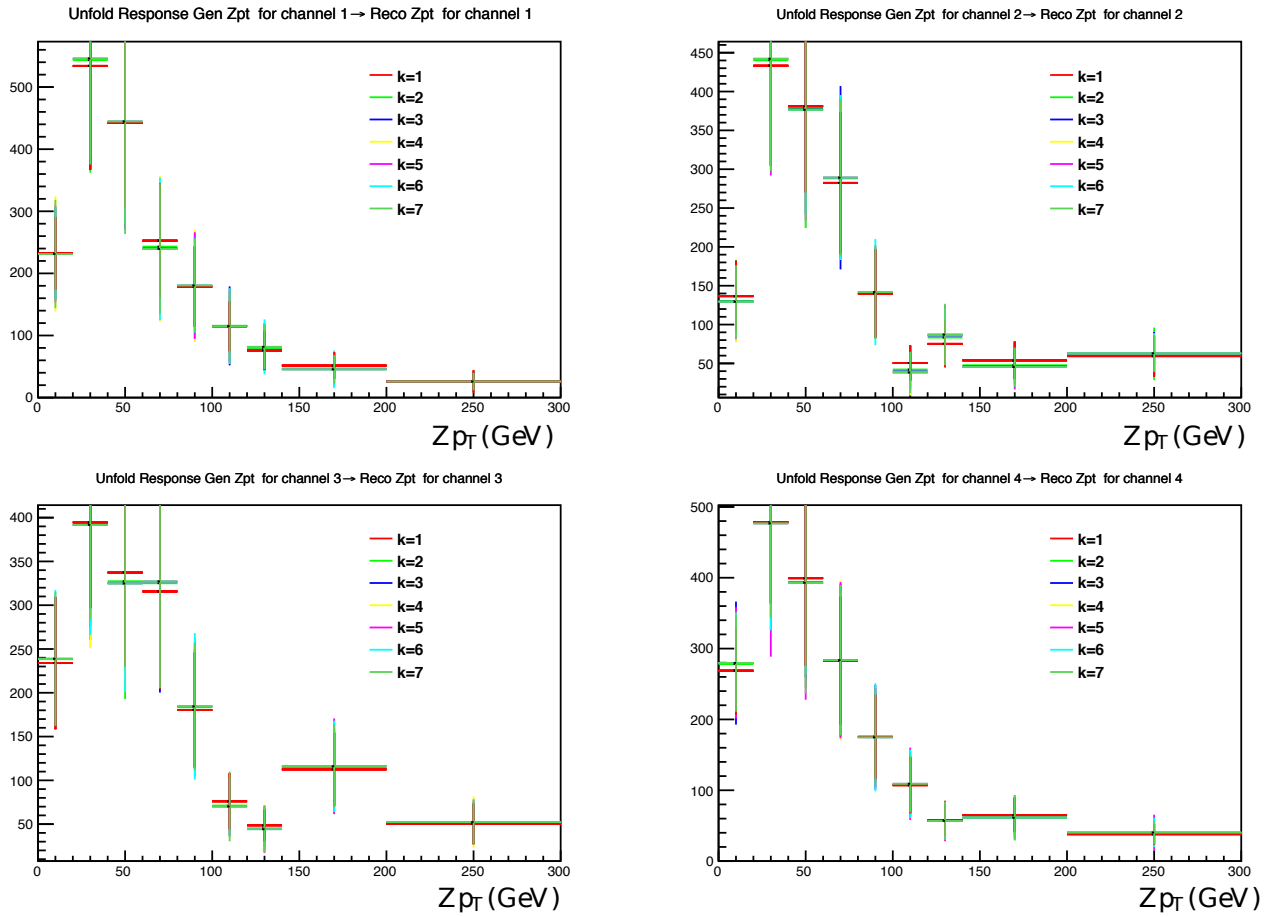

Figure 7.30: Unfolded data spectra for different values of the regularization parameter for the Z transverse momentum. The upper left plot corresponds to 3 electron channel, then 2 electrons and 1 muon (upper right), 1 electron and 2 muons (bottom left) and 3 muons (bottom right)

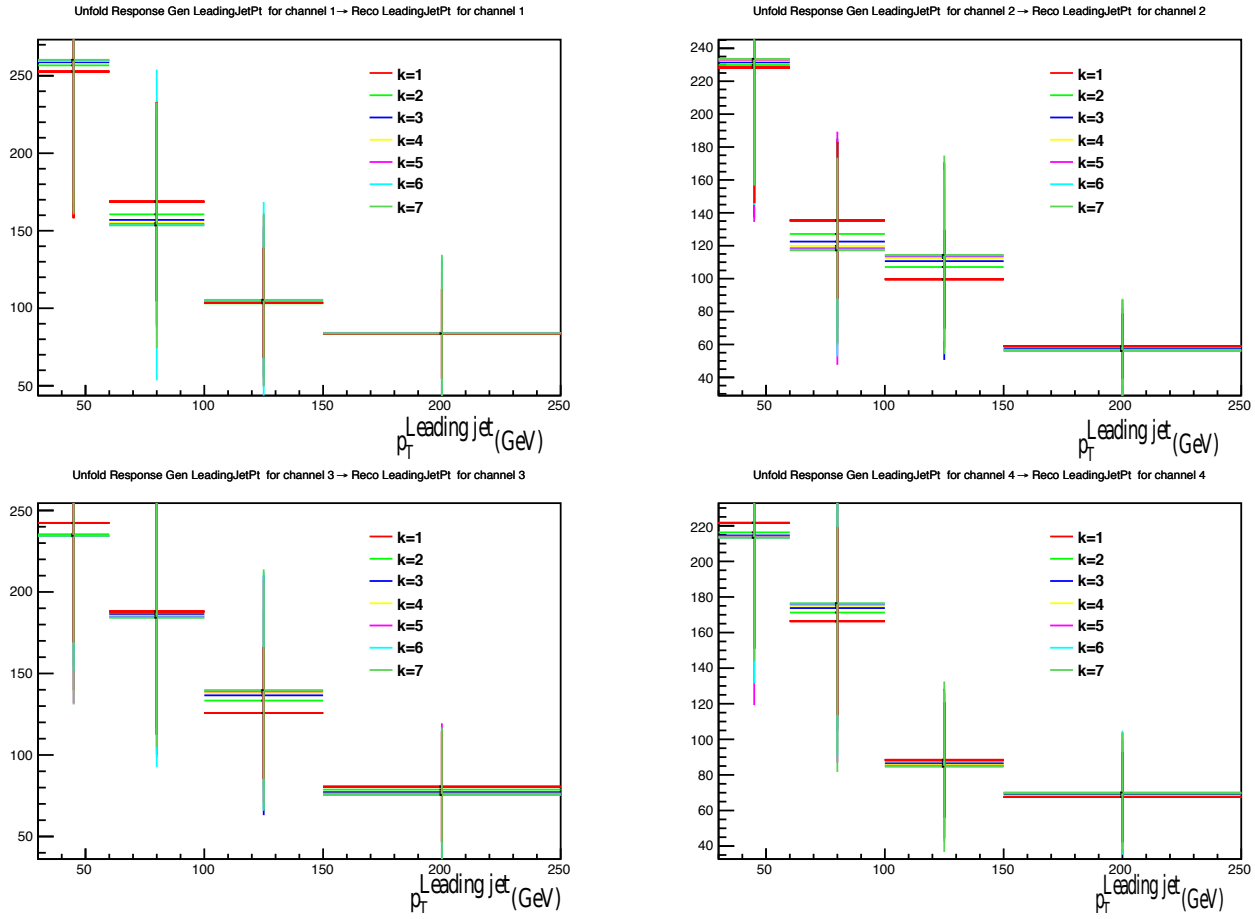

Figure 7.31: Unfolded data spectra for different values of the regularization parameter for the leading jet transverse momentum. The upper left plot corresponds to 3 electron channel, then 2 electrons and 1 muon (upper right), 1 electron and 2 muons (bottom left) and 3 muons (bottom right)

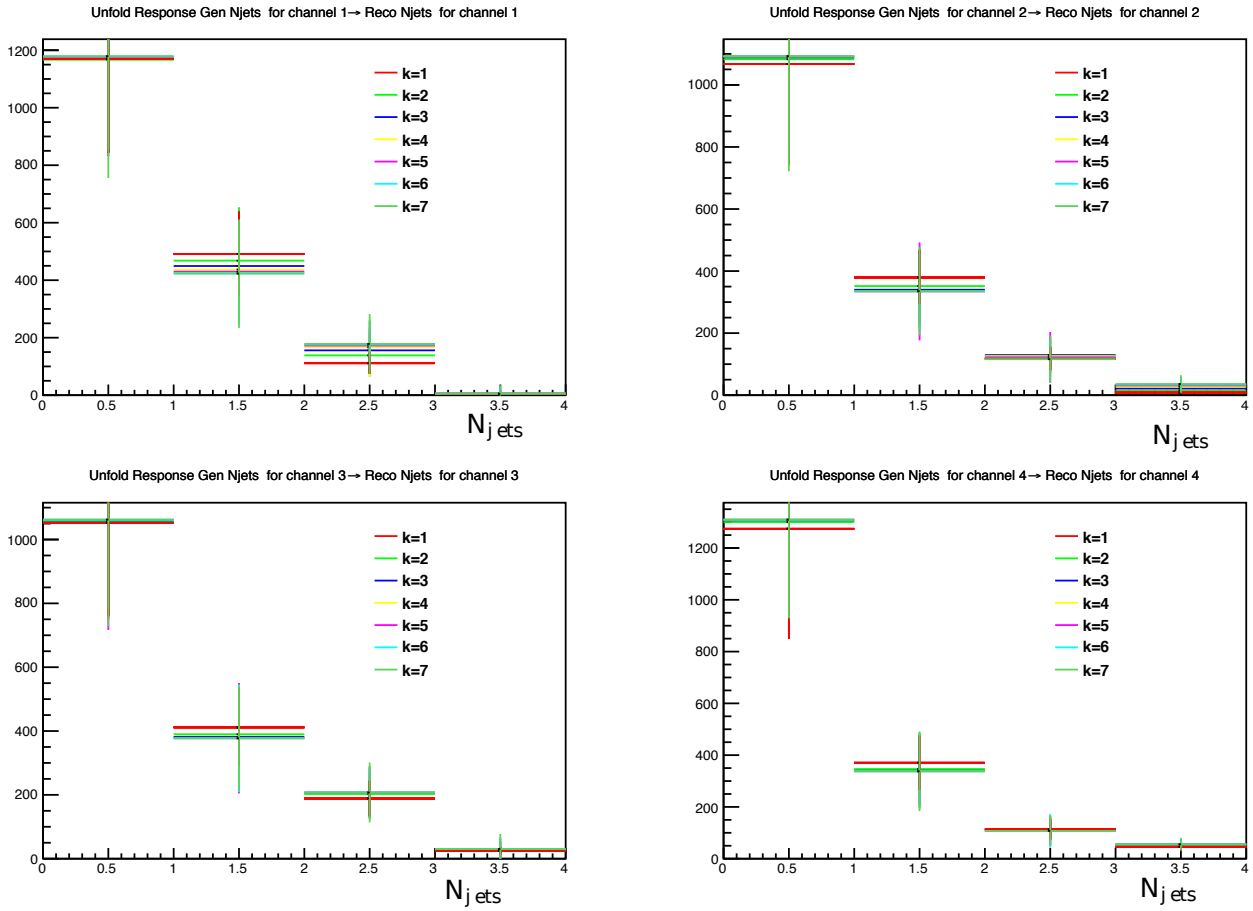

Figure 7.32: Unfolded data spectra for different values of the regularization parameter for the number of jets. The upper left plot corresponds to 3 electron channel, then 2 electrons and 1 muon (upper right), 1 electron and 2 muons (bottom left) and 3 muons (bottom right)

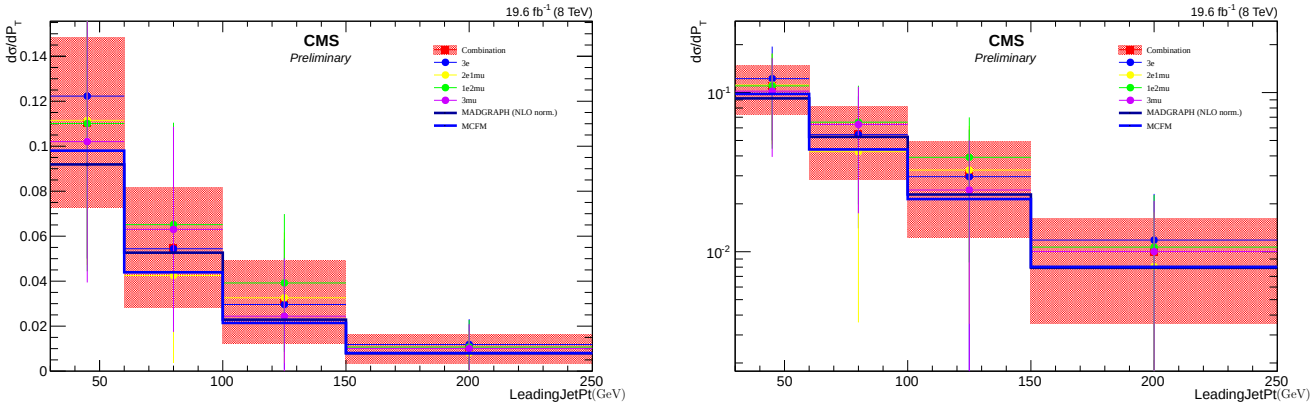

Figure 7.33: Differential cross section for leading jet pt, for 4 channels and combination in linear (left) and log (right) scale.

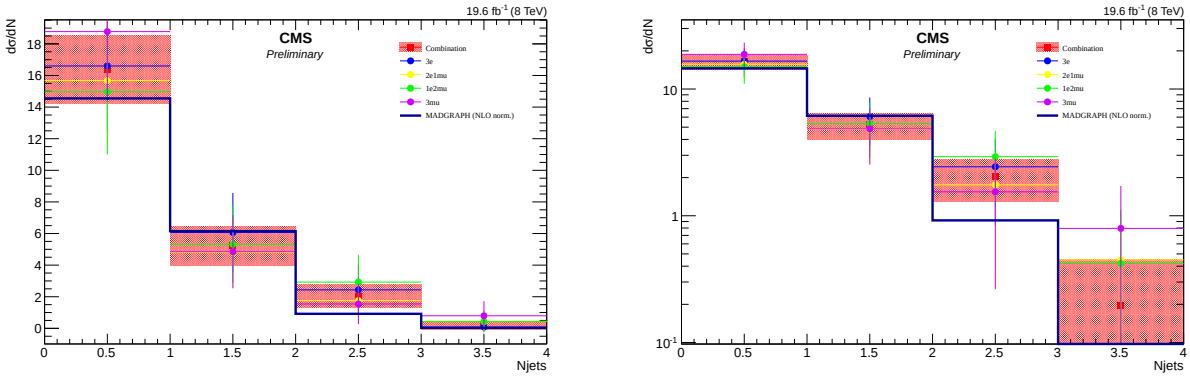

Figure 7.34: Differential cross section for number of jets, for 4 channels and combination in linear (left) and log (right) scale.

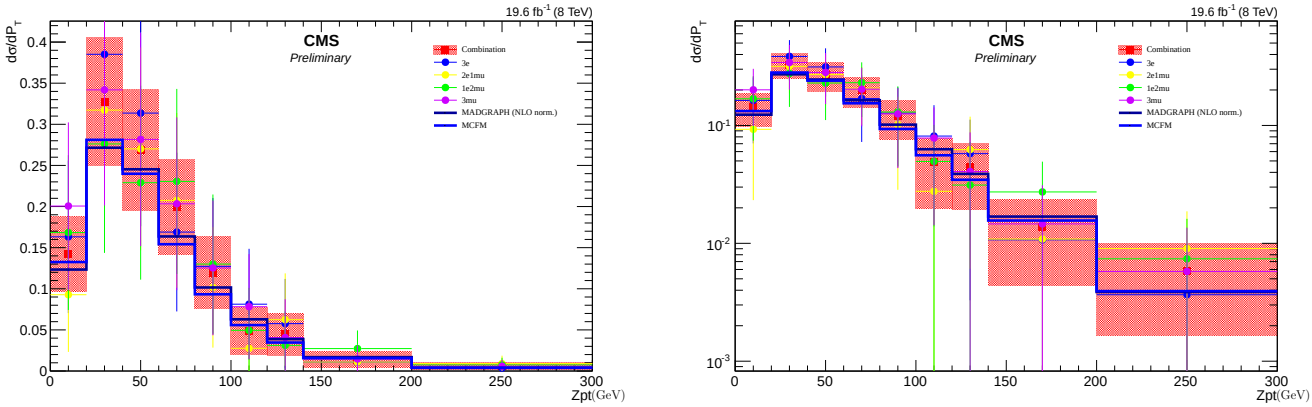

Figure 7.35: Differential cross section for Z pt, for 4 channels and combination in linear (left) and log (right) scale.

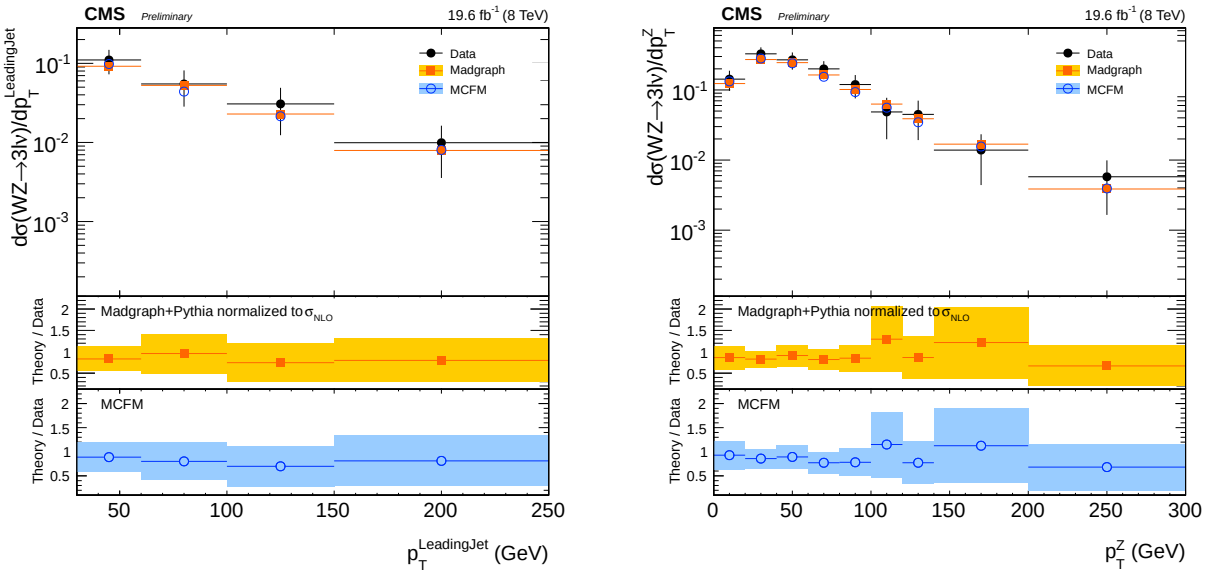

Figure 7.36: Differential cross section for Z pt and LeadingJet Pt, comparison with theory.

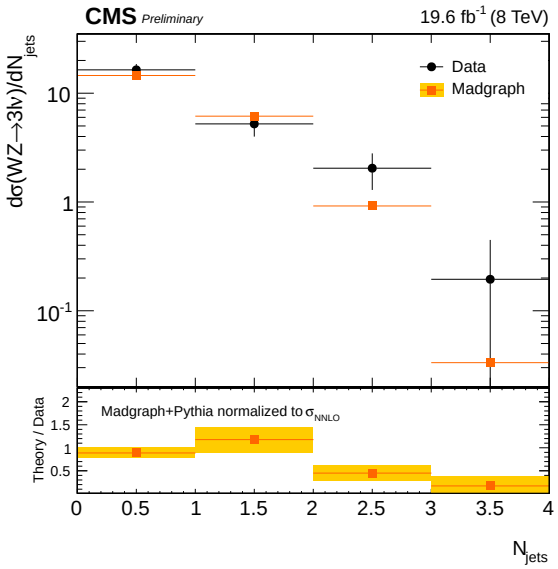

Figure 7.37: Differential cross section for number of jets, comparison with theory.

7.5 Differential cross section

First two steps in computing differential cross section are exactly the same as for inclusive cross section: extracting prompt yield, using data driven method and substracting Monte Carlo background estimation bin by bin. After this unfolding is applied on resulting spectra. The unfolded spectra are used to extract differential cross sections for all four leptonic final states. The four channels are then combined bin by bin. Besides taking into account correlated systematic uncertainties as for the total cross section, the correlation between bins introduced by the unfolding procedure for each channel are also taken into account. This is done by using a generalization of the BLUE method explained in Section 6.5.1, which takes into account all correlations:

- The correlations in systematic uncertainties between all channels.
- The correlation between different bins in one channel coming from the unfolding procedure.

We define the problem and the indices used:

- We measure the same differential cross section in n_{ch} different channels, indexed by latin indices i, j. In our case, $n_{ch} = 4$, $ij \in \{eee, ee\mu, \mu\mu e, \mu\mu\mu\}$.
- In each channel, we measure the differential cross section in n_{bins} different bins, indexed by greek indices $\alpha, \beta, ...$

We consider the following covariance matrices as input:

- n_{ch} unfodling matrices E_i^{unf} containing the covariance matrix from unfolding.
- n_{bins} matrices E_α^{sys} containing the covariance matrices containing systematic correlations between channels. These are the same correlations as used in the BLUE combination for the inclusive cross section.

We have therefore $n_{ch} \times n_{bins}$ different measurements. The covariances between any such two measurements can be written as:

$$Cov(\text{bin ff}, \text{bin fi}, \text{ch. i}, \text{ch. j}) = \begin{cases} (E_{\alpha}^{sys})_{ij} & , \text{if ff} = \text{fi} \\ (E_{i}^{unf})_{\alpha\beta} & , \text{if i} = \text{j} \\ 0, & , \text{if ff} \neq \text{fi}, \text{i} \neq \text{j} \end{cases} \tag{7.7}$$

We now follow the following steps to combine the four channels in each bin:

1. We define an index function $\mathscr{I}(\alpha, i)$ which maps the bin number α ($\in \{1, ..., n_{bins}\}$) and channel number i ($\in \{1, ..., n_{ch}\}$) to a one dimensional index in the range 1, ..., $n_{ch} \times n_{bins}$:

$$\mathscr{I}(\alpha, i) = n_{bins} * i + \alpha$$

2. Build a global covariance matrix C containing all covariances from Equ. 7.7, following the following convention for rows and columns:

$$C_{\mathscr{I}(\alpha,i),\mathscr{I}(\beta,j)} = Cov(\text{bin ff}, \text{bin fi}, \text{ch. i}, \text{ch. j})$$

3. Build a vector **a** containing all measurements:

$$a_{\mathscr{I}(\alpha,i)} = \text{M}easurement\ in\ bin\ \alpha\ for\ channel\ i$$

4. Invert he covariance matrix $M \equiv C^{-1}$ amd build the vector $\mathbf{f} = M \cdot a$
5. Build a $n_{bins} \times n_{bins}$ matrix D as:

$$D_{\alpha\beta} = \sum_{i,j} M_{\mathscr{I}(\alpha,i),\mathscr{I}(\beta,j)}$$

6. Build a n_{bins} component vector g as

$$g_{\alpha} = \sum_{\text{ch. } i} f_{\mathscr{I}(\alpha,i)}$$

7. The combined result, an n_{bins} dimensional vector, **r** is obtained as

$$r = D^{-1}\mathbf{g}$$

8. The covariance matrix for r is

$$E_r = D^{-1}$$

The correlation matrices for the unfolding correlation are shown in 7.39, 7.38, 7.40.

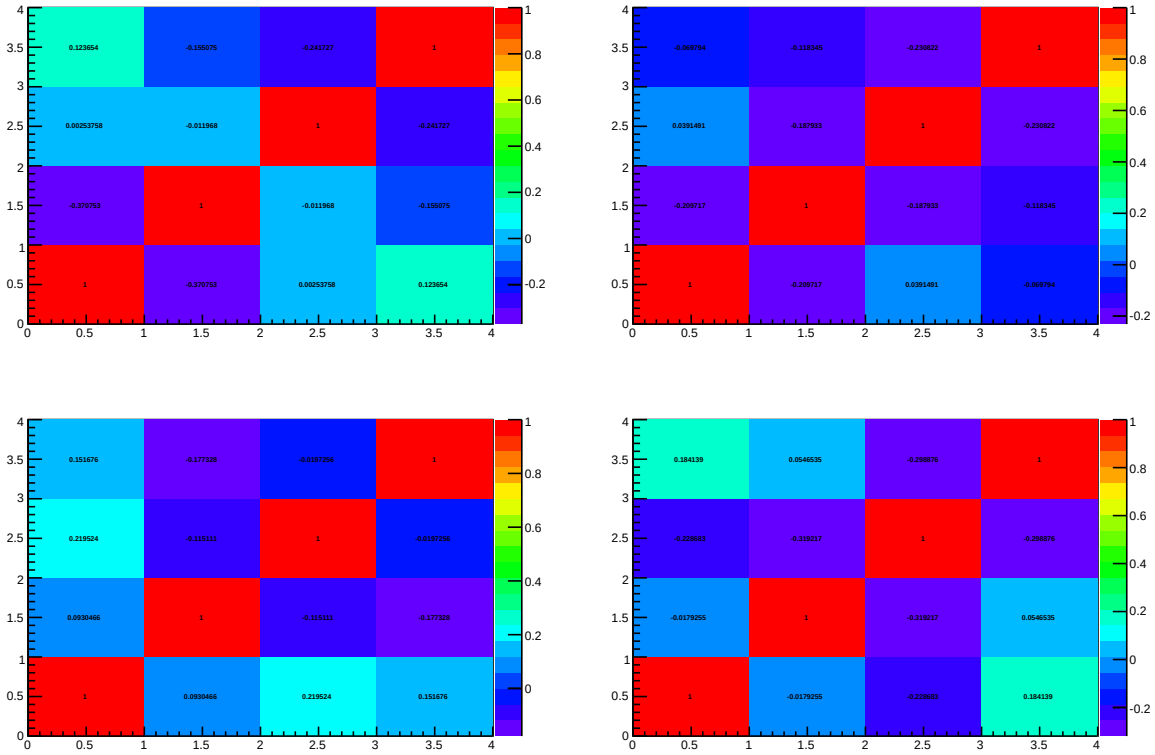

Figure 7.38: Correlation matrix for the unfolding correlation for number of jets.

The unfolded spectra are then used to extract differential cross sections for all four leptonic final states.

7.6 Comparison with theory

The measured differential cross sections are given in Tables 9.6, 9.5 and 9.4 for each of the four channels and the combined results are given in Table 9.7, and shown in Figures 7.34, 7.36 and 7.37. The differential cross sections are compared with MCFM and Madgraph predictions. The Madgraph spectra are normalized to the NLO cross section as predicted by MCFM. The predictions agree with the measured differential cross sections within uncertainties for the Z and leading jet transverse momentum. The data show however an excess over the prediction at larger jet multiplicity in the $\frac{d\sigma}{dN_{jets}}$. This can be explained as signal Madgraph sample is WZ process and two or less jets (at matrix element level).

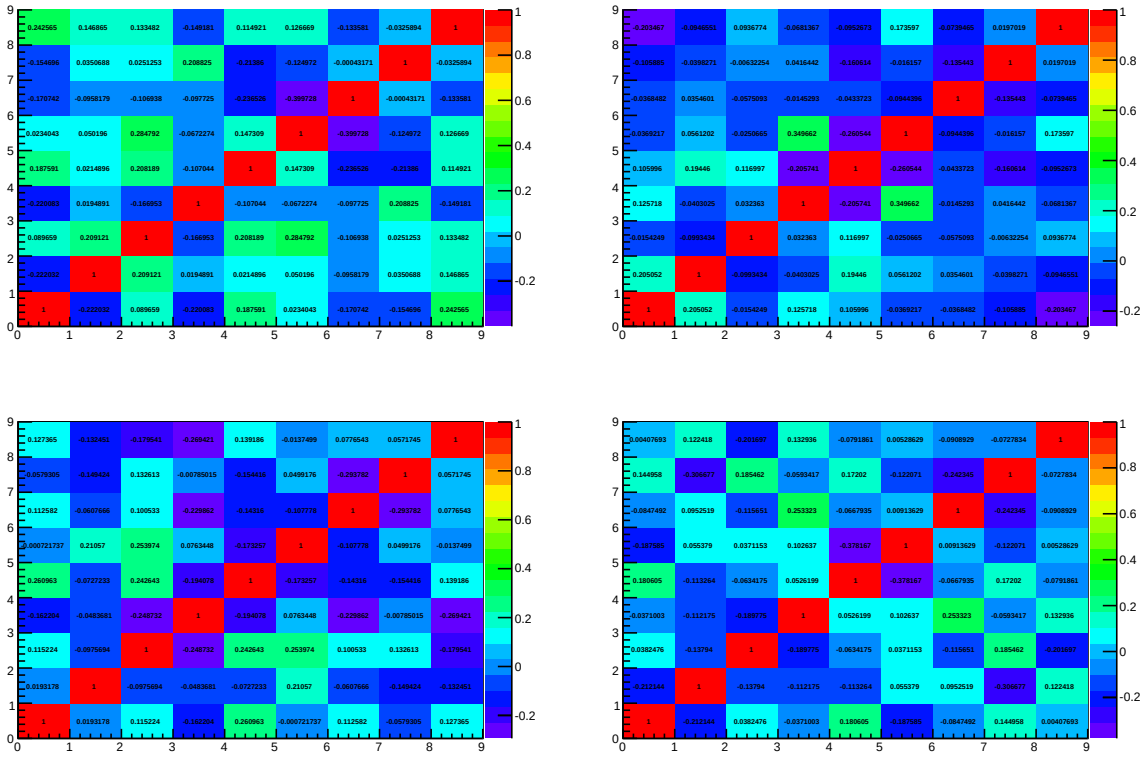

Figure 7.39: Correlation matrix fot the unfolding correlation for number of Zp_T.

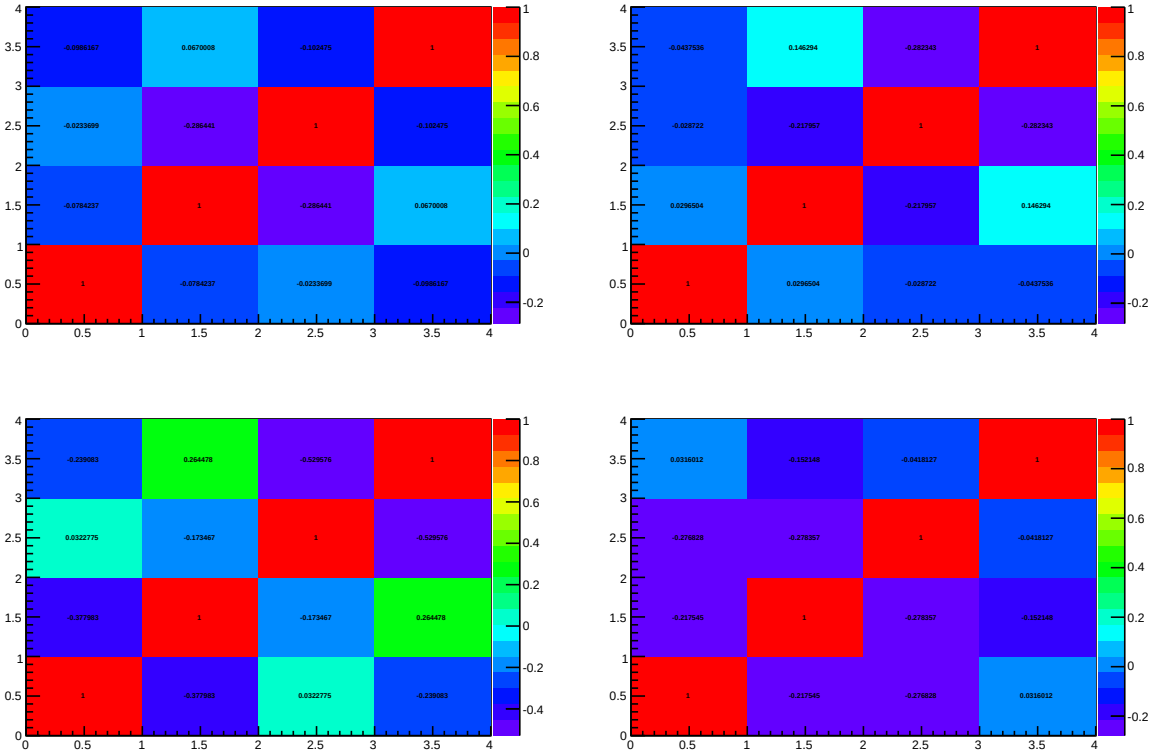

Figure 7.40: Correlation matrix fot the unfolding correlation for number of leading jet p_T.

Table 7.1: Differential WZ cross section as a function of the Z transverse momentum at $\sqrt{s} = 8$ TeV for the four leptonic final states. The first uncertainty is statistical, the second is systematic, and the third is the integrated luminosity.

p_T^Z [GeV]	$d\sigma/dp_T^Z$ [pb /GeV]			
	eee	$ee\mu$	$\mu\mu e$	$\mu\mu\mu$
0–20	$(1.63 \pm 0.90 \pm 0.22 \pm 0.04) \times 10^{-1}$	$(9.3 \pm 6.8 \pm 1.3 \pm 0.2) \times 10^{-2}$	$(1.68 \pm 0.92 \pm 0.21 \pm 0.04) \times 10^{-1}$	$(2.01 \pm 1.00 \pm 0.20 \pm 0.05) \times 10^{-1}$
20–40	$(3.9 \pm 1.4 \pm 0.5 \pm 0.1) \times 10^{-1}$	$(3.17 \pm 1.26 \pm 0.39 \pm 0.08) \times 10^{-1}$	$(2.76 \pm 1.18 \pm 0.62 \pm 0.07) \times 10^{-1}$	$(3.42 \pm 1.31 \pm 0.57 \pm 0.09) \times 10^{-1}$
40–60	$(3.14 \pm 1.25 \pm 0.60 \pm 0.08) \times 10^{-1}$	$(2.70 \pm 1.16 \pm 0.43 \pm 0.07) \times 10^{-1}$	$(2.29 \pm 1.07 \pm 0.48 \pm 0.06) \times 10^{-1}$	$(2.82 \pm 1.19 \pm 0.56 \pm 0.07) \times 10^{-1}$
60–80	$(1.69 \pm 0.92 \pm 0.30 \pm 0.04) \times 10^{-1}$	$(2.07 \pm 1.02 \pm 0.31 \pm 0.05) \times 10^{-1}$	$(2.31 \pm 1.07 \pm 0.33 \pm 0.06) \times 10^{-1}$	$(2.03 \pm 1.01 \pm 0.31 \pm 0.05) \times 10^{-1}$
80–100	$(1.27 \pm 0.80 \pm 0.23 \pm 0.03) \times 10^{-1}$	$(1.02 \pm 0.71 \pm 0.17 \pm 0.03) \times 10^{-1}$	$(1.30 \pm 0.81 \pm 0.25 \pm 0.03) \times 10^{-1}$	$(1.25 \pm 0.79 \pm 0.21 \pm 0.03) \times 10^{-1}$
100–120	$(8.1 \pm 6.4 \pm 2.2 \pm 0.2) \times 10^{-2}$	$(2.76 \pm 3.72 \pm 1.55 \pm 0.07) \times 10^{-2}$	$(5.0 \pm 5.0 \pm 1.4 \pm 0.1) \times 10^{-2}$	$(7.8 \pm 6.3 \pm 1.4 \pm 0.2) \times 10^{-2}$
120–140	$(5.8 \pm 5.4 \pm 0.9 \pm 0.1) \times 10^{-2}$	$(6.2 \pm 5.6 \pm 0.8 \pm 0.2) \times 10^{-2}$	$(3.12 \pm 3.95 \pm 1.13 \pm 0.08) \times 10^{-2}$	$(4.1 \pm 4.5 \pm 1.2 \pm 0.1) \times 10^{-2}$
140–200	$(1.07 \pm 1.34 \pm 0.58 \pm 0.03) \times 10^{-2}$	$(1.09 \pm 1.35 \pm 0.62 \pm 0.03) \times 10^{-2}$	$(2.73 \pm 2.13 \pm 0.56 \pm 0.07) \times 10^{-2}$	$(1.46 \pm 1.56 \pm 0.53 \pm 0.04) \times 10^{-2}$
200–300	$(3.66 \pm 6.05 \pm 1.58 \pm 0.10) \times 10^{-3}$	$(9.0 \pm 9.5 \pm 1.7 \pm 0.2) \times 10^{-3}$	$(7.4 \pm 8.6 \pm 1.7 \pm 0.2) \times 10^{-3}$	$(5.8 \pm 7.6 \pm 1.8 \pm 0.2) \times 10^{-3}$

Table 7.2: Differential WZ cross section as a function of the jet multiplicity at $\sqrt{s} = 8$ TeV for the four leptonic final states. Notations are as in Table 9.4.

N_{jets}	$d\sigma/dN_{\text{jets}}$ [pb]			
	eee	$ee\mu$	$\mu\mu e$	$\mu\mu\mu$
0 jets	$16.60 \pm 4.07 \pm 1.04 \pm 0.43$	$15.68 \pm 3.96 \pm 1.03 \pm 0.41$	$14.97 \pm 3.87 \pm 0.93 \pm 0.39$	$18.78 \pm 4.33 \pm 1.11 \pm 0.49$
1 jet	$6.06 \pm 2.46 \pm 0.48 \pm 0.16$	$4.80 \pm 2.19 \pm 0.57 \pm 0.12$	$5.32 \pm 2.31 \pm 0.61 \pm 0.14$	$4.84 \pm 2.20 \pm 0.72 \pm 0.13$
2 jets	$2.43 \pm 1.56 \pm 0.34 \pm 0.06$	$1.75 \pm 1.32 \pm 0.32 \pm 0.05$	$2.93 \pm 1.71 \pm 0.26 \pm 0.08$	$1.54 \pm 1.24 \pm 0.32 \pm 0.04$
3 jets	$(7.8 \pm 27.9 \pm 7.3 \pm 0.2) \times 10^{-2}$	$0.45 \pm 0.67 \pm 0.17 \pm 0.01$	$0.42 \pm 0.65 \pm 0.21 \pm 0.01$	$0.79 \pm 0.89 \pm 0.26 \pm 0.02$

Table 7.3: Differential WZ cross section as a function of the leading jet transverse momentum at $\sqrt{s} = 8$ TeV for the four leptonic final states. Notations are as in Table 9.4.

$p_T^{\text{leading jet}}$ [GeV]	$d\sigma/dp_T^{\text{leading jet}}$ [pb/GeV]			
	eee	$ee\mu$	$\mu\mu e$	$\mu\mu\mu$
30–60	$(1.22 \pm 0.64 \pm 0.34 \pm 0.03) \times 10^{-1}$	$(1.11 \pm 0.61 \pm 0.20 \pm 0.03) \times 10^{-1}$	$(1.10 \pm 0.61 \pm 0.24 \pm 0.03) \times 10^{-1}$	$(1.02 \pm 0.58 \pm 0.24 \pm 0.03) \times 10^{-1}$
60–100	$(5.4 \pm 3.7 \pm 1.7 \pm 0.1) \times 10^{-2}$	$(4.3 \pm 3.3 \pm 2.1 \pm 0.1) \times 10^{-2}$	$(6.5 \pm 4.0 \pm 2.0 \pm 0.2) \times 10^{-2}$	$(6.3 \pm 4.0 \pm 2.3 \pm 0.2) \times 10^{-2}$
100–150	$(2.96 \pm 2.43 \pm 1.57 \pm 0.08) \times 10^{-2}$	$(3.26 \pm 2.55 \pm 1.40 \pm 0.08) \times 10^{-2}$	$(3.9 \pm 2.8 \pm 1.2 \pm 0.1) \times 10^{-2}$	$(2.44 \pm 2.21 \pm 1.32 \pm 0.06) \times 10^{-2}$
150–250	$(1.18 \pm 1.09 \pm 0.29 \pm 0.03) \times 10^{-2}$	$(8.1 \pm 9.0 \pm 3.4 \pm 0.2) \times 10^{-3}$	$(1.07 \pm 1.03 \pm 0.61 \pm 0.03) \times 10^{-2}$	$(1.00 \pm 1.00 \pm 0.42 \pm 0.03) \times 10^{-2}$

Table 7.4: Combined result for the differential WZ cross sections at $\sqrt{s} = 8$ TeV.

p_T^Z [GeV]	$d\sigma/dp_T^Z$ [pb/GeV]
0–20	$[1.48 \pm 0.40(\text{stat.}) \pm 0.17(\text{syst.}) \pm 0.04(\text{lumi.})]\times 10^{-1}$
20–40	$[3.47 \pm 0.60(\text{stat.}) \pm 0.50(\text{syst.}) \pm 0.09(\text{lumi.})]\times 10^{-1}$
40–60	$[2.56 \pm 0.54(\text{stat.}) \pm 0.49(\text{syst.}) \pm 0.07(\text{lumi.})]\times 10^{-1}$
60–80	$[2.10 \pm 0.47(\text{stat.}) \pm 0.30(\text{syst.}) \pm 0.05(\text{lumi.})]\times 10^{-1}$
80–100	$[1.20 \pm 0.37(\text{stat.}) \pm 0.21(\text{syst.}) \pm 0.03(\text{lumi.})]\times 10^{-1}$
100–120	$[4.9 \pm 2.3\ (\text{stat.}) \pm 1.5\ (\text{syst.}) \pm 0.1\ (\text{lumi.})]\times 10^{-2}$
120–140	$[5.0 \pm 2.2\ (\text{stat.}) \pm 1.0\ (\text{syst.}) \pm 0.1\ (\text{lumi.})]\times 10^{-2}$
140–200	$[1.34 \pm 0.73(\text{stat.}) \pm 0.57(\text{syst.}) \pm 0.03(\text{lumi.})]\times 10^{-2}$
200–300	$[4.9 \pm 3.6\ (\text{stat.}) \pm 1.6\ (\text{syst.}) \pm 0.1\ (\text{lumi.})]\times 10^{-3}$

N_{jets}	$d\sigma/dN_{\text{jets}}$ [pb]
0 jets	$16.15 \pm 1.95\ (\text{stat.}) \pm 0.88\ (\text{syst.}) \pm 0.42\ (\text{lumi.})$
1 jet	$5.27 \pm 1.11\ (\text{stat.}) \pm 0.52\ (\text{syst.}) \pm 0.14\ (\text{lumi.})$
2 jets	$2.11 \pm 0.69\ (\text{stat.}) \pm 0.27\ (\text{syst.}) \pm 0.05\ (\text{lumi.})$
3 jets	$0.196 \pm 0.227(\text{stat.}) \pm 0.102(\text{syst.}) \pm 0.005(\text{lumi.})$

$p_T^{\text{leading jet}}$ [GeV]	$d\sigma/dp_T^{\text{leading jet}}$ [pb/GeV]
30–60	$[1.12 \pm 0.30(\text{stat.}) \pm 0.23(\text{syst.}) \pm 0.03(\text{lumi.})]\times 10^{-1}$
60–100	$[5.5 \pm 1.8\ (\text{stat.}) \pm 1.9\ (\text{syst.}) \pm 0.1\ (\text{lumi.})]\times 10^{-2}$
100–150	$[3.06 \pm 1.20(\text{stat.}) \pm 1.37(\text{syst.}) \pm 0.08(\text{lumi.})]\times 10^{-2}$
150–250	$[1.04 \pm 0.48(\text{stat.}) \pm 0.41(\text{syst.}) \pm 0.03(\text{lumi.})]\times 10^{-2}$

Chapter 8

Conclusion

The inclusive cross section of WZ production and differential cross sections have been measured at a center of mass energy of 8 TeV. The measurements are based on data collected in proton-proton collisions with the CMS detector. The total amount of data corresponds to an integrated luminosity of 19.6 pb^{-1}. Measured cross section for $71 < M_Z < 111$ GeV is:

$$\sigma(\mathrm{pp} \to \mathrm{WZ}) = 24.09 \pm 0.87(\mathrm{stat.}) \pm 1.62(\mathrm{syst.}) \pm 0.63(\mathrm{lumi.})\ \mathrm{pb} \tag{8.1}$$

The differential cross section is measured as a function of three variables: Z transverse momentum, number of jets and leading jet transverse momentum. The measured results agree with theoretical predictions within uncertainties. All measurements of the WZ cross section performed at LHC at $\sqrt{s}$=7, 8 and 13 TeV are shown in Figure 8.1 together woth NLO and NNLO predictions. It can be seen that the NNLO prediction is in a slightly better agreement with the data than the NLO prediction.

This channel was used in search for aTGC [64] and no evidence of deviations from the SM has been observed.

This measurement is part of a large program to test the validity of the SM at TeV scale (Figures 8.2 and 8.3). It can be seen for this and other VV measurements that the SM still holds at the TeV scale. Nevertheless it is interesing to note that several charged VV channels are slightly above the NLO predction. The 13 TeV results published in the mean time do not exhibit this feature, but it will be interesting to follow up new results with more data.

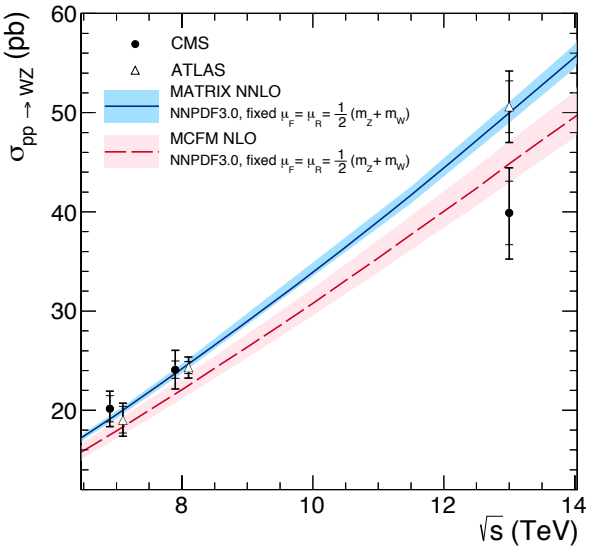

Figure 8.1: The WZ total cross section as a function of the proton-proton centre-of-mass energy. Results from the CMS and ATLAS experiments are compared to the predictions of MCFM and MATRIX. The data uncertainties are statistical (inner bars) and statistical plus systematic added in quadrature (outer bars). The band around the theoretical predictions reflects uncertainties generated by varying the factorization and renormalization scales up and down by a factor of two and also the (PDF+α_S) uncertainty of NNPDF3.0 for NLO predictions. The theoretical predictions and the CMS 13 TeV cross section are calculated for the Z boson mass window [60,120] GeV. The CMS 7 and 8 TeV cross sections presented in this paper are calculated for the Z boson mass window [71,111] GeV (estimated correction factor 2%), while all ATLAS measurements are performed with the Z boson mass window [66,116] GeV (1%) [64].

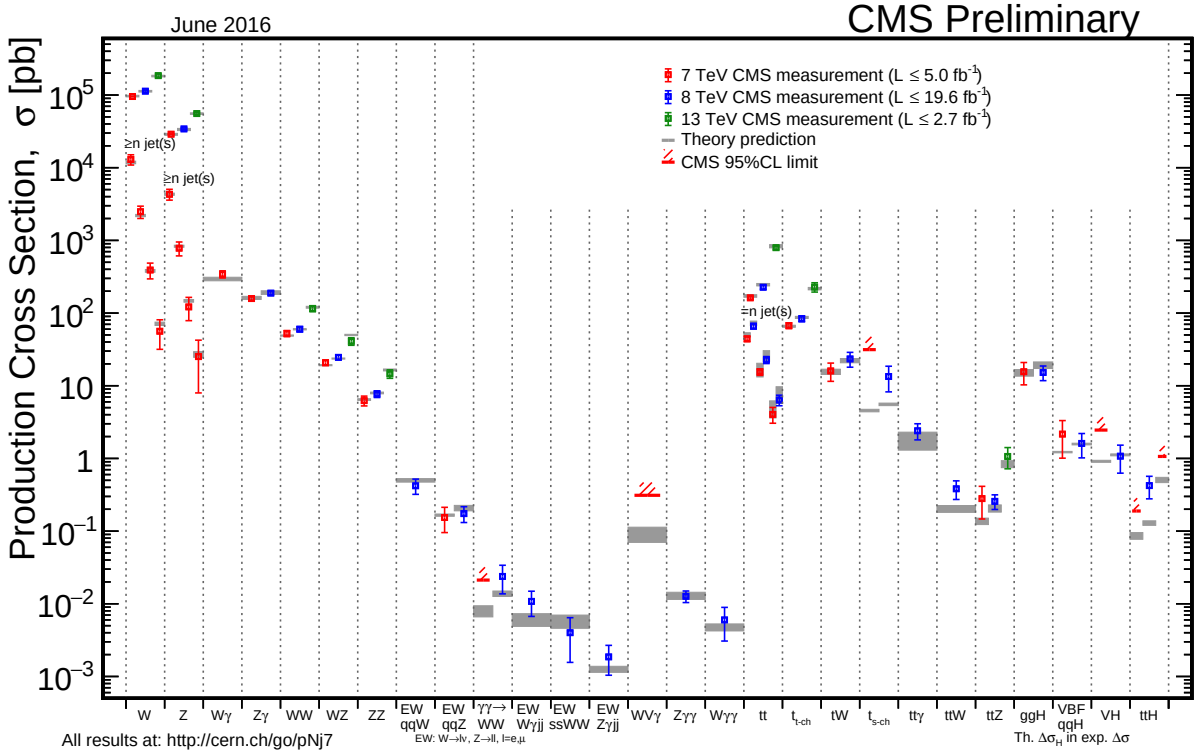

Figure 8.2: Measurements of SM process cross sections by the CMS epxeriment compared to theoretical predictions [65].

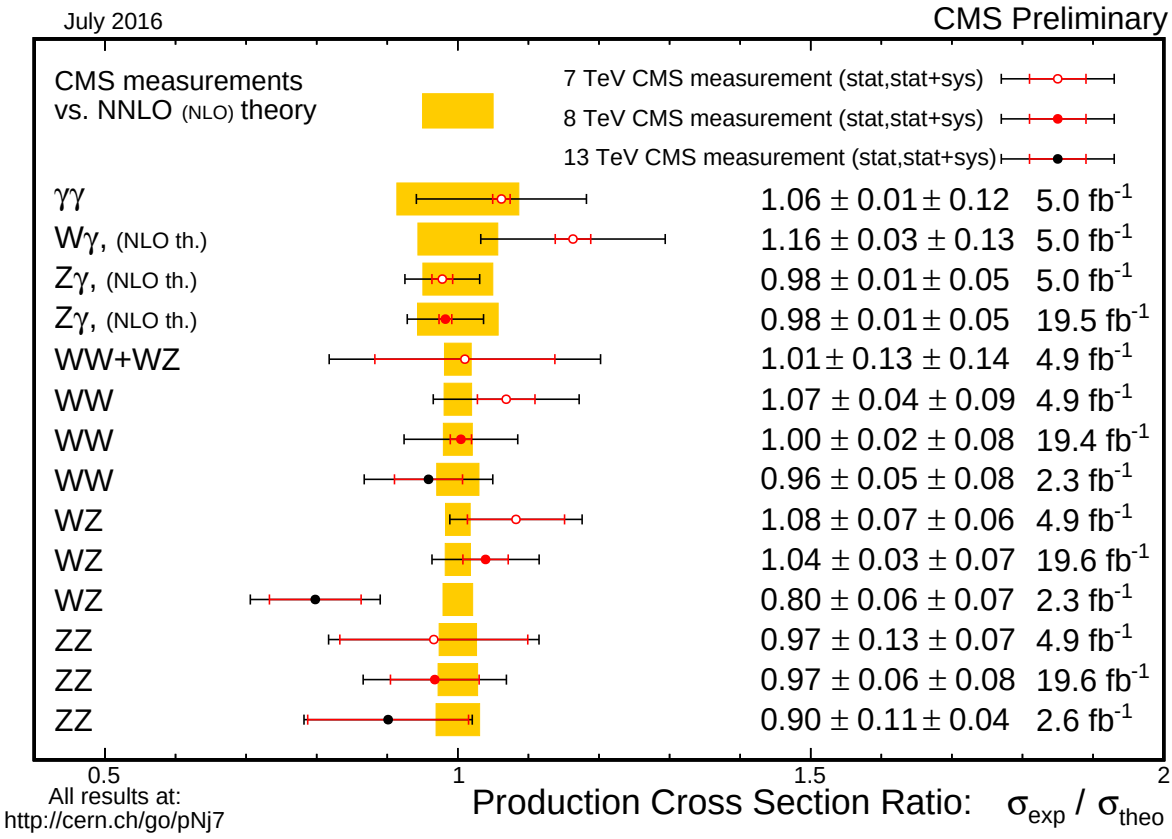

Figure 8.3: Ratios of measured to theoretical cross sections for diboson processes. Theory predictions updated to the latest NNLO calculations where available [65].

Chapter 9

Prošireni sažetak - Proučavanje zajedničke tvorbe bozona W i Z detektorom CMS u sudarima protona i protona na Velikom Hadronskom Sudarivaču

9.1 Uvod

Mjerenje produkcije parova elektroslabih teških bozona (dvobozonska produkcija) u sudarima protona predstavlja važan test Standardnog modela u opisu elektroslabih i jakih interakcija na TeV skali. Dvobozonska produkcija je osjetljiva na interakcije među baždarnim bozonima koji su predviđeni $SU(2)_L \times U(1)_Y$ baždarnom strukturom elektroslabih interakcija. Trostruka i četverosturka baždarna vezanja (TGC i QGC) mogu biti pod utjecajem nove fizike na višoj energiji.

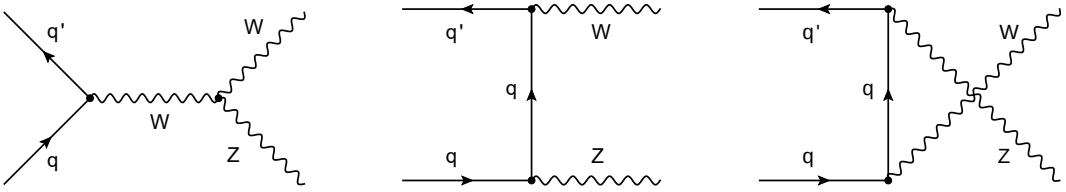

Figure 9.1: Feynmanovi dijagrami za WZ produkciju u prvom redu računa smetnje. Tri dijagrama predstavljaju doprinos (lijevo) *s*-kanala kroz TGC, (sredina) *t*-kanala, i (desno) *u*-kanala.

U ovom radu je predstavljeno mjerenje WZ produkcije u sudarima protona, napravljeno na podacima prikupljenim CMS detektorom na CERN LHC-u u 2012. godini, koje odgovara integriranom luminozitetu od 19.6 fb^{-1} prikupljenom na $\sqrt{s} = 8$ TeV. U mjerenju se koriste samo leptonska stanja u koja se raspadaju W i Z. U vodećem redu računa smetnje u SM, WZ produkcija u proton-proton sudarima događa se kroz interakcije kvarka i antikvarka u *s*-, *t*- and

u- kanalima, kao što je prikazano na Feynmanovim dijagramima na slici 9.1. Među njima, samo *s*- kanal ima TGC vrh. WZ produkcija na hadronskim sudarivačima do sada je opažena i na Tevatronu [22, 23] i na LHC-u [22, 23]

Mjerenje inkluzivnog udarnog presjeka za WZ produkciju ograničeno je na fazni prostor u kojem invarijantna masa dva leptona iz raspada Z bozona leži unutar intervala od 20 GeV oko nominalne mase Z bozona. Zahvaljujući većem integriranom luminozitetu koji je prikupljen na 8 TeV, izmjeren je i diferencijalni udarni presjek kao funkcija transverzalnog impulsa Z bozona, broja mlazova produciranih zajedno sa WZ parom i transverzalnog impulsa vodećeg mlaza. Mjerenja koja uključuju mlazove su osobito korisna za istraživanje doprinosa QCD procesa višeg reda udarnom presjeku.

9.2 Detektor CMS

Glavno svojstvo CMS detektora je supravodljivi solenoid unutarnjeg promjera 6 m koji stvara magnetsko polje od 3.8 T. Unutar solenoida nalaze se silicijski pixel i strip detektor (tragač), elektromagnetski kalorimetar (ECAL) i hadronski kalorimetar (HCAL), od kojih se svaki sastoji od središnjeg dijela i dva rubna dijela. Mioni se mjere u plinskim ionizacijskim detektorima koji koriste tri tehnologije: driftne cijevi, katodne strip komore i mionski spektrometar. Silikonski tragač mjeri nabijene čestice unutar pseudorapiditeta $|\eta|< 2.50$. ECAL pokriva $|\eta|< 1.48$ u središnjoj regiji i $1.48 < |\eta|< 3.00$ u dvjema rubnim regijama. Mioni se mjere u regiji do $|\eta|< 2.40$.

9.3 Simulirani uzorci

Nekoliko Monte Carlo (MC) generatora je korišteno da bi se simuliralo signalne i pozadinske procese. $t\bar{t}$, tW, and $q\bar{q} \rightarrow$ZZ procesi su generirani u drugom redu računa smetnje (NLO) sa paketom POWHEG 2.0 [47]. $gg \rightarrow$ZZ proces je simuliran u prvom redu sa GG2ZZ [66]. WZ signal i ostali pozadinski procesi su generirani u LO (vodećem redu računa smetnje) sa MADGRAPH 5.1 paketom[45]. Ostali pozadinski procesi uključuju Z+jets, $W\gamma^*$, $Z\gamma$ kao i procese sa barem tri bozona: WZZ, ZZZ, WWZ, WWW,$t\bar{t}$W, $t\bar{t}$Z, $t\bar{t}$WW, $t\bar{t}\gamma$ and WWγ, koje u daljnjem tekstu označavamo sa VVV. Dio $W\gamma^*$ uzorka u faznom prostoru sa $m_{\gamma*} > 12$ GeV je uključen u signalni uzorak.

Kako bi se opisali partonski pljuskovi i hadronizacija korišten je programski paket PYTHIA [41]. Za LO generatore, korišten je CTEQ6L1 [51] set paronskih distribucijskih funkcija a CT10 [67] je korišten za NLO (red do vodećeg) događaje. Za sve procese, odgovor detektora je simuliran sa GEANT paketom [29]. Rekonstrukcija događaja se radi pomoću istih algoritama koji su korišteni za podatke. Simulirani događaji sadrže dodatne interakcije u sudaru (pileup),

pa im je pridana težina kako bi pileup distribucija u simulaciji odgovarala onoj opaženoj u podacima.

9.4 Rekonstrukcija događaja i identifikacija objekata

Mjerenje WZ$\rightarrow 3l\nu$ raspada se oslanja na učinkovitu identifikaciju elektrona i miona i precizna mjerenja nedostajuceg transverzalnog impulsa. Zahtjevi za odabir leptona koji se koriste u ovom mjerenju su jednaki kao u mjerenju Higgsovog bozona H$\rightarrow$ WW $\rightarrow 2l2\nu$ [68]. Kinematička svojstva leptona u konačnom stanju u ta dva procesa su vrlo slična, a oba mjerenja imaju slične izvore leptonske pozadine. Pragovi transverzalnih impulsa na leptone u okidaču su 17 i 8 GeV. Elektroni su rekonstruirani kombiniranjem podataka iz elektromagnetskog kalorimetra i tragača [38]. Njihova identifikacija se oslanja na multivarijantnu analizu koja kombinira opservable osjetljive na količinu zakočnog zračenja duž elektronske putanje, geometrijsko podudaranje između elektronskih putanja u tragaču i energetskih depozita u kalorimetru i podudaranje impulsa u ta dva detektora, kao i oblik pljuska. Mioni su rekonstruirani pomoću informacija iz tragača i mionskog spektrometra [34]. Moraju zadovoljiti zatjev na broj mjerenja u slojevima tragača i u mionskom spektrometaru, i na kvalitetu prilagodbe traga. Za sve leptonske kandidate se traži da su u skladu sa primarnim verteksom, koji je izabran kao vrh s najvećim $\sum p_T^2$ povezanih tragova. I za elektrone i mione zahtjeva se $p_T > 20$ GeV. Elektroni (mioni) moraju zadovoljiti $|\eta| < 2.5$ (2.4).

Nabijeni leptoni iz raspada W i Z bozona su uglavnom izolirani od ostalih čestica u konačnom stanju. Zbog toga se za odabrane leptone zahtjeva da su izolirani od ostale aktivnosti u događaju, kako bi se smanjila pozadina od hadrona koju su krivo identificirani kao leptoni ili od leptona koji koji su producirani u raspadima hadrona koji se događaju unutar ili u blizini hadronskog mlaza. Udaljenost između dva rekonstruirana objekta u detektoru se mjeri pomoću varijable $\Delta R = \sqrt{(\Delta\eta)^2 + (\Delta\phi)^2}$, gdje je ϕ azimutalni kut. Kako bi izmjerili leptonsku izolaciju, promatramo konus veličine $\Delta R = 0.3$ u vrhu događaja oko traga leptonskog kandidata. Izolacijska varijabla se gradi kao skalarna suma transverzalnih impulsa svih PF objekata koji su konzistentni sa odabranim primarnim vrhom i nalaze se unutar konusa. Doprinos leptonskog kandidata koji promatramo se isključuje. Kako bi se uzeo u obzir doprinos izolaciji zbog pileupa i za elektrone i za mione se primjenjuje korekcija. U slučaju elektrona, prosječna energetska gustoća u izolacijskom konusu zbog pileupa je određena u svakom događaju posebno i koristi se kako bi se ispravila izolacijska varijabla [69]. Za mione, doprinos izolaciji od pileupa neutralnih četica se određuje korištenjem nabijenih čestica povezanih sa pileup interakcijama. Za tu izolacijsku varijablu se zahtjeva da bude manja od otprilike 10% transverzalnog impulsa leptonskog kandidata. Točna vrijednost praga ovisi okusu leptona i dijelu detektora. Za mione

se koristi malo drugačija strategija koja uzima veći pileup i kako bi se smanjila ovisnost te varijable o pileup interakcijama. Koristi se multivarijantni algoritam koji se bazira na sumi transverzalnih impulsa čestica oko leptoskog kandidata za konuse različitih ΔR veličina [37]. Leptonske rekonstrukcijske i selekcijske efikasnosti su izmjerene korištenjem $Z \rightarrow ll$ događaja [70]. Simulirani uzorci su korigirani za razliku u efikasnosti između podataka i simulacije. Ukupna nesigurnost na leptonske efikasnosti, uključujući i efekte okidača i selekcije iznosi oko 2% po leptonu. Leptonski selekcijski kriteriji su odabrani kako bi se zadržala stabilna efikasnost kroz cijeli uzorak podataka. Mlazovi hadrona su rekonstruirani od particle-flow objekata korištenjem anti-k_t algoritma za grupiranje [71, 72] sa iznosom parametra R =0.5.

PF (*Particle-Flow*) algoritam [36, 73] rekonstruira i identificira svaku individualnu česticu sa optimiziranom kombnacijom informacija iz različitih dijelova CMS detektora. Energija fotona se dobiva iz ECAL mjerenja. Energija elektrona se određuje iz kombinacije elektronskog impulsa u primarnom interakcijskom vrhu koji se određuje pomoću tragača, energije pripadajućeg ECAL klastera i sume energije svih izračenih fotona koji su prostorno kompatibilni sa elektronskim tragom. Energija miona se određuje iz zakrivljenosti pripadajućeg traga. Energija nabijenih hadrona se određuje iz kombinacije njihovih impulsa mjerenih u tragaču i pripadajućih ECAL i HCAL energetskih depozita, korigiranih za funkciju odgovora kalorimetara na hadronske pljuskove. Konačno, energija neutralnih hadrona se dobiva iz pripadajućih korigiranih HCAL i ECAL energija. Impuls mlaza se određuje kao vektorska suma svih impulsa čestica u mlazu. Na energije mlaza se primjenjuje korekcija koja uzima u obzir doprinos pileupa. Korekcije za energiju mlaza se dobivaju iz simulacija i potvrđena su mjerenjima ravnoteže energija u događajima sa dva mlaza i fotonom i mlazom [74]. Energijska rezolucija iznosi tipično 15% na 10 GeV, 8% na 100 GeV, i 4% na 1 TeV. Dodatni selekcijski kriteriji su primjenjeni na svaki događaj kako bi se ukolonile pojave slične mlazovima koje potječu od izoliranog šuma u pojedinim dijelovima HCAL-a.

Vektor nedostajućeg transverzalnog momenta $\vec{p_T^{miss}}$ je definiran kao negativna vektorska suma transverzalnih impulsa svih rekonstruiranih čestica u događaju. Vrijednost tog vektora je nedostajuća transverzalna enetgija E_T^{miss}.

9.5 Selekcija događaja i procjena pozadine

Selektiramo WZ$\rightarrow 3l\nu$ raspade gdje se W raspada na lepton i neutrino, a Z na dva leptona (elektrona ili miona). Te raspade karakterizira par izoliranih leptona istog okusa, sa invarijantnom masom koja odgovara masi Z bozona, zajedno sa trećim izoliranim leptonom i značajnom količinom nedostajuće transverzalne energije E_T^{miss} koja je povezana sa neutrinom koji nije detektiran. S obzirom na okus leptona razlikujemo četiri konačna stanja: eee, $ee\mu$, $e\mu\mu$, $\mu\mu\mu$. Oni se tretiraju neovisno za mjerenje udarnog presjeka i kombinirani su samo na razini kon-

ačnih rezultata.

Okidač zahtijeva prisutnost dva elektrona, dva miona ili elektron i mion. Izmjerena efikasnost okidača za događaje koji izgledaju kao signal je veća od 99%. Zahtijevaju se točno tri leptona koji zadovoljavaju sve selekcijske uvjete i čija je invarijantna masa veća od 100 GeV. Kandidati za Z bozon se grade od dva suprotno nabijena, izolirana leptona istog okusa. Za vodeći lepton se zahtijeva $p_T > 20$ GeV. Masa kandidata za Z bozon treba biti u intervalu od 20 GeV od nominalne mase Z bozona: 71<m_{ll}<111 GeV. Ako je nađeno više od jednog para koji odgovara, izabire se onaj par čija je invarijantna masa najbliže nominalnoj masi Z bozona. Preostali lepoton se pridružuje W bozonu i zahtijeva se da ima $p_T > 20$ GeV i da je udaljen od oba leptona iz Z raspada za $\Delta R > 0.1$. Konačno, kako bi se uzelo u obzir neutrino koji se ne može izmjeriti u detektoru, zahtijeva se da je E_T^{miss} veća od 30 GeV. Izvori pozadina sa tri rekonstruirana leptona uključuju događaje sa pravim leptonima produciranim u primarnom vrhu ili leptonima iz pomaknutih vrhova, kao i mlazove.

Doprinos od pozadina sa leptonima koji nisu pravi, dominiran je sa $t\bar{t}$ and Z+jets događajima u kojima je jedan od tri rekonstruirana leptona krivo identificiran, i procijenjuje se korištenjem procedure kao u referenci [50]. Metoda koristi razliku između slabe i jake leptonske selekcije. Jaka selekcija je identična konačnoj selekciji, dok su neki zahtijevi korišteni u konačnoj selekciji umanjeni u slaboj selekciji. Procedura počinje sa slabim uzorkom, sa tri leptona koji prolaze slabu selekciju i zadovoljavaju sve ostale zahtijeve WZ selekcije. Taj uzorak ima doprinose od događaja sa 3 prava (p) leptona, dva prava i jednog lažnog (n) leptona, jednog pravog i dva lažna i tri lažna leptona. Pravim leptonima nazivamo leptone koje dolaze iz raspada W ili Z bozona, dok lažnim leptonima nazivamo čestice krivo identificirane kao leptoni ili leptone iz mlazova. Broj događaja u slabom uzorku je N_{FFF} i možemo ga izraziti kao:

$$N_{FFF} = n_{ppp} + n_{ppn} + n_{pnp} + n_{npp} + n_{nnp} + n_{npn} + n_{pnn} + n_{nnn}. \tag{9.1}$$

U tom izrazu, prvi, drugi i treći indeks se odnose na vodeći i drugi lepton i raspada Z bozona, i na lepton iz raspada W bozona. Uzorak sa slabom selekcijom može se podijeliti u poduzorke ovisno o tome da li svaki od tri leptona prolazi jaku selekciju. Broj događaja u svakom poduzorku je označen sa N_{ijk} gdje su $i, j, k = T, F$, T i F označuju leptone koji prolaze tj. ne prolaze jaku selekciju. Broj leptona u svakom od tih poduzoraka može biti izražen kao linearna kombinacija nepoznatih brojeva u uzorku. $n_{\alpha\beta\gamma}$ $(\alpha, \beta, \gamma = p, n)$,

$$N_{ijk} = \sum_{\alpha,\beta,\gamma=p,n} C^{ijk}_{\alpha\beta\gamma} n_{\alpha\beta\gamma}, \quad i, j, k = T, F, \tag{9.2}$$

gdje koeficijenti $C^{ijk}_{\alpha\beta\gamma}$ ovise o efikasnostima ε_p i ε_n, koje su vjerojatnosti da pravi(lažni) leponi prođu jaku selekciju, ako su već prošli slabu selekciju. Na primjer, u jednadžbi (9.1) broj

događaja sa sva tri leptona koji prolaze jaku selekciju N_{TTT} se može napisati kao:

$$N_{TTT} = n_{ppp}\varepsilon_{p_1}\varepsilon_{p_2}\varepsilon_{p_3} + n_{ppn}\varepsilon_{p_1}\varepsilon_{p_2}\varepsilon_{n_3} + n_{pnp}\varepsilon_{p_1}\varepsilon_{n_2}\varepsilon_{p_3} + n_{npp}\varepsilon_{n_1}\varepsilon_{p_2}\varepsilon_{p_3} + n_{nnp}\varepsilon_{n_1}\varepsilon_{n_2}\varepsilon_{p_3} + n_{npn}\varepsilon_{n_1}\varepsilon_{p_2}\varepsilon_{n_3} + n_{pnn}\varepsilon_{p_1}\varepsilon_{n_2}\varepsilon_{n_3} + n_{nnn}\varepsilon_{n_1}\varepsilon_{n_2}\varepsilon_{n_3}. \quad (9.3)$$

Cilj je odrediti broj događaja sa tri prava leptona u TTT uzorku, koji odgovaraju selekciji koja je korištena u mjerenju. Taj broj je: $n_{ppp}\varepsilon_{p_1}\varepsilon_{p_2}\varepsilon_{p_3}$. Broj događaja s tri prava leptona u slabom uzorku, n_{ppp}, dobiva se rješavanjem sustava linearnih jednadžbi.

Neovisni uzorci su korišteni da se izmjere efikasnosti ε_p i ε_f [50]. Efikasnost za prave leptone ε_p se dobiva iz $Z \to ll$ uzorka, dok su efikasnosti za lažne leptone ε_f izmjerene korištenjem QCD uzorka sa više mlazova. Obje efikasnosti su izmjerene u nekoliko p_T i η binova. Izmjerene efikasnosti ε_f su u rasponu od 1-10 % za elektrone i 7-20 % za mione. Izmjerene efikasnosti ε_p su između 60 i 95 % za elektrone i 71 i 99 % za mione. Brojevi događaja sa lažnim leptonima u svakom konačnom stanju dobiveni ovom metodom prikazani su u Tablici 9.1. Iako ti rezultati uključuju doprinos događaja sa bilo kojim brojem krivo identificiranih leptona, simulacije pokazuju da je doprinos od pozadina sa dva ili tri krivo identificirana leptona kao W+mlaz i QCD procesa sa nekoliko mlazova, zanemariva i da je pozadina lažnih leptona dominirana sa $t\bar{t}$ and Z+jets procesima.

Ostatak pozadine se sastoji od događaja sa 3 prava leptona, kao što je $ZZ \to 4l$ proces u kojemu jedan od četiri leptona u konačnom stanju nije dobro identifician, kao i procesi sa tri ili više teških bozona u konačnom stanju (VVV) i $W\gamma^*$ i $\gamma^* \to l^+l^-$. Te pozadine su procijenjene iz simulacija. Relevantni Wγ^* proces je definiran za niske mase γ^*; $m_{\gamma^*} < 10$ GeV, pa se ne preklapa sa Wγ^* procesom koji je uključen u simulaciju signala i simuliran je posebno. To se smatra pozadinim jer ne ulazi u fazni prostor u kojem se radi mjerenje. Takav Wγ^* proces može biti prihvaćen u selekciji samo ako se nabijeni lepton iz W raspada krivo interpretira lepton iz Z/γ^* raspada.

Doprinos $Z\gamma$ događaja u kojima je foton krivo identificiran kao lepton je također određen iz simulacije.

Doprinos WZ raspada u kojima se W ili Z bozon raspada na τ lepton se rakođer uzima u obzir. Takvi raspadi se smatraju pozadinom za signal. Njihov doprinos se oduzima korišetnjem frakcije selektiranih WZ raspada koja ima τ leptone u konačnom stanju. Ta frakcija se označava s f_τ, i određuje se iz simulacije za svako od četiri konačna stanja i leži između 6.5 i 7.6%. Ta pozadina se gotovo potpuno sastoji od WZ događaja sa $W \to \tau\nu$ raspadaima gdje se τ lepton zatim raspada na elektron ili mion.

Primjenom opisanih selekcijskih kriterija 1559 događaja se selektira iz uzorka koji odgovara 19.6 fb^{-1}. Brojevi događaja za svaki leptonski kanal zajedno sa očekivanjima od MC simu-

lacije i kontrolnih uzoraka podataka dani su u Tablici 9.1. Inkluzivna distribucija dileptinske invarijantne mase m_{ll} je prikazana na slici 9.2.

Table 9.1: Brojevi događaja koji su prošli selekciju za Monte Carlo i podatke

sample	**eee**	**eeμ**	**$\mu\mu$e**	**$\mu\mu\mu$**	total
Non-prompt leptons	18.4 ± 12.7	32.0 ± 21.0	54.4 ± 33.0	62.4 ± 37.7	167.1 ± 55.8
ZZ	2.1 ± 0.3	2.4 ± 0.4	3.2 ± 0.5	4.7 ± 0.7	12.3 ± 1.0
Zγ	3.4 ± 1.3	0.4 ± 0.4	5.2 ± 1.8	0	9.1 ± 2.2
Wγ^*	0	0	0	2.8 ± 1.0	2.8 ± 1.0
VVV	6.7 ± 2.2	8.7 ± 2.8	11.6 ± 3.8	14.8 ± 5.1	41.9 ± 7.3
Total background (N_{bkg})	30.6 ± 13.0	43.5 ± 21.2	74.4 ± 33.3	84.7 ± 38.1	233.2 ± 56.3
WZ	211.1 ± 1.6	262.1 ± 1.8	346.7 ± 2.1	447.8 ± 2.4	1267.7 ± 4.0
Total expected	241.6 ± 13.1	305.7 ± 21.3	421.0 ± 33.3	532.4 ± 38.2	1500.8 ± 56.5
Data (N_{obs})	258	298	435	568	1559

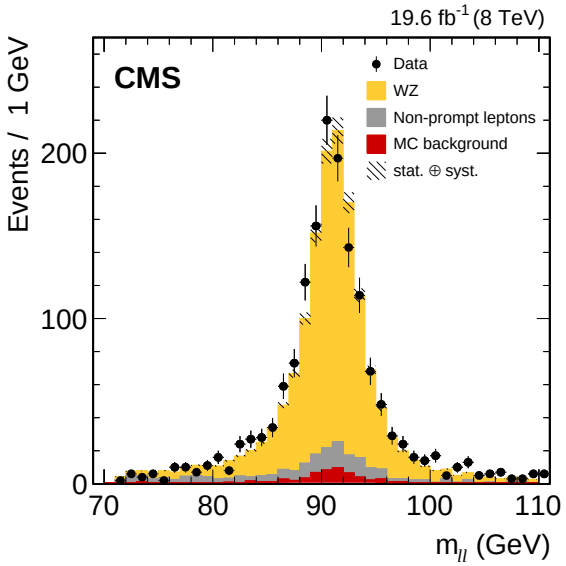

Figure 9.2: Distribucija dileptonske invarijantne mase za podatke i pozadinu.

9.6 Sistematske nesigurnosti

Sistematske nesigurnosti se mogu grupirati u nekoliko kategorija. Prva grupa uključuje nesigurnosti koje utječu na akceptancu i efikasnost, koja se označava sa $A \times \varepsilon$, i koja se određuje iz simulacije. Nesigurnosti na $A \times \varepsilon$ ovise teorijskim nesigurnostima u PDF-u. PDF nesigurnost se evaluira slijedeći proceduru u referenci [75] korištenjem CTEQ66 [51] PDF seta. Nesigurnost od normalizacijskih (μ_R) i faktorizacijskih (μ_F) skala se određuje variranjem obje skale neovisno u rasponu od $(0.5\mu_0, 2\mu_0)$ oko njihove nominalne vijednosti $\mu_0 = 0.5(M_Z + M_W)$ sa ograničenjem $0.5 < \mu_R/\mu_F < 2$. Na produkt $A \times \varepsilon$ također utječu eksperimentalne nesigurnosti u skali

mionskog impulsa, i skali elektronske energije, leptonskim rekonstrukcijskim i identifikacijskim efikasnostima, kalibracijskoj skali za E_T^{miss} i doprinosima pileupa. Efekt skale mionskog impulsa se određuje variranjem impulsa svakog miona u simuliranom signalnom uzorku untar nesigurnosti za skalu impusla koja je 0.2% [34]. Isto se radi za elektrone, variranjem energije rekonstruiranog elektrona unutar nesigurnosti za mjerenje energijske skale koja ovisi o p_T i η i tipično je ispod 1%. Produkt $A \times \varepsilon$ također ovisi o nesigurnostima u omjerima izmjerenih i simuliranih efikasnosti leptonskih okidača. Ti omjeri su korišteni u određivanju $A \times \varepsilon$ kako bi se uzela u obzir razlika u efikasnosti između podataka i simulacije. Oni su varirani unutar nesigurnosti koje ovise o leptonskom p_T i η i iznose oko 1%. Nesigurnost na kalibraciju E_T^{miss} je određena skaliranjem gore i dolje unutar nesigurnosti energije svih objekata koji su korišteni za određivanje E_T^{miss}. Konačno, na $A \times \varepsilon$ utječe nesigurnost na pileup doprinos. Simuliranim događajima je pridana težina kako bi odgovarali distribuciji pileup interakcija koja je određena korištenjem procedure koja ekstrahira pileup iz trenutnog luminoziteta i ukupnog inelastičnog udarnog presjeka za pp. Težine primjenjene na simulirane događaje su primjenjene variranjem tog udarnog presjeka za 5% [53].

Druga grupa su nesigurnosti na broj događaja pozadine. Nesigurnost na pozadinu od lažnih leptona [50] je određena variranjem praga za p_T vodećeg mlaza koji se koristi kako bi se selektirao kontrolni uzorak krivo identificiranih leptona, s obzirom da energija vodećeg mlaza određuje sastav uzorka. Nesigurnosti od drugih pozadinskih procesa su izračunate variranjem njihovih predviđenih udarnih presjeka unutar nesigurnosti. Udarni presjeci su varirani za 15%, za ZZ, za 15% za $Z\gamma$, za 50%, za VVV procese, i za 20% za $W\gamma^*$ temeljeno na nesigurnostima mjerenja tih procesa [54–58].

Konačno, nesigurnost na mjerenje integriranog luminoziteta je 2.6% [59]. Pregled svih nesigurnosti je dan u tablici 9.2.

9.6.1 Mjerenje inkluzivnog udarnog presjeka

Inkluzivni udarni presjek $\sigma(\text{pp} \to WZ + X)$ u $3l\nu$ konačnom stanju, povezan je sa brojem opaženih događaja u tom konačnom stanju N_{obs} preko slijedećeg izraza:

$$\sigma(\text{pp} \to \text{WZ+X})\,\mathscr{B}(W \to l\nu)\,\mathscr{B}(Z \to ll) = (1 - f_\tau)\,\frac{N_{obs} - N_{bkg}}{A \times \varepsilon\,\mathscr{L}}, \tag{9.4}$$

gdje su $\mathscr{B}(\text{W} \to ll\nu)$ i $\mathscr{B}(\text{Z} \to ll)$ faktori grananja za bozone W i Z, a f_τ uračunava očekivani omjer WZ$\to 3l\nu$ raspada u kojima je barem jedan τ raspad u konačnom stanju, nakon što se makne sva ostala pozadina. Broj očekivanih pozadinskih događaja je N_{bkg}, a broj događaja signala je određen oduzimanjem N_{bkg} od izmjerenog broja podataka N_{obs}. Produkt signalne efikasnosti ε i akceptance A se izračunava za svako od četiri konačna stanja korištenjem simuliranog WZ uzorka, tako da se izračuna omjer događaja koji prolaze cijelu selekciju i broja generi-

Table 9.2: Relativne nesigurnosti u postotcima.

Source	eee	$ee\mu$	$\mu\mu e$	$\mu\mu\mu$
Renorm. and fact. scales	3.0	3.0	3.0	3.0
PDFs	1.4	1.4	1.4	1.4
Pileup	0.2	0.4	0.3	0.2
Lepton and trigger efficiency	3.4	2.5	2.5	3.2
Muon momentum scale	—	0.5	0.8	1.3
Electron energy scale	1.4	0.8	0.8	—
E_T^{miss}	1.5	1.5	1.6	1.2
ZZ cross section	0.1	0.1	0.1	0.1
$Z\gamma$ cross section	0.2	0.0	0.2	0.0
$t\bar{t}$ and Z+jets	4.6	7.2	6.1	7.7
Other simulated backgrounds	1.0	1.1	1.1	1.0
Total systematic uncertainty	7.0	8.6	7.7	9.2
Statistical uncertainty	7.7	7.2	6.4	5.2
Integrated luminosity uncertainty	2.6	2.6	2.6	2.6

ranih WZ$\rightarrow 3l\nu$ događaja sa $71 < m_{ll} < 111$ GeV, gdje je m_{ll} dileptonska masa dva leptona iz raspada Z bozona prije radijacije fotona u konačnom stanju. Samo događaji koji se raspadaju u određeno konačno stanje se uzimaju u obzir u brojniku i nazivniku ovog omjera. Konačne vrijednosti udarnog presjeka dane su u tablici 9.3 za četiri leptonska kanala. Slaganje među četiri kanala je dobro. Četiri mjerenja su kombinirana korištenjem BLUE metode (Best linear

Table 9.3: Izmjereni WZ udarni presjek za četiri leptonska kanala.

Channel	σ(WZ) [pb]
eee	24.80 ± 1.92 (stat.) ± 1.74 (syst.) ± 0.64 (lumi.)
eeμ	22.38 ± 1.62 (stat.) ± 1.92 (syst.) ± 0.58 (lumi.)
$\mu\mu$e	23.94 ± 1.52 (stat.) ± 1.85 (syst.) ± 0.62 (lumi.)
$\mu\mu\mu$	24.93 ± 1.29 (stat.) ± 2.29 (syst.) ± 0.65 (lumi.)

unbiased estimator) [60].Pretpostavili smo punu korelaciju za sve nesigurnosti koje su zajedničke različitim kanalima. Kombiniranjem četiri leptonska kanala, ukupni WZ udarni presjek za $71 < m_Z < 111$ GeV, na 8 TeV, je:

$$\sigma(\text{pp} \rightarrow \text{WZ}) = 24.09 \pm 0.87 \text{ stat.} \pm 1.62 \text{ syst.} \pm 0.63 \text{ lumi. pb}$$

Ovi rezultati se mogu usporediti sa nedavnim NLO i NNLO računima u QCD-u pomoću Matrix paketa [62]. NLO (NNLO) predviđanje je $21.80^{+5.1\%}_{-3.9\%}$ ($23.68 \pm 1.8\%$) pb, gdje nesigurnosti uključuju samo varijacije skale. Sve predikcije su u skladu s izmjerenim vrijednostima unutar nesigurnosti. NLO predviđanja su malo niža od izmjerenih vrijednosi i bolje slaganje je opaženo za NNLO račun. Omjeri inkluzivnih udarnih presjeka do NLO i NNLO predviđanja su prikazani na slici 9.3.

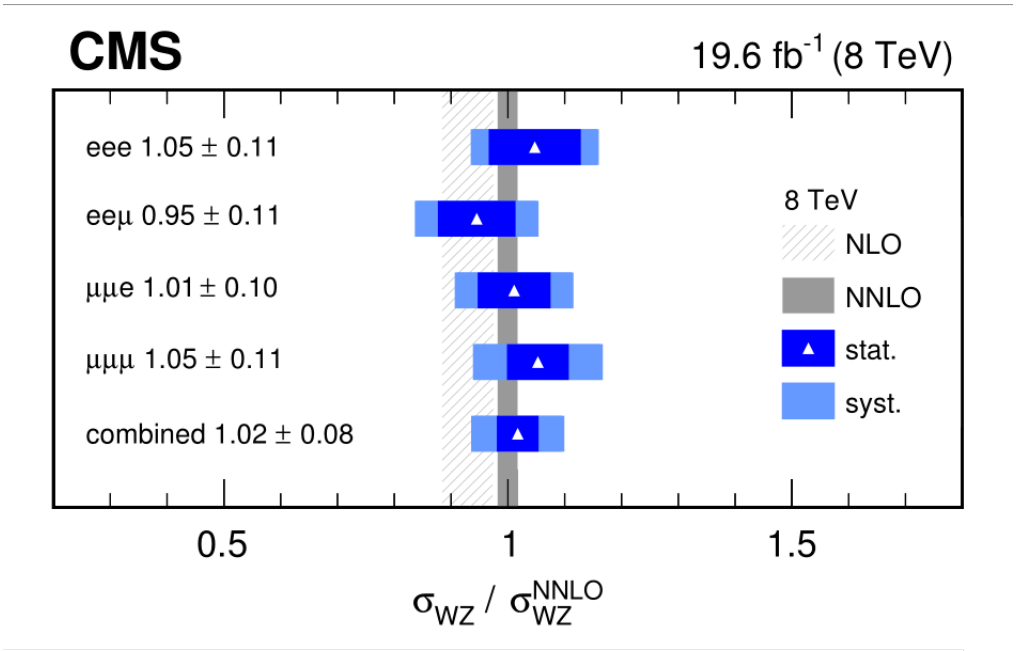

Figure 9.3: Omjer izmjerenog i teorijski predviđenog WZ udarnog presjeka

Ukupni produkcijski WZ udarni presjek za različite vrijednosti energija centra mase na CMS [76] i ALAS [77–79] detektoru su uspoređeni s teorijskim predviđanjima izračunatima sa MCFM(NLO) i Matrix(NNLO) prikazani su na slici 9.4. Teorijska predvđanja, unutar nesigurnosti opisuju energetsku ovisnost izmjerenog udarnog presjeka.

9.6.2 Mjerenje diferencijalnog udarnog presjeka

Izmjerili smo diferencijalni udarni presjek kao funkciju tri različite opservable: transverzalnog impulsa Z bozona, broja mlazova produciranih zajedno sa $3l\nu$ konačnim stanjem i transverzalnog impulsa vodećeg mlaza. Za zadnja dva mjerenja diferencijalni udarni presjeci su definirani za generirane mlazove sagrađene od svih stabilnih čestica korištenjem anti-k_T algoritma [80] sa parametrom udaljenosti 0.5, ali isključujući elektrone, mione i neutrine iz raspada W i Z bozona.

Za mlazove se zahtijeva da imaju $p_T > 30$ GeV i $|\eta| < 2.5$. Također, moraju biti odvojeni od nabijenih leptona iz raspada W i Z bozona za $\Delta R(\text{jet}, l) > 0.5$. Mlazovi konstruirani od PF kandidata, koji su okupljeni u mlazove korištenjem istog algoritma, moraju zadovoljavati iste zahtjeve. Kako bi se dobio udarni presjek u svakom binu, pozadinski doprinos je prvo oduzet od izmjerenog broja događaja u svakom binu posebno na isti način kao što je to napravljeno za inkluzivni udarni presjek. Izmjereni spektar signala se zatim korigira za detektorske efekte. To uključuje efikasnosti kao i migracije među binovima zbog konačne rezolucije. Oba efekta su tretirana korištenjem iterativne D'Agostinijeve tehnike za raspetljavanje (unfolding) [81] implementirane u ROOUNFOLD [82], sa 5 iteracija. Tehnika koristi matrice odgovora koje

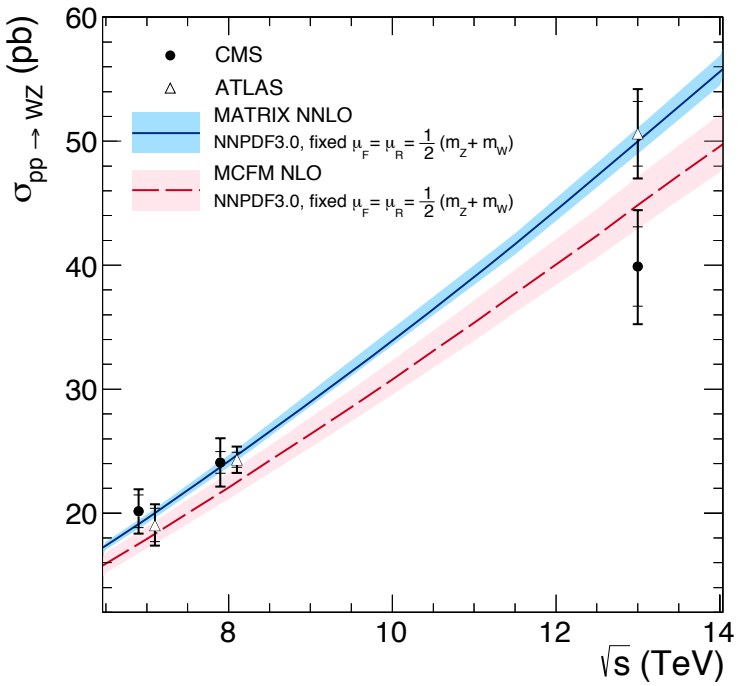

Figure 9.4: Ukupni WZ udarni presjek kao funkcija energije centra mase sudara protona. Rezultati s CMS i ATLAS eksperimenata su uspoređeni sa predviđanjima programskih paketa MCFM i Matrix. Nesigurnosti na podatke su statističke i statističke i sistematske zbrojene kvadratično. Nesigurnost na teorijsko predviđanje je nesigurnost koja se dobiva variranjem faktorizacijske i renormalizacijske skale gore i dolje za fakor dva i (PDF+α_S) nesigurnost NNPDF3.0 za NLO predviđanja. Teorijska predviđanja i CMS 13 TeV udarni presjek su izračunati za prozor Z mase [60,120] GeV. CMS 7 i 8 udarni presjeci su izra;unati u prozoru mase Z bozona [71,111] GeV, dok su ATLAS mjerenja napravljena u prozoru Z mase [66-116] GeV.

povezuju stvarnu distribuciju opservable sa izmjerenom distribucijom, nakon što se uključe efekti detektora. Matrice odgovora su napravljene korištenjem signalnog MC uzorka za svaki od četiri leptinska kanala posebno. Tako korigirani spektar je korišten da bi se dobio diferencijalni udarni presjek za sva četiri leptonska konačna stanja. Četiri kanala su kombinirana bin po bin. Nekoliko dodatnih izvora sistematskih nesigurnosti treba uzeti u obzir s obzirom na one opisane u poglavlju 9.6. Mjerenja koja uključuju mlazove imaju eksperimentalnu nesigurnost u skali energije mlaza i rezoluciji. Efekti na matricu odgovora su proučavani skaliranjem energija mlazova unutar nesigurnosti. Nesigurnost zbog konačne veličine simuliranog uzorka koji je korišten za stvaranje matrice odgovora je također uzeta u obzir. Procedura korigiranja za detektorske efekte unosi stastičke korelacije između binova koji su u rasponu od nekoliko posto do 40% u nekim slučajevima. Te korelacije su uzete u obzir zajedno sa koreliranim sistematskim nesigurnostim generaliziranom BLUE metodom koja je opisana u [61]. Diferencijalni udarni presjeci su dani u tablicama 9.4, 9.5, i 9.6 za svaki od četiri konačna stanja i kombinirani u tablici 9.7. Kombinirani diferencijalni udarni presjeci su prikazani na slikama 9.5 i 9.6.

Diferencijalni udarni presjeci su uspoređeni sa MCFM i MADGRAPH predviđanjima. MAD-

Table 9.4: Diferencijalni udarni presjek kao funkcija trasverzalnog impulsa Z bozona za četiri konačna stanja. Prva nesigurnost je statistička, druga je sistematska a treća je na luminozitet.

p_T^Z [GeV]	$d\sigma/dp_T^Z$ [pb /GeV]			
	eee	$ee\mu$	$\mu\mu e$	$\mu\mu\mu$
0–20	$(1.63 \pm 0.90 \pm 0.22 \pm 0.04) \times 10^{-1}$	$(9.3 \pm 6.8 \pm 1.3 \pm 0.2) \times 10^{-2}$	$(1.68 \pm 0.92 \pm 0.21 \pm 0.04) \times 10^{-1}$	$(2.01 \pm 1.00 \pm 0.20 \pm 0.05) \times 10^{-1}$
20–40	$(3.9 \pm 1.4 \pm 0.5 \pm 0.1) \times 10^{-1}$	$(3.17 \pm 1.26 \pm 0.39 \pm 0.08) \times 10^{-1}$	$(2.76 \pm 1.18 \pm 0.62 \pm 0.07) \times 10^{-1}$	$(3.42 \pm 1.31 \pm 0.57 \pm 0.09) \times 10^{-1}$
40–60	$(3.14 \pm 1.25 \pm 0.60 \pm 0.08) \times 10^{-1}$	$(2.70 \pm 1.16 \pm 0.43 \pm 0.07) \times 10^{-1}$	$(2.29 \pm 1.07 \pm 0.48 \pm 0.06) \times 10^{-1}$	$(2.82 \pm 1.19 \pm 0.56 \pm 0.07) \times 10^{-1}$
60–80	$(1.69 \pm 0.92 \pm 0.30 \pm 0.04) \times 10^{-1}$	$(2.07 \pm 1.02 \pm 0.31 \pm 0.05) \times 10^{-1}$	$(2.31 \pm 1.07 \pm 0.33 \pm 0.06) \times 10^{-1}$	$(2.03 \pm 1.01 \pm 0.31 \pm 0.05) \times 10^{-1}$
80–100	$(1.27 \pm 0.80 \pm 0.23 \pm 0.03) \times 10^{-1}$	$(1.02 \pm 0.71 \pm 0.17 \pm 0.03) \times 10^{-1}$	$(1.30 \pm 0.81 \pm 0.25 \pm 0.03) \times 10^{-1}$	$(1.25 \pm 0.79 \pm 0.21 \pm 0.03) \times 10^{-1}$
100–120	$(8.1 \pm 6.4 \pm 2.2 \pm 0.2) \times 10^{-2}$	$(2.76 \pm 3.72 \pm 1.55 \pm 0.07) \times 10^{-2}$	$(5.0 \pm 5.0 \pm 1.4 \pm 0.1) \times 10^{-2}$	$(7.8 \pm 6.3 \pm 1.4 \pm 0.2) \times 10^{-2}$
120–140	$(5.8 \pm 5.4 \pm 0.9 \pm 0.1) \times 10^{-2}$	$(6.2 \pm 5.6 \pm 0.8 \pm 0.2) \times 10^{-2}$	$(3.12 \pm 3.95 \pm 1.13 \pm 0.08) \times 10^{-2}$	$(4.1 \pm 4.5 \pm 1.2 \pm 0.1) \times 10^{-2}$
140–200	$(1.07 \pm 1.34 \pm 0.58 \pm 0.03) \times 10^{-2}$	$(1.09 \pm 1.35 \pm 0.62 \pm 0.03) \times 10^{-2}$	$(2.73 \pm 2.13 \pm 0.56 \pm 0.07) \times 10^{-2}$	$(1.46 \pm 1.56 \pm 0.53 \pm 0.04) \times 10^{-2}$
200–300	$(3.66 \pm 6.05 \pm 1.58 \pm 0.10) \times 10^{-3}$	$(9.0 \pm 9.5 \pm 1.7 \pm 0.2) \times 10^{-3}$	$(7.4 \pm 8.6 \pm 1.7 \pm 0.2) \times 10^{-3}$	$(5.8 \pm 7.6 \pm 1.8 \pm 0.2) \times 10^{-3}$

Table 9.5: Diferencijalni udarni presjek kao fukcija broja mlazova za četiri konačna stanja. Oznake su kao i u tablici 9.4.

N_{jets}	$d\sigma/dN_{\text{jets}}$ [pb]			
	eee	$ee\mu$	$\mu\mu e$	$\mu\mu\mu$
0 jets	$16.60 \pm 4.07 \pm 1.04 \pm 0.43$	$15.68 \pm 3.96 \pm 1.03 \pm 0.41$	$14.97 \pm 3.87 \pm 0.93 \pm 0.39$	$18.78 \pm 4.33 \pm 1.11 \pm 0.49$
1 jet	$6.06 \pm 2.46 \pm 0.48 \pm 0.16$	$4.80 \pm 2.19 \pm 0.57 \pm 0.12$	$5.32 \pm 2.31 \pm 0.61 \pm 0.14$	$4.84 \pm 2.20 \pm 0.72 \pm 0.13$
2 jets	$2.43 \pm 1.56 \pm 0.34 \pm 0.06$	$1.75 \pm 1.32 \pm 0.32 \pm 0.05$	$2.93 \pm 1.71 \pm 0.26 \pm 0.08$	$1.54 \pm 1.24 \pm 0.32 \pm 0.04$
3 jets	$(7.8 \pm 27.9 \pm 7.3 \pm 0.2) \times 10^{-2}$	$0.45 \pm 0.67 \pm 0.17 \pm 0.01$	$0.42 \pm 0.65 \pm 0.21 \pm 0.01$	$0.79 \pm 0.89 \pm 0.26 \pm 0.02$

Table 9.6: Diferencijalni udarni presjek kao funkcija transverzalnog impulsa vodećeg mlaza za četiri konačna stanja. Oznake su kao u tablici 9.4.

$p_T^{\text{leading jet}}$ [GeV]	$d\sigma/dp_T^{\text{leading jet}}$ [pb/GeV]			
	eee	$ee\mu$	$\mu\mu e$	$\mu\mu\mu$
30–60	$(1.22 \pm 0.64 \pm 0.34 \pm 0.03) \times 10^{-1}$	$(1.11 \pm 0.61 \pm 0.20 \pm 0.03) \times 10^{-1}$	$(1.10 \pm 0.61 \pm 0.24 \pm 0.03) \times 10^{-1}$	$(1.02 \pm 0.58 \pm 0.24 \pm 0.03) \times 10^{-1}$
60–100	$(5.4 \pm 3.7 \pm 1.7 \pm 0.1) \times 10^{-2}$	$(4.3 \pm 3.3 \pm 2.1 \pm 0.1) \times 10^{-2}$	$(6.5 \pm 4.0 \pm 2.0 \pm 0.2) \times 10^{-2}$	$(6.3 \pm 4.0 \pm 2.3 \pm 0.2) \times 10^{-2}$
100–150	$(2.96 \pm 2.43 \pm 1.57 \pm 0.08) \times 10^{-2}$	$(3.26 \pm 2.55 \pm 1.40 \pm 0.08) \times 10^{-2}$	$(3.9 \pm 2.8 \pm 1.2 \pm 0.1) \times 10^{-2}$	$(2.44 \pm 2.21 \pm 1.32 \pm 0.06) \times 10^{-2}$
150–250	$(1.18 \pm 1.09 \pm 0.29 \pm 0.03) \times 10^{-2}$	$(8.1 \pm 9.0 \pm 3.4 \pm 0.2) \times 10^{-3}$	$(1.07 \pm 1.03 \pm 0.61 \pm 0.03) \times 10^{-2}$	$(1.00 \pm 1.00 \pm 0.42 \pm 0.03) \times 10^{-2}$

Table 9.7: Kombinirani rezultati za WZ diferencijalni udarni presjek.

p_T^Z [GeV]	$d\sigma/dp_T^Z$ [pb/GeV]
0–20	$[1.48 \pm 0.40(\text{stat.}) \pm 0.17(\text{syst.}) \pm 0.04(\text{lumi.})]\times 10^{-1}$
20–40	$[3.47 \pm 0.60(\text{stat.}) \pm 0.50(\text{syst.}) \pm 0.09(\text{lumi.})]\times 10^{-1}$
40–60	$[2.56 \pm 0.54(\text{stat.}) \pm 0.49(\text{syst.}) \pm 0.07(\text{lumi.})]\times 10^{-1}$
60–80	$[2.10 \pm 0.47(\text{stat.}) \pm 0.30(\text{syst.}) \pm 0.05(\text{lumi.})]\times 10^{-1}$
80–100	$[1.20 \pm 0.37(\text{stat.}) \pm 0.21(\text{syst.}) \pm 0.03(\text{lumi.})]\times 10^{-1}$
100–120	$[4.9 \pm 2.3\ (\text{stat.}) \pm 1.5\ (\text{syst.}) \pm 0.1\ (\text{lumi.})]\times 10^{-2}$
120–140	$[5.0 \pm 2.2\ (\text{stat.}) \pm 1.0\ (\text{syst.}) \pm 0.1\ (\text{lumi.})]\times 10^{-2}$
140–200	$[1.34 \pm 0.73(\text{stat.}) \pm 0.57(\text{syst.}) \pm 0.03(\text{lumi.})]\times 10^{-2}$
200–300	$[4.9 \pm 3.6\ (\text{stat.}) \pm 1.6\ (\text{syst.}) \pm 0.1\ (\text{lumi.})]\times 10^{-3}$

N_{jets}	$d\sigma/dN_{\text{jets}}$ [pb]
0 jets	$16.15 \pm 1.95\ (\text{stat.}) \pm 0.88\ (\text{syst.}) \pm 0.42\ (\text{lumi.})$
1 jet	$5.27 \pm 1.11\ (\text{stat.}) \pm 0.52\ (\text{syst.}) \pm 0.14\ (\text{lumi.})$
2 jets	$2.11 \pm 0.69\ (\text{stat.}) \pm 0.27\ (\text{syst.}) \pm 0.05\ (\text{lumi.})$
3 jets	$0.196 \pm 0.227(\text{stat.}) \pm 0.102(\text{syst.}) \pm 0.005(\text{lumi.})$

$p_T^{\text{leading jet}}$ [GeV]	$d\sigma/dp_T^{\text{leading jet}}$ [pb/GeV]
30–60	$[1.12 \pm 0.30(\text{stat.}) \pm 0.23(\text{syst.}) \pm 0.03(\text{lumi.})]\times 10^{-1}$
60–100	$[5.5 \pm 1.8\ (\text{stat.}) \pm 1.9\ (\text{syst.}) \pm 0.1\ (\text{lumi.})]\times 10^{-2}$
100–150	$[3.06 \pm 1.20(\text{stat.}) \pm 1.37(\text{syst.}) \pm 0.08(\text{lumi.})]\times 10^{-2}$
150–250	$[1.04 \pm 0.48(\text{stat.}) \pm 0.41(\text{syst.}) \pm 0.03(\text{lumi.})]\times 10^{-2}$

GRAPH spektar je normalniziran na NLO udarni presjek kao što je predviđeno sa MCFM-om.

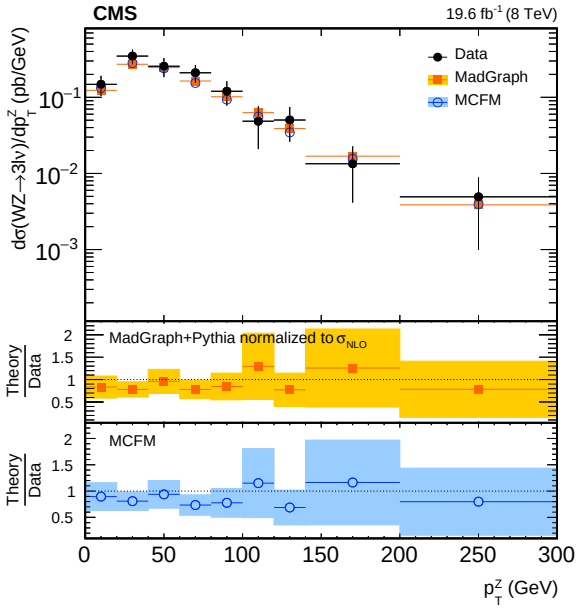

Figure 9.5: WZ diferencijalni udarni presjek kao funkcija transverzalnog umpulsa Z bozona. Mjerenje je uspoređeno sa MCFM i MADGRAPH predviđanjima. MADGRAPH predviđanja su skalirana na ukupni NLO udarni presjek koji je predviđen sa MCFM paketom. Relativne greške na podatke su statističke i sistematske i označene su u svakom binu.

9.7 Zaključak

U ovom radu izmjeren je WZ udarni presjek u sudarima protona na $\sqrt{s} = 8$ TeV za potpuno leptonski raspad WZ-a sa elektronima i mionima u konačnom stanju. Uzorak podataka odgovara integriranom luminozitetu od 19.6 fb^{-1}. Dobiveni rezultat je:

$$\sigma(\mathrm{pp} \to \mathrm{WZ}) = 24.09 \pm 0.87\ (\mathrm{stat.}) \pm 1.62\ (\mathrm{syst.}) \pm 0.63\ (\mathrm{lumi.})\mathrm{pb}^{-1}$$

Taj rezultat je konzistentan sa predviđanjima standardnog modela. Rezultati diferencijalnog udarnog presjeka su također predstavljeni i također odgovaraju teorijskim predviđanjima.

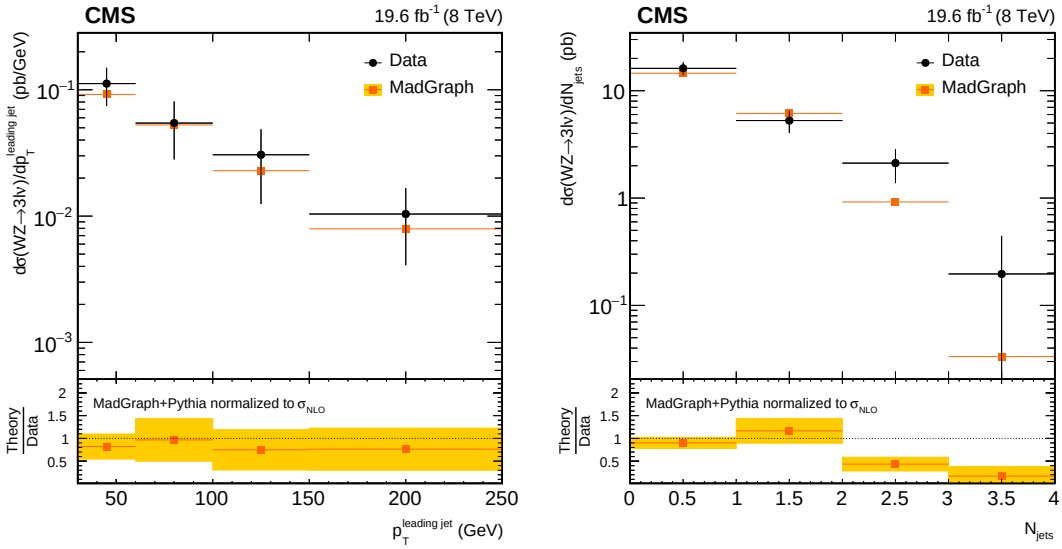

Figure 9.6: WZ diferencijalni udarni presjek kao funkcija transverzalnog impula vodećeg mlaza (lijevo) i broja mlazova. Mjerenja su uspoređena sa MADGRAPH predviđanjima. MADGRAPH predviđanja su skalirana na ukupni NLO udarni presjek koji je predviđen sa MCFM paketom. Relativne greške na podatke su statističke i sistematske i označene su u svakom binu.

Appendix A

Data driven method

In this appendix data driven method used in analysis will be explained more in detail.
We start from a sample with three leptons passing the loose lepton definition and all other WZ analysis cuts. We define:

- $N_{ijk}, i,j,k = T,F$: subset of the loose sample for which the 3 leptons have passed (T) or failed (F) the tight cuts.
- $n_{\alpha\beta\gamma}$: composition of loose sample in terms of promt (ℓ) or fake (j) leptons.

The number of events in each category can be expressed using the efficiencies p_i and ε_i.

$$\begin{bmatrix} N_{TTT} \\ N_{TTF} \\ N_{TFT} \\ N_{TFF} \\ N_{FTT} \\ N_{FTF} \\ N_{FFT} \\ N_{FFF} \end{bmatrix} = \begin{bmatrix} (\varepsilon_1)(\varepsilon_2)(\varepsilon_3) & (\varepsilon_1)(\varepsilon_2)(p_3) & (\varepsilon_1)(p_2)(\varepsilon_3) & (\varepsilon_1)(p_2)(p_3) & (p_1)(\varepsilon_2)(\varepsilon_3) & (p_1)(\varepsilon_2)(p_3) & (p_1)(p_2)(\varepsilon_3) & (p_1)(p_2)(p_3) \\ (\varepsilon_1)(\varepsilon_2)(1-\varepsilon_3) & (\varepsilon_1)(\varepsilon_2)(1-p_3) & (\varepsilon_1)(p_2)(1-\varepsilon_3) & (\varepsilon_1)(p_2)(1-p_3) & (p_1)(\varepsilon_2)(1-\varepsilon_3) & (p_1)(\varepsilon_2)(1-p_3) & (p_1)(p_2)(1-\varepsilon_3) & (p_1)(p_2)(1-p_3) \\ (\varepsilon_1)(1-\varepsilon_2)(\varepsilon_3) & (\varepsilon_1)(1-\varepsilon_2)(p_3) & (\varepsilon_1)(1-p_2)(\varepsilon_3) & (\varepsilon_1)(1-p_2)(p_3) & (p_1)(1-\varepsilon_2)(\varepsilon_3) & (p_1)(1-\varepsilon_2)(p_3) & (p_1)(1-p_2)(\varepsilon_3) & (p_1)(1-p_2)(p_3) \\ (\varepsilon_1)(1-\varepsilon_2)(1-\varepsilon_3) & (\varepsilon_1)(1-\varepsilon_2)(1-p_3) & (\varepsilon_1)(1-p_2)(1-\varepsilon_3) & (\varepsilon_1)(1-p_2)(1-p_3) & (p_1)(1-\varepsilon_2)(1-\varepsilon_3) & (p_1)(1-\varepsilon_2)(1-p_3) & (p_1)(1-p_2)(1-\varepsilon_3) & (p_1)(1-p_2)(1-p_3) \\ (1-\varepsilon_1)(\varepsilon_2)(\varepsilon_3) & (1-\varepsilon_1)(\varepsilon_2)(p_3) & (1-\varepsilon_1)(p_2)(\varepsilon_3) & (1-\varepsilon_1)(p_2)(p_3) & (1-p_1)(\varepsilon_2)(\varepsilon_3) & (1-p_1)(\varepsilon_2)(p_3) & (1-p_1)(p_2)(\varepsilon_3) & (1-p_1)(p_2)(p_3) \\ (1-\varepsilon_1)(\varepsilon_2)(1-\varepsilon_3) & (1-\varepsilon_1)(\varepsilon_2)(1-p_3) & (1-\varepsilon_1)(p_2)(1-\varepsilon_3) & (1-\varepsilon_1)(p_2)(1-p_3) & (1-p_1)(\varepsilon_2)(1-\varepsilon_3) & (1-p_1)(\varepsilon_2)(1-p_3) & (1-p_1)(p_2)(1-\varepsilon_3) & (1-p_1)(p_2)(1-p_3) \\ (1-\varepsilon_1)(1-\varepsilon_2)(\varepsilon_3) & (1-\varepsilon_1)(1-\varepsilon_2)(p_3) & (1-\varepsilon_1)(1-p_2)(\varepsilon_3) & (1-\varepsilon_1)(1-p_2)(p_3) & (1-p_1)(1-\varepsilon_2)(\varepsilon_3) & (1-p_1)(1-\varepsilon_2)(p_3) & (1-p_1)(1-p_2)(\varepsilon_3) & (1-p_1)(1-p_2)(p_3) \\ (1-\varepsilon_1)(1-\varepsilon_2)(1-\varepsilon_3) & (1-\varepsilon_1)(1-\varepsilon_2)(1-p_3) & (1-\varepsilon_1)(1-p_2)(1-\varepsilon_3) & (1-\varepsilon_1)(1-p_2)(1-p_3) & (1-p_1)(1-\varepsilon_2)(1-\varepsilon_3) & (1-p_1)(1-\varepsilon_2)(1-p_3) & (1-p_1)(1-p_2)(1-\varepsilon_3) & (1-p_1)(1-p_2)(1-p_3) \end{bmatrix} \begin{bmatrix} n_{\ell\ell\ell} \\ n_{\ell\ell j} \\ n_{\ell j\ell} \\ n_{\ell jj} \\ n_{j\ell\ell} \\ n_{j\ell j} \\ n_{jj\ell} \\ n_{jjj} \end{bmatrix} \tag{A.1}$$

The numbers of events $n_{\alpha\beta\gamma}(\alpha,\beta,\gamma = \ell, j)$ can then be extracted by solving this linear system of equations, *i.e.* inverting the matrix in Equation B.1:

$$A \equiv \frac{1}{(\varepsilon_1 - p_1)(\varepsilon_2 - p_2)(\varepsilon_3 - p_3)} \tag{A.2}$$

$$\begin{bmatrix} n_{\ell\ell\ell} \\ n_{\ell\ell j} \\ n_{\ell j\ell} \\ n_{\ell jj} \\ n_{j\ell\ell} \\ n_{j\ell j} \\ n_{jj\ell} \\ n_{jjj} \end{bmatrix} = A \begin{bmatrix} +(1-p_1)(1-p_2)(1-p_3) & -(1-p_1)(1-p_2)(p_3) & -(1-p_1)(p_2)(1-p_3) & +(1-p_1)(p_2)(p_3) & -(p_1)(1-p_2)(1-p_3) & +(p_1)(1-p_2)(p_3) & +(p_1)(p_2)(1-p_3) & -(p_1)(p_2)(p_3) \\ -(1-p_1)(1-p_2)(1-\varepsilon_3) & +(1-p_1)(1-p_2)(\varepsilon_3) & +(1-p_1)(p_2)(1-\varepsilon_3) & -(1-p_1)(p_2)(\varepsilon_3) & +(p_1)(1-p_2)(1-\varepsilon_3) & -(p_1)(1-p_2)(\varepsilon_3) & -(p_1)(p_2)(1-\varepsilon_3) & +(p_1)(p_2)(\varepsilon_3) \\ -(1-p_1)(1-\varepsilon_2)(1-p_3) & +(1-p_1)(1-\varepsilon_2)(p_3) & +(1-p_1)(\varepsilon_2)(1-p_3) & -(1-p_1)(\varepsilon_2)(p_3) & +(p_1)(1-\varepsilon_2)(1-p_3) & -(p_1)(1-\varepsilon_2)(p_3) & -(p_1)(\varepsilon_2)(1-p_3) & +(p_1)(\varepsilon_2)(p_3) \\ +(1-p_1)(1-\varepsilon_2)(1-\varepsilon_3) & -(1-p_1)(1-\varepsilon_2)(\varepsilon_3) & -(1-p_1)(\varepsilon_2)(1-\varepsilon_3) & +(1-p_1)(\varepsilon_2)(\varepsilon_3) & -(p_1)(1-\varepsilon_2)(1-\varepsilon_3) & +(p_1)(1-\varepsilon_2)(\varepsilon_3) & +(p_1)(\varepsilon_2)(1-\varepsilon_3) & -(p_1)(\varepsilon_2)(\varepsilon_3) \\ -(1-\varepsilon_1)(1-p_2)(1-p_3) & +(1-\varepsilon_1)(1-p_2)(p_3) & +(1-\varepsilon_1)(p_2)(1-p_3) & -(1-\varepsilon_1)(p_2)(p_3) & +(\varepsilon_1)(1-p_2)(1-p_3) & -(\varepsilon_1)(1-p_2)(p_3) & -(\varepsilon_1)(p_2)(1-p_3) & +(\varepsilon_1)(p_2)(p_3) \\ +(1-\varepsilon_1)(1-p_2)(1-\varepsilon_3) & -(1-\varepsilon_1)(1-p_2)(\varepsilon_3) & -(1-\varepsilon_1)(p_2)(1-\varepsilon_3) & +(1-\varepsilon_1)(p_2)(\varepsilon_3) & -(\varepsilon_1)(1-p_2)(1-\varepsilon_3) & +(\varepsilon_1)(1-p_2)(\varepsilon_3) & +(\varepsilon_1)(p_2)(1-\varepsilon_3) & -(\varepsilon_1)(p_2)(\varepsilon_3) \\ +(1-\varepsilon_1)(1-\varepsilon_2)(1-p_3) & -(1-\varepsilon_1)(1-\varepsilon_2)(p_3) & -(1-\varepsilon_1)(\varepsilon_2)(1-p_3) & +(1-\varepsilon_1)(\varepsilon_2)(p_3) & -(\varepsilon_1)(1-\varepsilon_2)(1-p_3) & +(\varepsilon_1)(1-\varepsilon_2)(p_3) & +(\varepsilon_1)(\varepsilon_2)(1-p_3) & -(\varepsilon_1)(\varepsilon_2)(p_3) \\ -(1-\varepsilon_1)(1-\varepsilon_2)(1-\varepsilon_3) & +(1-\varepsilon_1)(1-\varepsilon_2)(\varepsilon_3) & +(1-\varepsilon_1)(\varepsilon_2)(1-\varepsilon_3) & -(1-\varepsilon_1)(\varepsilon_2)(\varepsilon_3) & +(\varepsilon_1)(1-\varepsilon_2)(1-\varepsilon_3) & -(\varepsilon_1)(1-\varepsilon_2)(\varepsilon_3) & -(\varepsilon_1)(\varepsilon_2)(1-\varepsilon_3) & +(\varepsilon_1)(\varepsilon_2)(\varepsilon_3) \end{bmatrix} \begin{bmatrix} N_{TTT} \\ N_{TTF} \\ N_{TFT} \\ N_{TFF} \\ N_{FTT} \\ N_{FTF} \\ N_{FFT} \\ N_{FFF} \end{bmatrix} \tag{A.3}$$

$$
\begin{aligned}
N_{TTT} &= n_{j\ell\ell}p_1\varepsilon_2\varepsilon_3 + n_{j\ell j}p_1\varepsilon_2 p_3 + n_{jj\ell}p_1 p_2\varepsilon_3 + n_{jjj}p_1p_2p_3 \\
&\quad + n_{\ell\ell\ell}\varepsilon_1\varepsilon_2\varepsilon_3 + n_{\ell\ell j}\varepsilon_1\varepsilon_2 p_3 + n_{\ell j\ell}\varepsilon_1 p_2\varepsilon_3 + n_{\ell jj}\varepsilon_1 p_2 p_3 \\
N_{TTF} &= n_{j\ell\ell}p_1\varepsilon_2(1-\varepsilon_3) + n_{j\ell j}p_1\varepsilon_2(1-p_3) + n_{jj\ell}p_1p_2(1-\varepsilon_3) + n_{jjj}p_1p_2(1-p_3) \\
&\quad + n_{\ell\ell\ell}\varepsilon_1\varepsilon_2(1-\varepsilon_3) + n_{\ell\ell j}\varepsilon_1\varepsilon_2(1-p_3) + n_{\ell j\ell}\varepsilon_1 p_2(1-\varepsilon_3) + n_{\ell jj}\varepsilon_1 p_2(1-p_3) \\
N_{TFT} &= n_{j\ell\ell}p_1(1-\varepsilon_2)\varepsilon_3 + n_{j\ell j}p_1(1-\varepsilon_2)p_3 + n_{jj\ell}p_1(1-p_2)\varepsilon_3 + n_{jjj}p_1(1-p_2)p_3 \\
&\quad + n_{\ell\ell\ell}\varepsilon_1(1-\varepsilon_2)\varepsilon_3 + n_{\ell\ell j}\varepsilon_1(1-\varepsilon_2)p_3 + n_{\ell j\ell}\varepsilon_1(1-p_2)\varepsilon_3 + n_{\ell jj}\varepsilon_1(1-p_2)p_3 \\
N_{TFF} &= n_{j\ell\ell}p_1(1-\varepsilon_2)(1-\varepsilon_3) + n_{j\ell j}p_1(1-\varepsilon_2)(1-p_3) \\
&\quad + n_{jj\ell}p_1(1-p_2)(1-\varepsilon_3) + n_{jjj}p_1(1-p_2)(1-p_3) \\
&\quad + n_{\ell\ell\ell}\varepsilon_1(1-\varepsilon_2)(1-\varepsilon_3) + n_{\ell\ell j}\varepsilon_1(1-\varepsilon_2)(1-p_3) \\
&\quad + n_{\ell j\ell}\varepsilon_1(1-p_2)(1-\varepsilon_3) + n_{\ell jj}\varepsilon_1(1-p_2)(1-p_3) \\
N_{FTT} &= n_{j\ell\ell}(1-p_1)\varepsilon_2\varepsilon_3 + n_{j\ell j}(1-p_1)\varepsilon_2 p_3 + n_{jj\ell}(1-p_1)p_2\varepsilon_3 + n_{jjj}(1-p_1)p_2p_3 \\
&\quad + n_{\ell\ell\ell}(1-\varepsilon_1)\varepsilon_2\varepsilon_3 + n_{\ell\ell j}(1-\varepsilon_1)\varepsilon_2 p_3 + n_{\ell j\ell}(1-\varepsilon_1)p_2\varepsilon_3 + n_{\ell jj}(1-\varepsilon_1)p_2p_3 \\
N_{FTF} &= n_{j\ell\ell}(1-p_1)\varepsilon_2(1-\varepsilon_3) + n_{j\ell j}(1-p_1)\varepsilon_2(1-p_3) \\
&\quad n_{jj\ell}(1-p_1)p_2(1-\varepsilon_3) + n_{jjj}(1-p_1)p_2(1-p_3) \\
&\quad + n_{\ell\ell\ell}(1-\varepsilon_1)\varepsilon_2(1-\varepsilon_3) + n_{\ell j\ell}(1-\varepsilon_1)p_2(1-\varepsilon_3) \\
&\quad + n_{\ell\ell j}(1-\varepsilon_1)\varepsilon_2(1-p_3) + n_{\ell jj}(1-\varepsilon_1)p_2(1-p_3) \\
N_{FFT} &= n_{j\ell\ell}(1-p_1)(1-\varepsilon_2)\varepsilon_3 + n_{j\ell j}(1-p_1)(1-\varepsilon_2)p_3 \\
&\quad + n_{jj\ell}(1-p_1)(1-p_2)\varepsilon_3 + n_{jjj}(1-p_1)(1-p_2)p_3 \\
&\quad + n_{\ell\ell\ell}(1-\varepsilon_1)(1-\varepsilon_2)\varepsilon_3 + n_{\ell\ell j}(1-\varepsilon_1)(1-\varepsilon_2)p_3 \\
&\quad + n_{\ell j\ell}(1-\varepsilon_1)(1-p_2)\varepsilon_3 + n_{\ell jj}(1-\varepsilon_1)(1-p_2)p_3 \\
N_{FFF} &= n_{j\ell\ell}(1-p_1)(1-\varepsilon_2)(1-\varepsilon_3) + n_{j\ell j}(1-p_1)(1-\varepsilon_2)(1-p_3) \\
&\quad + n_{jjj}(1-p_1)(1-p_2)(1-p_3) + n_{jj\ell}(1-p_1)(1-p_2)(1-\varepsilon_3) \\
&\quad + n_{\ell\ell\ell}(1-\varepsilon_1)(1-\varepsilon_2)(1-\varepsilon_3) + n_{\ell j\ell}(1-\varepsilon_1)(1-p_2)(1-\varepsilon_3) \\
&\quad + n_{\ell\ell j}(1-\varepsilon_1)(1-\varepsilon_2)(1-p_3) + n_{\ell jj}(1-\varepsilon_1)(1-p_2)(1-p_3)
\end{aligned}
$$

Solving the system of equations above gives the result used in the analysis.

Appendix B

Data driven statistical uncertainties

In this appendix detailed procedure of computing statistical uncertainties for data driven method will be given. We start from a sample with three leptons passing the loose lepton definition and all other WZ analysis cuts. We define:

- $N_{ijk}, i, j, k = T, F$: subset of the loose sample for which the 3 leptons have passed (T) or failed (F) the tight cuts.
- $n_{\alpha\beta\gamma}$: composition of loose sample in terms of promt (ℓ) or fake (j) leptons.

The yield in each of these subsamples can be expressed as linear combination of the unknown yields $n_{\alpha\beta\gamma}$ $(\alpha, \beta, \gamma = p, f)$

$$N_{ijk} = \sum_{\alpha,\beta,\gamma=p,f} C^{ijk}_{\alpha\beta\gamma} n_{\alpha\beta\gamma}, \quad i, j, k = T, F \tag{B.1}$$

where the coefficients $C^{ijk}_{\alpha\beta\gamma}$ depend on the efficiencies p and ε, which stand for the probabilities of prompt or fake leptons, respectively, to pass the tight lepton selection provided they have passed the loose selection.

The number of signal events, *i.e.* events with three prompt leptons, can be obtained by solving the above system of equations, and is found to be:

$$\begin{aligned} n_{\ell\ell\ell} &= \frac{1}{(\varepsilon_1-p_1)(\varepsilon_2-p_2)(\varepsilon_3-p_3)} \\ &[\ N_{TTT}(1-p_1)(1-p_2)(1-p_3) \\ &-N_{TTF}(1-p_1)(1-p_2)(\ p_3) \\ &-N_{TFT}(1-p_1)(\ p_2)(1-p_3) \\ &+N_{TFF}(1-p_1)(\ p_2)(\ p_3) \\ &-N_{FTT}(\ p_1)(1-p_2)(1-p_3) \\ &+N_{FTF}(\ p_1)(1-p_2)(\ p_3) \\ &+N_{FFT}(\ p_1)(\ p_2)(1-p_3) \\ &-N_{FFF}(\ p_1)(\ p_2)(\ p_3)] \end{aligned} \tag{B.2}$$

The number of events with three prompt leptons in the TTT sample, which corresponds exactly to the final selection is

$$N_{prompt} = n_{\ell\ell\ell}\varepsilon_1\varepsilon_2\varepsilon_3. \tag{B.3}$$

Alternatively one can express the number of events with fake leptons in the final sample, which is simply:

$$N_{fake} = N_{TTT} - n_{\ell\ell\ell}\varepsilon_1\varepsilon_2\varepsilon_3 \tag{B.4}$$

Using the above relations, this can be rewritten as:

$$\begin{aligned} N_{fake} &= N_{TTT}\left[1-\frac{\varepsilon_1\varepsilon_2\varepsilon_3(1-p_1)(1-p_2)(1-p_3)}{(\varepsilon_1-p_1)(\varepsilon_2-p_2)(\varepsilon_3-p_3)}\right] \\ &+\frac{\varepsilon_1\varepsilon_2\varepsilon_3}{(\varepsilon_1-p_1)(\varepsilon_2-p_2)(\varepsilon_3-p_3)} \\ &[N_{TTF}(1-p_1)(1-p_2)(\ p_3) \\ &+N_{TFT}(1-p_1)(\ p_2)(1-p_3) \\ &-N_{TFF}(1-p_1)(\ p_2)(\ p_3) \\ &+N_{FTT}(\ p_1)(1-p_2)(1-p_3) \\ &-N_{FTF}(\ p_1)(1-p_2)(\ p_3) \\ &-N_{FFT}(\ p_1)(\ p_2)(1-p_3) \\ &+N_{FFF}(\ p_1)(\ p_2)(\ p_3)] \end{aligned} \tag{B.5}$$

Equations (B.2) and (B.5) are used to compute the number of events with three prompt leptons or the number of events with one or more fake leptons in the final sample, respectively. In the

first case, the factor $\varepsilon_1\varepsilon_2\varepsilon_3$ should be added. As the fake rates and prompt efficiencies p_i and ε_i depend on the lepton p_t and η, these expressions cannot be used as such as the same coefficient cannot be applied to all events in a given category ($TTT, TTF, ...$). Instead N_{prompt} and N_{fake} are computed as a sum of events over all events in the loose sample. The weight of each event is the coefficient of N_{ijk} corresponding to the category to which that event belongs ($TTT, TTF, ...$) in the above equations.

The uncertainties on those yields are obtained by applying full error propagations to these expressions.

B.1 Uncertainties on n_{prompt}

The actual yield of prompt events in the final selected sample is computed as a sum of weights over all events in the loose sample.

$$N_{prompt} = \sum_{i\in\{events\}} w_i \tag{B.6}$$

The weight w_i for each event is computed as the coefficient of N_{ijk} corresponding to the category ijk to which each event belongs (TTT, TTF, ...). We can rewrite the sum grouping events in groups with idential weight, and now looping over those groups

$$N_{prompt} = \sum_{i\in\{events\}} w_i = \sum_{k\in\{groups\}} w_k m_k \tag{B.7}$$

where m_k is the number of events in group k and w_k is the weight for events in this group. The variance of N_{prompt} can now be written as

$$\sigma^2_{N_p} = \underbrace{\sum_k \left(\frac{\partial N_p}{\partial m_k}\right)^2 \sigma^2_{m_k}}_{\equiv A} + \underbrace{\sum_\alpha \left(\frac{\partial N_p}{\partial p_\alpha}\right)^2 \sigma^2_{p_\alpha}}_{\equiv B} + \underbrace{\sum_\beta \left(\frac{\partial N_p}{\partial \varepsilon_\beta}\right)^2 \sigma^2_{\varepsilon_\beta}}_{\equiv C} \tag{B.8}$$

where the sums over α and β indices run over all values of fake rates and prompt efficiencies, respectively. The first term can be simply rewritten as a sum of squared weights

$$A = \sum_k w_k^2 m_k = \sum_i w_i^2 \tag{B.9}$$

The second term is

$$\begin{aligned} B &= \sum_{\alpha}\left(\sum_{i}\frac{\partial w_i}{\partial p_\alpha}\right)^2\sigma_{p_\alpha}^2 \\ &= \sum_{\alpha}\left(\sum_{i,j}\frac{\partial w_i}{\partial p_\alpha}\frac{\partial w_j}{\partial p_\alpha}\right)\sigma_{p_\alpha}^2 \\ &= \sum_{\alpha}\left[\sum_{i}\left(\frac{\partial w_i}{\partial p_\alpha}\right)^2+\sum_{i\neq j}\frac{\partial w_i}{\partial p_\alpha}\frac{\partial w_j}{\partial p_\alpha}\right]\sigma_{p_\alpha}^2 \\ &= \underbrace{\sum_{i}\sum_{\alpha}\left(\frac{\partial w_i}{\partial p_\alpha}\right)^2\sigma_{p_\alpha}^2}_{\equiv B_{diag}}+\sum_{\alpha}\sum_{i\neq j}\frac{\partial w_i}{\partial p_\alpha}\frac{\partial w_j}{\partial p_\alpha}\sigma_{p_\alpha}^2 \end{aligned} \tag{B.10}$$

The second sum ($\sum_{i\neq j}$) runs over all combinations of different events. Only pairs of events where the same fake rate, i.e. the same (p_t,η) bin of fake rates is used, will have a non-zero contribution. For the third term, C, exactly equivalent relations as for B are valid, replacing α with β and p_α with ε_β.

B.2 Computing weights and their errors

Looking at equations B.2 and B.3 for the prompt lepton contribution in the final sample, we can establish simple rules for computing the weight of a single event to compute the prompt yield:

- A factor $\frac{\varepsilon}{\varepsilon-p}$ for each lepton
- A factor $(1-p)$ for each tight lepton (T)
- A factor $-p$ for each lepton failing the tight selection (F) in the event

The total event weight can therefore be written as:

$$w=(-1)^{n_F}\underbrace{\prod_{\ell}\frac{\varepsilon_\ell}{\varepsilon_\ell-p_\ell}}_{\equiv w_1}\underbrace{\prod_{\ell\in T}(1-p_\ell)\prod_{\ell\in F}(p_\ell)}_{\equiv w_2} \tag{B.11}$$

where the products $\prod_{\ell\in T}$ and $\prod_{\ell\in F}$ run over all tight or failing leptons, respectively. Equation (B.11) allows us to simply express the derivatives of this weight with respect to fake rates and efficiencies. For tight leptons, the derivativ with respect to fake rates are:

$$\begin{aligned} \frac{\partial w}{\partial p_i} &= (-1)^{n_F}\left[\frac{1}{\varepsilon_i-p_i}\prod_{\ell}\frac{\varepsilon_\ell}{\varepsilon_\ell-p_\ell}\prod_{\ell\in T}(1-p_\ell)\prod_{\ell\in F}(p_\ell)-\prod_{\ell}\frac{\varepsilon_\ell}{\varepsilon_\ell-p_\ell}\prod_{\ell\in T,\ell\neq i}(1-p_\ell)\prod_{\ell\in F}(p_\ell)\right] \\ &= w\left[\frac{1}{\varepsilon_i-p_i}-\frac{1}{1-p_i}\right] \end{aligned} \tag{B.12}$$

while for fake leptons they are:

$$\begin{aligned}\frac{\partial w}{\partial p_i} &= (-1)^{n_F}\left[\frac{1}{\varepsilon_i - p_i}\prod_\ell \frac{\varepsilon_\ell}{\varepsilon_\ell - p_\ell}\prod_{\ell\in T}(1-p_\ell)\prod_{\ell\in F}(p_\ell) + \prod_\ell \frac{\varepsilon_\ell}{\varepsilon_\ell - p_\ell}\prod_{\ell\in T}(1-p_\ell)\prod_{\ell\in F,\ell\neq i}(p_\ell)\right] \\ &= w\left[\frac{1}{\varepsilon_i - p_i} + \frac{1}{p_i}\right] \end{aligned} \tag{B.13}$$

Summarizing, we can express the derivative with respect to fake rates as

$$\frac{\partial w}{\partial p_i} = \begin{cases} \frac{1-\varepsilon_i}{(\varepsilon_i - p_i)(1-p_i)} w, & \text{for } i \in T \\ \\ \frac{\varepsilon_i}{(\varepsilon_i - p_i)p_i} w, & \text{for } i \in F \end{cases} \tag{B.14}$$

The derivative of the prompt weight with respect to prompt efficiencies are:

$$\frac{\partial w}{\partial \varepsilon_i} = \left(\frac{1}{\varepsilon_i} - \frac{1}{\varepsilon_i - p_i}\right) w \tag{B.15}$$

B.3 Special case: 2 leptons in same fake rate bin

The derivatives in eqs. (B.14) have been computed assuming that only one lepton in the event depends on the same fake rate, i.e. falls in the same (p_t, η) bin. In case 2 leptons in the same event depend on the same fake rate, the above expressions need to be modified. For this, it will be useful to use the decomposition of the fake rate in two terms in eq. (B.11):

$$w = (-1)^{n_F} w_1 \cdot w_2 \tag{B.16}$$

The derivative is then simply:

$$\frac{\partial w}{\partial p_i} = (-1)^{n_F}\left(\frac{\partial w_1}{\partial p_i} w_2 + w_1 \frac{\partial w_2}{\partial p_i}\right) \tag{B.17}$$

We will assume that leptons i and k fall in the same bin, i.e. $p_i = p_k$. We distinguish three cases:

1. $\underline{i, j \in T}$: both leptons sharing the same fake rate are tight.
2. $\underline{i, j \in F}$: both leptons sharing the same fake rate are failing.
3. $\underline{i \in T, j \in F}$: one of the two leptons sharing the same fake is tight and the other one is failing.

The derivative of w_1 looks identical in all three cases

$$\frac{\partial w_1}{\partial p_i} = w_1 \cdot \left(\frac{1}{\varepsilon_i - p_i} + \frac{1}{\varepsilon_j - p_i}\right) \tag{B.18}$$

On the other side the derivative of w_2 takes on a different expression for each of the three cases:

$$\frac{\partial w_2}{\partial p_i} = w_2 \cdot \begin{cases} -\frac{2}{1-p_i} & , \text{ for } i,j \in T \\ \frac{2}{p_i} & , \text{ for } i,j \in F \\ +\frac{1}{p_i} - \frac{1}{1-p_i} & , \text{ for } i \in T, j \in F \end{cases} \tag{B.19}$$

$$\frac{\partial w}{\partial p_i} = w \cdot \begin{cases} \left[\frac{1}{\varepsilon_i - p_i} + \frac{1}{\varepsilon_j - p_i} - \frac{2}{1-p_i}\right] & , \text{ for } i,j \in T \\ \left[\frac{1}{\varepsilon_i - p_i} + \frac{1}{\varepsilon_j - p_i} + \frac{2}{p_i}\right] & , \text{ for } i,j \in F \\ \left[\frac{1}{\varepsilon_i - p_i} + \frac{1}{\varepsilon_j - p_i} + \frac{1}{p_i} - \frac{1}{1-p_i}\right] & , \text{ for } i \in T, j \in F \end{cases} \tag{B.20}$$

B.4 Weight and uncertainties on fake yields

In a similar way as was done for N_{prompt} we can establish simple rules for computing the weight of a single event to compute the fake yields N_{fake} from equation (B.5), and the total event weight can therefore be written as:

$$\begin{aligned} w_{fake} &= \delta_{ijk,TTT} + (-1)^{n_F+1} \prod_\ell \frac{\varepsilon_\ell}{\varepsilon_\ell - p_\ell} \prod_{\ell \in T} (1-p_\ell) \prod_{\ell \in F} (p_\ell) \\ &= \delta_{ijk,TTT} + \prod_\ell \frac{\varepsilon_\ell}{\varepsilon_\ell - p_\ell} \prod_{\ell \in T} (p_\ell - 1) \prod_{\ell \in F} (p_\ell) \end{aligned} \tag{B.21}$$

where $\delta_{ijk,TTT}$ equals 1 for TTT events and 0 otherwise.

Bibliography

[1] K. A. Olive et al. Review of Particle Physics. *Chin. Phys.*, C38:090001, 2014. doi: 10.1088/1674-1137/38/9/090001.

[2] Lyndon Evans and Philip Bryant. Lhc machine. *Journal of Instrumentation*, 3(08):S08001, 2008. URL `http://stacks.iop.org/1748-0221/3/i=08/a=S08001`.

[3] Jordi Duarte Campderrós, Ivan Vila Álvarez, and Teresa Rodrigo Anoro. *Medida de la sección eficaz de producción de dibosones WZ a 7 TeV y 8 TeV de energía del centro de masas en el experimento CMS.* PhD thesis, Cantabria Inst. of Phys., Dec 2013. URL `https://cds.cern.ch/record/1668166`. Presented 07 Feb 2014.

[4] S. L. Glashow. Partial Symmetries of Weak Interactions. *Nucl. Phys.*, 22:579–588, 1961. doi: 10.1016/0029-5582(61)90469-2.

[5] Steven Weinberg. A Model of Leptons. *Phys. Rev. Lett.*, 19:1264–1266, 1967. doi: 10.1103/PhysRevLett.19.1264.

[6] Abdus Salam and John Clive Ward. Weak and electromagnetic interactions. *Nuovo Cim.*, 11:568–577, 1959. doi: 10.1007/BF02726525.

[7] G. Arnison et al. Experimental Observation of Isolated Large Transverse Energy Electrons with Associated Missing Energy at s**(1/2) = 540-GeV. *Phys. Lett.*, B122:103–116, 1983. doi: 10.1016/0370-2693(83)91177-2. [,611(1983)].

[8] G. Arnison et al. Experimental Observation of Lepton Pairs of Invariant Mass Around 95-GeV/c**2 at the CERN SPS Collider. *Phys. Lett.*, B126:398–410, 1983. doi: 10.1016/0370-2693(83)90188-0.

[9] Georges Aad et al. Observation of a new particle in the search for the Standard Model Higgs boson with the ATLAS detector at the LHC. *Phys. Lett.*, B716:1–29, 2012. doi: 10.1016/j.physletb.2012.08.020.

[10] Serguei Chatrchyan et al. Observation of a new boson at a mass of 125 GeV with the CMS experiment at the LHC. *Phys. Lett.*, B716:30–61, 2012. doi: 10.1016/j.physletb.2012.08.021.

[11] J. H. Christenson, J. W. Cronin, V. L. Fitch, and R. Turlay. Evidence for the 2 pi Decay of the k(2)0 Meson. *Phys. Rev. Lett.*, 13:138–140, 1964. doi: 10.1103/PhysRevLett.13.138.

[12] A. Alavi-Harati et al. Observation of direct CP violation in $K_{S,L} \to \pi\pi$ decays. *Phys. Rev. Lett.*, 83:22–27, 1999. doi: 10.1103/PhysRevLett.83.22.

[13] V. Fanti et al. A New measurement of direct CP violation in two pion decays of the neutral kaon. *Phys. Lett.*, B465:335–348, 1999. doi: 10.1016/S0370-2693(99)01030-8.

[14] Bernard Aubert et al. Measurement of CP violating asymmetries in B^0 decays to CP eigenstates. *Phys. Rev. Lett.*, 86:2515–2522, 2001. doi: 10.1103/PhysRevLett.86.2515.

[15] Kazuo Abe et al. Observation of large CP violation in the neutral B meson system. *Phys. Rev. Lett.*, 87:091802, 2001. doi: 10.1103/PhysRevLett.87.091802.

[16] R Aaij et al. First observation of *CP* violation in the decays of B_s^0 mesons. *Phys. Rev. Lett.*, 110(22):221601, 2013. doi: 10.1103/PhysRevLett.110.221601.

[17] H. David Politzer. Reliable Perturbative Results for Strong Interactions? *Phys. Rev. Lett.*, 30:1346–1349, 1973. doi: 10.1103/PhysRevLett.30.1346.

[18] D. J. Gross and Frank Wilczek. Asymptotically Free Gauge Theories. 1. *Phys. Rev.*, D8: 3633–3652, 1973. doi: 10.1103/PhysRevD.8.3633.

[19] Peter W. Higgs. Broken Symmetries and the Masses of Gauge Bosons. *Phys. Rev. Lett.*, 13:508–509, 1964. doi: 10.1103/PhysRevLett.13.508.

[20] Guido Altarelli and G. Parisi. Asymptotic Freedom in Parton Language. *Nucl. Phys.*, B126:298–318, 1977. doi: 10.1016/0550-3213(77)90384-4.

[21] John M. Campbell, R. Keith Ellis, and Ciaran Williams. Vector boson pair production at the lhc. *Journal of High Energy Physics*, 2011(7):18, 2011. ISSN 1029-8479. doi: 10.1007/JHEP07(2011)018. URL `http://dx.doi.org/10.1007/JHEP07(2011)018`.

[22] Victor Mukhamedovich Abazov et al. A measurement of the WZ and ZZ production cross sections using leptonic final states in 8.6 fb^{-1} of $p\bar{p}$ collisions. *Phys. Rev. D*, 85:112005, 2012. doi: 10.1103/PhysRevD.85.112005.

[23] T. Aaltonen et al. Measurement of the WZ cross section and triple gauge couplings in $p\bar{p}$ collisions at $\sqrt{s} = 1.96$ TeV. *Phys. Rev. D*, 86:031104, 2012. doi: 10.1103/PhysRevD.86.031104.

[24] S. Chatrchyan et al. The CMS experiment at the CERN LHC. *JINST*, 3:S08004, 2008. doi: 10.1088/1748-0221/3/08/S08004.

[25] G. Aad et al. The ATLAS Experiment at the CERN Large Hadron Collider. *JINST*, 3: S08003, 2008. doi: 10.1088/1748-0221/3/08/S08003.

[26] K. Aamodt et al. The ALICE experiment at the CERN LHC. *JINST*, 3:S08002, 2008. doi: 10.1088/1748-0221/3/08/S08002.

[27] A. Augusto Alves, Jr. et al. The LHCb Detector at the LHC. *JINST*, 3:S08005, 2008. doi: 10.1088/1748-0221/3/08/S08005.

[28] D. Green. The physics of particle detectors. *Camb. Monogr. Part. Phys. Nucl. Phys. Cosmol.*, 12:1–361, 2000.

[29] S. Agostinelli et al. GEANT4: A Simulation toolkit. *Nucl. Instrum. Meth.*, A506:250–303, 2003. doi: 10.1016/S0168-9002(03)01368-8.

[30] Absolute Calibration of the Luminosity Measurement at CMS: Winter 2012 Update. Technical Report CMS-PAS-SMP-12-008, CERN, Geneva, 2012. URL `https://cds.cern.ch/record/1434360`.

[31] Absolute Calibration of the Luminosity Measurement at CMS: Winter 2012 Update. Technical Report CMS-PAS-SMP-12-008, CERN, Geneva, 2012. URL `https://cds.cern.ch/record/1434360`.

[32] S van der Meer. Calibration of the effective beam height in the ISR. Technical Report CERN-ISR-PO-68-31. ISR-PO-68-31, CERN, Geneva, 1968. URL `https://cds.cern.ch/record/296752`.

[33] The CMS collaboration. Performance of cms muon reconstruction in pp collision events at ,$\sqrt{s}$=7 tev. *Journal of Instrumentation*, 7(10):P10002, 2012. URL `http://stacks.iop.org/1748-0221/7/i=10/a=P10002`.

[34] Serguei Chatrchyan et al. Performance of CMS muon reconstruction in pp collision events at $\sqrt{s} = 7$ TeV. *JINST*, 7:P10002, 2012. doi: 10.1088/1748-0221/7/10/P10002.

[35] Rudolph Emil Kalman. A new approach to linear filtering and prediction problems. *Transactions of the ASME–Journal of Basic Engineering*, 82(Series D):35–45, 1960.

[36] CMS Collaboration. Particle–flow event reconstruction in CMS and performance for jets, taus, and $\vec{E}_{\mathrm{t}}^{\mathrm{miss}}$. CMS Physics Analysis Summary CMS-PAS-PFT-09-001, 2009. URL http://cdsweb.cern.ch/record/1194487.

[37] Serguei Chatrchyan et al. Measurement of Higgs boson production and properties in the WW decay channel with leptonic final states. *JHEP*, 01:096, 2014. doi: 10.1007/JHEP01(2014)096.

[38] Vardan Khachatryan et al. Performance of Electron Reconstruction and Selection with the CMS Detector in Proton-Proton Collisions at $\sqrt{s}$=8 TeV. *JINST*, 10(06):P06005, 2015. doi: 10.1088/1748-0221/10/06/P06005.

[39] Electron reconstruction and identification at sqrt(s) = 7 TeV. Technical Report CMS-PAS-EGM-10-004, CERN, Geneva, 2010. URL https://cds.cern.ch/record/1299116.

[40] Matteo Cacciari, Gavin P. Salam, and Gregory Soyez. The Anti-k(t) jet clustering algorithm. *JHEP*, 04:063, 2008. doi: 10.1088/1126-6708/2008/04/063.

[41] Torbjorn Sjostrand, Stephen Mrenna, and Peter Z. Skands. PYTHIA 6.4 Physics and Manual. *JHEP*, 05:026, 2006. doi: 10.1088/1126-6708/2006/05/026.

[42] Torbjorn Sjostrand, Stephen Mrenna, and Peter Z. Skands. A Brief Introduction to PYTHIA 8.1. *Comput.Phys.Commun.*, 178:852–867, 2008. doi: 10.1016/j.cpc.2008.01.036.

[43] Rick Field. Early LHC Underlying Event Data - Findings and Surprises. 2010.

[44] Serguei Chatrchyan et al. Jet and underlying event properties as a function of charged-particle multiplicity in proton–proton collisions at $\sqrt{s}$ = 7 TeV. *Eur.Phys.J.*, C73(12):2674, 2013. doi: 10.1140/epjc/s10052-013-2674-5.

[45] Johan Alwall, Michel Herquet, Fabio Maltoni, Olivier Mattelaer, and Tim Stelzer. MadGraph 5 : Going Beyond. *JHEP*, 1106:128, 2011. doi: 10.1007/JHEP06(2011)128.

[46] John M. Campbell and R. K. Ellis. MCFM for the Tevatron and the LHC. *Nucl. Phys. Proc. Suppl.*, 205-206:10, 2010. doi: 10.1016/j.nuclphysbps.2010.08.011.

[47] Carlo Oleari. The POWHEG-BOX. *Nucl.Phys.Proc.Suppl.*, 205-206:36–41, 2010. doi: 10.1016/j.nuclphysbps.2010.08.016.

[48] S. Jadach, Z. Was, R. Decker, and Johann H. Kuhn. The tau decay library TAUOLA: Version 2.4. *Comput.Phys.Commun.*, 76:361–380, 1993. doi: 10.1016/0010-4655(93)90061-G.

[49]

[50] Serguei Chatrchyan et al. Measurement of WW production and search for the Higgs boson in pp collisions at $\sqrt{s} = 7$ TeV. *Phys. Lett. B*, 699:25, 2011. doi: 10.1016/j.physletb.2011.03.056.

[51] Hung-Liang Lai, J. Huston, Z. Li, P. Nadolsky, J. Pumplin, D. Stump, and C.-P. Yuan. Uncertainty induced by QCD coupling in the CTEQ global analysis of parton distributions. *Phys. Rev. D*, 82:054021, 2010. doi: 10.1103/PhysRevD.82.054021.

[52] John M. Campbell, J. W. Huston, and W. J. Stirling. Hard Interactions of Quarks and Gluons: A Primer for LHC Physics. *Rept. Prog. Phys.*, 70:89, 2007. doi: 10.1088/0034-4885/70/1/R02.

[53] Serguei Chatrchyan et al. Measurement of the inelastic proton-proton cross section at $\sqrt{s} = 7$TeV. *Phys. Lett. B*, 722:5, 2013. doi: 10.1016/j.physletb.2013.03.024.

[54] Serguei Chatrchyan et al. Measurement of the W^+W^- and ZZ production cross sections in pp collisions at $\sqrt{s} = 8$ TeV. *Phys. Lett. B*, 721:190, 2013. doi: 10.1016/j.physletb.2013.03.027.

[55] Serguei Chatrchyan et al. Measurement of the zz production cross section and search for anomalous couplings in $2\ell 2\ell'$ final states in pp collisions at $\sqrt{s} = 7$TeV. *JHEP*, 01:063, 2013. doi: 10.1007/JHEP01(2013)063.

[56] Serguei Chatrchyan et al. Measurement of the Wγ and Zγ inclusive cross sections in pp collisions at $\sqrt{s} = 7$ TeV and limits on anomalous triple gauge boson couplings. *Phys. Rev. D*, 89:092005, 2014. doi: 10.1103/PhysRevD.89.092005.

[57] Vardan Khachatryan et al. Measurement of the Zγ production cross section in pp collisions at 8 TeV and search for anomalous triple gauge boson couplings. *JHEP*, 04:164, 2015. doi: 10.1007/JHEP04(2015)164.

[58] Vardan Khachatryan et al. Measurement of top quark-antiquark pair production in association with a W or Z boson in pp collisions at $\sqrt{s} = 8$ TeV. *Eur. Phys. J. C*, 74:3060, 2014. doi: 10.1140/epjc/s10052-014-3060-7.

[59] CMS Collaboration. CMS Luminosity Based on Pixel Cluster Counting - Summer 2013 Update. CMS Physics Analysis Summary CMS-PAS-LUM-13-001, 2013. URL `https://cds.cern.ch/record/1598864`.

[60] Louis Lyons, Duncan Gibaut, and Peter Clifford. How to combine correlated estimates of a single physical quantity. *Nucl. Instrum. Meth. A*, 270:110, 1988. doi: 10.1016/0168-9002(88)90018-6.

[61] A. Valassi. Combining correlated measurements of several different physical quantities. *Nucl. Instrum. Meth. A*, 500:391, 2003. doi: 10.1016/S0168-9002(03)00329-2.

[62] Massimiliano Grazzini, Stefan Kallweit, Dirk Rathlev, and Marius Wiesemann. $W^{\pm}Z$ production at hadron colliders in NNLO QCD. *Phys. Lett.*, B761:179–183, 2016. doi: 10.1016/j.physletb.2016.08.017.

[63] G. D'Agostini. A Multidimensional unfolding method based on Bayes' theorem. *Nucl. Instrum. Meth.*, A362:487–498, 1995. doi: 10.1016/0168-9002(95)00274-X.

[64] Vardan Khachatryan et al. Measurement of the WZ production cross section in pp collisions at $\sqrt{s} = 7$ and 8 TeV and search for anomalous triple gauge couplings at $\sqrt{s} = 8$ TeV. *Accepted in: Eur. Phys. J. C*, 2016.

[65] Cms twiki. `https://twiki.cern.ch/twiki/bin/view/CMSPublic/PhysicsResultsCombined`.

[66] T. Binoth, N. Kauer, and P. Mertsch. Gluon-induced QCD corrections to pp $\to$ ZZ $\to$ $\ell\bar{\ell}\ell'\bar{\ell}'$. In *Proceedings, 16th International Workshop on Deep Inelastic Scattering and Related Subjects (DIS 2008)*, page 142, 2008. doi: 10.3360/dis.2008.142.

[67] Huang-Liang Lai, M. Guzzi, J. Huston, Z. Li, P. Nadolsky, J. Pumplin, and C.-P. Yuan. New parton distributions for collider physics. *Phys. Rev. D*, 82:074024, 2010. doi: 10.1103/PhysRevD.82.074024.

[68] Serguei Chatrchyan et al. Measurement of Higgs boson production and properties in the WW decay channel with leptonic final states. *JHEP*, 01:096, 2014. doi: 10.1007/JHEP01(2014)096.

[69] Matteo Cacciari and Gavin P. Salam. Pileup subtraction using jet areas. *Phys. Lett. B*, 659:119, 2008. doi: 10.1016/j.physletb.2007.09.077.

[70] Vardan Khachatryan et al. Measurements of inclusive W and Z cross sections in pp collisions at $\sqrt{s} = 7$ TeV. *JHEP*, 01:080, 2011. doi: 10.1007/JHEP01(2011)080.

[71] Matteo Cacciari, Gavin P. Salam, and Gregory Soyez. The anti-k_t jet clustering algorithm. *JHEP*, 04:063, 2008. doi: 10.1088/1126-6708/2008/04/063.

[72] Matteo Cacciari, Gavin P. Salam, and Gregory Soyez. FastJet user manual. *Eur. Phys. J. C*, 72:1896, 2012. doi: 10.1140/epjc/s10052-012-1896-2.

[73] CMS Collaboration. Commissioning of the particle-flow event reconstruction with the first LHC collisions recorded in the CMS detector. CMS Physics Analysis Summary CMS-PAS-PFT-10-001, 2010. URL `http://cdsweb.cern.ch/record/1247373`.

[74] Serguei Chatrchyan et al. Determination of jet energy calibration and transverse momentum resolution in CMS. *JINST*, 6:P11002, 2011. doi: 10.1088/1748-0221/6/11/P11002.

[75] J. M. Campbell, W. Huston, J, and W. J. Stirling. Hard interactions of quarks and gluons: a primer for lhc physics. *Rep. Prog. Phys.*, 70:89, 2007. doi: 10.1088/0034-4885/70/1/R02.

[76] CMS Collaboration. Measurement of the WZ production cross section in pp collisions at $\sqrt{s} = 13$ TeV. Submitted to Phys. Lett. B, 2016.

[77] Georges Aad et al. Measurement of WZ production in proton-proton collisions at $\sqrt{s} =$ 7 TeV with the ATLAS detector. *Eur. Phys. J. C*, 72:2173, 2012. doi: 10.1140/epjc/s10052-012-2173-0.

[78] Georges Aad et al. Measurements of $W^{\pm}Z$ production cross sections in pp collisions at $\sqrt{s} = 8$ TeV with the ATLAS detector and limits on anomalous gauge boson self-couplings. *Phys. Rev. D*, 93:092004, 2016. doi: 10.1103/PhysRevD.93.092004.

[79] Morad Aaboud et al. Measurement of the $W^{\pm}Z$-boson production cross sections in pp collisions at $\sqrt{s} = 13$ TeV with the ATLAS detector. *Phys. Lett. B*, 759:601, 2016. doi: 10.1016/j.physletb.2016.06.023.

[80] Matteo Cacciari, Gavin P. Salam, and Gregory Soyez. The anti-k_t jet clustering algorithm. *JHEP*, 04:063, 2008. doi: 10.1088/1126-6708/2008/04/063.

[81] G. D'Agostini. A multidimensional unfolding method based on Bayes' theorem. *Nucl. Instrum. Meth. A*, 362:487, 1995. doi: 10.1016/0168-9002(95)00274-X.

[82] Tim Adye. Unfolding algorithms and tests using RooUnfold. In Harrison Prosper and Louis Lyons, editors, *PHYSTAT 2011 Workshop on Statistical Issues Related to Discovery Claims in Search Experiments and Unfolding*, page 313, Geneva, Switzerland, 2011. doi: 10.5170/CERN-2011-006.313.

Curriculum vitae

Personal

Name	Lucija (Tikvica) Sudić
Address	Ulica grada Vukovara 43, 10000 Zagreb, Croatia
Date of Birth	August 24, 1987
Place of birth	Zagreb, Croatia
Citizenship	Croatian
Phone	+385 98 355387
Email	`lucija87@gmail.com`
Languages	English, basic German, Croatian - native

Education

2012 -	**PhD**, Faculty of Science, Physics department *Title*: Study of associated W and Z boson production in proton proton collisions with the CMS detector at the Large Hadron Collider *Advisor:* Prof. Vuko Brigljević, thesis defence is scheduled for April 6th 2017.
2006 - 2011	**MSc**, Faculty of Science, Physics department *Title*: Study of muons associated with Z boson in pp collisions at the LHC *Advisor:* Prof. Vuko Brigljević, thesis defended on December, 7th 2011.
2002 - 2005	Gymnasium school "Gimnazija Lucijana Vranjanina" in Zagreb
1994 - 2002	Primary scool "Antun Augustinčić" in Zaprešić Primary music school (piano) "Ferdo Livadić" in Samobor

Professional experience

Since 2012 I've been a part of the CMS group at Ruđer Bošković Institute, working on WZ production cross section measurement and on technical aspects of CMS detector:

- One of the main contributors to WZ cross section measurement at $\sqrt{s} = 8$ TeV. Collaboration with Instituto de Fisica de Cantabria (IFCA), Spain and Universidad de Oviedo,

Spain.

- Participated in pixel detector recommissioning during the long shutdown.

Schools and Conferences

2010	CERN Summer Student Programme, Geneva, Switzerland
2013	CMSDAS - Data analysis school, Hamburg, Germany
2012	Silicon Detector Workshop, Split, Croatia

Computer skills

- Programing languages: C, C++, Fortran, Python
- Software: ROOT, Mathematica

Other

Participation in various physics and science outreach programs:

- Organization of International Masterclasses: lectures and laboratory exercises for high school students covering various topics in high energy physics.

Publications

1. **"Observation of the associated production of a single top quark and a W boson in pp collisions at $\sqrt{s}$ =8 TeV"**
   S. Chatrchyan *et al.* [CMS Collaboration].
   arXiv:1401.2942 [hep-ex]
   DOI:10.1103/PhysRevLett.112.231802
   Phys. Rev. Lett. **112**, no. 23, 231802 (2014)
   CMS-TOP-12-040, CERN-PH-EP-2013-237
2. **"Measurement of the $t\bar{t}$ production cross section in the dilepton channel in pp collisions at $\sqrt{s}$ = 8 TeV"**
   S. Chatrchyan *et al.* [CMS Collaboration].
   arXiv:1312.7582 [hep-ex], arXiv:1312.7582
   DOI:10.1007/JHEP02(2014)024, 10.1007/JHEP02(2014)102
   JHEP **1402**, 024 (2014), Erratum: [JHEP **1402**, 102 (2014)]
   CMS-TOP-12-007, CERN-PH-EP-2013-234

3. **"Measurement of the production cross section for a W boson and two b jets in pp collisions at $\sqrt{s}$=7 TeV"**
   S. Chatrchyan *et al.* [CMS Collaboration].
   arXiv:1312.6608 [hep-ex]
   DOI:10.1016/j.physletb.2014.06.041
   Phys. Lett. B **735**, 204 (2014)
   CMS-SMP-12-026, CERN-PH-EP-2013-223, CERN-PH-EP-2013-2223
4. **"Measurement of four-jet production in proton-proton collisions at $\sqrt{s} = 7$ TeV"**
   S. Chatrchyan *et al.* [CMS Collaboration].
   arXiv:1312.6440 [hep-ex]
   DOI:10.1103/PhysRevD.89.092010
   Phys. Rev. D **89**, no. 9, 092010 (2014)
   CMS-FSQ-12-013, CERN-PH-EP-2013-229
5. **"Event activity dependence of Y(nS) production in $\sqrt{s_{NN}}$=5.02 TeV pPb and $\sqrt{s}$=2.76 TeV pp collisions"**
   S. Chatrchyan *et al.* [CMS Collaboration].
   arXiv:1312.6300 [nucl-ex]
   DOI:10.1007/JHEP04(2014)103
   JHEP **1404**, 103 (2014)
   CMS-HIN-13-003, CERN-PH-EP-2013-219
6. **"Measurement of the muon charge asymmetry in inclusive $pp \to W + X$ production at $\sqrt{s} = 7$ TeV and an improved determination of light parton distribution functions"**
   S. Chatrchyan *et al.* [CMS Collaboration].
   arXiv:1312.6283 [hep-ex]
   DOI:10.1103/PhysRevD.90.032004
   Phys. Rev. D **90**, no. 3, 032004 (2014)
   CMS-SMP-12-021, CERN-PH-EP-2013-232
7. **"Study of double parton scattering using W + 2-jet events in proton-proton collisions at $\sqrt{s}$ = 7 TeV"**
   S. Chatrchyan *et al.* [CMS Collaboration].
   arXiv:1312.5729 [hep-ex]
   DOI:10.1007/JHEP03(2014)032
   JHEP **1403**, 032 (2014)
   CMS-FSQ-12-028, CERN-PH-EP-2013-224
8. **"Measurement of the properties of a Higgs boson in the four-lepton final state"**
   S. Chatrchyan *et al.* [CMS Collaboration].
   arXiv:1312.5353 [hep-ex]

DOI:10.1103/PhysRevD.89.092007
Phys. Rev. D **89**, no. 9, 092007 (2014)
CMS-HIG-13-002, CERN-PH-EP-2013-220

9. **"Evidence of b-Jet Quenching in PbPb Collisions at $\sqrt{s_{NN}} = 2.76$ TeV"**
S. Chatrchyan *et al.* [CMS Collaboration].
arXiv:1312.4198 [nucl-ex]
DOI:10.1103/PhysRevLett.115.029903, 10.1103/PhysRevLett.113.132301
Phys. Rev. Lett. **113**, no. 13, 132301 (2014), Erratum: [Phys. Rev. Lett. **115**, no. 2, 029903 (2015)]
CMS-HIN-12-003, CERN-PH-EP-2013-228
10. **"Search for Flavor-Changing Neutral Currents in Top-Quark Decays $t \to Zq$ in pp Collisions at $\sqrt{s} = 8$ TeV"**
S. Chatrchyan *et al.* [CMS Collaboration].
arXiv:1312.4194 [hep-ex]
DOI:10.1103/PhysRevLett.112.171802
Phys. Rev. Lett. **112**, no. 17, 171802 (2014)
CMS-TOP-12-037, CERN-PH-EP-2013-208
11. **"Search for top squark and higgsino production using diphoton Higgs boson decays"**
S. Chatrchyan *et al.* [CMS Collaboration].
arXiv:1312.3310 [hep-ex]
DOI:10.1103/PhysRevLett.112.161802
Phys. Rev. Lett. **112**, 161802 (2014)
CMS-SUS-13-014, CERN-PH-EP-2013-226
12. **"Search for top-quark partners with charge 5/3 in the same-sign dilepton final state"**
S. Chatrchyan *et al.* [CMS Collaboration].
arXiv:1312.2391 [hep-ex]
DOI:10.1103/PhysRevLett.112.171801
Phys. Rev. Lett. **112**, no. 17, 171801 (2014)
CMS-B2G-12-012, CERN-PH-EP-2013-216
13. **"Studies of azimuthal dihadron correlations in ultra-central PbPb collisions at $\sqrt{s_{NN}} =$ 2.76 TeV"**
S. Chatrchyan *et al.* [CMS Collaboration].
arXiv:1312.1845 [nucl-ex]
DOI:10.1007/JHEP02(2014)088
JHEP **1402**, 088 (2014)
CMS-HIN-12-011, CERN-PH-EP-2013-214

14. **"Measurement of Higgs boson production and properties in the WW decay channel with leptonic final states"**
    S. Chatrchyan *et al.* [CMS Collaboration].
    arXiv:1312.1129 [hep-ex]
    DOI:10.1007/JHEP01(2014)096
    JHEP **1401**, 096 (2014)
    CMS-HIG-13-023, CERN-PH-EP-2013-221
15. **"Inclusive search for a vector-like T quark with charge $\frac{2}{3}$ in pp collisions at $\sqrt{s}$ = 8 TeV"**
    S. Chatrchyan *et al.* [CMS Collaboration].
    arXiv:1311.7667 [hep-ex]
    DOI:10.1016/j.physletb.2014.01.006
    Phys. Lett. B **729**, 149 (2014)
    CMS-B2G-12-015, CERN-PH-EP-2013-215
16. **"Search for new physics in events with same-sign dileptons and jets in pp collisions at $\sqrt{s}$ = 8 TeV"**
    S. Chatrchyan *et al.* [CMS Collaboration].
    arXiv:1311.6736, arXiv:1311.6736 [hep-ex]
    DOI:10.1007/JHEP01(2015)014, 10.1007/JHEP01(2014)163
    JHEP **1401**, 163 (2014), Erratum: [JHEP **1501**, 014 (2015)]
    CERN-PH-EP-2013-213
17. **"Measurement of the triple-differential cross section for photon+jets production in proton-proton collisions at $\sqrt{s}$=7 TeV"**
    S. Chatrchyan *et al.* [CMS Collaboration].
    arXiv:1311.6141 [hep-ex]
    DOI:10.1007/JHEP06(2014)009
    JHEP **1406**, 009 (2014)
    CMS-QCD-11-005, CERN-PH-EP-2013-194
18. **"Probing color coherence effects in pp collisions at $\sqrt{s} = 7$ TeV"**
    S. Chatrchyan *et al.* [CMS Collaboration].
    arXiv:1311.5815 [hep-ex]
    DOI:10.1140/epjc/s10052-014-2901-8
    Eur. Phys. J. C **74**, no. 6, 2901 (2014)
    CMS-SMP-12-010, CERN-PH-EP-2013-200
19. **"Search for pair production of excited top quarks in the lepton + jets final state"**
    S. Chatrchyan *et al.* [CMS Collaboration].
    arXiv:1311.5357 [hep-ex]

DOI:10.1007/JHEP06(2014)125
JHEP **1406**, 125 (2014)
CMS-B2G-12-014, CERN-PH-EP-2013-206

20. **"Search for supersymmetry in pp collisions at $\sqrt{s}$=8 TeV in events with a single lepton, large jet multiplicity, and multiple b jets"**
S. Chatrchyan *et al.* [CMS Collaboration].
arXiv:1311.4937 [hep-ex]
DOI:10.1016/j.physletb.2014.04.023
Phys. Lett. B **733**, 328 (2014)
CMS-SUS-13-007, CERN-PH-EP-2013-209
21. **"Measurements of $t\bar{t}$ spin correlations and top-quark polarization using dilepton final states in pp collisions at $\sqrt{s}$ = 7 TeV"**
S. Chatrchyan *et al.* [CMS Collaboration].
arXiv:1311.3924 [hep-ex]
DOI:10.1103/PhysRevLett.112.182001
Phys. Rev. Lett. **112**, no. 18, 182001 (2014)
CMS-TOP-13-003, CERN-PH-EP-2013-211
22. **"Searches for light- and heavy-flavour three-jet resonances in pp collisions at $\sqrt{s} = 8$ TeV"**
S. Chatrchyan *et al.* [CMS Collaboration].
arXiv:1311.1799 [hep-ex]
DOI:10.1016/j.physletb.2014.01.049
Phys. Lett. B **730**, 193 (2014)
CMS-EXO-12-049, CERN-PH-EP-2013-204
23. **"Measurement of higher-order harmonic azimuthal anisotropy in PbPb collisions at $\sqrt{s_{NN}}$ = 2.76 TeV"**
S. Chatrchyan *et al.* [CMS Collaboration].
arXiv:1310.8651 [nucl-ex]
DOI:10.1103/PhysRevC.89.044906
Phys. Rev. C **89**, no. 4, 044906 (2014)
CMS-HIN-11-005, CERN-PH-EP-2013-196
24. **"Measurement of the differential and double-differential Drell-Yan cross sections in proton-proton collisions at $\sqrt{s} = 7$ TeV"**
S. Chatrchyan *et al.* [CMS Collaboration].
arXiv:1310.7291 [hep-ex]
DOI:10.1007/JHEP12(2013)030
JHEP **1312**, 030 (2013)

CMS-SMP-13-003, CERN-PH-EP-2013-168

25. **"Jet and underlying event properties as a function of charged-particle multiplicity in proton–proton collisions at $\sqrt{s}$ = 7 TeV"**
    S. Chatrchyan *et al.* [CMS Collaboration].
    arXiv:1310.4554 [hep-ex]
    DOI:10.1140/epjc/s10052-013-2674-5
    Eur. Phys. J. C **73**, no. 12, 2674 (2013)
    CMS-FSQ-12-022, CERN-PH-EP-2013-195
26. **"Search for the standard model Higgs boson produced in association with a W or a Z boson and decaying to bottom quarks"**
    S. Chatrchyan *et al.* [CMS Collaboration].
    arXiv:1310.3687 [hep-ex]
    DOI:10.1103/PhysRevD.89.012003
    Phys. Rev. D **89**, no. 1, 012003 (2014)
    CMS-HIG-13-012, CERN-PH-EP-2013-188
27. **"Rapidity distributions in exclusive Z + jet and γ + jet events in pp collisions at $\sqrt{s}$ = 7 TeV"**
    S. Chatrchyan *et al.* [CMS Collaboration].
    arXiv:1310.3082 [hep-ex]
    DOI:10.1103/PhysRevD.88.112009
    Phys. Rev. D **88**, no. 11, 112009 (2013)
    CMS-SMP-12-004, CERN-PH-EP-2013-169
28. **"Search for baryon number violation in top-quark decays"**
    S. Chatrchyan *et al.* [CMS Collaboration].
    arXiv:1310.1618 [hep-ex]
    DOI:10.1016/j.physletb.2014.02.033
    Phys. Lett. B **731**, 173 (2014)
    CMS-B2G-12-023, CERN-PH-EP-2013-179
29. **"Measurement of the cross section and angular correlations for associated production of a Z boson with b hadrons in pp collisions at $\sqrt{s} = 7$ TeV"**
    S. Chatrchyan *et al.* [CMS Collaboration].
    arXiv:1310.1349 [hep-ex]
    DOI:10.1007/JHEP12(2013)039
    JHEP **1312**, 039 (2013)
    CMS-EWK-11-015, CERN-PH-EP-2013-153
30. **"Measurement of associated W + charm production in pp collisions at $\sqrt{s}$ = 7 TeV"**
    S. Chatrchyan *et al.* [CMS Collaboration].

arXiv:1310.1138 [hep-ex]
DOI:10.1007/JHEP02(2014)013
JHEP **1402**, 013 (2014)
CMS-SMP-12-002, CERN-PH-EP-2013-149

31. **"Modification of jet shapes in PbPb collisions at $\sqrt{s_{NN}} = 2.76$ TeV"**
S. Chatrchyan *et al.* [CMS Collaboration].
arXiv:1310.0878 [nucl-ex]
DOI:10.1016/j.physletb.2014.01.042
Phys. Lett. B **730**, 243 (2014)
CERN-PH-EP-2013-189, CMS-HIN-12-002
32. **"Observation of a peaking structure in the $J/\psi\phi$ mass spectrum from $B^{\pm} \to J/\psi\phi K^{\pm}$ decays"**
S. Chatrchyan *et al.* [CMS Collaboration].
arXiv:1309.6920 [hep-ex]
DOI:10.1016/j.physletb.2014.05.055
Phys. Lett. B **734**, 261 (2014)
CMS-BPH-11-026, CERN-PH-EP-2013-167
33. **"Searches for new physics using the $t\bar{t}$ invariant mass distribution in pp collisions at $\sqrt{s}$=8 TeV"**
S. Chatrchyan *et al.* [CMS Collaboration].
arXiv:1309.2030 [hep-ex]
DOI:10.1103/PhysRevLett.111.211804, 10.1103/PhysRevLett.112.119903
Phys. Rev. Lett. **111**, no. 21, 211804 (2013), Erratum: [Phys. Rev. Lett. **112**, no. 11, 119903 (2014)]
CMS-B2G-13-001, CERN-PH-EP-2013-162
34. **"Measurement of the production cross section for $Z\gamma \to \nu\bar{\nu}\gamma$ in pp collisions at $\sqrt{s} =$ 7 TeV and limits on $ZZ\gamma$ and $Z\gamma\gamma$ triple gauge boson couplings"**
S. Chatrchyan *et al.* [CMS Collaboration].
arXiv:1309.1117 [hep-ex]
DOI:10.1007/JHEP10(2013)164
JHEP **1310**, 164 (2013)
CMS-SMP-12-020, CERN-PH-EP-2013-098
35. **"Search for a new bottomonium state decaying to $\Upsilon(1S)\pi^+\pi^-$ in pp collisions at $\sqrt{s}$ = 8 TeV"**
S. Chatrchyan *et al.* [CMS Collaboration].
arXiv:1309.0250 [hep-ex]
DOI:10.1016/j.physletb.2013.10.016

Phys. Lett. B **727**, 57 (2013)
CMS-BPH-11-016, CERN-PH-EP-2013-157

36. **"Measurement of the $W\gamma$ and $Z\gamma$ inclusive cross sections in pp collisions at $\sqrt{s} = 7$ TeV and limits on anomalous triple gauge boson couplings"**
S. Chatrchyan *et al.* [CMS Collaboration].
arXiv:1308.6832 [hep-ex]
DOI:10.1103/PhysRevD.89.092005
Phys. Rev. D **89**, no. 9, 092005 (2014)
CMS-EWK-11-009, CERN-PH-EP-2013-108
37. **"Measurement of the W-boson helicity in top-quark decays from $t\bar{t}$ production in lepton+jets events in pp collisions at $\sqrt{s} =$ 7 TeV"**
S. Chatrchyan *et al.* [CMS Collaboration].
arXiv:1308.3879 [hep-ex]
DOI:10.1007/JHEP10(2013)167
JHEP **1310**, 167 (2013)
CMS-TOP-11-020, CERN-PH-EP-2013-133
38. **"Angular analysis and branching fraction measurement of the decay $B^0 \to K^{*0}\mu^+\mu^-$"**
S. Chatrchyan *et al.* [CMS Collaboration].
arXiv:1308.3409 [hep-ex]
DOI:10.1016/j.physletb.2013.10.017
Phys. Lett. B **727**, 77 (2013)
CMS-BPH-11-009, CERN-PH-EP-2013-152
39. **"Search for top-squark pair production in the single-lepton final state in pp collisions at $\sqrt{s}$ = 8 TeV"**
S. Chatrchyan *et al.* [CMS Collaboration].
arXiv:1308.1586 [hep-ex]
DOI:10.1140/epjc/s10052-013-2677-2
Eur. Phys. J. C **73**, no. 12, 2677 (2013)
CMS-SUS-13-011, CERN-PH-EP-2013-148
40. **"Measurement of the prompt J/ψ and ψ(2S) polarizations in pp collisions at $\sqrt{s}$ = 7 TeV"**
S. Chatrchyan *et al.* [CMS Collaboration].
arXiv:1307.6070 [hep-ex]
DOI:10.1016/j.physletb.2013.10.055
Phys. Lett. B **727**, 381 (2013)
CMS-BPH-13-003, CERN-PH-EP-2013-140

41. **"Search for a Higgs boson decaying into a Z and a photon in pp collisions at sqrt(s) = 7 and 8 TeV"**
    S. Chatrchyan *et al.* [CMS Collaboration].
    arXiv:1307.5515 [hep-ex]
    DOI:10.1016/j.physletb.2013.09.057
    Phys. Lett. B **726**, 587 (2013)
    CMS-HIG-13-006, CERN-PH-EP-2013-113
42. **"Measurement of the B(s) to mu+ mu- branching fraction and search for B0 to mu+ mu- with the CMS Experiment"**
    S. Chatrchyan *et al.* [CMS Collaboration].
    arXiv:1307.5025 [hep-ex]
    DOI:10.1103/PhysRevLett.111.101804
    Phys. Rev. Lett. **111**, 101804 (2013)
    CMS-BPH-13-004, CERN-PH-EP-2013-129
43. **"Measurement of the top-quark mass in all-jets $t\bar{t}$ events in pp collisions at $\sqrt{s}$=7 TeV"**
    S. Chatrchyan *et al.* [CMS Collaboration].
    arXiv:1307.4617 [hep-ex]
    DOI:10.1140/epjc/s10052-014-2758-x
    Eur. Phys. J. C **74**, no. 4, 2758 (2014)
    CMS-TOP-11-017, CERN-PH-EP-2013-124
44. **"Study of the production of charged pions, kaons, and protons in pPb collisions at $\sqrt{s_{NN}} =$ 5.02 TeV"**
    S. Chatrchyan *et al.* [CMS Collaboration].
    arXiv:1307.3442 [hep-ex]
    DOI:10.1140/epjc/s10052-014-2847-x
    Eur. Phys. J. C **74**, no. 6, 2847 (2014)
    CMS-HIN-12-016, CERN-PH-EP-2013-096
45. **"Determination of the top-quark pole mass and strong coupling constant from the t t-bar production cross section in pp collisions at $\sqrt{s}$ = 7 TeV"**
    S. Chatrchyan *et al.* [CMS Collaboration].
    arXiv:1307.1907 [hep-ex]
    DOI:10.1016/j.physletb.2014.08.040, 10.1016/j.physletb.2013.12.009
    Phys. Lett. B **728**, 496 (2014), Erratum: [Phys. Lett. B **738**, 526 (2014)]
    CMS-TOP-12-022, CERN-PH-EP-2013-121
46. **"Search for top squarks in *R*-parity-violating supersymmetry using three or more leptons and b-tagged jets"**

S. Chatrchyan *et al.* [CMS Collaboration].
arXiv:1306.6643 [hep-ex]
DOI:10.1103/PhysRevLett.111.221801
Phys. Rev. Lett. **111**, no. 22, 221801 (2013)
CMS-SUS-13-003, CERN-PH-EP-2013-093

47. **"Energy Calibration and Resolution of the CMS Electromagnetic Calorimeter in pp Collisions at $\sqrt{s} = 7$ TeV"**
S. Chatrchyan *et al.* [CMS Collaboration].
arXiv:1306.2016 [hep-ex]
DOI:10.1088/1748-0221/8/09/P09009
JINST **8**, P09009 (2013), [JINST **8**, 9009 (2013)]
CMS-EGM-11-001, CERN-PH-EP-2013-097
48. **"Measurement of the W^+W^- Cross section in pp Collisions at $\sqrt{s} = 7$ TeV and Limits on Anomalous $WW\gamma$ and WWZ couplings"**
S. Chatrchyan *et al.* [CMS Collaboration].
arXiv:1306.1126 [hep-ex]
DOI:10.1140/epjc/s10052-013-2610-8
Eur. Phys. J. C **73**, no. 10, 2610 (2013)
CMS-SMP-12-005, CERN-PH-EP-2013-075
49. **"Measurement of the hadronic activity in events with a Z and two jets and extraction of the cross section for the electroweak production of a Z with two jets in pp collisions at $\sqrt{s}$ = 7 TeV"**
S. Chatrchyan *et al.* [CMS Collaboration].
arXiv:1305.7389 [hep-ex]
DOI:10.1007/JHEP10(2013)062
JHEP **1310**, 062 (2013)
CMS-FSQ-12-019, CERN-PH-EP-2013-060
50. **"Measurement of neutral strange particle production in the underlying event in proton-proton collisions at sqrt(s) = 7 TeV"**
S. Chatrchyan *et al.* [CMS Collaboration].
arXiv:1305.6016 [hep-ex]
DOI:10.1103/PhysRevD.88.052001
Phys. Rev. D **88**, 052001 (2013)
CMS-QCD-11-010, CERN-PH-EP-2013-086
51. **"Study of exclusive two-photon production of W^+W^- in pp collisions at $\sqrt{s} = 7$ TeV and constraints on anomalous quartic gauge couplings"**
S. Chatrchyan *et al.* [CMS Collaboration].

arXiv:1305.5596 [hep-ex]
DOI:10.1007/JHEP07(2013)116
JHEP **1307**, 116 (2013)
CMS-FSQ-12-010, CERN-PH-EP-2013-084

52. **"Search for gluino mediated bottom- and top-squark production in multijet final states in pp collisions at 8 TeV"**
S. Chatrchyan *et al.* [CMS Collaboration].
arXiv:1305.2390 [hep-ex]
DOI:10.1016/j.physletb.2013.06.058
Phys. Lett. B **725**, 243 (2013)
CMS-SUS-12-024, CERN-PH-EP-2013-076
53. **"Multiplicity and transverse momentum dependence of two- and four-particle correlations in pPb and PbPb collisions"**
S. Chatrchyan *et al.* [CMS Collaboration].
arXiv:1305.0609 [nucl-ex]
DOI:10.1016/j.physletb.2013.06.028
Phys. Lett. B **724**, 213 (2013)
CMS-HIN-13-002, CERN-PH-EP-2013-077
54. **"Searches for long-lived charged particles in pp collisions at $\sqrt{s}$=7 and 8 TeV"**
S. Chatrchyan *et al.* [CMS Collaboration].
arXiv:1305.0491 [hep-ex]
DOI:10.1007/JHEP07(2013)122
JHEP **1307**, 122 (2013)
CMS-EXO-12-026, CERN-PH-EP-2013-073
55. **"Measurement of the ratio of the inclusive 3-jet cross section to the inclusive 2-jet cross section in pp collisions at $\sqrt{s}$ = 7 TeV and first determination of the strong coupling constant in the TeV range"**
S. Chatrchyan *et al.* [CMS Collaboration].
arXiv:1304.7498 [hep-ex]
DOI:10.1140/epjc/s10052-013-2604-6
Eur. Phys. J. C **73**, no. 10, 2604 (2013)
CMS-QCD-11-003, CERN-PH-EP-2013-057
56. **"Measurement of the Λ_b^0 lifetime in pp collisions at $\sqrt{s} = 7$ TeV"**
S. Chatrchyan *et al.* [CMS Collaboration].
arXiv:1304.7495 [hep-ex]
DOI:10.1007/JHEP07(2013)163
JHEP **1307**, 163 (2013)

CMS-BPH-11-013, CERN-PH-EP-2013-065

57. **"Measurement of masses in the $t\bar{t}$ system by kinematic endpoints in pp collisions at $\sqrt{s}$ = 7 TeV"**
S. Chatrchyan *et al.* [CMS Collaboration].
arXiv:1304.5783 [hep-ex]
DOI:10.1140/epjc/s10052-013-2494-7
Eur. Phys. J. C **73**, 2494 (2013)
CMS-TOP-11-027, CERN-PH-EP-2013-059

58. **"Search for a standard-model-like Higgs boson with a mass in the range 145 to 1000 GeV at the LHC"**
S. Chatrchyan *et al.* [CMS Collaboration].
arXiv:1304.0213 [hep-ex]
DOI:10.1140/epjc/s10052-013-2469-8
Eur. Phys. J. C **73**, 2469 (2013)
CMS-HIG-12-034, CERN-PH-EP-2013-050

59. **"Search for microscopic black holes in pp collisions at sqrt(s) = 8 TeV"**
S. Chatrchyan *et al.* [CMS Collaboration].
arXiv:1303.5338 [hep-ex]
DOI:10.1007/JHEP07(2013)178
JHEP **1307**, 178 (2013)
CMS-EXO-12-009, CERN-PH-EP-2013-043

60. **"Studies of jet mass in dijet and W/Z + jet events"**
S. Chatrchyan *et al.* [CMS Collaboration].
arXiv:1303.4811 [hep-ex]
DOI:10.1007/JHEP05(2013)090
JHEP **1305**, 090 (2013)
CMS-SMP-12-019, CERN-PH-EP-2013-016

61. **"Observation of a new boson with mass near 125 GeV in pp collisions at $\sqrt{s}$ = 7 and 8 TeV"**
S. Chatrchyan *et al.* [CMS Collaboration].
arXiv:1303.4571 [hep-ex]
DOI:10.1007/JHEP06(2013)081
JHEP **1306**, 081 (2013)
CMS-HIG-12-036, CERN-PH-EP-2013-035

62. **"Measurement of associated production of vector bosons and top quark-antiquark pairs at sqrt(s) = 7 TeV"**
S. Chatrchyan *et al.* [CMS Collaboration].

arXiv:1303.3239 [hep-ex]
DOI:10.1103/PhysRevLett.110.172002
Phys. Rev. Lett. **110**, 172002 (2013)
CMS-TOP-12-014, CERN-PH-EP-2013-033

63. **"Search for supersymmetry in hadronic final states with missing transverse energy using the variables α_T and b-quark multiplicity in pp collisions at $\sqrt{s} = 8$ TeV"**
S. Chatrchyan *et al.* [CMS Collaboration].
arXiv:1303.2985 [hep-ex]
DOI:10.1140/epjc/s10052-013-2568-6
Eur. Phys. J. C **73**, no. 9, 2568 (2013)
CMS-SUS-12-028, CERN-PH-EP-2013-037
64. **"Search for the standard model Higgs boson produced in association with a top-quark pair in pp collisions at the LHC"**
S. Chatrchyan *et al.* [CMS Collaboration].
arXiv:1303.0763 [hep-ex]
DOI:10.1007/JHEP05(2013)145
JHEP **1305**, 145 (2013)
CMS-HIG-12-035, CERN-PH-EP-2013-027
65. **"Search for narrow resonances using the dijet mass spectrum in pp collisions at $\sqrt{s}$=8 TeV"**
S. Chatrchyan *et al.* [CMS Collaboration].
arXiv:1302.4794 [hep-ex]
DOI:10.1103/PhysRevD.87.114015
Phys. Rev. D **87**, no. 11, 114015 (2013)
CMS-EXO-12-016, CERN-PH-EP-2013-015
66. **"Measurement of the X(3872) production cross section via decays to J/psi pi pi in pp collisions at sqrt(s) = 7 TeV"**
S. Chatrchyan *et al.* [CMS Collaboration].
arXiv:1302.3968 [hep-ex]
DOI:10.1007/JHEP04(2013)154
JHEP **1304**, 154 (2013)
CMS-BPH-11-011, CERN-PH-EP-2013-014
67. **"Measurement of the cross section for electroweak production of Zγ in association with two jets and constraints on anomalous quartic gauge couplings in proton-proton collisions at $\sqrt{s} = 8$ TeV"**
V. Khachatryan *et al.* [CMS Collaboration].
arXiv:1702.03025 [hep-ex]

CMS-SMP-14-018, CERN-EP-2016-308

68. **"Search for supersymmetry with multiple charged leptons in proton-proton collisions at $\sqrt{s} = 13$ TeV"**
V. Khachatryan *et al.* [CMS Collaboration].
arXiv:1701.06940 [hep-ex]
CMS-SUS-16-003, CERN-EP-2016-306

69. **"Measurement of the $t\bar{t}$ production cross section using events with one lepton and at least one jet in pp collisions at $\sqrt{s}$=13 TeV"**
A. M. Sirunyan *et al.* [CMS Collaboration].
arXiv:1701.06228 [hep-ex]
CMS-TOP-16-006, CERN-EP-2016-321

70. **"Search for dark matter and unparticles in events with a Z boson and missing transverse momentum in proton-proton collisions at $\sqrt{s}$ = 13 TeV"**
A. M. Sirunyan *et al.* [CMS Collaboration].
arXiv:1701.02042 [hep-ex]
DOI:10.1007/JHEP03(2017)061
JHEP **1703**, 061 (2017)
CMS-EXO-16-010, CERN-EP-2016-309, FERMILAB-PUB-17-011-CMS

71. **"Search for light bosons in decays of the 125 GeV Higgs boson in proton-proton collisions at $\sqrt{s}$ = 8 TeV"**
V. Khachatryan *et al.* [CMS Collaboration].
arXiv:1701.02032 [hep-ex]
CMS-HIG-16-015, CERN-EP-2016-292

72. **"Search for supersymmetry in the all-hadronic final state using top quark tagging in pp collisions at $\sqrt{s}$ = 13 TeV"**
V. Khachatryan *et al.* [CMS Collaboration].
arXiv:1701.01954 [hep-ex]
CMS-SUS-16-009, CERN-EP-2016-293

73. **"Search for leptophobic Z' bosons decaying into four-lepton final states in proton-proton collisions at $\sqrt{s}$ =8 TeV"**
V. Khachatryan *et al.* [CMS Collaboration].
arXiv:1701.01345 [hep-ex]
CMS-EXO-14-006, CERN-EP-2016-295

74. **"Search for heavy gauge W' boson in events with an energetic lepton and large missing transverse momentum at $\sqrt{s} = 13$ TeV"**
V. Khachatryan *et al.* [CMS Collaboration].
arXiv:1612.09274 [hep-ex]

CMS-EXO-15-006, CERN-EP-2016-281

75. **"Measurement of electroweak-induced production of W gamma with two jets in pp collisions at $\sqrt{s}$ = 8 TeV and constraints on anomalous quartic gauge couplings"**
V. Khachatryan *et al.* [CMS Collaboration].
arXiv:1612.09256 [hep-ex]
CMS-SMP-14-011, CERN-EP-2016-289

76. **"Measurements of the charm jet cross section and nuclear modification factor in pPb collisions at $\sqrt{sNN}$ = 5.02 TeV"**
A. M. Sirunyan *et al.* [CMS Collaboration].
arXiv:1612.08972 [nucl-ex]
CMS-HIN-15-012, CERN-EP-2016-274

77. **"Search for electroweak production of a vector-like quark decaying to a top quark and a Higgs boson using boosted topologies in fully hadronic final states"**
A. M. Sirunyan *et al.* [CMS Collaboration].
arXiv:1612.05336 [hep-ex]
CMS-B2G-16-005, CERN-EP-2016-290

78. **"Search for heavy neutrinos or third-generation leptoquarks in final states with two hadronically decaying tau leptons and two jets in proton-proton collisions at sqrt(s) = 13 TeV"**
V. Khachatryan *et al.* [CMS Collaboration].
arXiv:1612.01190 [hep-ex]
DOI:10.1007/JHEP03(2017)077
JHEP **1703**, 077 (2017)
CMS-EXO-16-016, CERN-EP-2016-286

79. **"Search for single production of a heavy vector-like T quark decaying to a Higgs boson and a top quark with a lepton and jets in the final state"**
V. Khachatryan *et al.* [CMS Collaboration].
arXiv:1612.00999 [hep-ex]

CMS-B2G-15-008, CERN-EP-2016-279

80. **"Search for CP violation in top quark-antiquark production and decay in proton-proton collisions at $\sqrt{s}$ = 8 TeV"**
V. Khachatryan *et al.* [CMS Collaboration].
arXiv:1611.08931 [hep-ex]

CMS-TOP-16-001, CERN-EP-2016-266

81. **"Search for supersymmetry in events with photons and missing transverse energy in pp collisions at 13 TeV"**
V. Khachatryan *et al.* [CMS Collaboration].
arXiv:1611.06604 [hep-ex]

CMS-SUS-15-012, CERN-EP-2016-269

82. **"Search for heavy resonances decaying to tau lepton pairs in proton-proton collisions at $\sqrt{s} = 13$ TeV"**
V. Khachatryan *et al.* [CMS Collaboration].
arXiv:1611.06594 [hep-ex]
DOI:10.1007/JHEP02(2017)048
JHEP **1702**, 048 (2017)
CMS-EXO-16-008, CERN-EP-2016-273

83. **"Measurements of the associated production of a Z boson and b jets in pp collisions at $\sqrt{s}$ = 8 TeV"**
V. Khachatryan *et al.* [CMS Collaboration].
arXiv:1611.06507 [hep-ex]

CMS-SMP-14-010, CERN-EP-2016-254

84. **"Measurement of the $t\bar{t}$ production cross section using events in the eμ final state in pp collisions at $\sqrt{s} = 13$ TeV"**
V. Khachatryan *et al.* [CMS Collaboration].
arXiv:1611.04040 [hep-ex]
DOI:10.1140/epjc/s10052-017-4718-8
Eur. Phys. J. C **77**, 172 (2017)
CMS-TOP-16-005, CERN-EP-2016-265

85. **"Measurements of the differential production cross sections for a Z boson in association with jets in pp collisions at $\sqrt{s}$ = 8 TeV"**
V. Khachatryan *et al.* [CMS Collaboration].
arXiv:1611.03844 [hep-ex]

CMS-SMP-14-013, CERN-EP-2016-256

86. **"Charged-particle nuclear modification factors in PbPb and pPb collisions at $\sqrt{s_{\mathrm{NN}}} =$ 5.02 TeV"**
V. Khachatryan *et al.* [CMS Collaboration].
arXiv:1611.01664 [nucl-ex]

CMS-HIN-15-015, CERN-EP-2016-242

87. **"Suppression of $\Upsilon(1S)$, $\Upsilon(2S)$ and $\Upsilon(3S)$ production in PbPb collisions at $\sqrt{s_{NN}}$ = 2.76 TeV"**
V. Khachatryan *et al.* [CMS Collaboration].
arXiv:1611.01510 [nucl-ex]

CMS-HIN-15-001, CERN-EP-2016-248

88. **"Relative modification of prompt $\psi(2S)$ and J/ψ yields from pp to PbPb collisions at $\sqrt{s_{NN}} = 5.02$ TeV"**
A. M. Sirunyan *et al.* [CMS Collaboration].
arXiv:1611.01438 [nucl-ex]

CMS-HIN-16-004, CERN-EP-2016-258

89. **"A search for new phenomena in pp collisions at $\sqrt{s}$ = 13 TeV in final states with missing transverse momentum and at least one jet using the α_T variable"**
V. Khachatryan *et al.* [CMS Collaboration].
arXiv:1611.00338 [hep-ex]

CMS-SUS-15-005, CERN-EP-2016-246

90. **"Measurement of the mass difference between top quark and antiquark in pp collisions at sqrt(s) = 8 TeV"**
S. Chatrchyan *et al.* [CMS Collaboration].
arXiv:1610.09551 [hep-ex]
CMS-TOP-12-031, CERN-EP-2016-249

91. **"Searches for invisible decays of the Higgs boson in pp collisions at sqrt(s) = 7, 8, and 13 TeV"**
V. Khachatryan *et al.* [CMS Collaboration].
arXiv:1610.09218 [hep-ex]
DOI:10.1007/JHEP02(2017)135
JHEP **1702**, 135 (2017)
CMS-HIG-16-016, CERN-EP-2016-240

92. **"Search for heavy resonances decaying into a vector boson and a Higgs boson in final states with charged leptons, neutrinos, and b quarks"**
V. Khachatryan *et al.* [CMS Collaboration].
arXiv:1610.08066 [hep-ex]
DOI:10.1016/j.physletb.2017.02.040
Phys. Lett. B **768**, 137 (2017)

CMS-B2G-16-003, CERN-EP-2016-226

93. **"Observation of $\Upsilon(1S)$ pair production in proton-proton collisions at $\sqrt{s} = 8$ TeV"**
V. Khachatryan *et al.* [CMS Collaboration].
arXiv:1610.07095 [hep-ex]

CMS-BPH-14-008, CERN-EP-2016-237

94. **"Search for R-parity violating supersymmetry with displaced vertices in proton-proton collisions at sqrt(s) = 8 TeV"**
V. Khachatryan *et al.* [CMS Collaboration].
arXiv:1610.05133 [hep-ex]
DOI:10.1103/PhysRevD.95.012009
Phys. Rev. D, [Phys. Rev. D **95**, 012009 (2017)]
CMS-SUS-14-020, CERN-EP-2016-224

95. **"Search for electroweak production of charginos in final states with two tau leptons in pp collisions at sqrt(s) = 8 TeV"**
V. Khachatryan *et al.* [CMS Collaboration].
arXiv:1610.04870 [hep-ex]

CMS-SUS-14-022, CERN-EP-2016-225

96. **"Search for top quark decays via Higgs-boson-mediated flavor-changing neutral currents in pp collisions at $\sqrt{s} = 8$ TeV"**
V. Khachatryan *et al.* [CMS Collaboration].
arXiv:1610.04857 [hep-ex]
DOI:10.1007/JHEP02(2017)079
JHEP **1702**, 079 (2017)
CMS-TOP-13-017, CERN-EP-2016-208

97. **"Measurements of differential cross sections for associated production of a W boson and jets in proton-proton collisions at $\sqrt{s} = 8$ TeV"**
V. Khachatryan *et al.* [CMS Collaboration].
arXiv:1610.04222 [hep-ex]
DOI:10.1103/PhysRevD.95.052002
Phys. Rev. D, [Phys. Rev. D **95**, 052002 (2017)]
CMS-SMP-14-023, CERN-EP-2016-231, CERN-PH-EP-2016-231

98. **"Measurement of differential cross sections for top quark pair production using the lepton+jets final state in proton-proton collisions at 13 TeV"**
V. Khachatryan *et al.* [CMS Collaboration].
arXiv:1610.04191 [hep-ex]

CMS-TOP-16-008, CERN-EP-2016-227

99. **"Search for anomalous Wtb couplings and flavour-changing neutral currents in t-channel single top quark production in pp collisions at $\sqrt{s} = 7$ and 8 TeV"**
V. Khachatryan *et al.* [CMS Collaboration].
arXiv:1610.03545 [hep-ex]
DOI:10.1007/JHEP02(2017)028
JHEP **1702**, 028 (2017)
CMS-TOP-14-007, CERN-EP-2016-207

100. **"Search for high-mass Zγ resonances in $e^+e^-\gamma$ and $\mu^+\mu^-\gamma$ final states in proton-proton collisions at $\sqrt{s} = 8$ and 13 TeV"**
V. Khachatryan *et al.* [CMS Collaboration].
arXiv:1610.02960 [hep-ex]
DOI:10.1007/JHEP01(2017)076
JHEP **1701**, 076 (2017)
CMS-EXO-16-021, CERN-EP-2016-230

101. **"Cross section measurement of t-channel single top quark production in pp collisions at $\sqrt{s} = 13$ TeV"**
A. M. Sirunyan *et al.* [CMS Collaboration].
arXiv:1610.00678 [hep-ex]

CMS-TOP-16-003, CERN-EP-2016-233

102. **"Suppression and azimuthal anisotropy of prompt and nonprompt J/ψ production in PbPb collisions at $\sqrt{s_{NN}}$ = 2.76 TeV"**
V. Khachatryan *et al.* [CMS Collaboration].
arXiv:1610.00613 [nucl-ex]

CMS-HIN-14-005, CERN-EP-2016-243

103. **"Observation of charge-dependent azimuthal correlations in pPb collisions and its implication for the search for the chiral magnetic effect"**
V. Khachatryan *et al.* [CMS Collaboration].
arXiv:1610.00263 [nucl-ex]

CMS-HIN-16-009, CERN-EP-2016-236

104. **"Search for supersymmetry in events with one lepton and multiple jets in proton-proton collisions at $\sqrt{(s)} = 13$ TeV"**
V. Khachatryan *et al.* [CMS Collaboration].

arXiv:1609.09386 [hep-ex]
DOI:10.1103/PhysRevD.95.012011
Phys. Rev. D **95**, no. 1, 012011 (2017)
CMS-SUS-15-006, CERN-EP-2016-239

105. **"Search for long-lived charged particles in proton-proton collisions at $\sqrt{s} = 13$ TeV"**
V. Khachatryan *et al.* [CMS Collaboration].
arXiv:1609.08382 [hep-ex]
DOI:10.1103/PhysRevD.94.112004
Phys. Rev. D **94**, no. 11, 112004 (2016)
CMS-EXO-15-010, CERN-EP-2016-204

106. **"Inclusive search for supersymmetry using razor variables in pp collisions at $\sqrt{s} =$ 13 TeV"**
V. Khachatryan *et al.* [CMS Collaboration].
arXiv:1609.07658 [hep-ex]
DOI:10.1103/PhysRevD.95.012003
Phys. Rev. D **95**, no. 1, 012003 (2017)
CMS-SUS-15-004, CERN-EP-2016-214

107. **"Measurement of the WZ production cross section in pp collisions at $\sqrt{s}$ = 7 and 8 TeV and search for anomalous triple gauge couplings at $\sqrt{s}$ = 8 TeV"**
V. Khachatryan *et al.* [CMS Collaboration].
arXiv:1609.05721 [hep-ex]

CMS-SMP-14-014, CERN-EP-2016-205

108. **"Search for narrow resonances in dilepton mass spectra in proton-proton collisions at $\sqrt{s}$ = 13 TeV and combination with 8 TeV data"**
V. Khachatryan *et al.* [CMS Collaboration].
arXiv:1609.05391 [hep-ex]
DOI:10.1016/j.physletb.2017.02.010
Phys. Lett. B **768**, 57 (2017)
CMS-EXO-15-005, CERN-EP-2016-209, FERMILAB-PUB-16-491-CMS

109. **"Measurement of inclusive jet cross-sections in pp and PbPb collisions at $\sqrt{s_{NN}}$=2.76 TeV"**
V. Khachatryan *et al.* [CMS Collaboration].
arXiv:1609.05383 [nucl-ex]

CMS-HIN-13-005, CERN-EP-2016-217

110. **"Measurement and QCD analysis of double-differential inclusive jet cross-sections in pp collisions at $\sqrt{s} = 8$ TeV and ratios to 2.76 and 7 TeV"**
V. Khachatryan *et al.* [CMS Collaboration].
arXiv:1609.05331 [hep-ex]

CMS-SMP-14-001, CERN-EP-2016-196

111. **"Studies of inclusive four-jet production with two b-tagged jets in proton-proton collisions at 7 TeV"**
V. Khachatryan *et al.* [CMS Collaboration].
arXiv:1609.03489 [hep-ex]
DOI:10.1103/PhysRevD.94.112005
Phys. Rev. D **94**, no. 11, 112005 (2016)
CMS-FSQ-13-010, CERN-EP-2016-191

112. **"Search for high-mass diphoton resonances in proton–proton collisions at 13 TeV and combination with 8 TeV search"**
V. Khachatryan *et al.* [CMS Collaboration].
arXiv:1609.02507 [hep-ex]
DOI:10.1016/j.physletb.2017.01.027
Phys. Lett. B **767**, 147 (2017)
CMS-EXO-16-027, CERN-EP-2016-216, CMS-EXO-16-02

113. **"Decomposing transverse momentum balance contributions for quenched jets in PbPb collisions at $\sqrt{s_{\mathrm{NN}}} = 2.76$ TeV"**
V. Khachatryan *et al.* [CMS Collaboration].
arXiv:1609.02466 [nucl-ex]
DOI:10.1007/JHEP11(2016)055
JHEP **1611**, 055 (2016)
CMS-HIN-15-011, CERN-EP-2016-199

114. **"The CMS trigger system"**
V. Khachatryan *et al.* [CMS Collaboration].
arXiv:1609.02366 [physics.ins-det]
DOI:10.1088/1748-0221/12/01/P01020
JINST **12**, no. 01, P01020 (2017)
CMS-TRG-12-001, CERN-EP-2016-160

115. **"Measurement of the total and differential inclusive B^+ hadron cross sections in pp collisions at $\sqrt{s} =$ = 13 TeV"**
V. Khachatryan *et al.* [CMS Collaboration].
arXiv:1609.00873 [hep-ex]

CMS-BPH-15-004, CERN-EP-2016-198

116. **"Measurement of the production cross section of a W boson in association with two b jets in pp collisions at $\sqrt{s} = 8\,\text{TeV}$"**
V. Khachatryan *et al.* [CMS Collaboration].
arXiv:1608.07561 [hep-ex]
DOI:10.1140/epjc/s10052-016-4573-z
Eur. Phys. J. C **77**, no. 2, 92 (2017)
CMS-SMP-14-020, CERN-EP-2016-190

117. **"Measurement of the mass of the top quark in decays with a J/ψ meson in pp collisions at 8 TeV"**
V. Khachatryan *et al.* [CMS Collaboration].
arXiv:1608.03560 [hep-ex]
DOI:10.1007/JHEP12(2016)123
JHEP **1612**, 123 (2016)
CMS-TOP-15-014, CERN-EP-2016-202

118. **"Search for new physics in events with high jet multiplicity and low missing transverse momentum in proton-proton collisions at $\sqrt{s} = 8$ TeV"**
V. Khachatryan *et al.* [CMS Collaboration].
arXiv:1608.01224 [hep-ex]

CMS-EXO-13-001, CERN-EP-2016-187

119. **"Measurement of the ZZ production cross section and Z $\rightarrow l^+l^-l'^+l^{-'}$ branching fraction in pp collisions at $\sqrt{(s)}$=13 TeV"**
V. Khachatryan *et al.* [CMS Collaboration].
arXiv:1607.08834 [hep-ex]
DOI:10.1016/j.physletb.2016.10.054
Phys. Lett. B **763**, 280 (2016)
CMS-SMP-16-001, CERN-EP-2016-174

120. **"Measurement of electroweak production of a W boson and two forward jets in proton-proton collisions at $\sqrt{s} = 8$ TeV"**
V. Khachatryan *et al.* [CMS Collaboration].
arXiv:1607.06975 [hep-ex]
DOI:10.1007/JHEP11(2016)147
JHEP **1611**, 147 (2016)
CMS-SMP-13-012, CERN-EP-2016-093

121. **"Measurement of the WZ production cross section in pp collisions at $\sqrt{(}s) = 13$ TeV"**
V. Khachatryan *et al.* [CMS Collaboration].
arXiv:1607.06943 [hep-ex]
DOI:10.1016/j.physletb.2017.01.011
Phys. Lett. B **766**, 268 (2017)
CMS-SMP-16-002, CERN-EP-2016-169
122. **"Search for dark matter in proton-proton collisions at 8 TeV with missing transverse momentum and vector boson tagged jets"**
V. Khachatryan *et al.* [CMS Collaboration].
arXiv:1607.05764 [hep-ex]
DOI:10.1007/JHEP12(2016)083
JHEP **1612**, 083 (2016)
CMS-EXO-12-055, CERN-EP-2016-178
123. **"Jet energy scale and resolution in the CMS experiment in pp collisions at 8 TeV"**
V. Khachatryan *et al.* [CMS Collaboration].
arXiv:1607.03663 [hep-ex]
DOI:10.1088/1748-0221/12/02/P02014
JINST **12**, no. 02, P02014 (2017)
CMS-JME-13-004, CERN-PH-EP-2015-305
124. **"Search for lepton flavour violating decays of the Higgs boson to $e\tau$ and $e\mu$ in proton–proton collisions at $\sqrt{s} = 8$ TeV"**
V. Khachatryan *et al.* [CMS Collaboration].
arXiv:1607.03561 [hep-ex]
DOI:10.1016/j.physletb.2016.09.062
Phys. Lett. B **763**, 472 (2016)
CMS-HIG-14-040, CERN-EP-2016-112
125. **"Observation of the decay $B^+ \to \psi(2S)\phi(1020)K^+$ in pp collisions at $\sqrt{s} = 8$ TeV"**
V. Khachatryan *et al.* [CMS Collaboration].
arXiv:1607.02638 [hep-ex]
DOI:10.1016/j.physletb.2016.11.001
Phys. Lett. B **764**, 66 (2017)
CMS-BPH-13-009, CERN-EP-2016-161
126. **"Search for new physics in final states with two opposite-sign, same-flavor leptons, jets, and missing transverse momentum in pp collisions at sqrt(s) = 13 TeV"**
V. Khachatryan *et al.* [CMS Collaboration].
arXiv:1607.00915 [hep-ex]

DOI:10.1007/JHEP12(2016)013
JHEP **1612**, 013 (2016)
CMS-SUS-15-011, CERN-EP-2016-132

127. **"Measurement of the differential cross sections for top quark pair production as a function of kinematic event variables in pp collisions at $\sqrt{s}$=7 and 8 TeV"**
V. Khachatryan *et al.* [CMS Collaboration].
arXiv:1607.00837 [hep-ex]
DOI:10.1103/PhysRevD.94.052006
Phys. Rev. D **94**, no. 5, 052006 (2016)
CMS-TOP-12-042, CERN-EP-2016-139

128. **"Searches for *R*-parity-violating supersymmetry in ppcollisions at $\sqrt{(s)} =$ 8 TeV in final states with 0-4 leptons"**
V. Khachatryan *et al.* [CMS Collaboration].
arXiv:1606.08076 [hep-ex]
DOI:10.1103/PhysRevD.94.112009
Phys. Rev. D **94**, no. 11, 112009 (2016)
CMS-SUS-14-003, CERN-EP-2016-097

129. **"Evidence for collectivity in pp collisions at the LHC"**
V. Khachatryan *et al.* [CMS Collaboration].
arXiv:1606.06198 [nucl-ex]
DOI:10.1016/j.physletb.2016.12.009
Phys. Lett. B **765**, 193 (2017)
CMS-HIN-16-010, CERN-EP-2016-147

130. **"Measurement of the transverse momentum spectra of weak vector bosons produced in proton-proton collisions at $\sqrt{s} = 8$ TeV"**
V. Khachatryan *et al.* [CMS Collaboration].
arXiv:1606.05864 [hep-ex]
DOI:10.1007/JHEP02(2017)096
JHEP **1702**, 096 (2017)
CMS-SMP-14-012, CERN-EP-2016-152

131. **"Search for Resonant Production of High-Mass Photon Pairs in Proton-Proton Collisions at $\sqrt{s}$ =8 and 13 TeV"**
V. Khachatryan *et al.* [CMS Collaboration].
arXiv:1606.04093 [hep-ex]
DOI:10.1103/PhysRevLett.117.051802
Phys. Rev. Lett. **117**, no. 5, 051802 (2016)
CMS-EXO-16-018, CERN-EP-2016-154

132. **"Phenomenological MSSM interpretation of CMS searches in pp collisions at sqrt(s) = 7 and 8 TeV"**
V. Khachatryan *et al.* [CMS Collaboration].
arXiv:1606.03577 [hep-ex]
DOI:10.1007/JHEP10(2016)129
JHEP **1610**, 129 (2016)
CMS-SUS-15-010, CERN-EP-2016-094

133. **"Measurements of the Higgs boson production and decay rates and constraints on its couplings from a combined ATLAS and CMS analysis of the LHC pp collision data at $\sqrt{s} = 7$ and 8 TeV"**
G. Aad *et al.* [ATLAS and CMS Collaborations].
arXiv:1606.02266 [hep-ex]
DOI:10.1007/JHEP08(2016)045
JHEP **1608**, 045 (2016)
CERN-EP-2016-100, ATLAS-HIGG-2015-07, CMS-HIG-15-002

134. **"Measurement of the transverse momentum spectrum of the Higgs boson produced in pp collisions at $\sqrt{s} = 8$ TeV using $H \to WW$ decays"**
V. Khachatryan *et al.* [CMS Collaboration].
arXiv:1606.01522 [hep-ex]
DOI:10.1007/JHEP03(2017)032
JHEP **1703**, 032 (2017)
CMS-HIG-15-010, CERN-EP-2016-125

135. **"Search for Dark Matter and Supersymmetry with a Compressed Mass Spectrum in the Vector Boson Fusion Topology in Proton-Proton Collisions at $\sqrt{s} = 8$ TeV"**
V. Khachatryan *et al.* [CMS Collaboration].
arXiv:1605.09305 [hep-ex]
DOI:10.1103/PhysRevLett.118.021802
Phys. Rev. Lett. **118**, no. 2, 021802 (2017)
CMS-SUS-14-019, CERN-EP-2016-096

136. **"Measurement of the W boson helicity fractions in the decays of top quark pairs to lepton + jets final states produced in pp collisions at $\sqrt{s} = 8$TeV"**
V. Khachatryan *et al.* [CMS Collaboration].
arXiv:1605.09047 [hep-ex]
DOI:10.1016/j.physletb.2016.10.007
Phys. Lett. B **762**, 512 (2016)
CMS-TOP-13-008, CERN-EP-2016-118

137. **"Search for top squark pair production in compressed-mass-spectrum scenarios in proton-proton collisions at $\sqrt{s}$ = 8 TeV using the alpha[T] variable"**
V. Khachatryan *et al.* [CMS Collaboration].
arXiv:1605.08993 [hep-ex]
DOI:10.1016/j.physletb.2017.02.007
Phys. Lett. B **767**, 403 (2017)
CMS-SUS-14-006, CERN-EP-2016-103
138. **"Coherent J/Psi photoproduction in ultra-peripheral PbPb collisions at sqrt(s[NN]) = 2.76 TeV with the CMS experiment"**
V. Khachatryan *et al.* [CMS Collaboration].
arXiv:1605.06966 [nucl-ex]

CMS-HIN-12-009, CERN-EP-2016-098
139. **"Multiplicity and rapidity dependence of strange hadron production in pp, pPb, and PbPb collisions at the LHC"**
V. Khachatryan *et al.* [CMS Collaboration].
arXiv:1605.06699 [nucl-ex]
DOI:10.1016/j.physletb.2017.01.075
Phys. Lett. B **768**, 103 (2017)
CMS-HIN-15-006, CERN-EP-2016-105
140. **"Search for supersymmetry in pp collisions at $\sqrt{s} = 13$ TeV in the single-lepton final state using the sum of masses of large-radius jets"**
V. Khachatryan *et al.* [CMS Collaboration].
arXiv:1605.04608 [hep-ex]
DOI:10.1007/JHEP08(2016)122
JHEP **1608**, 122 (2016)
CMS-SUS-15-007, CERN-EP-2016-111
141. **"Measurement of the double-differential inclusive jet cross section in proton–proton collisions at $\sqrt{s} = 13$ TeV"**
V. Khachatryan *et al.* [CMS Collaboration].
arXiv:1605.04436 [hep-ex]
DOI:10.1140/epjc/s10052-016-4286-3
Eur. Phys. J. C **76**, no. 8, 451 (2016)
CMS-SMP-15-007, CERN-EP-2016-104
142. **"Search for new physics in same-sign dilepton events in proton–proton collisions at $\sqrt{s} = 13$ TeV"**
V. Khachatryan *et al.* [CMS Collaboration].

arXiv:1605.03171 [hep-ex]
DOI:10.1140/epjc/s10052-016-4261-z
Eur. Phys. J. C **76**, no. 8, 439 (2016)
CMS-SUS-15-008, CERN-EP-2016-119

143. **"Search for Higgs boson off-shell production in proton-proton collisions at 7 and 8 TeV and derivation of constraints on its total decay width"**
V. Khachatryan *et al.* [CMS Collaboration].
arXiv:1605.02329 [hep-ex]
DOI:10.1007/JHEP09(2016)051
JHEP **1609**, 051 (2016)
CMS-HIG-14-032, CERN-EP-2016-054

144. **"Measurement of the integrated and differential $t\bar{t}$ production cross sections for high-p_t top quarks in pp collisions at $\sqrt{s} = 8$ TeV"**
V. Khachatryan *et al.* [CMS Collaboration].
arXiv:1605.00116 [hep-ex]
DOI:10.1103/PhysRevD.94.072002
Phys. Rev. D **94**, no. 7, 072002 (2016)
CMS-TOP-14-012, CERN-EP-2016-078

145. **"Search for narrow resonances in dijet final states at $\sqrt{(}s) = 8$ TeV with the novel CMS technique of data scouting"**
V. Khachatryan *et al.* [CMS Collaboration].
arXiv:1604.08907 [hep-ex]
DOI:10.1103/PhysRevLett.117.031802
Phys. Rev. Lett. **117**, no. 3, 031802 (2016)
CMS-EXO-14-005, CERN-EP-2016-090

146. **"Pseudorapidity dependence of long-range two-particle correlations in pPb collisions at $\sqrt{s_{NN}} = 5.02$ TeV"**
V. Khachatryan *et al.* [CMS Collaboration].
arXiv:1604.05347 [nucl-ex]

CMS-HIN-14-008, CERN-EP-2016-042

147. **"Search for lepton flavour violating decays of heavy resonances and quantum black holes to an eμ pair in proton-proton collisions at $\sqrt{s}$ = 8 TeV"**
V. Khachatryan *et al.* [CMS Collaboration].
arXiv:1604.05239 [hep-ex]
DOI:10.1140/epjc/s10052-016-4149-y
Eur. Phys. J. C **76**, no. 6, 317 (2016)

CMS-EXO-13-002, CERN-EP-2016-068

148. **"Evidence for exclusive $\gamma\gamma \to W^+W^-$ production and constraints on anomalous quartic gauge couplings in pp collisions at $\sqrt{s} = 7$ and 8 TeV"**
V. Khachatryan *et al.* [CMS Collaboration].
arXiv:1604.04464 [hep-ex]
DOI:10.1007/JHEP08(2016)119
JHEP **1608**, 119 (2016)
CMS-FSQ-13-008, CERN-EP-2016-073

149. **"Search for dark matter particles in proton-proton collisions at $\sqrt{s} = 8$ TeV using the razor variables"**
V. Khachatryan *et al.* [CMS Collaboration].
arXiv:1603.08914 [hep-ex]
DOI:10.1007/JHEP12(2016)088
JHEP **1612**, 088 (2016)
CMS-EXO-14-004, CERN-EP-2016-025

150. **"Search for two Higgs bosons in final states containing two photons and two bottom quarks in proton-proton collisions at 8 TeV"**
V. Khachatryan *et al.* [CMS Collaboration].
arXiv:1603.06896 [hep-ex]
DOI:10.1103/PhysRevD.94.052012
Phys. Rev. D **94**, no. 5, 052012 (2016)
CMS-HIG-13-032, CERN-EP-2016-050

151. **"Measurement of the top quark mass using charged particles in pp collisions at $\sqrt{s} =$ 8 TeV"**
V. Khachatryan *et al.* [CMS Collaboration].
arXiv:1603.06536 [hep-ex]
DOI:10.1103/PhysRevD.93.092006
Phys. Rev. D **93**, no. 9, 092006 (2016)
CMS-TOP-12-030, CERN-EP-2016-062

152. **"Measurements of $t\bar{t}$ charge asymmetry using dilepton final states in pp collisions at $\sqrt{s} = 8$ TeV"**
V. Khachatryan *et al.* [CMS Collaboration].
arXiv:1603.06221 [hep-ex]
DOI:10.1016/j.physletb.2016.07.006
Phys. Lett. B **760**, 365 (2016)
CMS-TOP-15-009, CERN-EP-2016-059

153. **"Search for new physics with the M_{T2} variable in all-jets final states produced in pp collisions at $\sqrt{s} = 13$ TeV"**
V. Khachatryan *et al.* [CMS Collaboration].
arXiv:1603.04053 [hep-ex]
DOI:10.1007/JHEP10(2016)006
JHEP **1610**, 006 (2016)
CMS-SUS-15-003, CERN-EP-2016-067

154. **"Search for neutral resonances decaying into a Z boson and a pair of b jets or tau leptons"**
V. Khachatryan *et al.* [CMS Collaboration].
arXiv:1603.02991 [hep-ex]
DOI:10.1016/j.physletb.2016.05.087
Phys. Lett. B **759**, 369 (2016)
CMS-HIG-15-001, CERN-EP-2016-039

155. **"Υ(nS) polarizations versus particle multiplicity in pp collisions at $\sqrt{s} = 7$ TeV"**
V. Khachatryan *et al.* [CMS Collaboration].
arXiv:1603.02913 [hep-ex]
DOI:10.1016/j.physletb.2016.07.065
Phys. Lett. B **761**, 31 (2016)
CMS-HIN-15-003, CERN-PH-EP-2015-310

156. **"Search for s channel single top quark production in pp collisions at $\sqrt{s} = 7$ and 8 TeV"**
V. Khachatryan *et al.* [CMS Collaboration].
arXiv:1603.02555 [hep-ex]
DOI:10.1007/JHEP09(2016)027
JHEP **1609**, 027 (2016)
CMS-TOP-13-009, CERN-EP-2016-045

157. **"Measurement of the t-tbar production cross section in the e-mu channel in proton-proton collisions at sqrt(s) = 7 and 8 TeV"**
V. Khachatryan *et al.* [CMS Collaboration].
arXiv:1603.02303 [hep-ex]
DOI:10.1007/JHEP08(2016)029
JHEP **1608**, 029 (2016)
CMS-TOP-13-004, CERN-EP-2016-044

158. **"Search for heavy Majorana neutrinos in $e^{\pm}e^{\pm}$+ jets and $e^{\pm}$ $\mu^{\pm}$+ jets events in proton-proton collisions at $\sqrt{s} = 8$ TeV"**
V. Khachatryan *et al.* [CMS Collaboration].

arXiv:1603.02248 [hep-ex]
DOI:10.1007/JHEP04(2016)169
JHEP **1604**, 169 (2016)
CMS-EXO-14-014, CERN-EP-2016-032

159. **"Measurement of the differential cross section and charge asymmetry for inclusive $pp \to W^{\pm} + X$ production at $\sqrt{s} = 8$ TeV"**
V. Khachatryan *et al.* [CMS Collaboration].
arXiv:1603.01803 [hep-ex]
DOI:10.1140/epjc/s10052-016-4293-4
Eur. Phys. J. C **76**, no. 8, 469 (2016)
CMS-SMP-14-022, CERN-EP-2016-043

160. **"Search for direct pair production of supersymmetric top quarks decaying to all-hadronic final states in pp collisions at $\sqrt{s} = 8$ TeV"**
V. Khachatryan *et al.* [CMS Collaboration].
arXiv:1603.00765 [hep-ex]
DOI:10.1140/epjc/s10052-016-4292-5
Eur. Phys. J. C **76**, no. 8, 460 (2016)
CMS-SUS-13-023, CERN-EP-2016-040

161. **"Measurements of the $t\bar{t}$ production cross section in lepton+jets final states in pp collisions at 8 TeV and ratio of 8 to 7 TeV cross sections"**
V. Khachatryan *et al.* [CMS Collaboration].
arXiv:1602.09024 [hep-ex]
DOI:10.1140/epjc/s10052-016-4504-z
Eur. Phys. J. C **77**, no. 1, 15 (2017)
CMS-TOP-12-006, CERN-EP-2016-016

162. **"Search for supersymmetry in electroweak production with photons and large missing transverse energy in pp collisions at sqrt(s) = 8 TeV"**
V. Khachatryan *et al.* [CMS Collaboration].
arXiv:1602.08772 [hep-ex]
DOI:10.1016/j.physletb.2016.05.088
Phys. Lett. B **759**, 479 (2016)
CMS-SUS-14-016, CERN-EP-2016-012

163. **"Search for heavy resonances decaying to two Higgs bosons in final states containing four b quarks"**
V. Khachatryan *et al.* [CMS Collaboration].
arXiv:1602.08762 [hep-ex]
DOI:10.1140/epjc/s10052-016-4206-6

Eur. Phys. J. C **76**, no. 7, 371 (2016)
CMS-EXO-12-053, CERN-EP-2016-041

164. **"Measurement of the $Z\gamma \to \nu\bar{\nu}\gamma$ production cross section in pp collisions at $\sqrt{s} = 8$ TeV and limits on anomalous $ZZ\gamma$ and $Z\gamma\gamma$ trilinear gauge boson couplings"**
V. Khachatryan *et al.* [CMS Collaboration].
arXiv:1602.07152 [hep-ex]
DOI:10.1016/j.physletb.2016.06.080
Phys. Lett. B **760**, 448 (2016)
CMS-SMP-14-019, CERN-EP-2016-007

165. **"Search for supersymmetry in the multijet and missing transverse momentum final state in pp collisions at 13 TeV"**
V. Khachatryan *et al.* [CMS Collaboration].
arXiv:1602.06581 [hep-ex]
DOI:10.1016/j.physletb.2016.05.002
Phys. Lett. B **758**, 152 (2016)
CMS-SUS-15-002, CERN-EP-2016-036, FERMILAB-PUB-16-056-CMS

166. **"Measurement of dijet azimuthal decorrelation in pp collisions at $\sqrt{s} = 8\,\text{TeV}$"**
V. Khachatryan *et al.* [CMS Collaboration].
arXiv:1602.04384 [hep-ex]
DOI:10.1140/epjc/s10052-016-4346-8
Eur. Phys. J. C **76**, no. 10, 536 (2016)
CMS-SMP-14-015, CERN-EP-2016-013, CERN-SMP-14-015

167. **"Search for R-parity violating decays of a top squark in proton-proton collisions at $\sqrt{s}$ = 8 TeV"**
V. Khachatryan *et al.* [CMS Collaboration].
arXiv:1602.04334 [hep-ex]
DOI:10.1016/j.physletb.2016.06.039
Phys. Lett. B **760**, 178 (2016)
CMS-EXO-14-013, CERN-EP-2016-005

168. **"Combined search for anomalous pseudoscalar HVV couplings in VH(H $\to b\bar{b}$) production and H $\to$ VV decay"**
V. Khachatryan *et al.* [CMS Collaboration].
arXiv:1602.04305 [hep-ex]
DOI:10.1016/j.physletb.2016.06.004
Phys. Lett. B **759**, 672 (2016)
CMS-HIG-14-035, CERN-PH-EP-2015-331

169. **"Search for direct pair production of scalar top quarks in the single- and dilepton channels in proton-proton collisions at $\sqrt{s} = 8$ TeV"**
V. Khachatryan *et al.* [CMS Collaboration].
arXiv:1602.03169 [hep-ex]
DOI:10.1007/JHEP07(2016)027, 10.1007/JHEP09(2016)056
JHEP **1607**, 027 (2016), Erratum: [JHEP **1609**, 056 (2016)]
CMS-SUS-14-015, CERN-EP-2016-004

170. **"Search for supersymmetry in pp collisions at sqrt(s) = 8 TeV in final states with boosted W bosons and b jets using razor variables"**
V. Khachatryan *et al.* [CMS Collaboration].
arXiv:1602.02917 [hep-ex]
DOI:10.1103/PhysRevD.93.092009
Phys. Rev. D **93**, no. 9, 092009 (2016)
CMS-SUS-14-007, CERN-EP-2016-008

171. **"Azimuthal decorrelation of jets widely separated in rapidity in pp collisions at $\sqrt{s} =$ 7 TeV"**
V. Khachatryan *et al.* [CMS Collaboration].
arXiv:1601.06713 [hep-ex]
DOI:10.1007/JHEP08(2016)139
JHEP **1608**, 139 (2016)
CMS-FSQ-12-002, CERN-PH-EP-2015-309

172. **"Search for massive WH resonances decaying into the $\ell\nu\mathrm{b\bar{b}}$ final state at $\sqrt{s} = 8$ TeV"**
V. Khachatryan *et al.* [CMS Collaboration].
arXiv:1601.06431 [hep-ex]
DOI:10.1140/epjc/s10052-016-4067-z
Eur. Phys. J. C **76**, no. 5, 237 (2016)
CMS-EXO-14-010, CERN-PH-EP-2015-332

173. **"Forward–backward asymmetry of Drell–Yan lepton pairs in pp collisions at $\sqrt{s} = 8$ TeV"**
V. Khachatryan *et al.* [CMS Collaboration].
arXiv:1601.04768 [hep-ex]
DOI:10.1140/epjc/s10052-016-4156-z
Eur. Phys. J. C **76**, no. 6, 325 (2016)
CMS-SMP-14-004, CERN-PH-EP-2015-295

174. **"Measurement of inclusive jet production and nuclear modifications in pPb collisions at $\sqrt{s_{\mathrm{NN}}} = 5.02$ TeV"**

V. Khachatryan *et al.* [CMS Collaboration].
arXiv:1601.02001 [nucl-ex]
DOI:10.1140/epjc/s10052-016-4205-7
Eur. Phys. J. C **76**, no. 7, 372 (2016)
CMS-HIN-14-001, CERN-PH-EP-2015-334

175. **"Measurements of t t-bar spin correlations and top quark polarization using dilepton final states in pp collisions at sqrt(s) = 8 TeV"**
V. Khachatryan *et al.* [CMS Collaboration].
arXiv:1601.01107 [hep-ex]
DOI:10.1103/PhysRevD.93.052007
Phys. Rev. D **93**, no. 5, 052007 (2016)
CMS-TOP-14-023, CERN-PH-EP-2015-333

176. **"Correlations between jets and charged particles in PbPb and pp collisions at $\sqrt{s_{\mathrm{NN}}} =$ 2.76 TeV"**
V. Khachatryan *et al.* [CMS Collaboration].
arXiv:1601.00079 [nucl-ex]
DOI:10.1007/JHEP02(2016)156
JHEP **1602**, 156 (2016)
CMS-HIN-14-016, CERN-PH-EP-2015-329

177. **"Measurement of differential and integrated fiducial cross sections for Higgs boson production in the four-lepton decay channel in pp collisions at $\sqrt{s} = 7$ and 8 TeV"**
V. Khachatryan *et al.* [CMS Collaboration].
arXiv:1512.08377 [hep-ex]
DOI:10.1007/JHEP04(2016)005
JHEP **1604**, 005 (2016)
CMS-HIG-14-028, CERN-PH-EP-2015-285

178. **"Search for supersymmetry in events with soft leptons, low jet multiplicity, and missing transverse energy in proton–proton collisions at $\sqrt{s}$=8 TeV"**
V. Khachatryan *et al.* [CMS Collaboration].
arXiv:1512.08002 [hep-ex]
DOI:10.1016/j.physletb.2016.05.033
Phys. Lett. B **759**, 9 (2016)
CMS-SUS-14-021, CERN-PH-EP-2015-307

179. **"Study of Z boson production in pPb collisions at $\sqrt{sNN}$=5.02TeV"**
V. Khachatryan *et al.* [CMS Collaboration].
arXiv:1512.06461 [hep-ex]
DOI:10.1016/j.physletb.2016.05.044

Phys. Lett. B **759**, 36 (2016)
CMS-HIN-15-002, CERN-PH-EP-2015-302

180. **"Measurement of the inclusive jet cross section in pp collisions at $\sqrt{s} = 2.76$ TeV"**
V. Khachatryan *et al.* [CMS Collaboration].
arXiv:1512.06212 [hep-ex]
DOI:10.1140/epjc/s10052-016-4083-z
Eur. Phys. J. C **76**, no. 5, 265 (2016)
CMS-SMP-14-017, CERN-PH-EP-2015-299

181. **"Search for narrow resonances decaying to dijets in proton-proton collisions at $\sqrt{(}s) =$ 13 TeV"**
V. Khachatryan *et al.* [CMS Collaboration].
arXiv:1512.01224 [hep-ex]
DOI:10.1103/PhysRevLett.116.071801
Phys. Rev. Lett. **116**, no. 7, 071801 (2016)
CMS-EXO-15-001, CERN-PH-EP-2015-317

182. **"Event generator tunes obtained from underlying event and multiparton scattering measurements"**
V. Khachatryan *et al.* [CMS Collaboration].
arXiv:1512.00815 [hep-ex]
DOI:10.1140/epjc/s10052-016-3988-x
Eur. Phys. J. C **76**, no. 3, 155 (2016)
CMS-GEN-14-001, CERN-PH-EP-2015-291

183. **"Search for dark matter and unparticles produced in association with a Z boson in proton-proton collisions at $\sqrt{s} = 8$ TeV"**
V. Khachatryan *et al.* [CMS Collaboration].
arXiv:1511.09375 [hep-ex]
DOI:10.1103/PhysRevD.93.052011
Phys. Rev. D **93**, no. 5, 052011 (2016)
CMS-EXO-12-054, CERN-PH-EP-2015-297

184. **"Measurement of spin correlations in $t\bar{t}$ production using the matrix element method in the muon+jets final state in pp collisions at $\sqrt{s} = 8$ TeV"**
V. Khachatryan *et al.* [CMS Collaboration].
arXiv:1511.06170 [hep-ex]
DOI:10.1016/j.physletb.2016.05.005
Phys. Lett. B **758**, 321 (2016)
CMS-TOP-13-015, CERN-PH-EP-2015-289, FERMILAB-PUB-15-512-CMS

185. **"Search for anomalous single top quark production in association with a photon in pp collisions at $\sqrt{s} = 8$ TeV"**
V. Khachatryan *et al.* [CMS Collaboration].
arXiv:1511.03951 [hep-ex]
DOI:10.1007/JHEP04(2016)035
JHEP **1604**, 035 (2016)
CMS-TOP-14-003, CERN-PH-EP-2015-287

186. **"Search for a low-mass pseudoscalar Higgs boson produced in association with a $b\bar{b}$ pair in pp collisions at $\sqrt{s} = 8$ TeV"**
V. Khachatryan *et al.* [CMS Collaboration].
arXiv:1511.03610 [hep-ex]
DOI:10.1016/j.physletb.2016.05.003
Phys. Lett. B **758**, 296 (2016)
CMS-HIG-14-033, CERN-PH-EP-2015-284, FERMILAB-PUB-15-514-CMS

187. **"Measurement of top quark polarisation in t-channel single top quark production"**
V. Khachatryan *et al.* [CMS Collaboration].
arXiv:1511.02138 [hep-ex]
DOI:10.1007/JHEP04(2016)073
JHEP **1604**, 073 (2016)
CMS-TOP-13-001, CERN-PH-EP-2015-282

188. **"Search for excited leptons in proton-proton collisions at sqrt(s) = 8 TeV"**
V. Khachatryan *et al.* [CMS Collaboration].
arXiv:1511.01407 [hep-ex]
DOI:10.1007/JHEP03(2016)125
JHEP **1603**, 125 (2016)
CMS-EXO-14-015, CERN-PH-EP-2015-281

189. **"Reconstruction and identification of τ lepton decays to hadrons and ν_τ at CMS"**
V. Khachatryan *et al.* [CMS Collaboration].
arXiv:1510.07488 [physics.ins-det]
DOI:10.1088/1748-0221/11/01/P01019
JINST **11**, no. 01, P01019 (2016)
CMS-TAU-14-001, CERN-PH-EP-2015-261

190. **"Search for a very light NMSSM Higgs boson produced in decays of the 125 GeV scalar boson and decaying into τ leptons in pp collisions at $\sqrt{s} = 8$ TeV"**
V. Khachatryan *et al.* [CMS Collaboration].
arXiv:1510.06534 [hep-ex]
DOI:10.1007/JHEP01(2016)079

JHEP **1601**, 079 (2016)
CMS-HIG-14-019, CERN-PH-EP-2015-264

191. **"Measurement of the top quark pair production cross section in proton-proton collisions at $\sqrt{(}s) =$ 13 TeV"**
V. Khachatryan *et al.* [CMS Collaboration].
arXiv:1510.05302 [hep-ex]
DOI:10.1103/PhysRevLett.116.052002
Phys. Rev. Lett. **116**, no. 5, 052002 (2016)
CMS-TOP-15-003, CERN-PH-EP-2015-280

192. **"Search for a light charged Higgs boson decaying to $\mathrm{c\bar{s}}$ in pp collisions at $\sqrt{s} = 8$ TeV"**
V. Khachatryan *et al.* [CMS Collaboration].
arXiv:1510.04252 [hep-ex]
DOI:10.1007/JHEP12(2015)178
JHEP **1512**, 178 (2015)
CMS-HIG-13-035, CERN-PH-EP-2015-266

193. **"Transverse momentum spectra of inclusive b jets in pPb collisions at $\sqrt{s_{NN}} =$ 5.02 TeV"**
V. Khachatryan *et al.* [CMS Collaboration].
arXiv:1510.03373 [nucl-ex]
DOI:10.1016/j.physletb.2016.01.010
Phys. Lett. B **754**, 59 (2016)
CMS-HIN-14-007, CERN-PH-EP-2015-205

194. **"Measurement of $\mathrm{t\bar{t}}$ production with additional jet activity, including b quark jets, in the dilepton decay channel using pp collisions at $\sqrt{s} =$ 8 TeV"**
V. Khachatryan *et al.* [CMS Collaboration].
arXiv:1510.03072 [hep-ex]
DOI:10.1140/epjc/s10052-016-4105-x
Eur. Phys. J. C **76**, no. 7, 379 (2016)
CMS-TOP-12-041, CERN-PH-EP-2015-240

195. **"Measurement of long-range near-side two-particle angular correlations in pp collisions at $\sqrt{s} =$13 TeV"**
V. Khachatryan *et al.* [CMS Collaboration].
arXiv:1510.03068 [nucl-ex]
DOI:10.1103/PhysRevLett.116.172302
Phys. Rev. Lett. **116**, no. 17, 172302 (2016)
CMS-FSQ-15-002, CERN-PH-EP-2015-271

196. **"Searches for a heavy scalar boson H decaying to a pair of 125 GeV Higgs bosons hh or for a heavy pseudoscalar boson A decaying to Zh, in the final states with $h \to \tau\tau$"**
V. Khachatryan *et al.* [CMS Collaboration].
arXiv:1510.01181 [hep-ex]
DOI:10.1016/j.physletb.2016.01.056
Phys. Lett. B **755**, 217 (2016)
CMS-HIG-14-034, CERN-PH-EP-2015-211

197. **"Observation of top quark pairs produced in association with a vector boson in pp collisions at $\sqrt{s} = 8$ TeV"**
V. Khachatryan *et al.* [CMS Collaboration].
arXiv:1510.01131 [hep-ex]
DOI:10.1007/JHEP01(2016)096
JHEP **1601**, 096 (2016)
CMS-TOP-14-021, CERN-PH-EP-2015-248

198. **"Measurement of transverse momentum relative to dijet systems in PbPb and pp collisions at $\sqrt{s_{\mathrm{NN}}} = 2.76$ TeV"**
V. Khachatryan *et al.* [CMS Collaboration].
arXiv:1509.09029 [nucl-ex]
DOI:10.1007/JHEP01(2016)006
JHEP **1601**, 006 (2016)
CMS-HIN-14-010, CERN-PH-EP-2015-260

199. **"Search for the associated production of a Higgs boson with a single top quark in proton-proton collisions at $\sqrt{s} = 8$ TeV"**
V. Khachatryan *et al.* [CMS Collaboration].
arXiv:1509.08159 [hep-ex]
DOI:10.1007/JHEP06(2016)177
JHEP **1606**, 177 (2016)
CMS-HIG-14-027, CERN-PH-EP-2015-255

200. **"Search for the production of an excited bottom quark decaying to tW in proton-proton collisions at $\sqrt{s} = 8$ TeV"**
V. Khachatryan *et al.* [CMS Collaboration].
arXiv:1509.08141 [hep-ex]
DOI:10.1007/JHEP01(2016)166
JHEP **1601**, 166 (2016)
CMS-B2G-14-005, CERN-PH-EP-2015-246

201. **"Measurement of the $\mathrm{t\bar{t}}$ production cross section in the all-jets final state in pp collisions at $\sqrt{s} = 8$ TeV"**

V. Khachatryan *et al.* [CMS Collaboration].
arXiv:1509.06076 [hep-ex]
DOI:10.1140/epjc/s10052-016-3956-5
Eur. Phys. J. C **76**, no. 3, 128 (2016)
CMS-TOP-14-018, CERN-PH-EP-2015-243

202. **"Search for $W' \to tb$ in proton-proton collisions at $\sqrt{s} = 8$ TeV"**
V. Khachatryan *et al.* [CMS Collaboration].
arXiv:1509.06051 [hep-ex]
DOI:10.1007/JHEP02(2016)122
JHEP **1602**, 122 (2016)
CMS-B2G-12-009, CERN-PH-EP-2015-231

203. **"Search for vector-like charge 2/3 T quarks in proton-proton collisions at sqrt(s) = 8 TeV"**
V. Khachatryan *et al.* [CMS Collaboration].
arXiv:1509.04177 [hep-ex]
DOI:10.1103/PhysRevD.93.012003
Phys. Rev. D **93**, no. 1, 012003 (2016)
CMS-B2G-13-005, CERN-PH-EP-2015-228

204. **"Measurement of the top quark mass using proton-proton data at $\sqrt{(s)}$ = 7 and 8 TeV"**
V. Khachatryan *et al.* [CMS Collaboration].
arXiv:1509.04044 [hep-ex]
DOI:10.1103/PhysRevD.93.072004
Phys. Rev. D **93**, no. 7, 072004 (2016)
CMS-TOP-14-022, CERN-PH-EP-2015-234

205. **"Measurement of the inelastic cross section in proton–lead collisions at $\sqrt{s_{NN}} = 5.02$ TeV"**
V. Khachatryan *et al.* [CMS Collaboration].
arXiv:1509.03893 [hep-ex]
DOI:10.1016/j.physletb.2016.06.027
Phys. Lett. B **759**, 641 (2016)
CMS-FSQ-13-006, CERN-PH-EP-2015-210

206. **"Search for single production of scalar leptoquarks in proton-proton collisions at $\sqrt{s} = 8$ *TeV*"**
V. Khachatryan *et al.* [CMS Collaboration].
arXiv:1509.03750 [hep-ex]
DOI:10.1103/PhysRevD.95.039906, 10.1103/PhysRevD.93.032005

Phys. Rev. D **93**, no. 3, 032005 (2016), Erratum: [Phys. Rev. D **95**, no. 3, 039906 (2017)]
CMS-EXO-12-043, CERN-PH-EP-2015-149

207. **"Search for pair production of first and second generation leptoquarks in proton-proton collisions at sqrt(s) = 8 TeV"**
V. Khachatryan *et al.* [CMS Collaboration].
arXiv:1509.03744 [hep-ex]
DOI:10.1103/PhysRevD.93.032004
Phys. Rev. D **93**, no. 3, 032004 (2016)
CMS-EXO-12-041, CERN-PH-EP-2015-197

208. **"Measurement of differential cross sections for Higgs boson production in the diphoton decay channel in pp collisions at $\sqrt{s} = 8$ TeV"**
V. Khachatryan *et al.* [CMS Collaboration].
arXiv:1508.07819 [hep-ex]
DOI:10.1140/epjc/s10052-015-3853-3
Eur. Phys. J. C **76**, no. 1, 13 (2016)
CMS-HIG-14-016, CERN-PH-EP-2015-195

209. **"Search for a charged Higgs boson in pp collisions at $\sqrt{s} = 8$ TeV"**
V. Khachatryan *et al.* [CMS Collaboration].
arXiv:1508.07774 [hep-ex]
DOI:10.1007/JHEP11(2015)018
JHEP **1511**, 018 (2015)
CMS-HIG-14-023, CERN-PH-EP-2015-221

210. **"Search for supersymmetry in the vector-boson fusion topology in proton-proton collisions at $\sqrt{s} = 8$ TeV"**
V. Khachatryan *et al.* [CMS Collaboration].
arXiv:1508.07628 [hep-ex]
DOI:10.1007/JHEP11(2015)189
JHEP **1511**, 189 (2015)
CMS-SUS-14-005, CERN-PH-EP-2015-213

211. **"Study of B Meson Production in p+Pb Collisions at $\sqrt{(}s_{NN} =$5.02 TeV Using Exclusive Hadronic Decays"**
V. Khachatryan *et al.* [CMS Collaboration].
arXiv:1508.06678 [nucl-ex]
DOI:10.1103/PhysRevLett.116.032301
Phys. Rev. Lett. **116**, no. 3, 032301 (2016)
CMS-HIN-14-004, CERN-PH-EP-2015-209

212. **"Search for W' decaying to tau lepton and neutrino in proton-proton collisions at $\sqrt{(s)} =$ 8 TeV"**
V. Khachatryan *et al.* [CMS Collaboration].
arXiv:1508.04308 [hep-ex]
DOI:10.1016/j.physletb.2016.02.002
Phys. Lett. B **755**, 196 (2016)
CMS-EXO-12-011, CERN-PH-EP-2015-190

213. **"Measurement of the charge asymmetry in top quark pair production in pp collisions at $\sqrt{(s)} =$ 8 TeV using a template method"**
V. Khachatryan *et al.* [CMS Collaboration].
arXiv:1508.03862 [hep-ex]
DOI:10.1103/PhysRevD.93.034014
Phys. Rev. D **93**, no. 3, 034014 (2016)
CMS-TOP-13-013, CERN-PH-EP-2015-189

214. **"Search for neutral MSSM Higgs bosons decaying to $\mu^+\mu^-$ in pp collisions at $\sqrt{s} =$ 7 and 8 TeV"**
V. Khachatryan *et al.* [CMS Collaboration].
arXiv:1508.01437 [hep-ex]
DOI:10.1016/j.physletb.2015.11.042
Phys. Lett. B **752**, 221 (2016)
CMS-HIG-13-024, CERN-PH-EP-2015-148

215. **"Search for supersymmetry in events with a photon, a lepton, and missing transverse momentum in pp collisions at $\sqrt{s} =$ 8 TeV"**
V. Khachatryan *et al.* [CMS Collaboration].
arXiv:1508.01218 [hep-ex]
DOI:10.1016/j.physletb.2016.03.039
Phys. Lett. B **757**, 6 (2016)
CMS-SUS-14-013, CERN-PH-EP-2015-169

216. **"Angular analysis of the decay $B^0 \to K^{*0}\mu^+\mu^-$ from pp collisions at $\sqrt{s} = 8$ TeV"**
V. Khachatryan *et al.* [CMS Collaboration].
arXiv:1507.08126 [hep-ex]
DOI:10.1016/j.physletb.2015.12.020
Phys. Lett. B **753**, 424 (2016)
CMS-BPH-13-010, CERN-PH-EP-2015-178

217. **"Measurement of the CP-violating weak phase ϕ_s and the decay width difference $\Delta\Gamma_s$ using the $B_s^0 \to J/\psi\phi(1020)$ decay channel in pp collisions at $\sqrt{s} =$ 8 TeV"**
V. Khachatryan *et al.* [CMS Collaboration].

arXiv:1507.07527 [hep-ex]
DOI:10.1016/j.physletb.2016.03.046
Phys. Lett. B **757**, 97 (2016)
CMS-BPH-13-012, CERN-PH-EP-2015-192

218. **"Measurement of the underlying event activity using charged-particle jets in proton-proton collisions at sqrt(s) = 2.76 TeV"**
V. Khachatryan *et al.* [CMS Collaboration].
arXiv:1507.07229 [hep-ex]
DOI:10.1007/JHEP09(2015)137
JHEP **1509**, 137 (2015)
CMS-FSQ-12-025, CERN-PH-EP-2015-176

219. **"Search for pair-produced vectorlike B quarks in proton-proton collisions at $\sqrt{s}$=8 TeV"**
V. Khachatryan *et al.* [CMS Collaboration].
arXiv:1507.07129 [hep-ex]
DOI:10.1103/PhysRevD.93.112009
Phys. Rev. D **93**, no. 11, 112009 (2016)
CMS-B2G-13-006, CERN-PH-EP-2015-170

220. **"Limits on the Higgs boson lifetime and width from its decay to four charged leptons"**
V. Khachatryan *et al.* [CMS Collaboration].
arXiv:1507.06656 [hep-ex]
DOI:10.1103/PhysRevD.92.072010
Phys. Rev. D **92**, no. 7, 072010 (2015)
CMS-HIG-14-036, CERN-PH-EP-2015-159

221. **"Pseudorapidity distribution of charged hadrons in proton-proton collisions at $\sqrt{s}$ = 13 TeV"**
V. Khachatryan *et al.* [CMS Collaboration].
arXiv:1507.05915 [hep-ex]
DOI:10.1016/j.physletb.2015.10.004
Phys. Lett. B **751**, 143 (2015)
CMS-FSQ-15-001, CERN-PH-EP-2015-180

222. **"Measurement of the W^+W^- cross section in pp collisions at $\sqrt{s} = 8$ TeV and limits on anomalous gauge couplings"**
V. Khachatryan *et al.* [CMS Collaboration].
arXiv:1507.03268 [hep-ex]
DOI:10.1140/epjc/s10052-016-4219-1

Eur. Phys. J. C **76**, no. 7, 401 (2016)
CMS-SMP-14-016, CERN-PH-EP-2015-122

223. **"Inclusive and differential measurements of the $t\bar{t}$ charge asymmetry in pp collisions at $\sqrt{s} = 8$ TeV"**
V. Khachatryan *et al.* [CMS Collaboration].
arXiv:1507.03119 [hep-ex]
DOI:10.1016/j.physletb.2016.03.060
Phys. Lett. B **757**, 154 (2016)
CMS-TOP-12-033, CERN-PH-EP-2015-141

224. **"Search for a Higgs boson decaying into $\gamma^*\gamma \to \ell\ell\gamma$ with low dilepton mass in pp collisions at $\sqrt{s} = 8$ TeV"**
V. Khachatryan *et al.* [CMS Collaboration].
arXiv:1507.03031 [hep-ex]
DOI:10.1016/j.physletb.2015.12.039
Phys. Lett. B **753**, 341 (2016)
CMS-HIG-14-003, CERN-PH-EP-2015-137

225. **"Search for supersymmetry with photons in pp collisions at $\sqrt{s}$=8 TeV"**
V. Khachatryan *et al.* [CMS Collaboration].
arXiv:1507.02898 [hep-ex]
DOI:10.1103/PhysRevD.92.072006
Phys. Rev. D **92**, no. 7, 072006 (2015)
CMS-SUS-14-004, CERN-PH-EP-2015-129

226. **"Search for exotic decays of a Higgs boson into undetectable particles and one or more photons"**
V. Khachatryan *et al.* [CMS Collaboration].
arXiv:1507.00359 [hep-ex]
DOI:10.1016/j.physletb.2015.12.017
Phys. Lett. B **753**, 363 (2016)
CMS-HIG-14-025, CERN-PH-EP-2015-131

227. **"Production of leading charged particles and leading charged-particle jets at small transverse momenta in pp collisions at sqrt(s) = 8 TeV"**
V. Khachatryan *et al.* [CMS Collaboration].
arXiv:1507.00233 [hep-ex]
DOI:10.1103/PhysRevD.92.112001
Phys. Rev. D **92**, no. 11, 112001 (2015)
CMS-FSQ-12-032, CERN-PH-EP-2015-135

228. **"Search for neutral MSSM Higgs bosons decaying into a pair of bottom quarks"**
V. Khachatryan *et al.* [CMS Collaboration].
arXiv:1506.08329 [hep-ex]
DOI:10.1007/JHEP11(2015)071
JHEP **1511**, 071 (2015)
CMS-HIG-14-017, CERN-PH-EP-2015-133

229. **"Search for resonant $t\bar{t}$ production in proton-proton collisions at $\sqrt{s} = 8$ TeV"**
V. Khachatryan *et al.* [CMS Collaboration].
arXiv:1506.03062 [hep-ex]
DOI:10.1103/PhysRevD.93.012001
Phys. Rev. D **93**, no. 1, 012001 (2016)
CMS-B2G-13-008, CERN-PH-EP-2015-126